AFIT/DS/ENY/96-2

MODELING OF PROGRESSIVE DAMAGE IN FIBER-REINFORCED

CERAMIC MATRIX COMPOSITES

DISSERTATION
James P. Solti
Captain, USAF

AFIT/DS/ENY/96-2

19960304 006

Approved for public release; distribution unlimited

AFIT/DS/ENY/96-2

MODELING OF PROGRESSIVE DAMAGE IN
FIBER-REINFORCED CERAMIC MATRIX COMPOSITES

DISSERTATION

Presented to the Faculty of the Graduate School of Engineering

of the Air Force Institute of Technology

Air Education and Training Command

In Partial Fulfillment of the

Requirements for the Degree of

Doctor of Philosophy

James P. Solti, B.S., M.S.M., M.S.
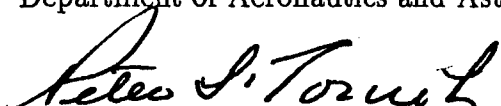
Captain, USAF

March, 1996

MODELING OF PROGRESSIVE DAMAGE IN
FIBER-REINFORCED CERAMIC MATRIX COMPOSITES

James P. Solti, B.S., M.S.M., M.S.

Captain, USAF

Approved:
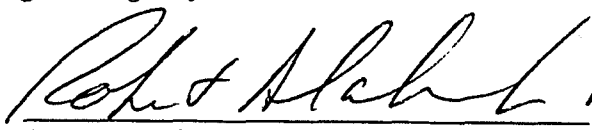
15 Feb 1996

SHANKAR MALL, Research Advisor
Professor and Department Head
Department of Aeronautics and Astronautics

15 Feb 1996

PETER J. TORVIK, Committee Member
Professor of Aerospace Engineering and Engineering Mechanics
Department of Aeronautics and Astronautics

15 Feb 1996

ALAN V. LAIR, Committee Member
Professor and Department Head
Department of Mathematics and Statistics

15 Feb 1996

DAVID D. ROBERTSON, Committee Member
Major, USAF
Department of Aeronautics and Astronautics

15 Feb 1996

KIRK A. MATHEWS, Dean's Representative
Associate Professor of Nuclear Engineering
Department of Engineering Physics

16 Feb 96

Robert A. Calico, Jr.
Dean, Graduate School of Engineering

Acknowledgements

This work is dedicated to my parents
George and Joan Solti

I'd like to express my sincere appreciation to the many individuals who had a hand in the completion of this research. This document represents only a small part of what these people have taught me about dedication, determination and friendship.

I would like to begin by thanking the Wright Laboratory Propulsion Directorate for their support and sponsorship. In particular, Mr. Ted Fecke and Mrs. Sylvin Oxley for their insight and knowledge of practical applications for ceramic matrix composites. Their help is much appreciated.

I owe a great debt to my research advisor, Prof. Shankar Mall, who's support and direction has meant a great deal to me. The same is true of my co-advisor, Major David Robertson, who was also their every step of the way. I'd like to thank these two gentlemen for their tireless efforts, great insight, and especially for their friendship. I'd also like to thank my other committee members, Prof. Peter Torvik, Prof. Alan Lair, and, representing the dean, Prof. Kirk Mathews for their support and time spent in evaluation of the research. It is very much appreciated.

Thanks especially to Jim Greer and Rich Cobb for making it fun.

As in anything, it's the support community that makes things happen. A special thanks to Kristin Larsen, Robert Forbes, Jan Long, Kathy Dillon, Jennifer Wedekind and all the lab technicians: Jay Anderson, Mark Derriso, Andy Pitts, Dan Rioux, Susan Wellbaum and Charley McNeely.

Thanks to my wife, Christine, who gave me the strength and desire each and every day.

Finally, I'd like to thank God for giving me the opportunities, strength, and friendships which have developed over the course of this program.

James P. Solti

Preface

The research presented in this document is a synthesis of (1) existing theories as they were originally proposed, (2) existing theories modified or extended to be consistent with the current analysis, and (3) new work formulated by the author over the past three years. In an attempt to make the text of the document cohesive and smooth, these three areas are occasionally blended together for the purpose of forming a single consistent and comprehensive idea. To clarify, the material presented in chapters three through five and appendices C through I represents work accomplished as part of the current research except for the introductory shear-lag work [Eqs (3.1) through (3.11); the interface debonding criterion (section 3.2.2); the development of the frictional slip distances for a completely debonded system (section C.1) and, of course, instances where previous works from different authors are appropriately referenced.

Also, at this point and time, a note on some terminology is appropriate. In an attempt to be consistent with the literature, the notation τ_i, $\tau_i(x)$ and $\tau_i(N)$ are used independently. The parameter τ_i is the interface shear stress which develops within regions where the fiber/matrix constituents have debonded. Furthermore, this stress is assumed to be of constant magnitude within each loading and unloading cycle in order to make the analysis tractable as is common to the literature. Within regions where the fiber and matrix remain physically bonded, the interface shear is denoted $\tau_i(x)$ since it varies as a function of the axial coordinate x. The formulation of these stresses, τ_i and $\tau_i(x)$, as well as their mathematical representations are fundamentally different and should not be confused. In addition, when considering fatigue loading environments, the interface shear τ_i is allowed to vary *between* loading cycles and is, therefore, denoted with the term $\tau_i(N)$ to emphasize its dependence on the loading cycle, N.

iv

Finally, phrases such as "current analysis" and "present model" are intended to indicate work accomplished by the author over the past three years and are *not* intended to be synonymous with "recent" or "up to date" work accomplished by other authors.

James P. Solti

Table of Contents

List of Figures

xv

List of Tables

List of Symbols

The following list of terms defines some of the variables used in this document. The use of the term *axial* refers to the coordinate direction parallel to the fibers in the 0° plies. This direction also corresponds with the loading axis. The term *transverse* implies the coordinate direction orthogonal to the axial direction and parallel with the fibers in the 90° plies.

a .... assumed length of a microstructural flaw

A_f .... cross-sectional area of the composite fiber

A_m .... cross-sectional area of the composite matrix

A_c .... composite cross-sectional area

α_c .... coefficient of thermal expansion for the composite laminate

α_f .... coefficient of thermal expansion for the composite fiber

α_m .... coefficient of thermal expansion for the composite matrix

α_1 .... laminate thermal coefficient in the axial direction

α_2 .... laminate thermal coefficient in the transverse direction

b .... half thickness of the 0° plies in a cross-ply laminate

β .... shear-lag parameter

CD .... crack density

d .... interface debond length for the unidirectional laminate

d .... half thickness of the 90° plies in a cross-ply laminate

d_l .... interface debond length for $x < 0$ in the cross-ply laminate

d_r .... interface debond length for $x > 0$ in the cross-ply laminate

$\delta(N)$ .... fiber crack opening displacement

Δ .... relative spacing between transverse and matrix cracks

$\Delta\sigma(N)$ .... additional fiber stress resulting from fiber pull-out

$\Delta\sigma_r(N)$ .... modified fiber pull-out stress (relaxation)

ΔT .... temp. differential from max. processing temperature

E_c .... elastic (Young's) modulus of a laminate

E_f .... elastic modulus of the fiber

E_L .... loading modulus

E_m .... elastic modulus of the matrix

E_s .... secant modulus

E_u .... unloading modulus

E_1 .... composite modulus in the axial direction

E_{1_o} .... original or undamaged longitudinal modulus for a given laminate

E_2 .... composite modulus in the transverse direction

ϵ, ϵ_c .... total axial strain of the laminate

ϵ_p .... permanent (residual) strain

ϵ^{th} .... thermal strain

ϵ_{ult} .... ultimate strain of the laminate

g_m .... strain energy release rate (matrix)

g_m^c .... critical strain energy release rate (matrix)

g_{db}^c .... critical strain energy release rate (debonding)

G .... reference page E-10

G_f .... shear modulus of the fiber

G_m .... shear modulus of the matrix

G_{12}, G_{13}, G_{23} . composite shear modulus (in the corresponding directions)

γ_m .... matrix surface energy per unit area

γ_{db} .... surface energy per unit area for a fiber/matrix interface

H .... reference page E-10

$\mathcal{H}$ ...... proportionality (shear-lag) constant for the unidirectional model

$\mathcal{H}_x$ .... proportionality (shear-lag) constant for the cross-ply model

K .... stress intensity factor

K_1^c .... mode I fracture toughness

L .... average crack spacing of the matrix cracks in the 0° plies

L_{init} .... initial crack spacing

L_{sat} .... minimum (saturated) crack spacing

L_t .... average crack spacing of the transverse cracks in the 90° plies

λ .... shear-lag parameter for the cross-ply model

N .... numerical index indicating the number of fatigue cycles

N_{max} .... maximum number of loading cycles

ν .... Poisson's ratio

r_f .... fiber radius

$\overline{r_f}$ .... the closed interval $[0,\ r_f]$

$\overline{r_m}$ .... the closed interval $[r_f,\ R]$

R .... outer radius of shear-lag model

R .... ratio of the minimum to maximum stress during fatigue loading

σ_{cr} .... critical composite stress

σ_{cr}^0 .... critical stress in the 0° ply of a cross-ply laminate

σ_{cr}^{90} .... critical stress in the 90° ply of a cross-ply laminate

σ_{cr_0} .... critical composite stress for a unidirectional laminate

$\sigma_{cr_{90}}$ .... critical composite stress for a 90° ply/laminate

$\sigma_f(x)$ .... axial fiber stress

σ_{f_o} .... rule-of-mixtures fiber stress in the axial direction

σ_{ff} .... stress corresponding to fiber fracture initiation

$\sigma_m(x)$ .... axial matrix stress

σ_{m_o} .... rule-of-mixtures matrix stress in the axial direction

$\sigma_{m_{ult}}$ .... ultimate matrix stress

σ .... applied stress

σ_L^o .... rule-of-mixtures stress for a 0° ply in a cross-ply laminate

$\sigma_L(x)$ .... axial stress in a 0° ply of a cross-ply laminate

σ_t^o .... rule-of-mixtures stress for a 90° ply in a cross-ply laminate

z_{90} .... the closed interval $\pm[d,\ b+d]$

z_l .... left counter-counter-slip distance for the cross-ply model

z_r .... right counter-counter-slip distance for the cross-ply model

Superscripts

th .... thermal

o .... degree

0 .... 0° ply

90 .... 90° ply

Subscripts

c .... composite

f .... fiber

$init$ .... initial

l .... left

m .... matrix

max .... maximum

min .... minimum

r .... right

sat .... saturation

t, T .... transverse

ult .... ultimate

1 .... axial direction

2 .... transverse direction

Nomenclature

$\doteq$ .... defined as

$\equiv$ .... equivalence

$\simeq$ .... approximate

$\mp$ .... minus/plus

$\pm$ .... plus/minus

% .... percent

[] .... closed interval

() .... open interval

{} .... set

∈ {} .... belonging to the set

∈ .... in, an element of

∋ .... such that

∀ .... for all

$\mathcal{F}()$ .... function

Units

GPa .... giga-Pascal

m .... meters

mm .... millimeters

μm .... micrometers

MPa .... mega-Pascal

N .... Newton

°C .... degree Celsius

AFIT/DS/ENY/96-2

Abstract

Ceramic matrix composites exhibit a remarkable increase in strain-to-failure as compared with their monolithic counterparts. The incorporation of the fiber-reinforcement phase into the brittle matrix leads to microstructural interactions which reduce the propensity for catastrophic failure of the laminate. However, ceramic composites are energetically prone to the formation of multiple matrix cracks prior to complete laminate failure. This, combined with the inherent complexities and stochastic nature of failure in non-homogeneous materials, makes the modeling of ceramic matrix composites quite difficult.

The purpose of the research undertaken during this doctoral program and which is detailed in this manuscript is to develop a methodology for predicting the evolution of these damages, as well as the resulting material behavior for fiber-reinforced ceramic matrix composites. In particular, the response of unidirectional and cross-ply laminates when subjected to quasi-static, repeated and fatigue loadings is considered. Towards this end, a set of failure criteria for estimating the progression of microstructural damages and a representative model based on the one-dimensional shear-lag formulation are presented.

The failure criteria introduced in this document are formulated in a manner that is amenable to a variety of solution techniques. The damages considered in the analysis include matrix cracking, fiber/matrix interface slip and debonding, fiber failure and fiber pull-out. The criterion adopted to govern the initiation and evolution of matrix cracks within the ceramic matrix focuses on the instantaneous strain energy of the matrix, whereas the extent of interface debonding is determined in a more traditional manner via a maximum stress criterion. Finally, the evolution of fractures within the fibers is assumed to follow a Weibull type failure distribution where all Weibull parameters are determined explicitly from the analysis except for

the statistical modulus which is determined empirically owing to the variability of failure in different composite systems.

The stress-strain response under monotonic tensile loading, the fatigue life (S-N) relationship, and stress-strain hysteresis under cyclic loading obtained from the present analytical methodology are compared with their experimental counterparts. In all cases, the predicted material behavior is consistent with the experimental data. Modeling of the stress-strain hysteresis requires estimates for the extent of frictional sliding along the fiber/matrix interface. Therefore, formulations of frictional slip for a partially bonded and debonded interface are accomplished herein. Previously, only the fully debonded case was considered. In addition, an analytical approach which is required to capture the continuous development of permanent strain, as experienced under fatigue loading conditions, is developed and presented in this manuscript. The latter allows for the strain ratchetting behavior observed during the fatigue cycling. Degradation of the fiber/matrix interface resulting from frictional wear is also considered.

As expected, the interface plays a dominant role in determining the evolutions of damages and ultimately the material response itself. In particular, the controlling properties are the frictional shear resistance along debonded regions and the bonding strength within fully constrained (bonded) areas. Both parameters may be determined with the current analysis. Moreover, these interface properties determine the strength of coupling between the matrix cracking and interface debonding damage modes, and also the stress transfer rate between the constituents. Under fatigue type loadings, since the properties of the interface can change as a result of frictional wear, the mechanical behavior of the laminate can be significantly altered during conditions of repeated loadings. In addition, the interface degradation allows additional damages to develop as a function of the loading cycle. These are unique phenomena associated with ceramic matrix composites.

This study provides a consistent, systematic and comprehensive methodology for investigating the behavior of unidirectional and cross-ply ceramic matrix composites when subjected to quasi-static, repeated and fatigue loading. The developed models and failure criteria which comprise the present analysis illustrate the procedure for employing analytic solutions for modeling numerous complex mechanisms such as those observed in fracture of brittle composites. Furthermore, this study illustrates that damages such as fiber fracture, interface slip and fiber pull-out can be successfully modeled for a partially bonded interface in fiber-reinforced composites. These permit stress-strain hysteresis and strain ratchetting behaviors to be modeled, whereas in the past these mechanisms were not considered in such an analysis. Finally, this study provides a means for evaluating many interface properties such as the fiber/matrix bond strength, the interface frictional shear resistance, the degradation in shear under fatigue loadings and the evolutions of interface debonds. This is significant since such data are difficult to obtain experimentally.

MODELING OF PROGRESSIVE DAMAGE IN FIBER-REINFORCED CERAMIC MATRIX COMPOSITES

I. Overview

This chapter serves as a general overview for some of the intricacies involved with the science and engineering of fiber-reinforced ceramic matrix composites and the proposed study. The chapter is divided into three sections. First, a brief discussion of monolithic ceramics and ceramic matrix composites is presented, including the various damage modes inherent to these materials and the importance of modeling these damages. The second section reviews several failure criteria which have been used in predicting the evolution and impact of the microstructural damages on the structural integrity of the ceramic composites. Finally, the third section outlines the present study to model the failure progression and material response of the fiber-reinforced ceramic composite under various loading conditions.

1.1 Introduction

The technological advancement for many structural components is contingent upon the continued development of high-performance materials which can survive in demanding operating environments. As a result, the demand for advanced materials in aerospace and other high-temperature applications has steadily increased over the past few decades. Unfortunately, the supply has not maintained the pace. A good example is the limited success researchers have had in designing and manufacturing advanced supersonic and hypersonic aerospace vehicles. Much of the progress in this area has been hampered by the non-availability of structural materials which can withstand the necessary operating conditions since in many cases, materials in

today's advanced aerospace arena are required to operate in environments where severe thermal-mechanical and fatigue loadings can be expected.

Ceramic materials are a natural fit for these environments as a result of their innate resistance to heat, chemicals and wear [15,52]. What makes ceramic materials so appealing is that they possess high strength and modulus even at elevated temperatures. The service temperature limits for today's ceramic materials, for example, are approaching 1600°C. This is compared to 1000°C for current super-alloys, 750°C for stainless steels, and 400°C for advanced polymeric composite [25]. Ironically however, the phenomenon which provides the ceramic material with its exceptional strength and stiffness also causes the ceramic to be very brittle. As a result, when monolithic ceramics fail, they typically fail catastrophically and without warning. Hence, these materials are not amenable to many structural applications.

With the addition of high-strength reinforcing fibers, however, the overall strength of the ceramic, as well as its fracture toughness, can be increased significantly. For this reason, ceramic matrix composites (CMCs) have received a great deal of attention. Unfortunately, since the fiber/matrix constituents are themselves brittle materials, CMCs are still susceptible to fracture. In particular, CMCs are energetically prone to the formation of *multiple* matrix cracks within the composite structure [8,126]. This makes them difficult to model. The fractures form first within the matrix and not the fiber since typically the strain-to-failure of the ceramic matrix is less than that of the reinforcing fibers. Furthermore, multiple cracks can form since laminate failure is prevented by fibers which continue to bridge the crack planes. In this manner, the fibers provide the CMC with improved toughness and perhaps even more importantly the observed gradual non-catastrophic failure mode.

As would be expected, however, an increase in material compliance is accompanied with the formation of the matrix cracks [65]. Moreover, this relaxation in stiffness can be observed as changes in the slope of the laminate's stress-strain response. In actuality, since the formation and growth of the matrix cracks occurs over

a finite stress range, the shape of the stress-strain curve may be quite non-linear in appearance due to the varying composite compliance over this stress range. For this reason, the shape of the stress-strain curve is a good indicator of the extent of composite damage. Hence, modeling the stress-strain response of CMCs is a challenging task due to the complex interaction effects between the damaged constituents. This is accomplished only by modeling the presence and influence of the matrix cracks and other damages.

Not much needs to be said about the importance or utility in formulating models which provide insight into the probable behavior of a material under various loading conditions. Models, whether analytical, numerical or empirical, can save countless man-hours and monies by permitting "papers studies" to replace or supplement experimental analyses. There is no need to manufacture and test each material variant. In order to model a material, such as a ceramic matrix composite, which has several prominent damage modes, two items are required. First, a *representative model* or volume element, and constitutive relations are needed. Second, a set of *failure criteria* for each damage mode must be available in order to determine the extent of damage within the composite microstructure. Since the formulations of the model and the failure criteria are typically independent, researchers can mix and match as necessary.

Since the early 1970's, a large number of models and failure criteria have been presented for analyzing the behavior of ceramic composites, and these will be reviewed in chapter two. Many of these studies are based upon the theory of *micromechanics* in which strength-of-material solutions are applied to unit-cells consisting typically of only a single fiber and surrounding matrix. The advantage of the micromechanics approach is that the mechanical response of the laminate may be easily obtained since this approach avoids many of the subtle intricacies and complexities associated with the stochastic nature of brittle fracture in non-homogeneous materials. More detailed fracture mechanics techniques may provide a better depiction

for the evolution of damage within the composite; however, they are limited in their ability to model complex loading conditions due to the inherent complexity of the analysis.

1.2 Background

As mentioned previously, when cracks form within the matrix of a ceramic matrix composite, the reinforcing fibers prevent catastrophic failure if they continue to bridge across the crack plane. Moreover, it has been well established that near these bridging fibers, several microstructural interactions occur between the composite's constituents which promote toughness through load transfer and energy dissipation [18,52]. Clearly, the proper modeling of the composite's behavior resides in the ability to understand and capture these phenomena. To this end, a number of micromechanics analyses have been developed for predicting the onset and progression of failure within brittle composites [8,37,113,201]. In what is now considered a classical analysis, Aveston, Cooper and Kelly (ACK) discussed in detail the "energetics of multiple fracture" in brittle composites [8]. This work has fueled similar studies for over twenty-five years.

Many of the models presented over this time period are based upon the classical *shear-lag* formulation presented by Hedgepeth [71]. The approach parallels the method employed by Cox who first investigated the influence of a single short fiber embedded in an infinite medium [32], but can be adapted to investigate the response of unidirectional and cross-ply laminates *if an equivalent damage state for the laminate can be determined.* Unfortunately, this can be quite a difficult task. The complexities of brittle failure in composite materials have forced many researchers to rely on empirical data which has thereby reduced the utility of the analytical models. In addition, many existing analytical solutions employ failure criteria which significantly over-predict the rate of matrix cracking. The most obvious case is the original ACK model in which all of the matrix cracks were assumed to form at a

single applied stress [8]. This resulted in a "stepped" or "plateau-ed" stress-strain response where the material response curve is initially linear followed by a single large jump in strain during matrix failure then the response becomes linear again albeit with a smaller slope. Hence, even though the micromechanics approach is appealing because of its simplicity, solutions from many of the existing models do not mirror experimental data [8,113] and, therefore, alternate approaches are sought.

Within the literature, there are a number of more detailed analyses which avoid some of the simplifying assumptions employed under the micromechanics approach [53,137]. For example, a number of solutions employ traditional fracture mechanics techniques to investigate the conditions for crack growth near a bi-material (fiber/matrix) interface [109]. These models are useful since the development of valid design and failure criteria are contingent upon a full understanding of the microstructural behavior of the laminate during loading. Unfortunately, modeling the behavior of an individual crack in this manner may require integration of many complex theories, e.g. linear elastic fracture mechanics, statistical analysis and variational mechanics; therefore, when considering the large number of cracks which are continually developing and growing in a CMC, the analysis can be quite complex. To further compound the problem, the crack formation within the composite is dependent not only on the lamina properties, but also on laminate and component geometries. In addition, matrix cracking is not the only damage mode observed in CMCs. Cracks can also develop within the fibers or along the fiber/matrix interface. Since the evolution of all these damages is dependent on the magnitude and type of loading, the operating environment must also be accounted for in the analysis. When considering all these effects, the problem quickly becomes overwhelming. Perhaps this explains why a large number of first-order models have been reported in the literature [67,152,179].

The present research addresses many of the above considerations by presenting a systematic and comprehensive model capable of analyzing the fatigue response of

unidirectional and cross-ply ceramic matrix composites. Moreover, the analysis is developed under a unified and consistent methodology. The literature is inundated with studies investigating portions of the analysis; however, none of these provide comprehensive solutions (model and failure criteria) as introduced in the present research. The foundation of the current approach is rooted in simple analytic formulations which allow the analysis to be extended to consider many complex loading environments and laminate geometries. Further, the present analysis eliminates the requirement for gathering empirical crack density data; a tedious and costly endeavor.

1.3 Approach

The objective of the current research is to develop and formulate a methodology (model and failure criteria) for predicting the stress-strain response of unidirectional and cross-ply fiber-reinforced ceramic matrix composite when subjected to quasi-static, repeated, and fatigue loading conditions. The model formulation is an extension of traditional shear-lag theory, and considers a general damage state consisting of matrix cracking, interface debonding, as well as fiber failure. These damage modes are modeled by a set of failure criteria with the minimum reliance on empirical data which can be easily employed in a variety of numerical or analytical methods. The criteria used to estimate the extent of matrix cracking and interface debonding are closed-form and require the basic material properties. The failure criterion for fiber failure requires *a priori* knowledge of a single empirical constant. This parameter, however, may be determined without microscopic investigation of the laminate microstructure.

For the present analysis, the modified shear-lag approach to model the behavior of *unidirectional* CMCs is based upon work presented by Kuo and Chou [106]. However, the present theory is not restricted to their particular formulation. For *cross-ply* laminates, a new model is formulated which considers a general damage

1-6

state consisting of matrix cracking in both the transverse and longitudinal plies, interface debonding, fiber fracture, slip and pull-out. The cross-ply formulation assumes that the matrix crack spacing within any ply is uniform, but generalizes the solution for any relative crack configuration between plies. In addition, unlike the previous study [106], the present analysis does not require empirical crack density data. Instead, a specific failure criterion for each damage mode is formulated.

As mentioned, the failure criteria used in estimating the extent of composite damage are formulated to minimize the reliance on empirical data. Closed-form solutions are provided for estimating the instantaneous matrix crack density and interface debond length. The latter is determined through incorporation of a maximum stress criterion along the interface. The matrix crack density is determined at each stress level by a unique failure criterion which requires the strain energy in the matrix to remain constant at a critical value. This approach is analogous to a total energy failure criterion for an isotropic material, and has been entitled the *critical matrix strain energy* approach by the author. The extent of fiber damage is determined using an energy-based Weibull failure distribution. This distribution requires *a priori* knowledge of a single material constant, namely the percentage of fractured fibers at laminate failure. The latter may be determined if the ultimate stress and corresponding failure strain of the unidirectional laminate are known.

The remainder of this document is divided into six chapters and several appendices. Chapter two presents an overview of ceramic matrix composites. It examines what they are; why they are of interest, and how they can be modeled. For the latter, chapter two also includes an introduction to the theory of micromechanics, details of several classical failure criteria, and a summary of previous studies involving the modeling of ceramic matrix composites.

The theory used in the present study for the analysis of both unidirectional and cross-ply laminates is presented in chapter three. In addition, failure criteria

for various damage modes are provided. This chapter concludes with a discussion of specific considerations required for different loading environments.

In chapter four, modeling of *unidirectional* ceramic matrix composites under quasi-static, repeated and cyclic loading is presented. A summary of the model development is provided along with a comparison of the predicted results and the corresponding empirical data.

Chapter five is similar in outline to chapter four; but investigates the behavior of *cross-ply* laminates. The final chapters, chapters six and seven, provide closing remarks on the present work and also several recommendations for future research. In supplement of the seven main chapters, several appendices appear in the final pages.

II. Perspective

The intent of this chapter is to provide the reader with background on the science and engineering of ceramic matrix composites (CMCs), including the various damage modes of CMCs and how these damages may be modeled. The first section (section 2.1) serves to motivate the research while section 2.2 begins the general overview of CMCs. The latter includes a discussion of what CMCs are; why they are of interest, and how damages induced during loading can impact the mechanical properties of the laminate. The dependence of the macromechanical response on the "strength" of fiber/matrix interface is also emphasized. Greater detail on these is provided in supplemental appendices.

In section 2.3, the impact of the microstructural damages on the macromechanical response of the laminate is examined. This is accomplished by reviewing the salient features of the stress-strain response for several brittle composite laminates, and serves as a transition between the details of microstructural failure modes presented in section 2.2 and the goals of the micromechanics theory which are presented in section 2.4. Next, section 2.5 provides a partial listing of existing theories (models and failure criteria) which have been employed over the past few decades. It serves only as a general overview, and groups the theories into broad categories characterized by the predominant features of the models and failure criteria. The purpose is to provide a general introduction to some of the more traditional failure criteria, as well as to make apparent some of the advantages and disadvantages of these classical solutions. The final section of this chapter, section 2.6, summarizes the existing work and re-motivates the present analysis. Chapter three provides more detail on the specific theory (model and failure criteria) used in the present investigation.

2.1 Motivation

Ceramic matrix composites have emerged as viable material candidates for many structural components. In particular, CMCs are under increasing consideration for many high temperature applications in the aerospace industry where large thermal and mechanical loadings can be expected. Unfortunately, within these harsh operating environments, extensive damage can develop within the composite microstructure due to the limited ductility of the constituents in CMCs [85]. Such damages fundamentally alter the characteristics of the material behavior and, therefore, the key to modeling the behavior of a ceramic matrix composite resides in the ability to accurately estimate the extent and influence of these damages within each ply during each load cycle. Unfortunately, for fatigue analyses which can involve many loading conditions over millions of cycles, modeling microstructural damage is quite a challenging task. In addition, the inherent complexities and stochastic nature of failure in brittle non-homogeneous materials further complicates the modeling process. This has forced many researchers to rely on empirical data in order to estimate the residual laminate property, and has resulted in the proliferation of costly and time-consuming non-destructive evaluation techniques.

An attempt is made within the present study to formulate a set of failure criteria which can be easily employed and which accurately estimate the damage state of the laminate. The focus is to reduce the current reliance on empirical data because even in the most benign case, e.g. laboratory experiments of material coupons, empirical damage estimates are typically quite tedious to obtain. A prime example is the rigorous microstructural investigation, with acetate replicas, often performed for estimating the extent of matrix cracking within a CMC. Researchers must examine each replica under a microscope and physically count the number of matrix cracks at each load step. Inherent in this process is a subjective interpretation of what constitutes a full matrix crack and what does not. Failure criteria which reduce the need for such undertakings are, therefore, of great utility.

The failure criteria employed in the present analysis are purposely kept as simple as possible so that not only can the analysis be easily adapted to consider more complex loading conditions and component geometries but also so that it can be employed in a variety of numerical or analytical solutions. For completeness, however, all predominant damage modes are considered. These include matrix cracking, interface debonding, fiber fracture and fiber pull-out. The criteria used to estimate the extent of matrix cracking and interface debonding are closed-form and require the basic material properties. The failure criterion for fiber failure requires *a priori* knowledge of a single empirical constant. This parameter, however, may be determined without microscopic investigation of the laminate microstructure.

2.2   Ceramic Matrix Composites

A *composite* is a material which embeds a distinct reinforcement phase (fiber) within a continuous medium (matrix). This study is concerned exclusively with *ceramic matrix composites* (CMCs) in which continuous cylindrical fibers are embedded in a high performance ceramic matrix which is typically some derivative (oxide, nitride, or carbide) of silicon, aluminum, titanium or zirconium. An example is a SiC/CAS CMC which embeds small diameter (15 μm) silicon carbide (SiC) fibers into a calcium aluminosilicate (CAS) matrix.

Ceramic materials are of interest because they are ideal for many high temperature applications such as those found in jet engines or as external structure on supersonic or hypersonic vehicles. What makes ceramic materials so appealing is that they are excellent thermal and electrical insulators which are able to withstand most environmental and chemical attacks. More importantly, they retain significant structural integrity (strength and modulus) even at elevated temperatures. The major drawback of ceramic materials, however, is their inability to resist fracture. They are brittle. Theoretically, due to the unique ionic-covalent bonding at the molecular level, ceramics have the potential of being stronger than many metals, including the

latest super-alloys. However, this strength is never realized due to the ceramics' low toughness [18].

Ironically, the complex bonding responsible for exceptional strength, stiffness and environmental resistance in ceramic materials also prevents localized plastic deformation. As a result, the voids and inclusions inherent to a ceramics atomic structure act as nucleation sites where crack growth initiates. Once the cracks form, the large crack-tip stresses allow the fracture to propagate quickly through the material. Growth of the fracture is typically unstable since the brittle material has no inherent means of arresting the growth. Anyone who has ever dropped a china plate knows first hand the consequences of fracture in a brittle material. When they fail, they fail catastrophically, and when discussing jet engines, the phrase "catastrophic failure" is not something people like to hear.

Fiber-reinforced ceramic composites, however, exhibit a remarkable increase in toughness when compared to their monolithic counterparts. More specifically CMCs are characterized by a large strain-to-failure, pseudo-ductility, and most importantly, a gradual non-catastrophic failure mode. The demand for these advanced materials in aerospace and other high-temperature applications has prompted numerous studies of ceramic matrix composites over the past few decades. These include both analytical and experimental investigations. However, before investigating some of these models, a brief discussion of failure in CMCs is appropriate. The purpose is to familiarize the reader with the reasons why cracks propagate so readily though ceramic materials and what can be done to prevent it.

A monolithic brittle ceramic is unable to resist fracture due to its low fracture toughness, K_I^c (reference appendix A). One method of increasing K_I^c in a brittle material is to reduce the number and size of pre-existing microstructural imperfections. This is accomplished primarily through modifications in the manufacturing processes. Unfortunately, improvements in the *flaw control* processes have been slow and expensive to implement. As a consequence, the primary means of improving the

fracture behavior of ceramics has been accomplished through *fiber reinforcement*. This approach is not new; in fact, the addition of straw to clay roofs, and animal hair to pottery are examples of early composites where brittle materials are made stronger through reinforcement. In addition, careful study of beetle shells and human teeth illustrates that nature has also used this practice. However, recent advancements in the science and engineering of reinforcement has permitted the concept to be successfully adapted to advanced materials. Ceramic matrix composites represent a prime example of how reinforcement can be used to improve the toughness of a material. The reinforcement phase can be in the form of particles, whisker or short fibers, continuous fibers or sheets. For this particular study, ceramics reinforced by continuous fibers are investigated. The toughening effect resulting from the addition of continuous fibers in a ceramic matrix is discussed next.

Since the ceramic matrix which binds the fibers together in CMCs is typically of adequate strength for most applications, the fibers do not need to act as the main load carrying members as is the case in polymer or metal matrix composites; rather *the fibers in CMCs serve to transfer stress across broken matrix blocks.* In addition, *fibers which continue to bridge the crack plane provide closing tractions which tend to reduce the crack-tip stress intensity factor.* Hence, the survivability of the fiber is a major concern.

Ideally, material engineers would like to add ductile fibers with high fracture toughness; however, the design (temperature) considerations which dictate the use of ceramics also preclude the use of such fibers. Ceramic composites are therefore composed of brittle fibers in a brittle matrix. Realizing that brittle fibers have low fracture toughness and are likely to fail in the presence of high crack-tip stresses, the original problem: an inherent inability to resist fracture, still appears to exist. However, as will be discussed, this is not the case. As matrix cracks propagate around the fibers, energy is dissipated due to the mechanical interactions which develop between

the constituents.[†] Hence, the *fibers induce toughening (energy dissipating) mechanisms* simply due to the presence of the bi-material interface. Energy dissipation is discussed in greater detail in the following sections.

In summary, the fibers perform three roles: (1) the fibers aid in load transfer; (2) they produce closing tractions which reduce the crack-tip stress intensity, and (3) they induce energy dissipating mechanisms which reduce the propensity for the creation of additional damages. These effects are what provide CMCs with their exceptional toughness, and gradual non-catastrophic failure mode. As discussed in the following sections, the "strength" of the interface governs these three phenomena.

2.2.1 Toughening Mechanisms and Interface Design. The shape of a stress-strain response tells a lot about a material and may even be used to categorize materials. For example, materials can be classified as brittle or ductile based upon the appearance of the stress-strain curve. This is illustrated in Fig. 2.1. In addition, the material's strength, modulus, strain-to-failure and toughness are all characterized by the stress-strain response. In this manner, given a material, one might conjecture the shape of the stress-strain curve. However, the latter is more difficult especially when considering non-homogeneous materials. For example, the shape of the stress-strain curve for a CMC is similar in appearance to one produced by a ductile metal. Initially, the response is linear, however, at some stress level, the response becomes distinctly non-linear. The point of onset of non-linearity is defined as the material's *proportional limit* (Fig. 2.1). For ductile metals, the non-linear behavior is associated with the movement and coalescence of dislocations within the microstructure (i.e. plasticity). For CMCs, on the other hand, the increasing material compliance associated with the non-linear region is a direct result of the break-up of the matrix. Since the constituents in the ceramic composite are brittle (linear-elastic) materials,

---

[†]The term *energy dissipation* is perhaps a misnomer since the energy is, of course, not eliminated, but rather simply *transferred* to some other form. For example, the energy available to split molecules along a crack front may be "dissipated" in the form of heat if frictional sliding occurs along the fiber/matrix interface as the crack opens.
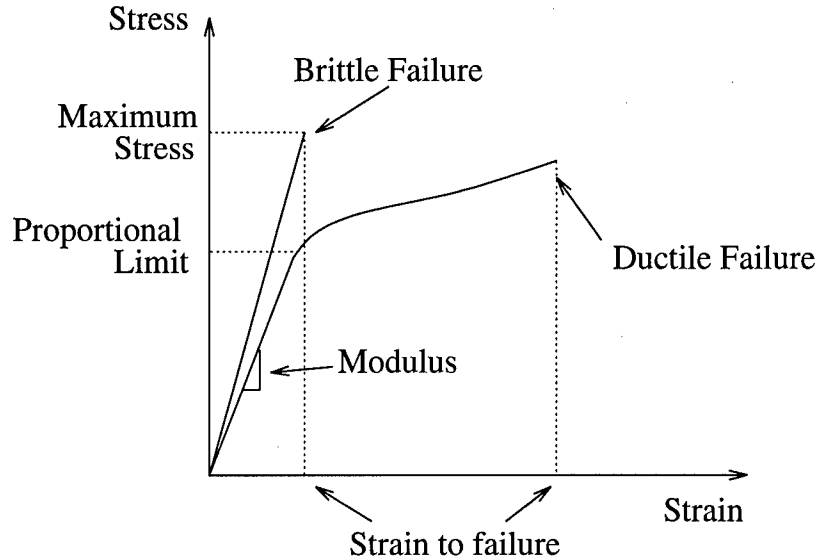
Figure 2.1   Stress-strain response illustrating brittle and ductile failure modes.

and yet the material response resembles that of a non-brittle material, CMCs are occasionally referred to as possessing pseudo-ductility or pseudo-toughness.

The degree of toughening exhibited by CMCs is, in large part, a function of the strength of the interface, in particular, the constituent bonding stress and the frictional shear resistance within debonded regions. Weaker interfaces reduce the functionality of the fibers whereas strong interfaces increase the probability of fiber fracture as large crack-tip stresses from matrix fractures are readily transferred across the interface. In both cases (strong and weak) interfaces, no appreciable improvement in the mechanical response of the CMC is realized over the monolithic matrix.

Toughening results from the ability to dissipate energy which is otherwise available to propagate existing fractures. Therefore, in this case, crack formation, interface debonding and frictional slip all contribute positively towards toughening. Moreover, if the interface is properly designed, the percentage of fibers which continue to bridge the crack plane can be enhanced. This promotes toughness through load transfer and continued frictional energy losses and, therefore, "tuning" the in-

terface strength though proper design and manufacturing is a very important area of research in composite engineering. In fact, because of this ability to tune material properties, such as with CMCs, there has been a fundamental change over the past thirty years in how material engineering is approached. In the past, materials were simply *applied* to structural components. Today, through improved understanding of material science, advanced materials are *designed* for specific applications. Ceramic matrix composites represent an excellent example of this change in philosophy.

For composite materials, this design process not only includes optimizing the *laminate* by adjusting the interlaminar properties (e.g. ply orientation, stacking sequence), but also includes the optimization of *lamina* properties. This involves improving both the strength and failure characteristics of the individual plies, and can be accomplished in large part by controlling the properties along the fiber/matrix interface. A strong interface allows for an efficient transfer of stresses between the constituents; however, it also increases the probability of fiber failure. Weaker interfaces reduce the chances for fiber failure, but the fiber also carries less load. For this reason *interface design* is a major area of research in composite engineering [16, 27, 59, 78, 82, 83, 88, 92, 94, 99, 107, 116, 121, 135, 166, 208]. It is accomplished primarily by two techniques: (1) by adjusting the residual stresses across the plane of the interface and (2) through the application of interface coatings. These are examined in appendix A.

2.2.2 Damage Modes. Due to the low fracture toughness of the ceramic matrix, an extensive amount of damage can develop within the CMC's microstructure prior to composite failure. Matrix cracking, interface slip and debonding, fiber failure and fiber pull-out are some of the damage mechanisms common to brittle composites. Unfortunately, the evolution of these damages is difficult to model since they are dependent upon a number of factors. For example, the composite's geometry, interface properties, residual stresses, and loading environment all influence the damage progression within the laminate. Therefore, even though the microstructure

of a unidirectional CMC may be relatively simple to model, the myriad of damage mechanisms and their relationships with one another and outside influences are not. As such, simply identifying and characterizing the relevant factors associated with the damage progression is far from trivial [12]. Furthermore, "modeling damage in these (ceramic matrix) composites presents unique challenges ... owing to uncertainties about various damage mechanisms that occur in the composite microstructure" [196].

When loading CMCs, cracks typically initiate within the composite matrix since the strain-to-failure of the matrix is usually less than that of the fiber. The evolution of matrix cracking within a ceramic matrix composite is shown schematically in Fig. 2.2. The three stresses shown in the figure are the stress at which
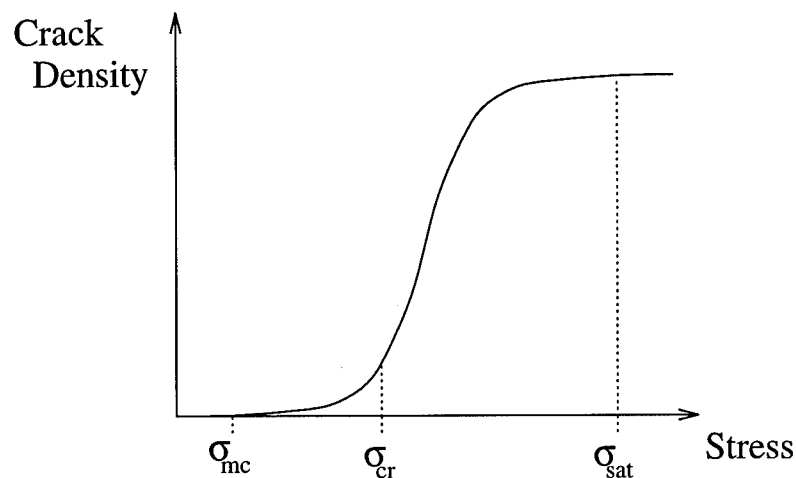
Figure 2.2   Crack density evolution in a brittle composite.

matrix cracking initiates, σ_{mc}; the *critical composite stress*, σ_{cr}, for which a sufficient accumulation of cracking has taken place to produce a noticeable decline in the laminate modulus, and the maximum stress beyond which the crack density no longer changes, σ_{sat}. The latter is referred to as the *saturation stress*.

For $\sigma < \sigma_{cr}$, the influence of matrix cracking on the material response is limited and, therefore, need not be considered. Hence for the present analysis, matrix

cracking is only considered for $\sigma_{cr} \leq \sigma \leq \sigma_{sat}$. The average crack spacing at $\sigma = \sigma_{cr}$ is defined as the *initial crack spacing* L_{init}, and the final crack spacing at $\sigma = \sigma_{sat}$ is denoted L_{sat} for the saturation spacing. Matrix cracking saturates since the average matrix stress decreases with its failure; thus reducing the impetus for further failure. In addition, as the debonding and fiber fracture modes become increasingly prevalent, the energy available for matrix cracking is reduced. For conditions where the composite is repeatedly loaded and unloaded, matrix cracking can evolve beyond the static saturation limit; however, the effect is limited. The influence of loading on the damage progression and material response is discussed in more detail in the next two sections.

The large extent of matrix cracking which can develop within CMCs is illustrated in Fig. 2.3. This figure shows a large number of matrix cracks which have formed in a $[0/90]_{2s}$, SiC/CAS laminate. The large cracks in the center of the figure are *transverse cracks* which have formed in the 90° plies. In addition to these cracks, a number of matrix cracks are apparent in the outer 0° plies. These *matrix cracks* run perpendicular to the local fiber axis, as well as the direction of loading.

As matrix cracks form within the composite, they can also induce interface debonds. These usually result from the large stress fields near the matrix crack-tip; however, debonds can also originate from matrix cracks which are deflected along the fiber axis. However, the latter is rare in cases involving uniaxial loads. As the number of matrix cracks increases, the fibers are forced to carry a larger percentage of the load. Eventually, the fibers may fail. In addition, once fractured, the fibers may pull-out from the matrix. After a critical number of fibers fracture, the laminate fails.
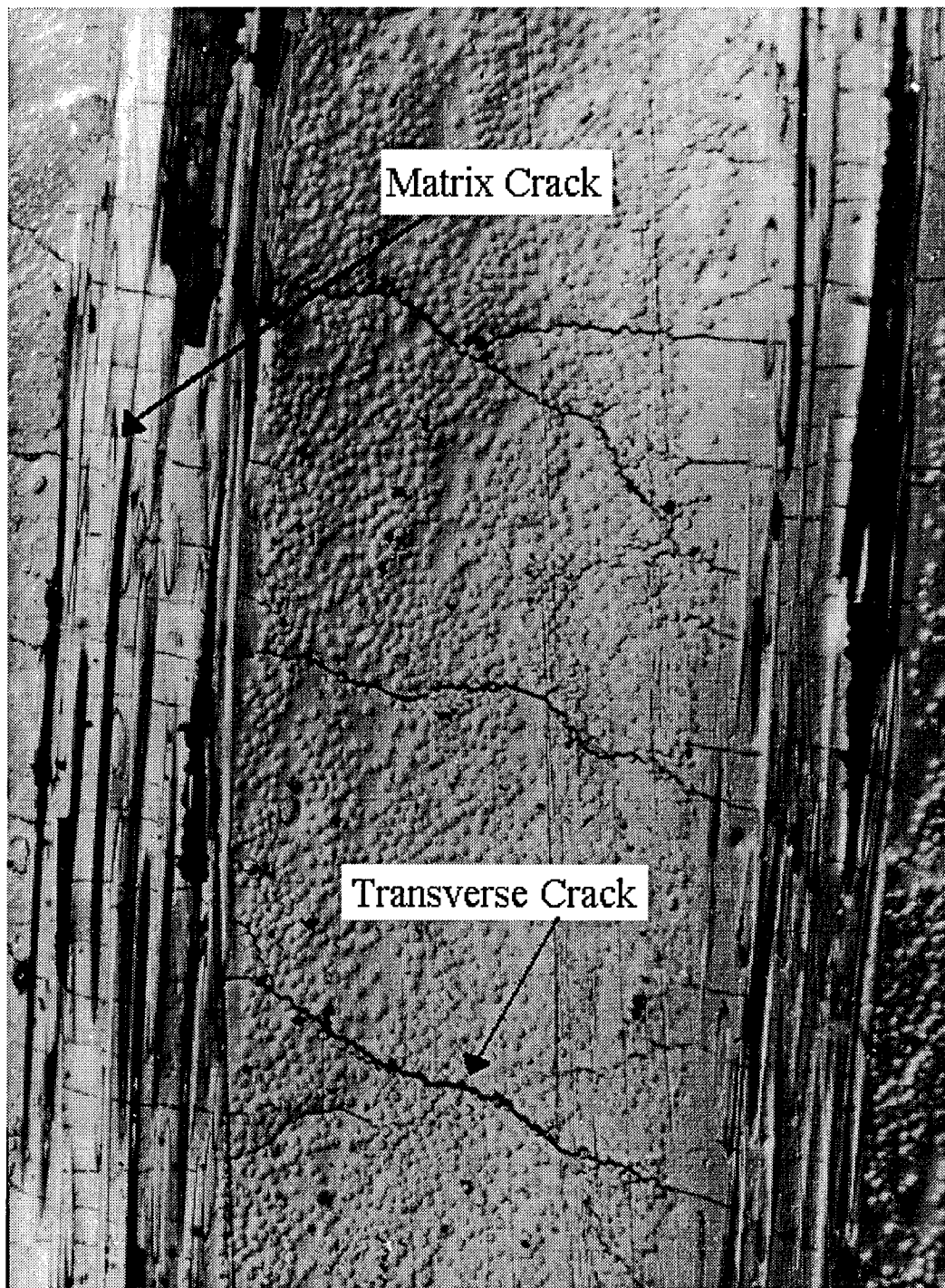
Figure 2.3   Matrix cracking within a cross-ply ceramic matrix composite.

2.2.3 Loading Considerations. In order to successfully model the stress-strain response of a ceramic composite, a representative state of damage must be determined. Under conditions of *quasi-static* loading in which a continuous monotonically increasing tensile load is slowly applied to the composite, the evolution of damages is fairly well understood although difficult to predict analytically.[†] For other loading conditions such as cyclic fatigue, not only is it more difficult to predict (analytically) the extent of damage, but also the evolution of the damages is not well understood. In this study, three loading conditions are considered: quasi-static, repeated and cyclic loading.

Under *repeated loading*, the laminate is assumed to be subjected to only a few (< 10) loading and unloading cycles such that under the conditions of repeated loading, the interface properties (e.g. τ_i) are not assumed to change. Therefore, the stress-strain hysteresis loops produced from repeated loading are equivalent to loops produced from virgin specimens. Also, repeated loadings to the same maximum stress will produce stress-strain curves which are identical. For this reason, a typical repeated loading scenario includes three or four cycles in which a laminate is loaded to some maximum stress, σ_{max_1}; unloaded to some lower stress, σ_{min}, and subsequently reloaded to a higher stress, σ_{max_2}, i.e. $\sigma_{max_2} > \sigma_{max_1}$.

Under such loading conditions, stress-strain hysteresis develops due to frictional sliding along the interface. For example, a predicted stress-strain response for a cross-ply laminate during loading and unloading is illustrated in Fig. 2.4. The response shown represents the hysteresis behavior of a cross-ply, $[0_3/90/0_3]$, SiC/CAS laminate under two loading cycles. In particular, the laminate is initially loaded to 175 MPa after which the applied load is removed. The laminate is then reloaded to 250 MPa; unloaded to zero load, and subsequently reloaded to 250 MPa. The shape of the hysteresis loop is dependent on the extent of composite damage and the interface

---

[†]The term *slowly applied* implies that inertial and dynamic effects can be neglected. Furthermore, it implies that the loading processes are isothermal such that the theory of elasticity and the first two laws of thermodynamics are applicable.

shear, τ_i. The expected increase in the size of the hysteresis loop for the second cycle corresponds to an increase in the laminate's microstructural damage.
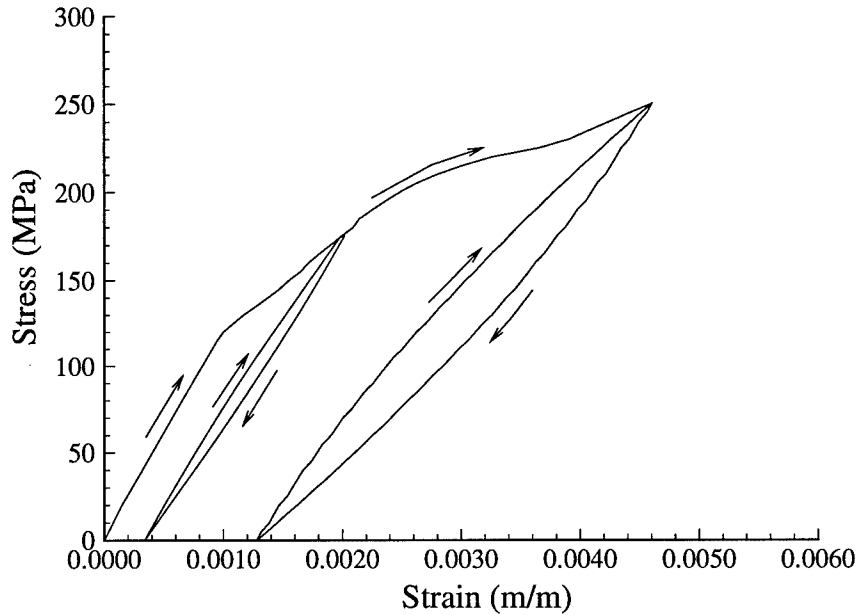
Figure 2.4   Stress-strain hysteresis of a ceramic matrix composite as predicted under the current analysis.

For *fatigue analyses*, the composite laminate is assumed to undergo a large number of loading and unloading cycles under which the interface is assumed to wear due to the friction. As the interface wears the frictional interface shear stress τ_i degrades and the strength of the interface changes, i.e. $\tau_i = \tau_i(N)$ where N is the number of cycles. Since the properties of the interface are changing during the load cycling, the behavior of the laminate (e.g. strength and failure characteristics) will also vary.

In particular, as the interface wears, the ability of the fiber to transfer load, dissipate energy and produce closing tractions which reduce the crack-tip stress intensities all decrease. This permits additional damages (i.e. matrix cracking and debonding) to occur specifically due to the loading environment. In general, because

of the nature of fracture in brittle materials, the extent of damage typically remains constant if the maximum stress is not exceeded. However, under fatigue type loading environments, the damage within CMCs can increase since the properties of the material itself are changing [155, 156, 203]. These damages will be referred to as *fatigue specific damages.*

The stress-strain response of a brittle composite under cyclic fatigue may be characterized by a number of salient features: elastic modulus, stress-strain hysteresis, strain ratchetting[†] and S-N behavior (Fig. 2.5). A sketch of several hysteresis loops is illustrated in Fig. 2.5 (a). In general, the hysteresis and ratchetting behavior depend upon the composite system and loading environment [100]. As with repeated loading, the shape of the hysteresis loops under fatigue loading is dependent on the composite damage, as well as the interface shear. Strain ratchetting, on the other hand, is more a function of fiber pull-out [153]. The maximum and minimum applied stresses are assumed to remain constant for all loading and unloading cycles of the fatigue test. The ratio of the minimum stress during unloading to the maximum stress during reloading is denoted with the parameter $\mathcal{R}$, i.e.

$$\mathcal{R} = \frac{\sigma_{min}}{\sigma_{max}} \tag{2.1}$$

where $\mathcal{R}$ remains constant. In addition, only tension-tension fatigue tests are considered in this study. Hence, $\mathcal{R} \geq 0$.

In addition to the hysteresis behavior CMCs also form definitive S-N curves characterized by a distinct threshold stress, σ_{th}. For applied stresses less than σ_{th}, the laminate will not fail over a standard fatigue life; typically defined as 10^6 cycles. For $\sigma > \sigma_{th}$, the composite fails before 10^6 cycles. A typical S-N curve is illustrated in Fig. 2.5 (b). The arrows indicate that the composite did not fail within 10^6 cycles. Note that long term environmental effects such as oxidation embrittlement have not

---

[†]The increase in permanent strain with load cycling is defined as *strain ratchetting.*

been considered. In general, fatigue tests can last for an extended period of time; increasing the opportunity for the interface to oxidize.

(a) Hysteresis Loops   (b) S-N Diagram
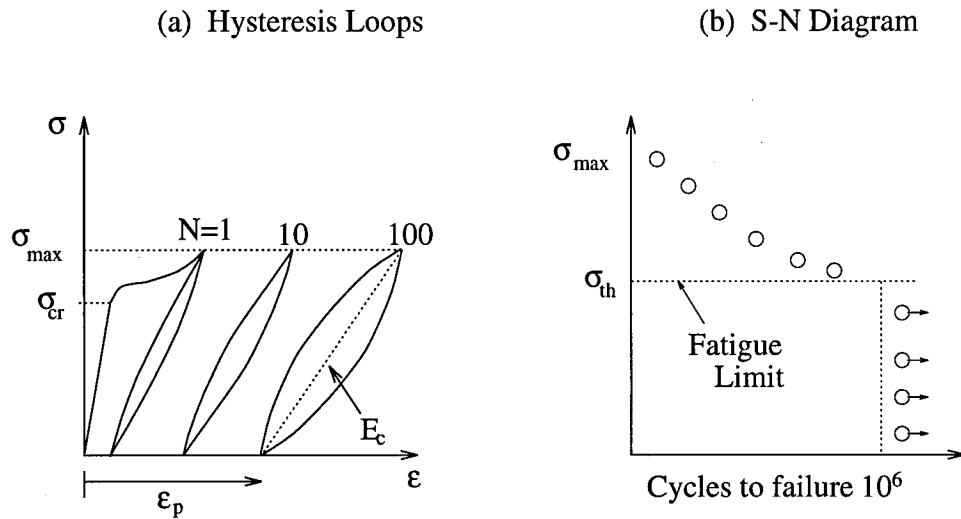
Figure 2.5   Fatigue life of a ceramic matrix composite. (a) Stress-strain hysteresis accompanied by a continuous progression in residual strain (strain ratchetting). (b) Peak stress versus cycles to failure (S-N) diagram.

2.3   Salient Features of the Loading Response.

A common characteristic of the stress-strain response for a unidirectional laminate under uniaxial tensile loading is that two distinct regions, one linear and the other non-linear, are observed. Initially the composite's response is linear, however, once damage begins to accumulate within the composite's microstructure, the response begins to deviate from linearity. The point at which the stress-strain curve becomes non-linear is referred to as the composite's proportional limit. In the present study, the stress level which corresponds to the composite's proportional limit is re-

ferred to as the *critical composite stress*[†] and is denoted σ_{cr_0}, or simply σ_{cr} for a unidirectional laminate (Fig. 2.6).
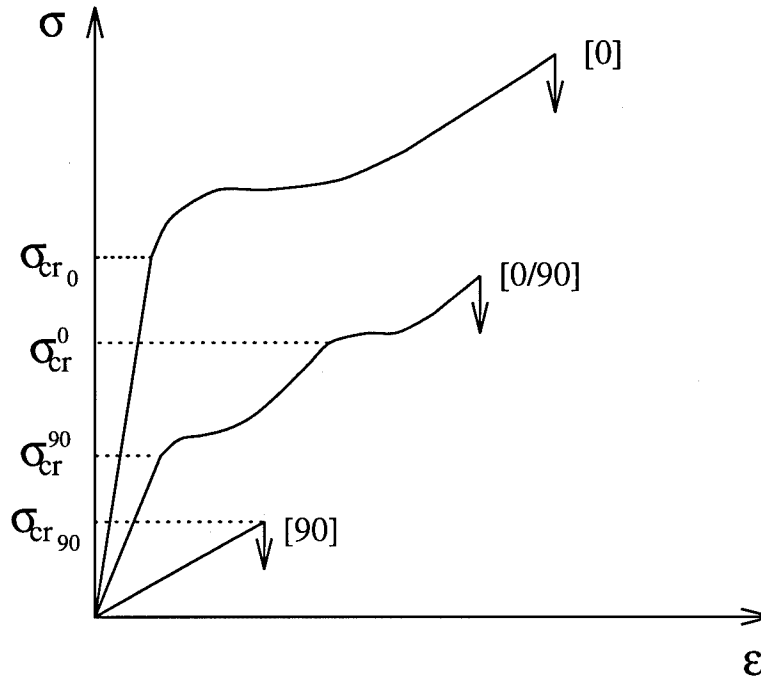
Figure 2.6   Stress-strain responses illustrating the proportional limits for 0°, 90°, and cross-ply laminates.

The stress-strain response of a 90° laminate (i.e. 0° ply loaded transversely) is noticeably different than the unidirectional response since the stress-strain response of a 90° laminate is linear up to its failure under quasi-static loading. Hence, the critical composite stress for this laminate, $\sigma_{cr_{90}}$, corresponds to the composites ultimate strength [125]. For a cross-ply laminate, two proportional limits are typically observed [209]. The first occurs after damage accumulates in the 90° ply and the

---

[†]The definition for the *critical composite stress* is sometimes ambiguous. One possible definition for the critical stress is the stress required to cause a single crack to form within the matrix from a dominant flaw. For the present document, this stress is referred to as the *crack initiation stress*, or the stress at which matrix cracking initiates, and is denoted by σ_{mc}. The second definition for the critical composite stress is the stress level at which the laminate stress-strain response becomes non-linear. This first point of non-linearity corresponds to the accumulation of matrix cracks since the composite stiffness is virtually unaffected by the presence of a single crack provided a sufficient number of fibers continue to bridge the crack plane. This latter definition will be used in defining the critical composite stress, and will be denoted by σ_{cr}. For most ceramic composites, $\sigma_{cr} > \sigma_{mc}$.

second deviation results from damage accumulation in the 0° ply. The two critical stresses for the cross-ply laminate are denoted in this paper as σ_{cr}^{90} and σ_{cr}^{0}, respectively, where a superscript as opposed to a subscript is used (Fig. 2.6).

For cross-ply laminates, matrix cracks may develop within both the 90° ply and the 0° ply. In order to differentiate between matrix cracks in the transverse (90°) and longitudinal (0°) plies of the cross-ply laminate, matrix cracks in the 90° plies are referred to as *transverse cracks* and the term *matrix cracks* is reserved for cracks in the 0° plies of the cross-ply laminate. Both transverse and matrix cracks are assumed to propagate orthogonal to the loading directions. Thus, cracks propagate perpendicular to the fibers in the 0° plies and parallel to the fibers of the 90° plies. A detailed description on the evolution of damage within unidirectional and cross-ply composites may be found in references 193 and 205.

It has become customary to divide the stress-strain curve of a CMC into discrete regions which characterize the dominant damage modes [193]. Figures 2.7 and 2.8 are examples of this process for a unidirectional and cross-ply CMC, respectively. Dividing the macromechanical stress-strain response into regions associated with certain damage mechanisms is not only convenient for describing the material behavior, but it also aids in the modeling process. In the present study, the stress-strain relationships for quasi-static, repeated and fatigue loading are predicted. In addition, the present analysis has been formulated to consider both unidirectional and cross-ply laminates. In all cases, the theory of micromechanics, as presented next, is used.

2.4   Micromechanics

This section presents the modeling assumptions for the composite's geometry, damage progression, and load transfer in the case of a damage free composite, as well as when microstructural damages are present. The model formulations are presented in chapter three, and a review of *rule-of-mixtures* constitutive relations
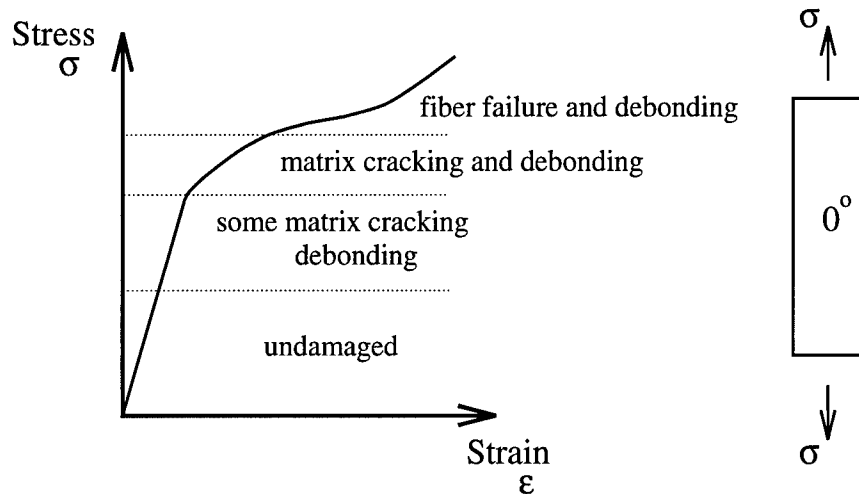
Figure 2.7   Stress-strain response of a unidirectional CMC. The stress-strain response is divided into regions characterized by the composite's damage modes.

for an undamaged laminate, and an introduction to shear-lag theory for a damaged laminate are presented in appendix B.

2.4.1 Modeling Assumptions.   For purposes of analysis, a number of simplifying assumptions are made. Further, for convenience, these assumptions are presented in two sections. First, the assumptions concerning the geometric arrangement of the laminate are discussed. These assumptions permit the laminate to be modeled using a simplified representative volume element (RVE) consisting only of a single fiber and surrounding matrix. The second set of assumptions centers around the assumed symmetry in the composite's damage state which allows use of the RVE with damage.

Laminate Geometry.   It has been well established that the stress-strain response for an *undamaged* composite [polymer matrix composite (PMC), metal matrix composite (MMC) and ceramic matrix composite (CMC)] can be accurately predicted using a simplified unit-cell (RVE) in which only the basic constituent properties are considered. Such solutions are typically referred to as *rule-of-mixtures*

2-18
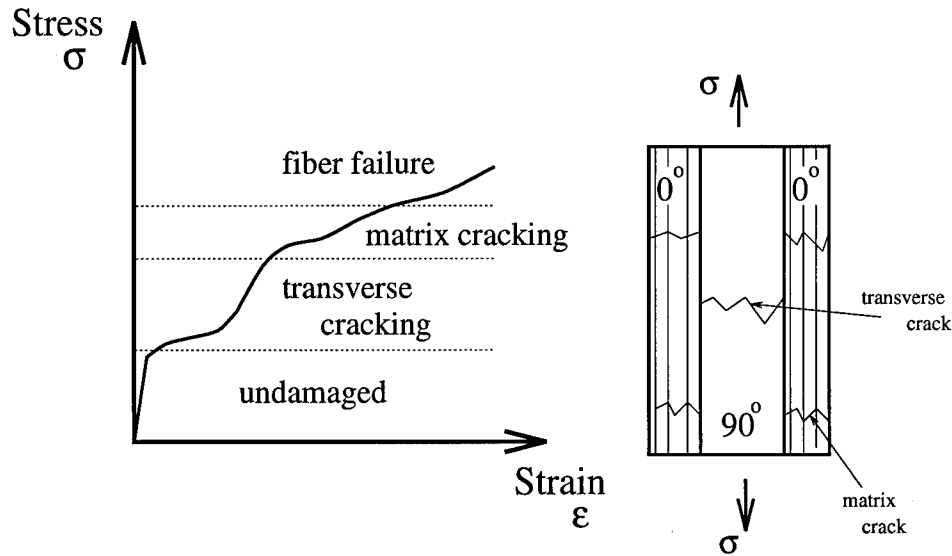
Figure 2.8 Stress-strain response of a cross-ply CMC. The stress-strain response is divided into regions characterized by the composite's damage modes.

approximations [3]. Implicit to the theory, however, are a number of assumptions. For example, the arrangement of the fibers in the composite's matrix is assumed to be uniform and symmetric. In particular, the fibers are assumed to be prismatic, continuous and embedded as a regular rectangular array within the matrix (Fig. 2.9). As illustrated in Fig. 2.10, this is most certainly an approximation; however, experi-
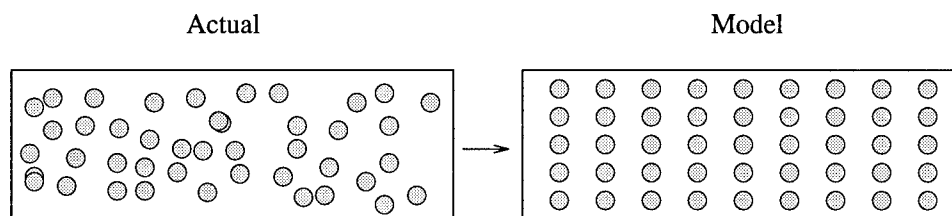
Figure 2.9 Assumed geometric arrangement of fibers.

mental data depicting the macro-mechanical behavior of the composite indicate that the assumption is reasonable. In addition to the assumed symmetry in the fiber arrangement, the fiber/matrix constituents are also assumed to be void of any imperfections, and therefore they respond in a perfectly linear-elastic fashion. Finally, the constituent interface is assumed to be smooth and perfectly bonded.
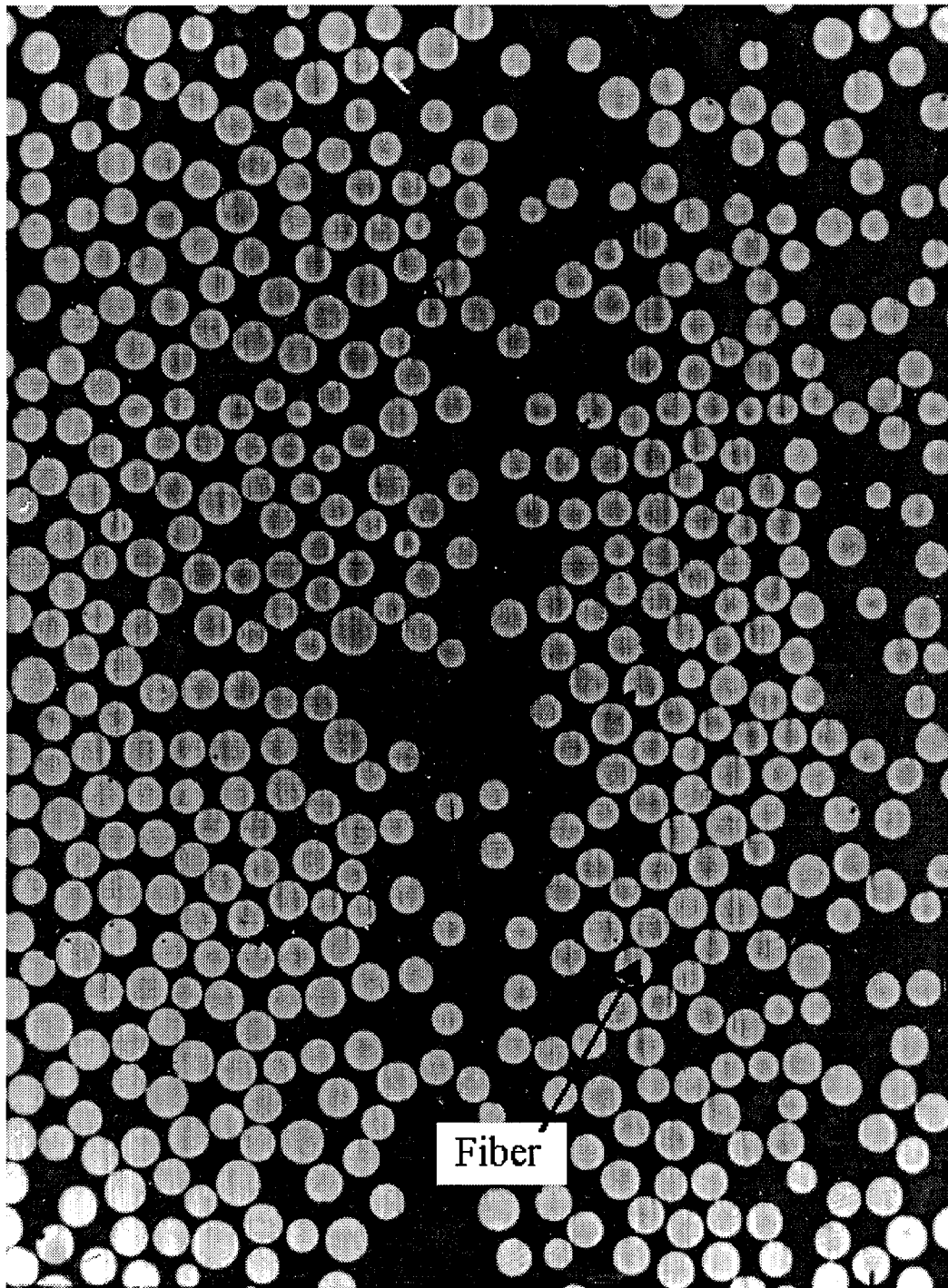
Figure 2.10   Actual geometric arrangement of fibers

The geometric symmetry which results from the aforementioned assumptions creates three mutually perpendicular planes of symmetry. Such a composite material is *orthotropic* in nature, and can be described by nine independent constants [164]. These reduce to five[†] if the material properties are assumed to be the same in the 2-3 direction (Fig. 2.11). The latter is referred to as a *transversely isotropic* material. In addition, because of the assumed symmetry in the laminate's geometry, the composite response can be modeled using a representative volume element (RVE) consisting only of a single fiber and its surrounding matrix. This simplification is at the core of micromechanics theory in which the laminate behavior can be modeled using a simple unit-cell as illustrated in Fig. 2.11. For convenience, the unit-cell is typically
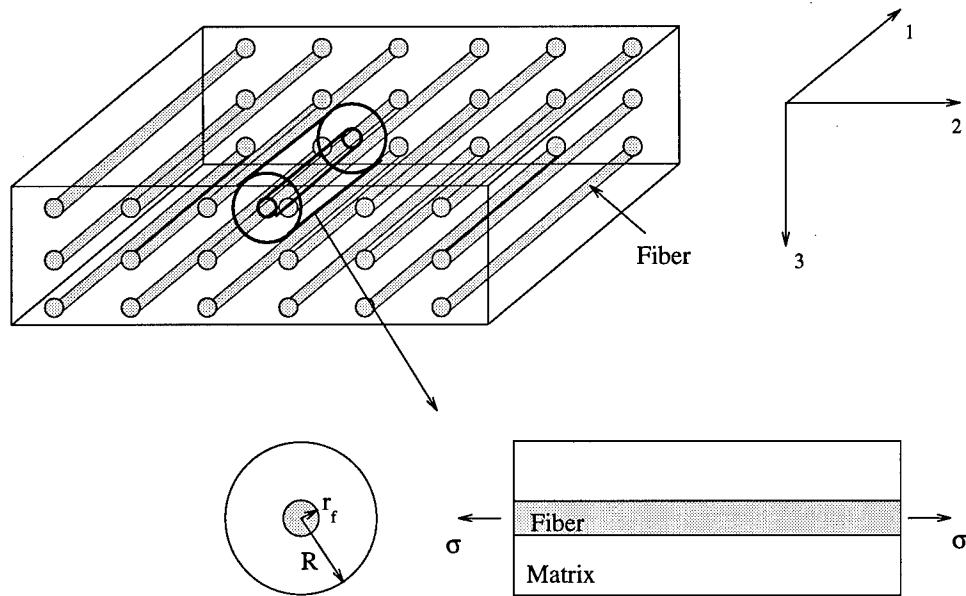
Figure 2.11 Simplification of the assumed idealized laminate geometry to a one-dimensional unit-cell.

assumed to be comprised of a pair of concentric cylinders each representing a given constituent. For the cell shown in Fig. 2.11, r_f is the fiber radius and R is the outer radius of the matrix. The latter is dependent on the relative fiber spacing. If A_f, A_m

---

[†]The composite's elastic moduli, E_1 and E_2; the composite's shear modulus, G_{12}; and the Poisson's ratios, ν_{12} and ν_{23}.

and A_c represent the cross-sectional areas of the fiber, matrix and composite such that $A_f = \pi r_f^2$, $A_m = \pi \left(R^2 - r_f^2 \right)$ and $A_c = \pi R^2$ then the parameters $v_f = A_f/A_c$ and $v_m = A_m/A_c$ define the fiber and matrix volume fractions, respectively. It follows that $R = r_f \sqrt{1 + v_m/v_f}$. The geometry of the undamaged unit-cell is now completely defined. The constitutive equations for the unit-cell are provided in appendix B. Next, the geometric assumptions regarding the incorporation of damage in the unit-cell are discussed.

Damage State. In order to model a *damaged* laminate with the unit-cell described above, symmetry with respect to the damage configuration must be assumed. Toward this end, the matrix cracks within any given ply are assumed to extend throughout the entire lamina cross-section. In particular, each crack describes an infinitely thin plane orthogonal to the loading axis. If multiple matrix cracks exist, the fractures are assumed to be uniformly spaced over the length of the composite. Experimental data indicate that such a periodic distribution of cracks is reasonable [44, 138]. In addition to the matrix cracks, interface debonds may also form during loading. For simplicity, these debonds are assumed only to originate from the crack planes; extend uniformly around the fibers, and to be of constant length for all fiber/crack pairs. Finally, as will be discussed later, the distribution of fiber fractures is assumed to be uniform. The above assumptions allow the composite to again be modeled with a simple RVE consisting of a single fiber and surrounding matrix. In addition, when matrix cracks are considered, the unit-cell is assumed to span a pair of matrix cracks as illustrated in Fig. 2.12. The length of the cell is, therefore, equal to the average crack spacing which is denoted by L.

Numerous models have been proposed for investigating the initiation and evolution of matrix cracking during tensile loading of brittle unidirectional laminates. Despite this, few theories have been proposed which are both representative of the empirical data and amenable to various numerical and analytical methods. Two
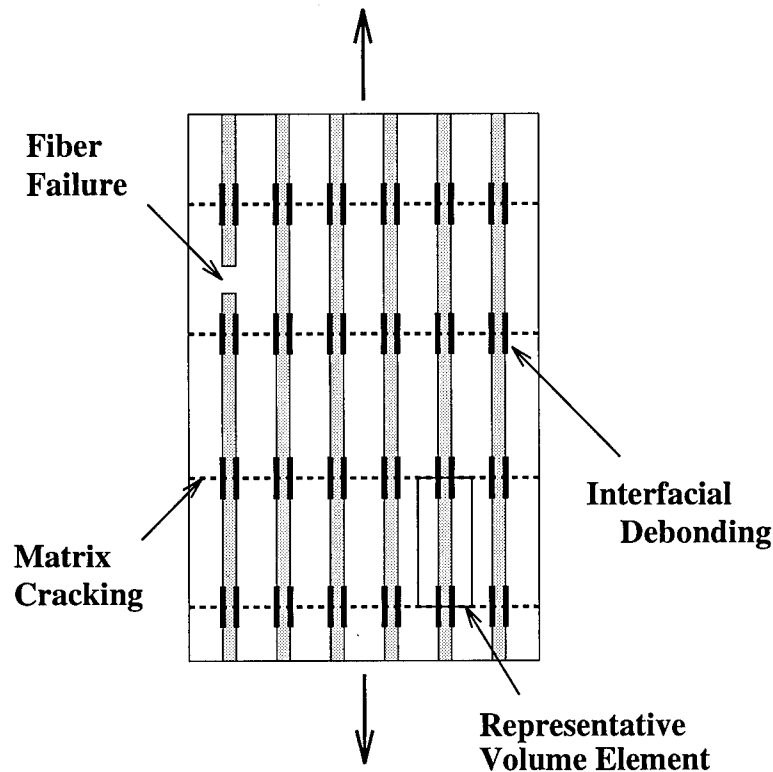
Figure 2.12   Assumed geometric symmetry and corresponding representative volume element.

dominant failure criteria have been presented in the literature: maximum stress (strain) theories and the more traditional fracture mechanics approaches. The latter category includes both the energy balance techniques (discrete solutions) of Aveston, Cooper and Kelly [8], as well as the stress intensity solutions (continuum solutions) similar to those proposed by Marshal, Cox and Evans [127]. The solutions from Aveston, Cooper & Kelly, and Marshal, Cox & Evans are typically referred to as the ACK and MCE theories, respectively.

Previous models yield information on the stress level at which matrix cracking initiates, as well as providing bounding limits for the expected crack densities [8, 179]. Other models investigate the influence of various parameters (fiber volume fraction, fiber radius, thermal stresses, etc) on the expected cracking behavior [113]. Others consider the effects of flaw size and location, and possible variations in the

strain energy release rate [77,102,107,180,196]. Unfortunately, none of the existing analytical solutions provide an accurate representation of the *evolution* of matrix cracks during loading. The limited success of these models has led researchers to rely on empirical crack density data obtained through tedious and time consuming microscopic investigation of the composite microstructure [41,193]. Several of the classical solutions are presented in the next section and in appendix A.

2.5 Existing Models

A tremendous amount of research dealing with ceramic matrix composites has appeared in the literature over the past few decades. Because of this, a number of journals have been established in support of the research. The purpose of this section is to introduce and categorize a portion of the published work which is directly relevant to the present study. The literature review is presented in two subsections which consider *unidirectional* and *cross-ply* lay-ups separately. In addition, both experimental and numerical studies are presented.

As mentioned earlier, in order to model a material such as a ceramic matrix composite which has several prominent damage modes, two items are required. In addition to a representative volume element (RVE) which defines the geometry and constitutive relations, a set of failure criteria for each damage mode must also be selected in order to determine the extent of damage within the composite microstructure. Since the formulations of the RVE and the failure criteria are typically independent, researchers can mix and match as necessary. As such, within each subsection an attempt is made to list the referenced publications by these two categories. Hopefully, in doing so, this section serves as a convenient reference list for many of the ideas used in the present research.

2.5.1 Unidirectional Laminates.   References 5–8,11,12,16,17,20–22,26,28,
33–35,37,38,40,41,44,46,54,64,68,70,76,79,89–91,93,96,97,100,103,110,113,117,127,

129, 133, 134, 137–139, 145, 146, 150–153, 163, 178, 181, 182, 184–186, 193, 196, 200–202, 207, 210, 212, 213 represent most of the studies conducted on brittle unidirectional composites. A few experimental studies have been included in the review [5, 6, 12, 21, 41, 68, 76, 151, 193, 210]; however, the majority are theoretical analyses which investigate the fracture behavior of brittle composite systems [7, 8, 16, 17, 20, 22, 26, 28, 35, 37, 38, 40, 44, 46, 54, 64, 70, 79, 90, 93, 100, 103, 110, 113, 117, 127, 129, 133, 134, 137–139, 146, 152, 153, 163, 178, 181, 182, 184–186, 196, 200, 201, 207, 212, 213]. Furthermore, in their analysis, many of these latter studies incorporate shear-lag models [7, 20, 26, 40, 46, 103, 113, 117, 133, 138, 152, 182] or similar techniques involving a single unit-cell [54, 79, 139, 153, 186, 200, 201, 212]. Some of the studies utilize finite element techniques [11, 16, 44, 97, 178].

The failure criteria for estimating the extent of matrix cracking can be loosely divided into three categories: maximum stress theories [22, 28, 40, 113], fracture mechanics approaches [8, 26, 70, 90, 110, 127, 129, 137, 196, 201, 213], and statistical estimates [37, 117, 181, 182, 207]. Of course, this is not an exhaustive list of possible criteria, and there is some over-lap between these categories. In addition, the studies employing traditional fracture mechanics techniques can be further sub-divided into energy balance solutions and stress intensity approaches. References 8, 46, 201, 213 and 127, 129, 196 provide examples of models which fall in these two categories, respectively. It is also convenient to highlight studies which consider different damage modes, as well as loading conditions. References 22, 35, 38, 64, 212 investigate interface debonding and references 113, 134, 146, 186 focused on fiber failure, whereas fiber pull-out is the main focus of references 93, 134. Conditions of repeated and fatigue loading are considered in references 8, 100, 153, 178 and 17, 54, 163, 181, 184 respectively.

2.5.2 Cross-Ply Laminates. A number of experimental and numerical studies for cross-ply polymeric and ceramic matrix composites have also been reported over the years. References 9, 10, 14, 19, 39, 40, 49, 50, 56–58, 63, 66, 67, 69, 72,

84, 85, 106, 111, 112, 115, 118, 119, 124, 125, 139, 142, 143, 147, 152–154, 157, 158, 183, 194, 195, 198, 205, 206, 209, 211 represent some of this effort. As reported in references 85, 124, 125, 143, 152, 209, cross-ply ceramic composites also exhibit extensive microstructural damage prior to failure. Hence, both a representative model, as well as an appropriate failure criterion for each damage mode are required if the composite's behavior is to be modeled. Studies reported in references 9, 10, 14, 39, 40, 49, 50, 56–58, 63, 66, 67, 69, 72, 84, 106, 111, 112, 115, 118, 139, 142, 147, 153, 154, 157, 158, 183, 194, 195, 198, 205, 206, 211 represent a variety of modeling techniques which combine a myriad of failure criteria to predict the cross-ply composite's behavior. Many of the model formulations in the above studies are based upon the classical shear-lag formulation [9, 10, 39, 40, 56–58, 67, 72, 106, 111, 112, 118, 147, 153, 154, 157, 211]. A number of failure criteria have been used in conjunction with the shear-lag approach to estimate the laminate's damage. Some examples of common failure criteria are the maximum stress criterion in which a single-value of matrix strength is assumed to control matrix cracking [39, 58, 112, 153]; the traditional fracture mechanics approaches which employ a critical energy release rate or stress intensity factor, [9, 10, 56, 67, 111, 118, 147, 198, 211], and statistical failure analyses in which the inherently stochastic nature of brittle failure is considered [57]. Empirical data have also been used [106, 153, 154]. Laws and Dvorak combined a critical energy release rate approach with a statistical analysis [111], while Zhang *et al* [211] employed a critical energy release rate approach with an empirical resistance curve technique. References 14, 40, 84, 106, 205, 206 consider matrix cracking in both the $90°$ ply and the $0°$ ply in ceramic composites. The models from Beyerle *et al* [14] and Xia and Hutchinson [205] represent more sophisticated analyses whereas models from Kuo and Chou [106] and Daniel and Anastassopoulos [40] are shear-lag approximations.

The majority of the above mentioned studies analyze matrix cracking in polymer-based glass/epoxy and graphite/epoxy cross-ply laminates [49, 56–58, 66, 69, 111, 112, 118, 139, 183, 195]. Recently, several studies have been reported to investigate the

behavior of ceramic matrix composites [14, 40, 84, 106, 154, 205, 206], including the initiation and evolution of matrix cracking [14, 84, 205, 206], as well as the general laminate response (e.g. stress-strain behavior and modulus change) [40, 106, 154].

2.6 Summary of Existing Work

As illustrated in the previous section, there has been a large amount of research accomplished in the area of ceramic matrix composites. However, prior to this study, there did not exist a systematic micromechanics approach for modeling the fatigue response of a ceramic matrix laminate. Several shear-lag models have been successfully employed in predicting the response of CMCs, but only under limited loading and damage conditions [7, 20, 26, 40, 46, 103, 113, 117, 133, 138, 152, 182]. For example, Daniel *et al* utilize a shear-lag model in order to investigate the modulus degradation in unidirectional CMCs under conditions of matrix cracking and interface debonding resulting from quasi-static loading [40]. The analysis is similar to the original work by Aveston, Cooper and Kelly (ACK) who first modeled the behavior of CMCs under quasi-static conditions [8]. Karandikar [86] and Kuo [103] also use a similar approach to investigate the behavior of both unidirectional and cross-ply laminates, however, again their studies are limited in scope. For the unidirectional laminate, matrix cracking and interface debonding are considered. For the cross-ply laminate, transverse cracking is also considered; however, the analysis is constrained to only a few discrete damage configurations [103]. The general solution is not determined. Furthermore, many of the other shear-lag models investigating cross-ply laminates consider only transverse cracking of the $90°$ plies [9, 10, 39, 56–58, 67, 72, 111, 118, 147, 157, 211]. Hence, *there is a need for a micromechanics model which not only incorporates the additional damages associated with ceramic matrix composites, e.g. fiber fracture and fiber pull-out, but also considers a generalized state of damage.*

In addition to the model itself, failure criteria for each of the damage mechanisms are required. As mentioned, simple analytic criteria are desired. For matrix cracking, the maximum stress criteria employed by ACK [8] and Daniel *et al* [40] are appealing due to their simplicity; however, the analytic crack densities predicted under these approaches do not match well with the empirical data. In theory, the predicted crack densities evolve rapidly over a narrow stress range whereas experimentally, a gradual evolution of matrix cracking is observed. The energy balance solution presented by Spearing and Zok suffers similarly [179]. The criterion adopted by Weitsman and Zhu demonstrates a more realistic stress range for the matrix breakup; however, the predicted response still only matches the empirical data in piecewise segments [201]. This results because the predicted crack densities are forced to jump in a discrete manner. In particular, the crack density is assumed to double each time the failure criterion is satisfied [201]. The latter is also a limitation of the maximum stress criterion [8]. Finally, the failure criteria presented by Spearing and Zok [179] and Weitsman and Zhu [201] are dependent on the critical energy release rate of the composite which has proven quite difficult to quantify in CMCs [37]. As a result, researchers have been forced to rely on empirical data for determining the extent of microstructural damage. Unfortunately, such data are tedious and costly to obtain, if they can be determined at all.[†] Hence, *there is a need for better and reliable failure criteria which can be easily employed in a comprehensive micromechanics analysis. Moreover, these criteria need to be consistent with the experimental data, and finally the solutions should minimize the current reliance on empirical data.*

Despite the large number of models which have been proposed (section 2.5), there are only a small number of micromechanics studies that compare predicted stress-strain responses with empirical data for CMCs under quasi-static loading [8, 40, 154]. Results under fatigue loading are even more scarce [54, 153]. In par-

---

[†]Empirical data on fiber fractures and interface debonds are virtually impossible to obtain due to the nature of the fracture modes.

ticular, the analyses presented by Pryce and Smith [153] and Evans *et al* [54] are the only papers found by the author which compared predicted and experimental results for fatigue type loadings. The analysis by Pryce and Smith uses empirical crack density data and is limited to small strain values since matrix cracking is the only damage mode considered [153]. Evans *et al* provide a more comprehensive analysis; however, the study is limited to unidirectional composites. Furthermore, the model and failure criteria are quite complex and rely on empirical data. No analytic predictions of the composite's fatigue limit and fatigue life are known by the author to exist. Hence, *there is a need for analytical (micromechanics) models which predict the stress-strain response under different loadings, including the complete fatigue behavior,[†] for unidirectional and cross-ply CMC laminates.*

The model and failure criteria formulated here provide a systematic methodology satisfying the aforementioned requirements. The micromechanics models account for a general set of damages under the micromechanics assumptions, and the failure criteria are simple, analytic and provide good agreement with experimental data. Moreover, their reliance on empirical data is minimized. Finally, as demonstrated in chapters four and five, the results predicted by the present analysis compare well with experimental data for both unidirectional and cross-ply CMC laminates subjected to quasi-static, repeated and fatigue loadings.

[†]S-N behavior, hysteresis, modulus degradation and strain ratchetting.

III. Theory

The goal of the present analysis is to generate stress-strain responses which are representative of empirical data for unidirectional and cross-ply ceramic matrix composites. This study focuses on the stress-strain behavior since such responses yield the residual laminate properties (e.g. strength and stiffness) which are ultimately the desired quantities in the real applications of CMCs. Moreover, if the predicted stress-strain response matches well with experimental tests then one can assume that the microstructural damages are being adequately characterized. The methodology adopted for the current analysis is outlined in Fig. 3.1.

MODEL

Laminate Geometry

Constitutive Law

Stress-Strain
S-N Behavior
Strain Ratchetting
Modulus Degradation
Laminate Failure
Hysteresis

FAILURE CRITERIA

Matrix Cracking

Interfacial Debonding

Fiber Fracture

LOADING
CONSIDERATIONS

Quasi-Static

Repeated

Cyclic
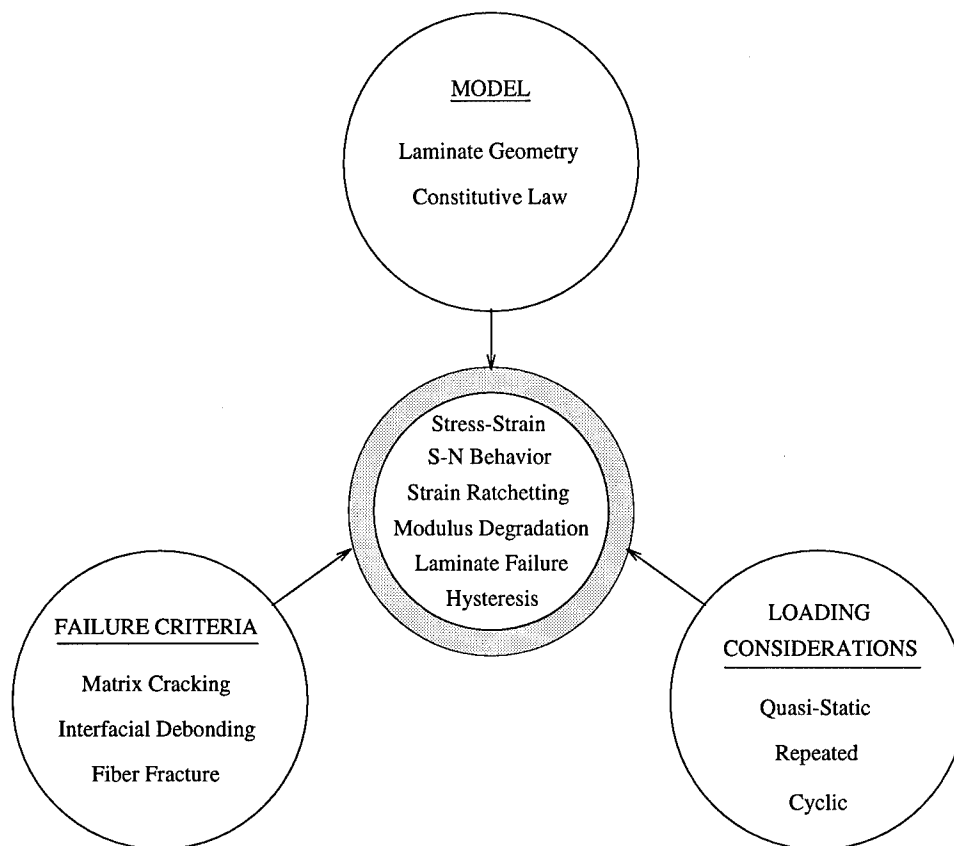
Figure 3.1   Methodology overview.

Three concepts are incorporated in the analysis. These are (1) the representative

volume element (*model*) which defines the laminate's geometry and constitutive relations, (2) the *failure criteria* which yield the state of damage in the laminate, and (3) some additional microstructural mechanisms which are required when analyzing the loading and unloading behavior, e.g. frictional slip. The latter are labeled under the heading of *loading considerations* in Fig. 3.1.

For modeling purposes, two constitutive laws are used to generate the stress-strain curves depending on whether or not damage is present within the composite (appendix E). For an undamaged laminate, a rule-of-mixtures constitutive law is used (appendix B). This allows for a extremely efficient means for determining the composite strain, ϵ_c. In theory, since the composite's constituents are assumed to deform linear-elastically, the composite strain is completely defined by the Hookean relation

$$\sigma = E_c \epsilon_c \tag{3.1}$$

where σ is the applied stress and E_c is the elastic modulus of the composite. Note that the latter is only a function of the laminate geometry and the constitutive properties, i.e.

$$E_c = v_f E_f + v_m E_m \tag{3.2}$$

for a unidirectional laminate and

$$E_c = \frac{b}{b+d} E_1 + \frac{d}{b+d} E_2 \tag{3.3}$$

for a cross-ply laminate where

$$E_1 = v_f E_f + v_m E_m, \tag{3.4}$$

$$E_2 = \left\{ \frac{v_f}{E_f} + \frac{v_m}{E_m} \right\}^{-1}. \tag{3.5}$$

In Eqs. (3.2) and (3.3), v_f and v_m are the volume fractions of the fiber and matrix constituents, respectively. The parameters E_f and E_m are the corresponding elastic moduli, and b and d are the half-thicknesses for the 90° ply and the 0° ply in a cross-ply laminate.

Once damage forms within the laminate, the composite strain is determined from Eq. (3.6) which assumes that the composite strain is equivalent to the average strain in an undamaged fiber.

$$\epsilon_c = \frac{1}{E_f L} \int_L \sigma_f(x) \, dx + (\alpha_f - \alpha_c)\Delta T \qquad (3.6)$$

Furthermore, the fiber stress, $\sigma_f(x)$, is, in general, dependent on the extent of matrix cracking, interface debonding, and fiber fracture. Moreover, the specific equation relating $\sigma_f(x)$ to the laminate geometry and damages is determined from the shear-lag formulation as presented in the next section. The extent of damage is determined from the appropriate failure criteria (section 3.2).

In short, given the proper laminate parameters and loading history, the material stress-strain response can be determined from Eqs. (3.1) through (3.6). The remainder of this chapter provides details of the theoretical formulation for the present study. The theory is presented in three sections: model formulation, failure criteria, and loading considerations.

3.1 Model Formulation

As mentioned, prior to the formation of any damages, Eqs. (3.1), (3.2) and (3.3) are used to generate the laminate's stress-strain response. This rule-of-mixtures theory is well established and is outlined in appendix B. The interesting case is when damage is present and $\sigma_f(x)$ varies over the length of the unit-cell. This is now addressed.

3.1.1 Modeling Damage. When introducing a matrix crack into the analysis, the axial constituent stresses vary in the vicinity of the fracture since the stress in the matrix vanishes at the free boundary (Fig. 3.2). Furthermore, along the plane
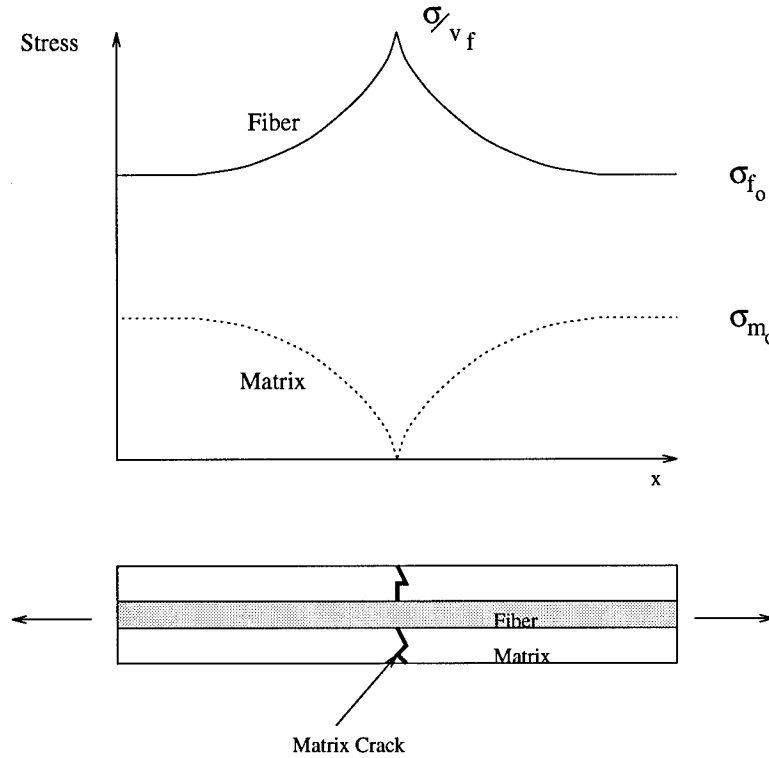
Figure 3.2   Stress redistribution near a matrix crack.

of the crack, the fiber stress reaches a maximum since the bridging fiber is forced to carry the entire load. The magnitude of the maximum fiber stress is

$$\sigma_f(x)_{max} = \frac{\sigma}{v_f}. \tag{3.7}$$

Away from the crack plane, the stresses are redistributed within the constituents and eventually return to a magnitude equal to their original rule-of-mixtures value. These stresses are denoted as σ_{f_o} and σ_{m_o} for the fiber and matrix, respectively. Hence, the effect of the crack is a localized phenomenon which helps explain why the stress-strain response is not influenced by a single crack ($\sigma = \sigma_{mc}$), but rather

3-4

only deviates from linearity after a significant accumulation of cracks ($\sigma = \sigma_{cr}$). It may be shown that at any point equilibrium requires

$$\sigma = v_f \sigma_f(x) + v_m \sigma_m(x). \qquad (3.8)$$

If multiple cracks are considered, then the pattern in Fig. 3.2 simply repeats. That is, along each fracture plane, the matrix stress vanishes and the stress in the fiber is a maximum (Fig. 3.3). Away from the crack plane, the stresses are redistributed between the constituents.
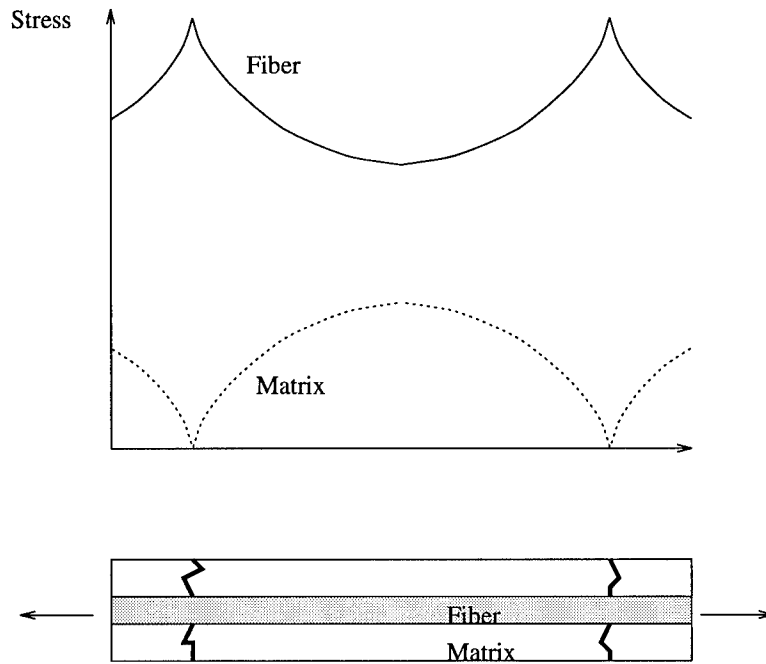
Figure 3.3 Stress redistribution for multiple cracks.

In examining a simplified free body diagram of a unit-cell spanning a pair of matrix cracks, it becomes quite apparent that the vehicle that the fiber uses to transfer load back into the matrix is exactly the shear stress which develops along the fiber/matrix interface (Fig. 3.4). And indeed when carrying out the mathematics for the equilibrium of forces on the fiber (Fig. 3.5), the rate of change of the axial
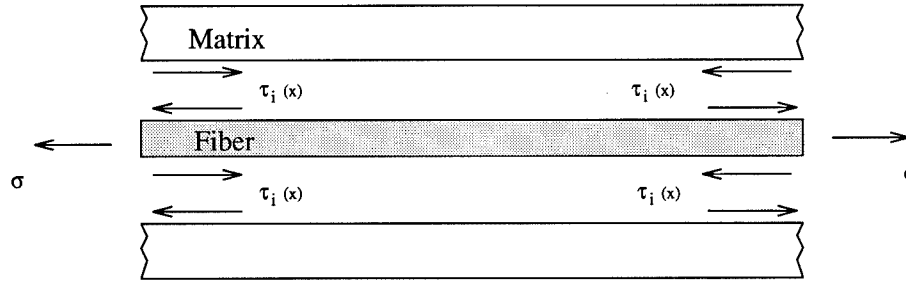
Figure 3.4   Simplified free body diagram of a unit-cell spanning a pair of matrix cracks.

fiber stress is found to be directly proportional to the interface shear according to

$$\pi r_f^2 \left\{ -\sigma_f(x) + \sigma_f(x) + \frac{d\sigma_f(x)}{dx}dx \right\} + 2\pi r_f \cdot \tau_i(x) \cdot dx = 0 \qquad (3.9)$$

or equivalently

$$\frac{d\sigma_f(x)}{dx} = \frac{-2\tau_i(x)}{r_f}. \qquad (3.10)$$

From Eq. (3.8), the matrix stress, $\sigma_m(x)$, is also dependent only on the interface shear. Hence, if the interface shear stress, $\tau_i(x)$, can be determined, or somehow defined, then the constituent stresses and ultimately the composite strain may be determined from Eqs. (3.6), (3.8) and (3.10). This is the basic premise of *shear-lag*
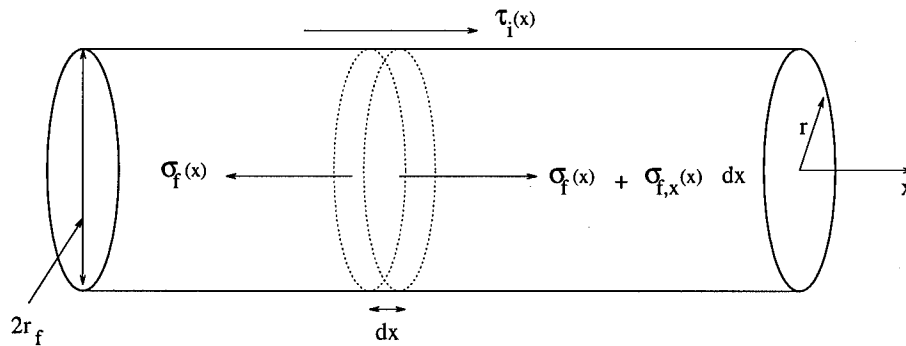
Figure 3.5   Equilibrium of forces on the fiber.

theory in which an approximate expression for $\tau_i(x)$ is assumed. In particular, shear-lag theory assumes that the interface shear stress is proportional to the difference in the average displacements of the constituent. That is,

$$\tau_i(x) = \mathcal{H}\left\{\bar{u}_f(x) - \bar{u}_m(x)\right\} \tag{3.11}$$

where $\mathcal{H}$ is the proportionality constant. The average displacements for the fiber and matrix, $\bar{u}_f(x)$ and $\bar{u}_m(x)$, are determined by considering the deformation of a line which is initially orthogonal to the loading axis. These displacements, as shown in Fig. 3.6, are determined from Eqs. (3.12) and (3.13).

$$\bar{u}_f = \frac{1}{\pi r_f^2} \int_0^{r_f} \int_0^{2\pi} u_f(x,r) \, r \, d\theta \, dr \tag{3.12}$$

$$\bar{u}_m = \frac{1}{\pi(R^2 - r_f^2)} \int_{r_f}^{R} \int_0^{2\pi} u_m(x,r) \, r \, d\theta \, dr \tag{3.13}$$

where $u_f(x,r)$ and $u_m(x,r)$ are the two-dimensional in-plane constituent displacements illustrated by the deformed line in Fig. 3.6. Note that the deformed line,
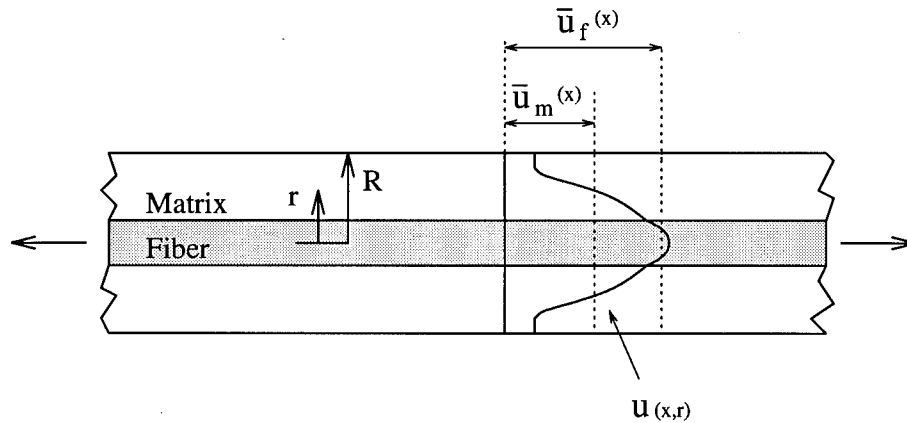
Figure 3.6   Deformation of a line, initially orthogonal to the fiber axis, during loading of a composite with damage.

$u(x,r)$, illustrated in Fig. 3.6 is only an illustration and may not be representative of the actual deformation. In theory, the strain, i.e. the derivative of the displacement,

must be continuous within each of the constituents, but may be discontinuous along their common interface. Furthermore, the shear stress vanishes along any planes of symmetry, e.g. at $r = 0$ and R. The latter boundary condition requires that the matrix-to-matrix interface of adjacent cells have continuous displacements and be free of any shear such that the deformation of each cell is equivalent. Given the average constituent displacements, Eqs. (3.8), (3.10) and (3.11) completely define the state of stress $[\sigma_f(x),\ \sigma_m(x)$ and $\tau_i(x)]$ within the unit-cell.

Under the traditional shear-lag formulation, these stresses can represented by Eqs. (3.14) through (3.16) [25].

$$\sigma_f(x) = \sigma_{f_o} + \frac{v_m}{v_f}\frac{\cosh(\beta x)}{\cosh(\beta L/2)}\sigma_{m_o} \tag{3.14}$$

$$\sigma_m(x) = \sigma_{m_o}\left\{1 - \frac{\cosh(\beta x)}{\cosh(\beta L/2)}\right\} \tag{3.15}$$

$$\tau_i(x) = -\frac{\beta r_f}{2}\frac{v_m}{v_f}\frac{\sinh(\beta x)}{\cosh(\beta L/2)}\sigma_{m_o} \tag{3.16}$$

Furthermore, if these distributions are known then the laminate's stress-strain response may be determined from Eq. (3.6). This procedure is, of course, contingent upon *a priori* knowledge of the average crack spacing, i.e. the parameter L in Eqs. (3.14) through (3.16) must be known. This requires the use of a predetermined failure criterion. Moreover, if other damage mechanisms, laminate geometries and loading conditions are considered, Eqs. (3.14) through (3.16) must be appropriately modified. This is the focus of the current research in which Eqs. (3.14) through (3.16) are modified to account for other damages such as interface debonding and fiber fracture. In addition, a myriad of other items required to model the mechanical response of unidirectional and cross-ply laminates when subjected to repeated loading conditions are developed. These are presented in the remainder of this chapter, as well as appendices B through I. The predicted composite response is presented in chapters four and five.

As presented in the previous chapter, several shear-lag models have been proposed for analyzing unidirectional and cross-ply brittle fiber-reinforced composites. The primary difference between many of the shear-lag models resides not in their formulations, but rather in the procedure on how the instantaneous damage configuration (crack spacing, debond length, etc) is determined. For the current analysis, the fundamental theory used in the development of the two models for the unidirectional and cross-ply laminates is the same. More specifically, the models differ only in their representative volume element (RVE) geometries (e.g. cross-sections) and choice of coordinate system. These formulations of the unidirectional and cross-ply shear-lag models are now presented.

3.1.2 Unidirectional Model. For the unidirectional laminate, the only stresses considered are the axial fiber stress, $\sigma_f(x)$, the axial matrix stress, $\sigma_m(x)$, and the interface shear, $\tau_i(x)$. Moreover, these stresses are related to one another through the following equilibrium relations [25, 103].[†]

$$\sigma = v_f \sigma_f(x) + v_m \sigma_m(x) \tag{3.8}$$

$$\frac{d\sigma_f(x)}{dx} = \frac{-2\tau_i(x)}{r_f} \tag{3.10}$$

Equations (3.8) and (3.10) represent two equations in three unknowns, $\sigma_f(x)$, $\sigma_m(x)$ and $\tau_i(x)$. Under shear-lag theory, two additional relations are assumed. The first equation from the shear-lag analysis relates the interface shear to the average constituent displacements according to Eq. (3.11) [25, 103].

$$\tau_i(x) = \mathcal{H} \left\{ \bar{u}_f(x) - \bar{u}_m(x) \right\} \tag{3.11}$$

[†]See also appendix B.

In addition, the current shear-lag formulation also assumes the following kinematic relations:

$$\sigma_f(x) + E_f \alpha_f \Delta T = E_f \epsilon_f(x) \doteq E_f \left(\frac{d\bar{u}_f(x)}{dx} \right) \tag{3.17}$$

and

$$\sigma_m(x) + E_m \alpha_m \Delta T = E_m \epsilon_m(x) \doteq E_m \left(\frac{d\bar{u}_m(x)}{dx} \right). \tag{3.18}$$

It is these latter relations where the problem is reduced to one dimension. The problem formulation now consists of four equations[†] in four unknowns, $\sigma_f(x)$, $\sigma_m(x)$, $\tau_i(x)$ and $\mathcal{H}$. The derivations of $\mathcal{H}$ and $\sigma_f(x)$ are now presented. Given these solutions, determination of $\sigma_m(x)$ and $\tau_i(x)$ is trivial from Eqs. (3.8) and (3.10).

3.1.2.1 Determination of the Shear-Lag Constant, $\mathcal{H}$.

Under the current formulation, the *difference* in the average constituent displacements, $\bar{u}_f(x) - \bar{u}_m(x)$, is dependent only on the interface shear, $\tau_i(x)$, because of the assumed problem kinematics. This allows the shear-lag parameter, $\mathcal{H}$, to be determined easily from Eq. (3.11); however, the formulation of the right hand side of this equation is somewhat involved.

To begin the analysis, consider the unit-cell illustrated in Fig. 3.7. As is typical of micromechanics analyses, the unit-cell is assumed to consist of a single fiber and its surrounding matrix (appendix B). Furthermore, these entities are modeled as a pair of concentric cylinders of length L which is the average matrix crack spacing. Also, note that the fiber/matrix constituents are permitted to debond with the length of the debond being denoted d. Within the debonded region, the interface shear stress is assumed constant in order to make the analysis tractable. Hence Eq. (3.11) only applies over the range $-L/2 + d \leq x \leq L/2 - d$.

Let the geometry of the cylindrical model be defined by the coordinates, r, θ and x as defined in this figure. Furthermore, let $\overline{r_f} \in [0, \ r_f]$ and $\overline{r_m} \in [r_f, \ R]$

[†]Equations (3.17) and (3.18) are not independent.
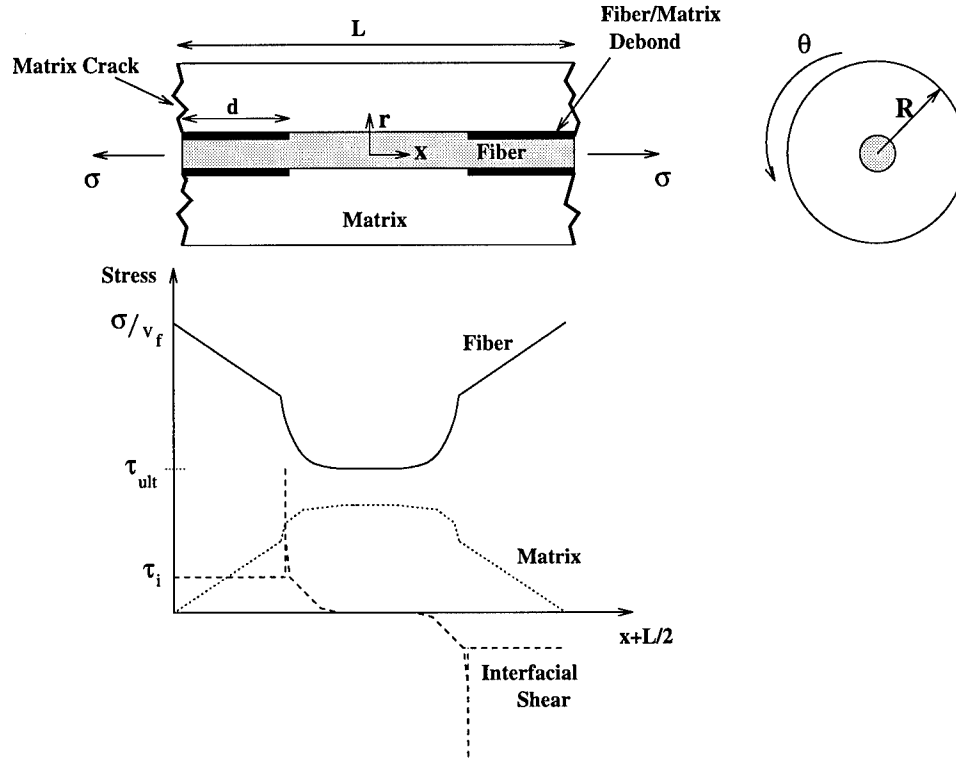
Figure 3.7   One-dimensional shear-lag model and corresponding constituent and interface stresses.

define the boundaries of the individual constituent cylinders. Now for this system of coordinates, equilibrium requires

$$\frac{\partial \sigma_{rr}}{\partial r} + \frac{1}{r}\frac{\partial \tau_{\theta r}}{\partial \theta} + \frac{\partial \tau_{xr}}{\partial x} + \frac{1}{r}\left(\sigma_{rr} - \sigma_{\theta\theta}\right) = 0, \tag{3.19}$$

$$\frac{\partial \tau_{r\theta}}{\partial r} + \frac{1}{r}\frac{\partial \sigma_{\theta\theta}}{\partial \theta} + \frac{\partial \tau_{x\theta}}{\partial x} + \frac{2}{r}\tau_{r\theta} = 0, \tag{3.20}$$

$$\frac{\partial \tau_{rx}}{\partial r} + \frac{1}{r}\frac{\partial \sigma_{\theta x}}{\partial \theta} + \frac{\partial \sigma_{xx}}{\partial x} + \frac{1}{r}\tau_{rx} = 0. \tag{3.21}$$

From all the simplifying micromechanics assumptions outlined in the previous chapter, the constituent stresses are independent of the circumferential angle θ. Hence Eq. (3.20) is satisfied directly, and Eqs. (3.19) and (3.21) reduce appropriately. Furthermore, the radial normal stress, σ_{rr}, and the radial displacement, u_r, will be

3-11

neglected. As a result, Eq. (3.19) will not be satisfied. Based upon these assumptions, the governing equilibrium equation becomes

$$\frac{\partial \tau_{rx}}{\partial r} + \frac{\partial \sigma_{xx}}{\partial x} + \frac{1}{r}\tau_{rx} = 0. \tag{3.22}$$

When considering the two regions $\overline{r_f}$ and $\overline{r_m}$, as well as Eqs. (3.8) and (3.10), Eq. (3.22) can be represented by the following relations.

$$\frac{d\tau(x,r)}{dr} - \frac{2\tau_i(x)}{r_f} + \frac{1}{r}\tau(x,r) = 0 \quad \text{for } r \in \overline{r_f} \tag{3.23}$$

$$\frac{d\tau(x,r)}{dr} + \frac{2v_f\tau_i(x)}{v_m r_f} + \frac{1}{r}\tau(x,r) = 0 \quad \text{for } r \in \overline{r_m} \tag{3.24}$$

where $\tau(x,r) = \tau_{xr}$. Further, $\tau(x,r)$ is the two-dimensional *constituent* shear stress which results from the two-dimensional deformations of the fiber and matrix (reference Fig. 3.6 on page 3-7). Solving Eqs. (3.23) and (3.24), the following relations are found.

$$\tau(x,r) = \frac{r}{r_f}\tau_i(x) \quad \text{for } r \in \overline{r_f} \tag{3.25}$$

$$\tau(x,r) = \left(\frac{R^2}{r_f} - r_f\right)^{-1}\left(\frac{R^2}{r} - r\right)\tau_i(x) \quad \text{for } r \in \overline{r_m} \tag{3.26}$$

Equation (3.26) is more apparent when considering that

$$\frac{v_f}{v_m} = r_f\left(\frac{R^2}{r_f} - r_f\right)^{-1}. \tag{3.27}$$

Additionally, the linear-elastic kinematic relation between the constituent stress and displacements is given by

$$\tau(x,r) = G\left(\frac{\partial u_r}{\partial x} + \frac{\partial u_x}{\partial r}\right) \tag{3.28}$$

when considering small strain theory. Recall, however, that under the current formulation, the radial displacement, u_r, is neglected; hence Eq. (3.28) reduces to

$$\frac{\partial u(x,r)}{\partial r} = \frac{1}{G_f}\frac{r}{r_f}\tau_i(x) \quad \text{for } r \in \overline{r_f}, \tag{3.29}$$

$$\frac{\partial u(x,r)}{\partial r} = \frac{1}{G_m}\left(\frac{R^2}{r_f} - r_f\right)^{-1}\left(\frac{R^2}{r} - r\right)\tau_i(x) \quad \text{for } r \in \overline{r_m} \tag{3.30}$$

where Eqs. (3.25) and (3.26) have also been considered and where u_x is now written as $u(x,r)$. Integrating Eqs. (3.29) and (3.30), the two-dimensional constituent displacements are found to be

$$u_f(x,r) = u_o(x) - \frac{1}{2r_f G_f}\left(r_f^2 - r^2\right)\tau_i(x) \quad \text{for } r \in \overline{r_f} \tag{3.31}$$

and

$$u_m(x,r) = u_o(x) + \frac{1}{2r_f G_m}\frac{v_f}{v_m}\left(2R^2\ln\frac{r}{r_f} + r_f^2 - r^2\right)\tau_i(x) \quad \text{for } r \in \overline{r_m}. \tag{3.32}$$

The displacement $u_o(x)$ is the axial displacement along the interface [i.e. $u_o(x) = u_f(x,r_f) = u_m(x,r_f)$]. Moreover, since Eq. (3.11) is only valid within *bonded* interface regions, the interface displacements are continuous, i.e. slip is not permitted, and $u_o(x) = \int_0^x \sigma/E_1 \, d\eta$. Defining the average displacements as

$$\bar{u}_f = \frac{1}{\pi r_f^2}\int_0^{r_f}\int_0^{2\pi} u_f(x,r) \, r \, d\theta \, dr, \tag{3.12}$$

$$\bar{u}_m = \frac{1}{\pi(R^2 - r_f^2)}\int_{r_f}^{R}\int_0^{2\pi} u_m(x,r) \, r \, d\theta \, dr \tag{3.13}$$

yields the following when Eqs. (3.31) and (3.32) are employed.

$$\bar{u}_f(x) = u_o(x) - \frac{r_f}{4G_f}\tau_i(x) \tag{3.33}$$

$$\bar{u}_m(x) = u_o(x) + \frac{r_f}{G_m}\left\{\frac{1}{2v_m^2}\ln\frac{1}{v_f} - \frac{3}{4} - \frac{v_f}{2v_m}\right\}\tau_i(x) \tag{3.34}$$

From which in applying Eq. (3.11), the shear-lag parameter $\mathcal{H}$ is determined.

$$\mathcal{H} = -\frac{4}{r_f}\left\{\frac{1}{G_f} + \frac{1}{G_m}\left(\frac{2}{v_m^2}\ln\frac{1}{v_f} - 3 - 2\frac{v_f}{v_m}\right)\right\}^{-1} \tag{3.35}$$

3.1.2.2 Determination of the Axial Fiber Stress, $\sigma_f(x)$. As with the shear-lag parameter, the axial fiber stress, $\sigma_f(x)$ is determined from Eq. (3.11). In addition, Eqs. (3.17) and (3.18) are also employed in the derivation. The solution for this stress is not determined directly; rather the formulation consists in finding a linear second-order differential equation whose solution yields the desired stress. In particular, the governing equation is determined through differentiation of the shear-lag equation [Eq. (3.11)]. Hence, from Eqs. (3.10) and (3.11), the following relation holds

$$\frac{d\sigma_f(x)}{dx} = \hat{\mathcal{H}}\{\bar{u}_f(x) - \bar{u}_m(x)\} \tag{3.36}$$

where $\hat{\mathcal{H}} = -2\mathcal{H}/r_f$. Now, in differentiating Eq. (3.36) and applying Eqs. (3.17) and (3.18), Eq. (3.37) is determined.

$$\frac{d^2\sigma_f(x)}{dx^2} = \hat{\mathcal{H}}\left\{\frac{\sigma_f(x)}{E_f} + \alpha_f\Delta T - \left(\frac{\sigma_m(x)}{E_m} + \alpha_m\Delta T\right)\right\} \tag{3.37}$$

Note again, it has been assumed that all constituent displacements, on average, result solely from the axial (normal) constituent stresses. This is a consequence of the assumed one-dimensional nature of the problem. Also, from Eq. (3.8),

$$\sigma_m(x) = \frac{1}{v_m}\{\sigma - v_f\sigma_f(x)\}. \tag{3.38}$$

3-14

Finally, in substituting Eq. (3.38) into Eq. (3.37), the following linear second-order differential equation with constant coefficients is determined.

$$\frac{d^2\sigma_f(x)}{dx^2} - \beta^2\sigma_f(x) = -\beta^2\sigma_{f_o} \tag{3.39}$$

where

$$\beta^2 = \frac{E_1}{v_m E_m E_f}\hat{\mathcal{H}} \tag{3.40}$$

The solution to the above equation provides an expression for the axial fiber stress as developed under the current shear-lag analysis. The final form may be expressed as

$$\sigma_f(x) = A\cosh(\beta x) + B\sinh(\beta x) + \sigma_{f_o}. \tag{3.41}$$

The constants A and B are determined from the appropriate boundary conditions which for the unidirectional model are that (1) along the plane of a matrix crack, the stress in the matrix vanishes due to the free boundary, and (2) the interface shear stress vanishes along the plane of symmetry. For the model shown in Fig. 3.7, these conditions require that

$$\sigma_m\left(x = \pm\frac{L}{2}\right) = 0, \tag{3.42}$$

$$\tau_i(x = 0) = 0. \tag{3.43}$$

These develop since the unit-cell is assumed to span a pair of matrix cracks with L as the average matrix crack spacing (Fig. 3.7). More specifically, since the coordinate system shown in Fig. 3.7 is referenced at the center of the unit-cell, the matrix cracks occur at $x = \pm L/2$. Moreover, since symmetry with respect to the extent of debonding is also assumed and since the interface shear stress, τ_i, is assumed

constant within debonded regions, Eq. (3.42) may be written as

$$\sigma_f\left(x = L/2 - d\right) = \frac{\sigma}{v_f} - \frac{2\tau_i}{r_f}d \qquad (3.44)$$

where d is the length of the debonded region. The average matrix crack density, i.e. the number of cracks per unit length, is $1/L$.

Finally, upon solving the system of equations defined by Eqs. (3.41) through (3.44), the desired stresses are determined to be as follows:

$$\sigma_f(x) = \begin{cases} \sigma_{f_o} + \dfrac{\cosh(\beta x)}{\cosh[\beta(L/2 - d)]}\left(\dfrac{v_m}{v_f}\sigma_{m_o} - 2\dfrac{d}{r_f}\tau_i\right) & \text{bonded region} \\[2ex] \dfrac{\sigma}{v_f} - \dfrac{2}{r_f}\tau_i(L/2 - |x|) & \text{debonded region} \end{cases}$$

$$\sigma_m(x) = \begin{cases} \sigma_{m_o} - \dfrac{\cosh(\beta x)}{\cosh[\beta(L/2 - d)]}\left(\sigma_{m_o} - 2\dfrac{v_f}{v_m}\dfrac{d}{r_f}\tau_i\right) & \text{bonded region} \\[2ex] \dfrac{v_f}{v_m}\dfrac{2}{r_f}\tau_i(L/2 - |x|) & \text{debonded region} \end{cases}$$

$$\tau_i(x) = \begin{cases} -\dfrac{\beta r_f}{2}\dfrac{\sinh(\beta x)}{\cosh[\beta(L/2 - d)]}\left(\dfrac{v_m}{v_f}\sigma_{m_o} - 2\dfrac{d}{r_f}\tau_i\right) & \text{bonded region} \\[2ex] \tau_i & \text{debonded region} \end{cases}$$

$$(3.45)$$

where

$$\sigma_{m_o} = \frac{E_m}{E_1}\sigma + E_m(\alpha_1 - \alpha_m)\Delta T \qquad (3.46)$$

$$\sigma_{f_o} = \frac{E_f}{E_1}\sigma + E_f(\alpha_1 - \alpha_f)\Delta T \qquad (3.47)$$

$$\beta^2 = \frac{8}{r_f{}^2}\frac{E_1}{E_f E_m v_m}\left[\frac{1}{G_f} + \frac{1}{G_m}\left(\frac{2}{v_m{}^2}\ln\frac{1}{v_f} - 3 - 2\frac{v_f}{v_m}\right)\right]^{-1}. \qquad (3.48)$$

Typical distributions for these stresses are shown schematically in Fig. 3.7. Note that within the bonded region, the transfer of stresses between the constituents is quite efficient due to the large interface shear stresses; whereas within the debonded region, the stress transfer is less pronounced since the maximum interface shear is limited by Coulomb friction. As mentioned earlier, the interface shear stress in the

debonded regions is assumed constant; having magnitude τ_i. With the stress state now defined, the stress-strain response can be predicted from Eq. (3.6) *provided the extent of composite damage is known.* These damages are estimated by the failure criteria outlined following the formulation of the cross-ply model.

3.1.3 Cross-ply Model. The development of the cross-ply model is similar to the unidirectional model; however, due to the presence of the off-axis plies (e.g. 90° plies), some additional simplifying assumptions are required. As an illustration, for the present analysis, the cross-ply lay-up is assumed to be of the form $[(0_m/90_n)]_s$ so that the symmetry may be exploited during modeling. In addition, the plies are assumed to be perfectly bonded and void of any imperfections. The *interlaminar* shear stress is defined by $\tau(x)$. The half thickness of the 0° ply and 90° ply are b and d, respectively as shown in Fig. 3.8, and the unit-cell is assumed to be of unit depth (y direction).
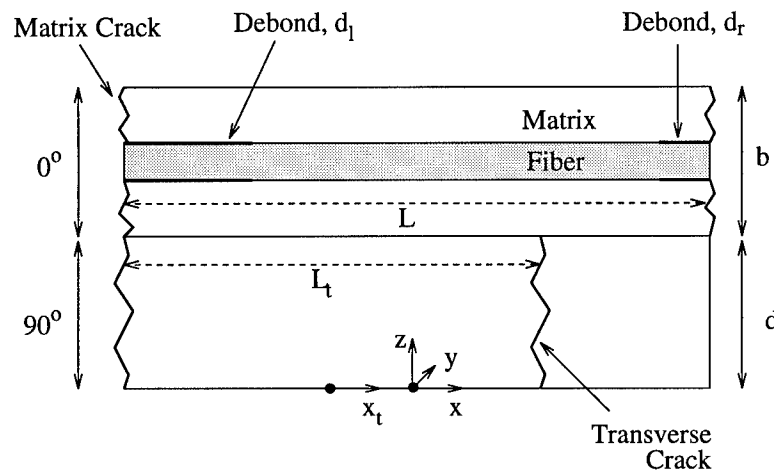
Figure 3.8 Representative volume element used in the analysis of cross-ply laminates.

A free body diagram of the representative cell, Fig. 3.9, yields the following equilibrium relations:

$$\left\{ \sigma_L(x) + \frac{d\sigma_L(x)}{dx}dx - \sigma_L(x) \right\} b - \tau(x)dx = 0, \tag{3.49}$$

$$\left\{ -\sigma_T(x) + \sigma_T(x) + \frac{d\sigma_T(x)}{dx}dx \right\} d + \tau(x)dx = 0 \tag{3.50}$$

where $\sigma_L(x)$ is the average axial stress in the 0° (longitudinal) plies, and $\sigma_T(x)$ is the average axial stress in the 90° (transverse) plies.
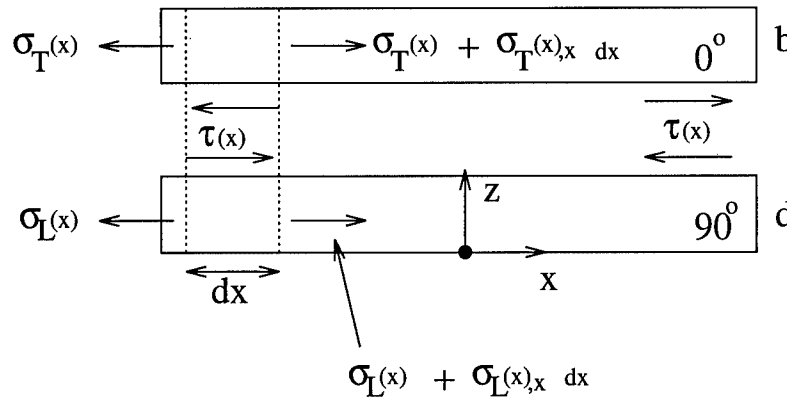
Figure 3.9   Free-body diagram illustrating the stresses considered in the cross-ply analysis.

It is clear from Eqs. (3.49) and (3.50) that the stress transfer between the 90° ply and the 0° ply is governed by the *interlaminar* shear stress, $\tau(x)$, which develops along their common boundaries. More specifically,

$$\tau(x) = b\frac{d\sigma_L(x)}{dx} = -d\frac{d\sigma_T(x)}{dx}. \tag{3.51}$$

Equation (3.51) is a standard relation from which most cross-ply shear-lag models begin their development [111].

In determining the state of stress within the cross-ply laminate, three entities are considered: the fiber of the 0° plies, the matrix of the 0° plies, and the 90° plies.

Hence, the behavior of the zero degree plies are considered on a *constituent* level, whereas the behavior of the off-axis (90°) plies are viewed on a *lamina* level. This assumption is valid since the fibers of 90° plies are orthogonal to the loading direction and contribute little to the strength of the composite. Additionally, to completely define the state of stress within the representative cell, five stresses are required: the axial fiber stress of the 0° plies, $\sigma_f(x)$; the axial matrix stress of the 0° plies, $\sigma_m(x)$; the fiber/matrix interface shear stress in the 0° plies, $\tau_i(x)$; the normal stress within the 90° ply, $\sigma_T(x)$, and the interlaminar shear stress, $\tau(x)$. As in the unidirectional case, the equilibrium relations are insufficient to solve the problem since they constitute only four equations in five unknowns. For the cross-ply laminate, the four equilibrium equations are Eq. (3.10) and Eqs. (3.51) through (3.53).

$$\sigma_L(x) = v_f \sigma_f(x) + v_m \sigma_m(x) \tag{3.52}$$

$$\sigma = \frac{b}{b+d} \sigma_L(x) + \frac{d}{b+d} \sigma_T(x) \tag{3.53}$$

The final equations are again derived from the shear-lag theory.

For the analysis of cross-ply laminates, the basic premise of shear-lag theory is that the interlaminar shear is proportional to the difference in the average displacements of the 90° ply and the 0° ply [111]. For the cross-ply laminate, this may be expressed as

$$\tau(x) = \mathcal{H}_x \left[\bar{u}_L(x) - \bar{u}_T(x) \right] \tag{3.54}$$

where $\mathcal{H}_x$ is the proportionality constant commonly referred to as the shear-lag parameter [103, 104]. As with the unidirectional analysis, Eq. (3.54) along with the kinematic relations comprise the remainder of the required equations for the cross-ply analysis. In this case, the problem consists of solving six equations in six unknowns: $\sigma_f(x)$, $\sigma_m(x)$, $\tau_i(x)$, $\sigma_T(x)$, $\tau(x)$ and $\mathcal{H}_x$. The derivations of $\mathcal{H}_x$, $\sigma_f(x)$ and $\sigma_T(x)$ are now presented. The remaining unknowns follow directly from the equilibrium relations.

3.1.3.1 Determination of the Shear-Lag Constant, $\mathcal{H}_x$. As in the previous unidirectional case, $\mathcal{H}_x$ may be determined directly from Eq. (3.54) since the difference in the average lamina displacements are assumed to be proportional only to $\tau(x)$. Once again, the analysis is somewhat involved and calls for an *assumed* form of the two-dimensional (laminate) shear stresses, $\tau(x, z)$, For the present cross-ply analysis, these stresses are assumed to given by Eqs. (3.55) and (3.56)

$$\tau(x,z) = \left\{ \frac{(b+d)^2}{z+b} - \left\{ z + \frac{(b+d)^2}{b} \right\} \right\} \left\{ b - \frac{(b+d)^2}{b} \right\}^{-1} \tau(x) \quad \text{if} \quad z \in \overline{z_{90}}$$

$$\tag{3.55}$$

$$\tau(x,z) = \frac{b+d-z}{b}\tau(x) \qquad \text{if} \quad z \in \overline{z_0} \tag{3.56}$$

where $\overline{z_{90}} = [\text{-}d, d]$ and $\overline{z_0} = \pm[d, b+d]$. Note that in the above equations, no coupling between the x and z variables is present. Furthermore, it is only because of the assumed *separation of variables* that the solution simplifies under the shear-lag formulation. In addition, the shear stresses satisfy the required boundary conditions, namely

$$\tau(x,0) = \tau(x, b+d) = 0, \tag{3.57}$$

$$\tau(x,d) = \tau(x). \tag{3.58}$$

For the present system of coordinates, equilibrium requires

$$\frac{\partial \sigma_{xx}}{\partial x} + \frac{\partial \tau_{yx}}{\partial y} + \frac{\partial \tau_{zx}}{\partial z} = 0, \tag{3.59}$$

$$\frac{\partial \tau_{xy}}{\partial x} + \frac{\partial \sigma_{yy}}{\partial y} + \frac{\partial \tau_{zy}}{\partial z} = 0, \tag{3.60}$$

$$\frac{\partial \tau_{xz}}{\partial x} + \frac{\partial \tau_{yz}}{\partial y} + \frac{\partial \sigma_{zz}}{\partial z} = 0. \tag{3.61}$$

This system of equations reduces from the assumed geometry since the stresses are independent of the coordinate y. Hence,

$$\frac{\partial \sigma_{xx}}{\partial x} + \frac{\partial \tau_{zx}}{\partial z} = 0, \tag{3.62}$$

$$\frac{\partial \tau_{xz}}{\partial x} + \frac{\partial \sigma_{zz}}{\partial z} = 0. \tag{3.63}$$

As with the previous unidirectional model, the second equilibrium equation is not satisfied. Moreover, note that Eq. (3.56) satisfies Eq. (3.62) directly, however, due to the separation of variables assumption, Eq. (3.55) only satisfies Eq. (3.62) in an average sense, i.e.

$$\frac{\partial \sigma_{xx}}{\partial x} + \frac{1}{d} \int_0^d \frac{\partial \tau_{zx}}{\partial z} dz = 0. \tag{3.64}$$

Also, in reducing the problem to one dimension, the normal stress σ_{zz} and the displacement u_z are neglected. From this, the kinematic relation becomes

$$\int_d^z \frac{\partial u(x,\zeta)}{\partial \zeta} d\zeta = \frac{1}{G} \int_d^z \tau(x,\zeta) d\zeta$$

and the displacements within the two plies are

$$u_T(x,z) = \frac{A\tau(x)}{G_{23}} \left\{ (b+d)^2 \ln\left(\frac{z+b}{b+d}\right) - \frac{1}{2}\left(z^2 - d^2\right) - \frac{(b+d)^2}{b}(z-d) \right\} + u_o(x) \tag{3.65}$$

$$u_L(x,z) = \frac{\tau(x)}{2bG_{12}} \left\{ 2(b+d)(z-d) - \left(z^2 - d^2\right) \right\} + u_o(x) \tag{3.66}$$

where $u_o(x)$ is the displacement along the interlaminar boundary of the two plies and

$$A = \left\{ b - \frac{(b+d)^2}{b} \right\}^{-1}. \tag{3.67}$$

In addition, the average displacements are given by

$$\bar{u}_T(x) = \frac{1}{d} \int_0^d u_T(x,z) \, dz \tag{3.68}$$

and

$$\bar{u}_L(x) = \frac{1}{b} \int_d^{b+d} u_L(x,z) \, dz. \tag{3.69}$$

Performing this integration yields

$$\bar{u}_T(x) = \frac{A\tau(x)(b+d)^2}{dG_{23}} \left\{ \frac{d^3}{3(b+d)^2} + \frac{d^2}{2b} - d - b\ln\left(\frac{b}{b+d}\right) \right\} + u_o(x) \tag{3.70}$$

$$\bar{u}_L(x) = \frac{d \cdot \tau(x)}{6b^2 G_{12}} \left\{ 3b^2 - d^2 \right\} + u_o(x). \tag{3.71}$$

Substituting these relations into Eq. (3.54), the shear-lag parameter, $\mathcal{H}_x$, is determined to be

$$\mathcal{H}_x = -\left\{ \frac{d\left(d^2 - 3b^2\right)}{6b^2 G_{12}} + \frac{1}{(2b+d)G_{23}} \left\{ \frac{(2b+3d)\left(3b^2 - d^2\right)}{6d} + \left(\frac{b}{d}(b+d)\right)^2 \ln\left(\frac{b}{b+d}\right) \right\} \right\}^{-1}. \tag{3.72}$$

3.1.3.2 Determination of the Axial Fiber Stress, $\sigma_f(x)$, and the Average Stress in the Transverse Ply, $\sigma_T(x)$.

As presented earlier, the axial fiber stress varies according to

$$\frac{d\sigma_f(x)}{dx} = \hat{\mathcal{H}} \left\{ \bar{u}_f(x) - \bar{u}_m(x) \right\}. \tag{3.73}$$

Differentiating the above relation and substituting Eq. (3.52) into the resultant equation yields the following second-order linear differential equation.

$$\frac{d^2\sigma_f(x)}{dx^2} - \beta^2 \sigma_f(x) = -\beta^2 \left\{ \sigma_f^o - \frac{E_f}{E_1} \frac{d}{b} \left(\sigma_T(x) - \sigma_T^o \right) \right\} \tag{3.74}$$

The constant β is again the shear-lag parameter from the unidirectional analysis, i.e. Eq. (3.48). Unfortunately, under the shear-lag formulation, no solution to Eq. (3.74) exists since the distribution $\sigma_T(x)$ is unknown. This results because the shear-lag theory is formulated to consider only two entities whereas the present problem has three: the fiber and matrix of the 0° ply and the 90° ply. As a result, an additional assumption of the stress distribution in the 90° ply is required. In particular, it is

3-22

assumed that the matrix cracks which develop within the $0°$ ply do not effect the transverse stress $\sigma_T(x)$ in the $90°$ ply.[†] This is the same assumption made by Kuo and Chou [106]. The other shear-lag models which consider cross-ply laminates do not require this assumption since matrix cracks within the $0°$ ply are not considered. With this additional assumption, the shear-lag theory requires that

$$\frac{d^2 \sigma_T(x)}{dx^2} = \lambda^2 \left\{ \sigma_T(x) - \sigma_T^o \right\} \tag{3.75}$$

from Eqs. (3.51) and (3.54), and where

$$\lambda^2 = \frac{\mathcal{H}_x}{d} \left\{ \frac{E_c}{E_1 E_2} \left(\frac{b+d}{b} \right) \right\} \tag{3.76}$$

and

$$\sigma_T^o = \frac{E_2}{E_c} \sigma + E_2 (\alpha_c - \alpha_2) \Delta T. \tag{3.77}$$

Equation (3.77) is recognized as the rule-of-mixtures solution for the transverse stress in the $90°$ ply of a cross-ply laminate which is free of any damage. The solution to Eq. (3.75) is

$$\sigma_T(x) = c_1 \sinh(\lambda x) + c_2 \cosh(\lambda x) + \sigma_T^o. \tag{3.78}$$

Substituting the latter into Eq. (3.74) yields

$$\frac{d^2 \sigma_f(x)}{dx^2} - \beta^2 \sigma_f(x) = -\beta^2 \left\{ \sigma_f^o - \frac{E_f}{E_1} \frac{d}{b} \left[c_1 \sinh(\lambda x) + c_2 \cosh(\lambda x) \right] \right\}. \tag{3.79}$$

A solution to the above differential equation can be determined using the *method of variational parameters* in which the problem is posed as: $y'' - \beta^2 y = -f(x),$[‡] and whose solution is: $y = y^H + y^P$ with $y^H = c_3 \sinh(\beta x) + c_4 \cosh(\beta x)$ and $y^P = u_1 y_1 + u_2 y_2$. The variables y_1 and y_2 are independent solutions of the ho-

---

[†]Alternate solutions are presented in chapter seven.

[‡]y'' denotes two derivatives of the dependent variable y with respect to the independent variable x.

mogeneous problem, and u_1, u_2 are arbitrary functions which are assumed to satisfy $y_1 u_1' + y_2 u_2' = 0$. Letting $y_1 = \sinh(\beta x)$ and $y_2 = \cosh(\beta x)$, the solution for the fiber axial stress is found to be

$$\sigma_f(x) = c_3 \sinh(\beta x) + c_4 \cosh(\beta x) + \frac{E_f}{E_1} \frac{d}{b} \frac{\beta^2}{\lambda^2 - \beta^2} \{c_1 \sinh(\lambda x) + c_2 \cosh(\lambda x)\} + \sigma_f^o \tag{3.80}$$

where

$$\sigma_f^o = \frac{E_f}{E_c} \sigma + E_f(\alpha_c - \alpha_f)\Delta T. \tag{3.81}$$

The latter is the rule-of-mixtures solution for the fiber stress in an undamaged cross-ply laminate. Note that Eq. (3.80) can be determined more directly by assuming that the particular solution, y^P, is of the same form as the forcing function, $f(x)$, i.e.

$$\begin{aligned} y^P &= c_1 \sinh(\beta x) + c_2 \cosh(\beta x) + c_3 \\ &= -\beta^2 \left\{\sigma_f^o - \frac{E_f}{E_1} \frac{d}{b} [c_1 \sinh(\lambda x) + c_2 \cosh(\lambda x)]\right\} \\ &= -f(x). \end{aligned} \tag{3.82}$$

From Eqs. (3.78) and (3.80), the axial matrix stress in the 0° ply may be determined from Eq. (3.83).

$$\sigma_m(x) = \frac{1}{v_m} \left\{\frac{b+d}{b} \sigma - \frac{d}{b} \sigma_T(x_{t_{|x}})\right\} - \frac{v_f}{v_m} \sigma_f(x) \tag{3.83}$$

where $\sigma_T(x_{t_{|x}})$ is $\sigma_T(x_t)$ evaluated at $x_t = x$ as defined below. Finally, the interface and interlaminar shears, $\tau_i(x)$ and $\tau(x)$, can be determined from Eqs. (3.10) and (3.51), respectively. Note that since the stress fields in the 0° ply are not symmetric, in general, the extent of debonding on the left side of the model ($x < 0$) may not equal the extent of debonding on the right side of the model ($x > 0$). The two debond lengths will be denoted as d_l and d_r, respectively. The boundary conditions required to solve

for the unknown constants, c_1 through c_4, in Eqs. (3.78) and (3.80) are dependent upon the damage configuration. These are now investigated.

As previously mentioned, uniform crack spacing is assumed within each ply; however, nothing has been stated about the relative location of the transverse and matrix cracks. For example, the two configurations shown in Fig. 3.10 are both valid for $L_t = L/2$ where L_t is the spacing of the transverse cracks in the 90° ply and L is the spacing of the matrix cracks in the 0° ply. Within the actual composite, a large
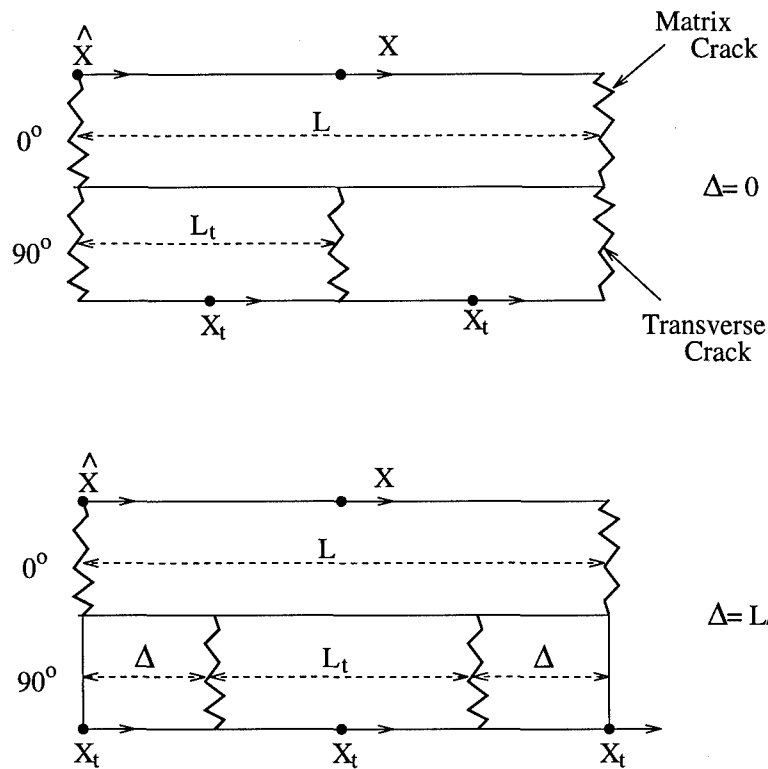
Figure 3.10 Two possible damage configurations for a cross-ply laminate with uniformly spaced cracks in both the 90° ply and the 0° ply. For both figures shown, the transverse crack spacing is one-half the crack spacing of the 0° ply.

number of configurations will exist. The proposed analysis assumes that all possible configuration have an equal probability of occurring and that in , every configuration is represented. To ensure all possible configurations are considered, the relative crack spacing, Δ, as illustrated in Fig. 3.10, is assumed to span $[0, L_t/2]$ if $L_t < L$ and

$[0, L/2]$ if $L < L_t$. For convenience, a global coordinate system, $\hat{x} \in [0, L]$, is used. Equation (3.78) is valid between a pair of transverse cracks only. Hence if $L_t < L$ (i.e. the representative volume element spans more than two transverse cracks), a local coordinate system, x_t, is required for each pair of adjacent transverse cracks (Fig. 3.10). It may be shown that

$$x = \hat{x} - \frac{L}{2} \qquad\qquad x_t = \hat{x} - \delta \qquad\qquad (3.84)$$

where

$$\delta = \begin{cases} L_t \left(n + 1/2 \right) + \Delta & \text{if } L_t \leq L \\ \hat{n} L_t / 2 + \Delta & \text{if } L_t > L \end{cases} \qquad\qquad (3.85)$$

$$n = \begin{cases} -1 & \text{if } \hat{x} - \Delta < 0 \\ \text{Int} \left(\dfrac{\hat{x} - \Delta}{L_t} \right) & \text{otherwise} \end{cases}$$

$$\hat{n} = \begin{cases} -1 & \text{if } \hat{x} \leq \Delta \\ +1 & \text{if } \hat{x} > \Delta \end{cases}$$

and Int() represents the integer function.

Clearly, the constants c_1-c_4 appearing in Eqs. (3.78) and (3.80) are not only a function of the extent of matrix cracking, but also depend on the relative crack spacing, Δ. Three cases need to be considered: (1) transverse cracking only; (2) matrix cracking only, and (3) transverse and matrix cracking. These are the same configurations as investigated by Kuo [103], and are now considered.

3.1.3.3 *Transverse Cracking Only.* Upon loading of CMCs, transverse cracks will develop prior to any failure in the 0° ply. The representative volume element for this case is assumed to span two transverse cracks $(-L_t/2 \leq x \leq L_t/2)$. In order to determine the axial stress in the 90° ply and the axial stress in the fiber of the 0° ply, four boundary conditions are required to solve for the unknown constants $(c_1, c_2, c_3, \text{ and } c_4)$ in Eqs. (3.78) and (3.80). Two boundary conditions,

$\sigma_T(\pm L_t/2) = 0$, are derived from the fact that no load is carried in the 90° ply along the plane of the crack. A third boundary condition, $d\sigma_f(0)/dx = 0$, results from symmetry. Finally, since the matrix in the 0° ply has not failed, the final boundary condition requires $\bar{u}_m(L_t/2) = \bar{u}_f(L_t/2)$ where $\bar{u}_m(x)$ and $\bar{u}_f(x)$ are the axial displacements of the matrix and fiber in the 0° ply, respectively. This condition requires the strain in the matrix and fiber of the 0° ply to be equal (i.e. $\epsilon_m = \epsilon_f$). With these four boundary conditions, the stresses within the 90° ply and fiber in the 0° ply may now be determined [Eqs. (3.86) and (3.87)].

$$\sigma_T(x) = \sigma_T^o \left\{ 1 - \frac{\cosh(\lambda x)}{\cosh(\lambda L_t/2)} \right\} \tag{3.86}$$

$$\sigma_f(x) = c_4 \cosh(\beta x) + \mathcal{T} \frac{\cosh(\lambda x)}{\cosh(\lambda L_t/2)} + \sigma_f^o \tag{3.87}$$

where

$$\mathcal{T} = \frac{E_f}{E_1} \frac{d}{b} \frac{\beta^2}{\beta^2 - \lambda^2} \sigma_T^o \tag{3.88}$$

$$c_4 = \frac{\beta L_t}{2 \sinh(\beta L_t/2)} \left\{ \frac{2}{\lambda L_t} \frac{E_f}{E_1} \frac{d}{b} \frac{\lambda^2}{\lambda^2 - \beta^2} \sigma_T^o \tanh(\lambda L_t/2) - \sigma_f^o + \frac{E_f}{E_1} \sigma_1^o + E_f(\alpha_1 - \alpha_f)\Delta T \right\} \tag{3.89}$$

$$\sigma_1^o = v_f \sigma_f^o + v_m \sigma_m^o \tag{3.90}$$

$$\sigma_m^o = \frac{E_m}{E_c} \sigma + E_m(\alpha_c - \alpha_m)\Delta T \tag{3.91}$$

3.1.3.4 Matrix Cracking Only.   If only matrix cracks exist, then the following conditions apply

$$\sigma_m(-L/2) = 0, \tag{3.92}$$

$$\sigma_m(L/2) = 0, \tag{3.93}$$

$$\frac{d\sigma_T(0)}{dx} = 0, \tag{3.94}$$

$$\epsilon_T = \epsilon_f. \tag{3.95}$$

For this case, the stresses are determined to be

$$\sigma_T(x) = c_2 \cosh(\lambda x) + \sigma_T^o, \tag{3.96}$$

$$\sigma_f(x) = c_4 \cosh(\beta x) + c_2 \mathcal{T} \cosh(\lambda x)/\sigma_T^o + \sigma_f^o \tag{3.97}$$

where

$$c_4 = \frac{\mathcal{B}\left\{\dfrac{b+d}{d}\sigma - \dfrac{b}{d}v_f\sigma_f^o - \sigma_T^o\right\} + \mathcal{A}\left\{\dfrac{\sigma_f^o}{E_f} - \dfrac{\sigma_T^o}{E_2} + (\alpha_f - \alpha_2)\Delta T\right\}}{\mathcal{B}\dfrac{d}{b}v_f\cosh\left(\beta L/2\right) - \mathcal{A}\dfrac{2}{\beta L E_f}\sinh\left(\beta L/2\right)}, \tag{3.98}$$

$$c_2 = \mathcal{B}\left\{\frac{b+d}{d}\sigma - \frac{b}{d}v_f\left[c_4\cosh\left(\beta L/2\right) - \sigma_f^o\right] - \sigma_T^o\right\}, \tag{3.99}$$

$$\mathcal{A} = \frac{\lambda L}{2\left\{\dfrac{\mathcal{T}}{E_f} - \dfrac{1}{E_2}\right\}\sinh\left(\lambda L/2\right)}, \tag{3.100}$$

$$\mathcal{B} = \frac{1}{\left\{1 + \dfrac{b}{d}v_f\dfrac{\mathcal{T}}{\sigma_T^o}\right\}\cosh\left(\lambda L/2\right)}. \tag{3.101}$$

3.1.3.5 Transverse and Matrix Cracking.   For a general damage state consisting of both transverse and matrix cracks, the amount of stress which is transferred to the fiber of the 0° ply along the plane of a matrix crack is unknown. Further, since both the matrix of the 0° ply and the 90° ply have failed, $\epsilon_T \neq \epsilon_f$ and $\epsilon_m \neq \epsilon_f$. Hence in order to solve the problem, the assumption that the local stress in the 90° ply near a matrix crack in the 0° ply is not influenced by this matrix cracking is made in this formulation as in the previous study [104]. Therefore, the stress within the transverse ply is again given by Eq. (3.86) since $\sigma_T(\pm L_t/2) = 0$. Given $\sigma_T(x)$, the remaining unknown constants [c_3 and c_4 in Eq. (3.80)] may be determined since

the fiber stress along the crack plane is known exactly, i.e.,

$$\sigma_f \left(x = \pm L/2\right) = \frac{1}{v_f} \left\{ \frac{b+d}{b}\sigma - \frac{d}{b}\sigma_T(x_{t_{|x=\pm L/2}}) \right\}. \tag{3.102}$$

In addition, the fiber stress is assumed to vary linearly within the debonded region according to the following.

$$\sigma_f(x) = \frac{1}{v_f} \left\{ \frac{b+d}{b}\sigma - \frac{d}{b}\sigma_T(x_{t_{|x=\pm L/2}}) \right\} - \frac{2\tau_i}{r_f}\left\{ \frac{L}{2} - |x| \right\} \tag{3.103}$$

Within the bonded region:

$$\sigma_f(x) = c_3 \sinh(\beta x) + c_4 \cosh(\beta x) + \mathcal{T}\frac{\cosh(\lambda x_t)}{\cosh(\lambda L_t/2)} + \sigma_f^o \tag{3.104}$$

where c_3 and c_4 depend on the damage configuration, as shown below. Prior to any debonding

$$\begin{aligned} c_3 = {} & \frac{1}{2v_f \sinh\left(\beta L/2\right)} \frac{d}{b}\left\{ \sigma_T\left(x_{t_{|x=-L/2}}\right) - \sigma_T\left(x_{t_{|x=L/2}}\right) \right\} \\ & + \frac{\mathcal{T}}{\cosh\left(\lambda L_t/2\right)}\left\{ \cosh\left(\lambda x_{t_{|x=-L/2}}\right) - \cosh\left(\lambda x_{t_{|x=L/2}}\right) \right\}, \end{aligned} \tag{3.105}$$

$$\begin{aligned} c_4 = {} & \frac{1}{2v_f \cosh\left(\beta L/2\right)}\left\{ \frac{b+d}{b}\sigma - \frac{d}{b}\sigma_T\left(x_{t_{|x=L/2}}\right) \right\} - c_3 \sinh\left(\beta L/2\right) \\ & - \mathcal{T}\frac{\cosh\left(\lambda x_{t_{|x=L/2}}\right)}{\cosh\left(\lambda L_t/2\right)} - \sigma_f^o. \end{aligned} \tag{3.106}$$

However, with the onset of debonding, these constants become

$$c_3 = \frac{\chi_l \cosh\phi_r - \chi_r \cosh\phi_l}{\sinh(\phi_l - \phi_r)}, \tag{3.107}$$

$$c_4 = \frac{\chi_r \sinh\phi_l - \chi_l \sinh\phi_r}{\sinh(\phi_l - \phi_r)} \tag{3.108}$$

where $\phi_l = \beta(-L/2 + d)$, $\phi_r = \beta(L/2 - d)$ and

$$\chi_l = \sigma_f^l - \mathcal{T}\frac{\cosh\left(\lambda x_{t|_{x=\phi_l}}\right)}{\cosh\left(\lambda L_t/2\right)} - \sigma_f^o, \tag{3.109}$$

$$\chi_r = \sigma_f^r - \mathcal{T}\frac{\cosh\left(\lambda x_{t|_{x=\phi_r}}\right)}{\cosh\left(\lambda L_t/2\right)} - \sigma_f^o, \tag{3.110}$$

$$\sigma_f^l = \frac{1}{v_f}\left\{\frac{b+d}{b}\sigma - \frac{d}{b}\sigma_T(x_{t|_{x=-L/2}})\right\} - \frac{2}{r_f}\tau_i d_l, \tag{3.111}$$

$$\sigma_f^r = \frac{1}{v_f}\left\{\frac{b+d}{b}\sigma - \frac{d}{b}\sigma_T(x_{t|_{x=L/2}})\right\} - \frac{2}{r_f}\tau_i d_r. \tag{3.112}$$

If $d_l = L/2$ and $0 < d_r < L/2$ then

$$c_3 = \frac{1}{\sinh\left(\phi_r\right)}\left\{\sigma_f^r - c_4\cosh(\phi_r) - \mathcal{T}\frac{\cosh\left(\lambda x_{t|_{x=\phi_r}}\right)}{\cosh\left(\lambda L_t/2\right)} - \sigma_f^o\right\}, \tag{3.113}$$

$$c_4 = \sigma_f^l - \frac{\mathcal{T}}{\cosh\left(\lambda L_t/2\right)} - \sigma_f^o. \tag{3.114}$$

If $d_r = L/2$ and $0 < d_l < L/2$ then

$$c_3 = \frac{1}{\sinh\left(\phi_l\right)}\left\{\sigma_f^l - c_4\cosh(\phi_l) - \mathcal{T}\frac{\cosh\left(\lambda x_{t|_{x=\phi_l}}\right)}{\cosh\left(\lambda L_t/2\right)} - \sigma_f^o\right\}, \tag{3.115}$$

$$c_4 = \sigma_f^r - \frac{\mathcal{T}}{\cosh\left(\lambda L_t/2\right)} - \sigma_f^o. \tag{3.116}$$

Figure 3.11 illustrates the microstresses in the 90° ply and the fiber and matrix of the 0° ply which result in a $[0_3/90/0_3]$ laminate with $\sigma = 200$ MPa, $L = 3L_t$, and $\Delta = L_t/4$. The influence of the 90° transverse cracks on the fiber and matrix axial stress in the 0° ply is evident, as well as the fact that the axial stresses in the 90° ply $[\sigma_T(x)]$ are not influenced by the matrix cracks in the 0° ply. As mentioned, the fiber stress gradients are assumed linear in any debonded regions within the 0° ply

of the cross-ply laminate. An example of the microstresses which may develop in a laminate with fiber/matrix debonding is shown in Fig. 3.12. The stresses are given for $\sigma = 300$ MPa, $L = 2L_t$, and $\Delta = 0$ in this figure.
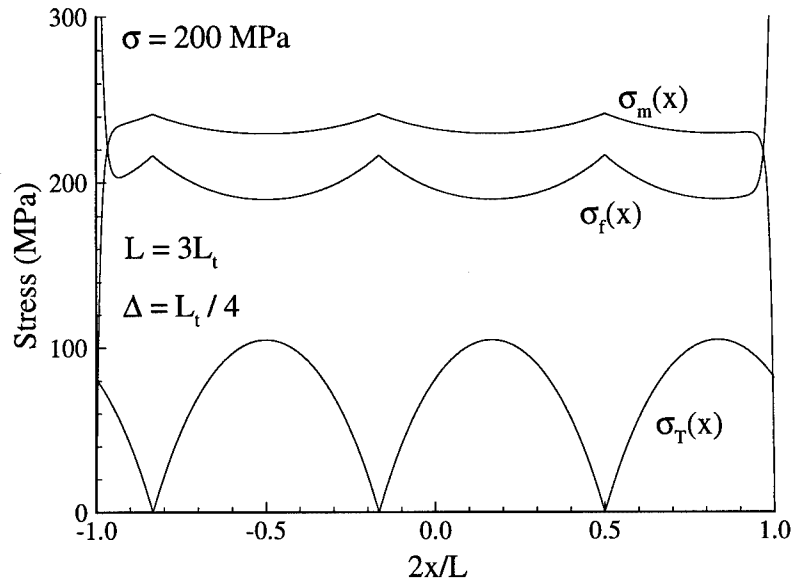
Figure 3.11   Microstresses for a $[0_3/90/0_3]$ laminate where the crack density of the matrix cracks in the $0°$ ply is one-third the transverse $(90°)$ crack density. Matrix cracks are located at abscissa values of ± 1.

Clearly, the laminate stresses are contingent upon *a priori* knowledge of the damage configuration. The latter, of which, requires the establishment of a set of failure criteria for each of the damage mechanisms considered in the analysis. These are discussed in the following sections.

3.2   Failure Criterion

The predominant modes of damage within the unidirectional laminate are matrix cracking, interface debonding and fiber failure. For the cross-ply laminates, transverse cracking of the $90°$ plies is also considered. Failure criteria for these damage mechanisms are now addressed.
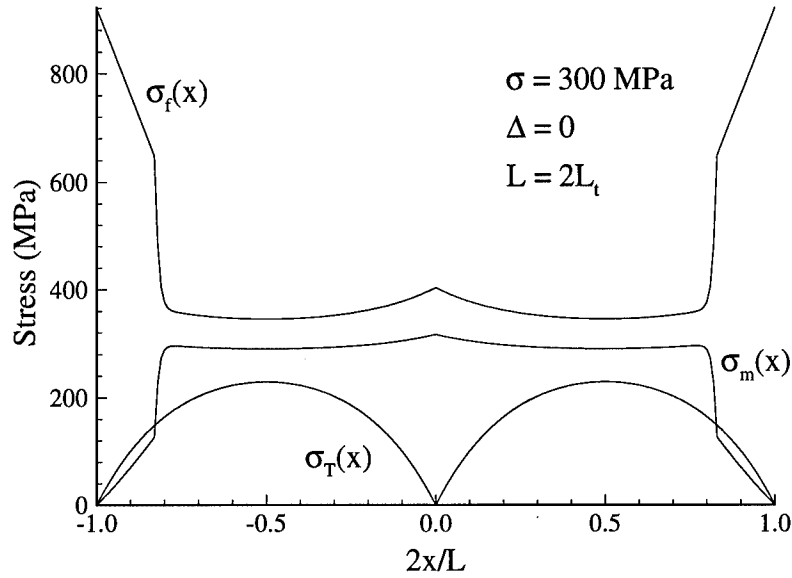
Figure 3.12   Microstresses within a $[0_3/90/0_3]$ cross-ply laminate when fiber/matrix debonding is considered.

3.2.1   Transverse and Matrix Cracking.   The transverse and matrix crack spacings are determined by means of the *critical matrix strain energy* (CMSE) criterion in which the average crack spacings, L and L_T, are determined via Eqs. (3.117) and (3.118).

$$U_{m_o} + U_m(L) = U_{cr_m} \quad \text{for} \ \ \sigma \geq \sigma_{cr}^0 \tag{3.117}$$

$$U_{T_o} + U_T(L_t) = U_{cr_T} \quad \text{for} \ \ \sigma \geq \sigma_{cr}^{90} \tag{3.118}$$

The left hand sides of Eqs. (3.117) and (3.118) represents the instantaneous strain energies in the matrix of the $0°$ ply and the transverse ply, respectively. The quantities U_{m_o} and U_{T_o} are the (rule-of-mixtures) strain energies in the $0°$ and $90°$ ply for laminates free of any damages. The remaining terms, $U_m(L)$ and $U_T(L_t)$, account for the redistribution of energies as a result of damage formation. The right hand sides of Eqs. (3.117) and (3.118) are the critical strain energies which can be determined provided the critical composite stresses are known *a priori*. Kuo and Chou provide

3-32

estimates for these stresses [106]. Also, U_{cr_m} and U_{cr_T} are assumed constant, known laminate properties.

The CMSE failure criterion is discussed in detail in appendix E; however, in summary, the concept of a critical matrix strain energy presupposes the existence of an ultimate or critical strain energy limit beyond which the matrix fails. Beyond this, as more energy is placed into the composite, the matrix, unable to support the additional load, continues to fail. Initially, the composite is assumed to be undamaged. As the applied load increases from zero, the energy within the constituents of the composite increases. With further loading, since the strain to failure of the matrix is less than that of the fiber, the matrix eventually reaches its maximum load carrying capacity. The stress level at which the matrix reaches this maximum limit is assumed to be the critical composite stress, σ_{cr}. This process is illustrated in Fig. 3.13. The reference point, $\sigma = \sigma_{cr}$, is chosen since experimentally the composite response is linear to this point (i.e. $\sigma < \sigma_{cr}$) due to the limited microstructural damage. As more energy is added to the system with further loading, any additional energy going into the matrix is assumed to produce more damage. The assumption
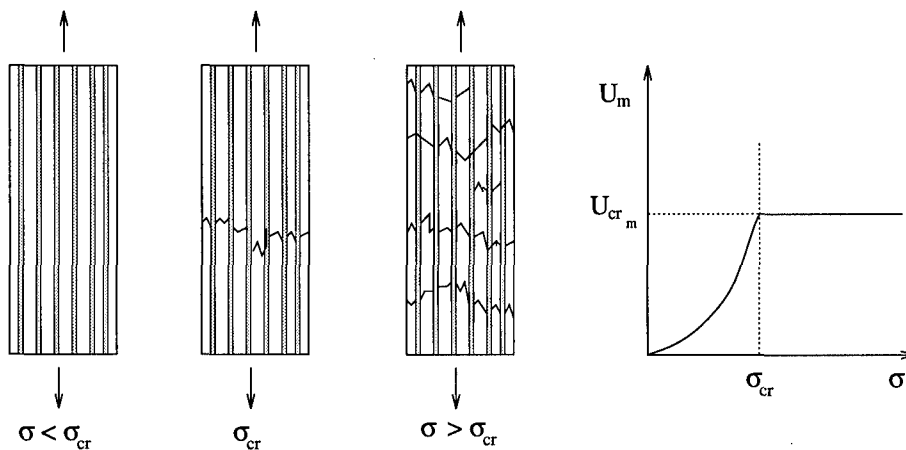
Figure 3.13   Critical matrix strain energy (CMSE) criterion.

that the matrix strain energy remains constant is analogous to a *total strain energy*

failure theory for isotropic materials in which now a single homogeneous matrix block with applied tractions σ, $\tau_i(x)$ and τ_i becomes the focus of the investigation.

Consider the stress-strain response during monotonic loading of a homogeneous brittle ceramic [Fig. 3.14 (a)]. The stress at failure is often defined as the ultimate
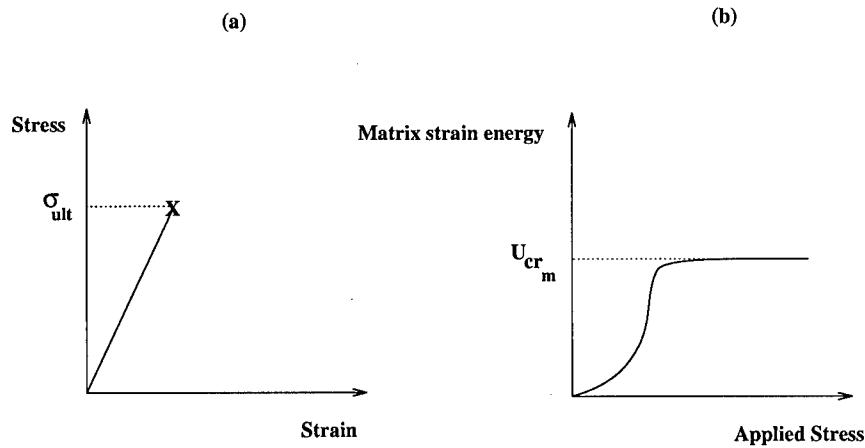
Figure 3.14   Assumed material response: (a) stress-strain response for a monolithic ceramic; (b) strain energy versus applied stress for a ceramic composite.

stress of the matrix and is considered a material property. Clearly, the same argument may be posed using an energy criterion. That is, failure occurs when the matrix strain energy reaches its ultimate or *critical strain energy*, U_{cr_m} [170,174]. In a similar fashion, matrix failure in a non-homogeneous brittle system (e.g. CMC) will result when the matrix strain energy reaches this critical value. As more energy is placed into the system, the matrix fails such that all the additional energy is transferred to the fibers [Fig. 3.14 (b)]. Failure may consist of the formation of matrix cracks, the propagation of existing cracks or interface debonding. The failure pattern within any two CMCs will differ due to the variability (i.e. stochastic nature) of material flaws (size and location), as well as laminate geometry. However, the basic premise of the micromechanics approach is that the average behavior of the laminate may be modeled. Hence, if an equivalent or average damage configuration can be determined, the composite stress-strain response can be predicted. Two advantages

of the CMSE criterion are that the crack densities are determined analytically and that since no restriction is placed on the location where the new cracks form, the CMSE is able to capture a continuous evolution of matrix cracking.

3.2.2 Interface Debonding. Interface debonding results from the large shear stresses which develop along the fiber/matrix interface in the presence of matrix cracking. Since the debond is in reality a crack which propagates along the fiber/matrix interface, the extent of debonding can by estimated using classical fracture mechanics techniques [24, 45, 81]. However, to avoid the complexities which accompany such approaches, a simple and more common approach is to employ a maximum stress criterion in which the interface is assumed to debond whenever the interface shear stress exceeds the ultimate bond strength of the interface, τ_{ult} [7, 28, 113]. The parameter τ_{ult} is assumed to be a material constant, and, if known, the extent of interface debonding can be determined by ensuring that the maximum shear along the interface never exceeds this maximum amount, i.e.

$$\tau_i(x)_{max} = \tau_{ult}. \tag{3.119}$$

For more insight into the debonding process, note that the interface shear reaches a maximum along the plane of the matrix crack as illustrated in Fig. 3.15. At some level of applied stress, the maximum interface shear will exceed the bond strength of the interface, i.e. $\tau_i(x)_{max} \geq \tau_{ult}$. As the interface debonds, the magnitude of $\tau_i(x)_{max}$ decreases. Hence, for the coordinate system illustrated in Fig. 3.15, Eq. (3.119) requires that

$$\tau_i\left(x = L/2 - d\right) = \tau_{ult}. \tag{3.120}$$

The shear stress in the *debonded region* is typically assumed to be constant and governed by Coulomb friction with magnitude τ_i [103, 113].
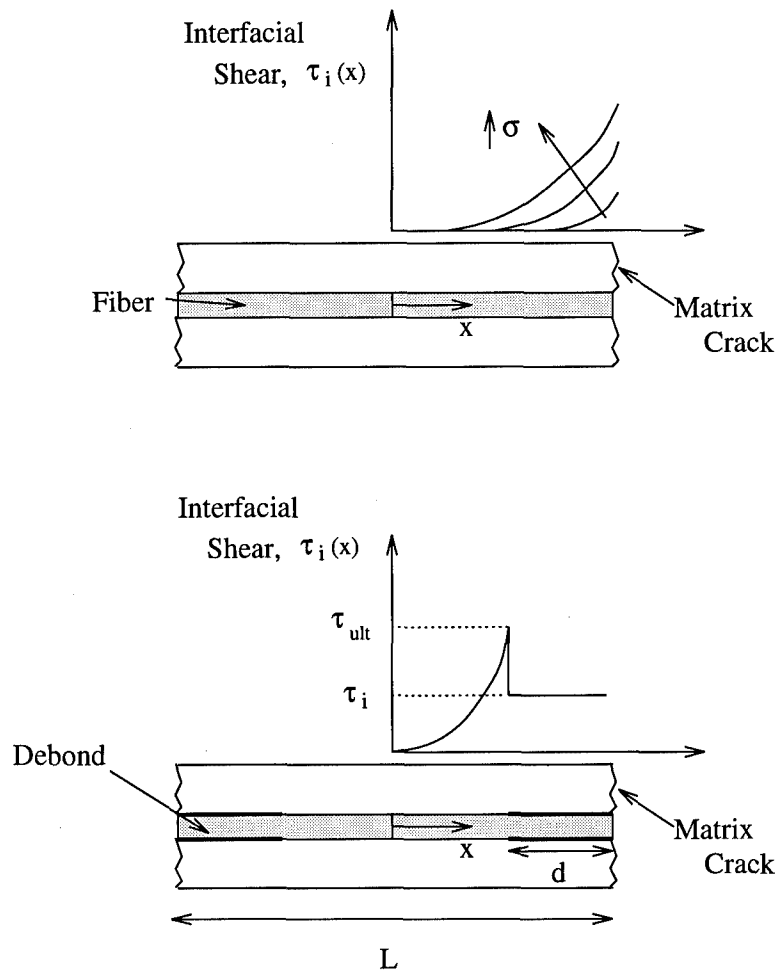
Figure 3.15   Evolution of the interface shear stress as a function of debonding.

3.2.3   Fiber Fracture.   The percentage of fractured fibers, D, is determined via a unique Weibull failure distribution in which fiber breakage depends on a function of the instantaneous fiber strain energy rather than the fiber stress as traditionally assumed. In this manner, the traditional Weibull shape and scaling parameters do not need to be determined. Furthermore, no inconsistencies arise since compressive loading conditions are not considered, i.e. $\mathcal{R} \geq 0$. The statistical distribution for the current analysis is shown in Eq. (3.121) where U_{cr_f} is the critical fiber strain energy and $\hat{m}$ is the Weibull modulus. Presently, the Weibull modulus is (empirically) based upon the quasi-static response of the ceramic laminate.

Appendix F examines, in depth, the break-up of the fibers in ceramic composites.

$$D = 1 - \left\{ \exp \left[\left(1 - \frac{U_{cr_f}}{U_f} \right)^{\hat{m}} \right] \right\}^{-1} \qquad (3.121)$$

3.3 Loading Considerations

For the current analysis, three loading conditions are considered: quasi-static, repeated and fatigue loading. This section investigates some of the unique modeling considerations for each of these loading conditions.

3.3.1 Quasi-Static Loading.

For modeling purposes, the predicted stress-strain response is accomplished in two steps. For stresses below the critical composite stress (σ_{cr}), as defined earlier, the composite strain is determined using the traditional rule-of-mixtures expression

$$\sigma = E_c \left(\epsilon - \epsilon_c^{th} \right) \qquad (3.122)$$

where ϵ_c^{th} is the residual thermal strain resulting during processing. For applied loads exceeding the critical stress, the shear-lag relations are employed and the composite strain is determined from Eq. (3.6). In this manner, the analysis is more efficient. Greater detail on the solution scheme is provided in appendix B.

$$\epsilon_c = \frac{1}{E_f L} \int_L \sigma_f(x) \, dx + (\alpha_f - \alpha_c) \Delta T \qquad (3.6)$$

3.3.2 Repeated Loading.

For cyclic loading environments, stress-strain hysteresis is a concern. The origin of hysteresis is a function of the frictional slip which occurs along any debonded regions during loading and unloading of CMCs. Since τ_i has been assumed constant in the present analysis, as is typical of most studies [8, 106, 113], the extent of interface slip during loading and unloading may be determined analytically [132, 153]. The ratio of the slip distance over the debond

length, $\mathcal{D}$, is determined by ensuring that all constituent deformations "outside the slip zone" are elastic [174]. For a *partially bonded* interface in a unidirectional laminate, for example,

$$\mathcal{D} = \begin{cases} \dfrac{1}{2}\left(1 - \dfrac{v_m\sigma_{m_o}r_f}{2v_f\tau_i d} + \dfrac{\tau_{ult}}{\tau_i\beta d\tanh[\beta(L/2-d)]}\right) & \text{unloading} \\[2ex] \mathcal{D}_u - \dfrac{1}{2}\left(1 - \dfrac{v_m\sigma_{m_o}r_f}{2v_f\tau_i d} + \dfrac{\tau_{ult}}{\tau_i\beta d\tanh[\beta(L/2-d)]}\right) & \text{reloading.} \end{cases} \tag{3.123}$$

where $\mathcal{D}_u$ is $\mathcal{D}$ at $\sigma = \sigma_{min}$ (unloaded). Since slip cannot occur within any bonded regions, $0 \le \mathcal{D} \le 1$. For a *completely debonded* interface,

$$\mathcal{D} = \begin{cases} \dfrac{1}{2}\left(\dfrac{v_m E_m r_f}{v_f(1-D)E_1 L}\dfrac{\sigma_{max}-\sigma}{\tau_i}\right) & \text{unloading} \\[2ex] \dfrac{1}{2}\left(\dfrac{v_m E_m r_f}{v_f(1-D)E_1 L}\dfrac{\sigma-\sigma_{min}}{\tau_i}\right) & \text{reloading.} \end{cases} \tag{3.124}$$

For the cross-ply laminate, the expressions for $\mathcal{D}$ are algebraically more complicated. The specific equations are provided in appendix C which also includes a detailed discussion of frictional slip and the resulting hysteresis.

3.3.3 Cyclic Loading.

Under fatigue (cyclic) loading, the stress-strain response is characterized not only by hysteresis, but also by a significant development of permanent strain, i.e. strain ratchetting. As mentioned in the previous chapter, the shape of the hysteresis loop is dependent on the extent of composite damage and the interface shear, τ_i. Strain ratchetting, on the other hand, is more a function of fiber pull-out [153]. Unfortunately, traditional shear-lag models have no means for accounting for the latter, and therefore some additional work is required. The procedure undertaken to model fiber pull-out, and subsequently the observed strain ratchetting, is now discussed.

3.3.3.1 Strain Ratchetting.

Strain ratchetting occurs when fractured fibers permanently slip (e.g. fiber pull-out). As illustrated in Fig. 3.16, this slip

results in a finite crack opening of the fiber which is governed, in large part, by the interface shear, τ_i. This fiber crack opening displacement is assumed to be of length $\delta(N)$ (Fig. 3.16). Upon unloading, the fiber separation is unlikely to vanish due to Poisson and "knife-edge" effects, as well as debris and fiber warping which all act to prevent the crack opening from closing. $\delta(N)$ is a measure of the average fiber pull-out distance and depends on both the state of composite damage (L, d, D) and the interface resistance, τ_i. For simplicity, the interface shear and the crack opening displacement are assumed to remain constant during a cycle [i.e. $\tau_i = \tau_i(N)$ and $\delta = \delta(N)$].
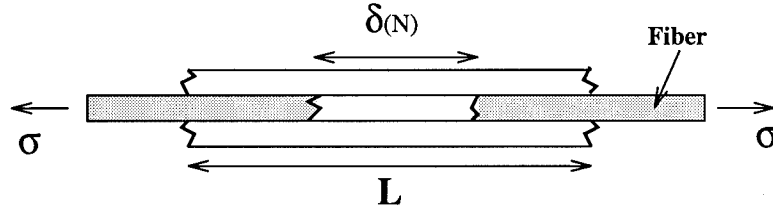
Figure 3.16   Crack opening displacement, $\delta(N)$, resulting from gross slip of a fractured fiber.

It has been observed in several experimental studies that the extent of constituent damage reaches steady-state during the first few cycles ($N < 20$), i.e. the elastic modulus remains almost constant after its initial drop over these first few cycles [54, 74, 86, 153, 210]. Interface slip and debonding, on the other hand, may continue with cycling, at least as long as $\tau_i(N)$ varies [184]. Unfortunately, the traditional shear-lag approach provides no means of capturing these phenomena once the interface completely debonds. Under the current shear-lag formulation, for example, the permanent strain upon complete unloading ($\sigma = 0$) for a completely debonded interface is

$$\epsilon_p = \frac{\tau_i(N)L}{2E_f r_f} \tag{3.125}$$

where the residual strain upon complete unloading, as predicted by the present analysis, is denoted by ϵ_p. Hence, from Eq. (3.125) and as evidenced in Figure 3.17, strain
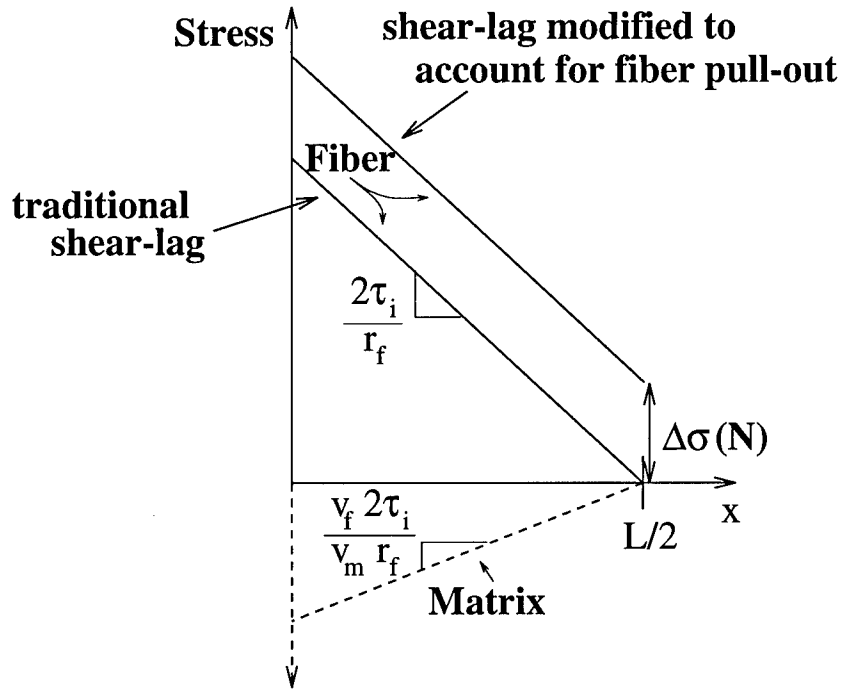
Figure 3.17 Constituent stresses after unloading of a unidirectional laminate with a completely debonded interface. Solutions are shown with and without fiber pull-out.

ratchetting either ceases once the interface debonds completely if $\tau_i(N)$ remains constant or decreases if $\tau_i(N)$ declines. The latter is illustrated in Fig. 3.18, and is, of course, physically unreasonable. If strain ratchetting is to be successfully modeled, the present shear-lag formulation must be modified to account for fiber pull-out (e.g. an estimate for $\delta(N)$ is required).

As fractured fibers slip and pull-out from the surrounding matrix, the local stress in adjacent unbroken fibers increases, and hence, the average stress in an undamaged fiber, as modeled under the shear-lag approach, also goes up. One approach to account for the additional stress in unbroken fibers resulting from gross slip of adjacent fractured fibers is to adjust the axial fiber stress by an amount $\Delta\sigma(N)$. This is illustrated in Fig. 3.17. If $\Delta\sigma(N)$ is chosen appropriately, a monotonically

increasing permanent strain develops according to

$$\epsilon_p = \frac{2}{LE_f} \int_0^{L/2} \left\{ \Delta\sigma(N) + \frac{2\tau_i(N)}{r_f} \left(\frac{L}{2} - x\right) \right\} dx. \qquad (3.126)$$

Figure 3.19 illustrates the strain ratchetting behavior when fiber pull-out is mod-
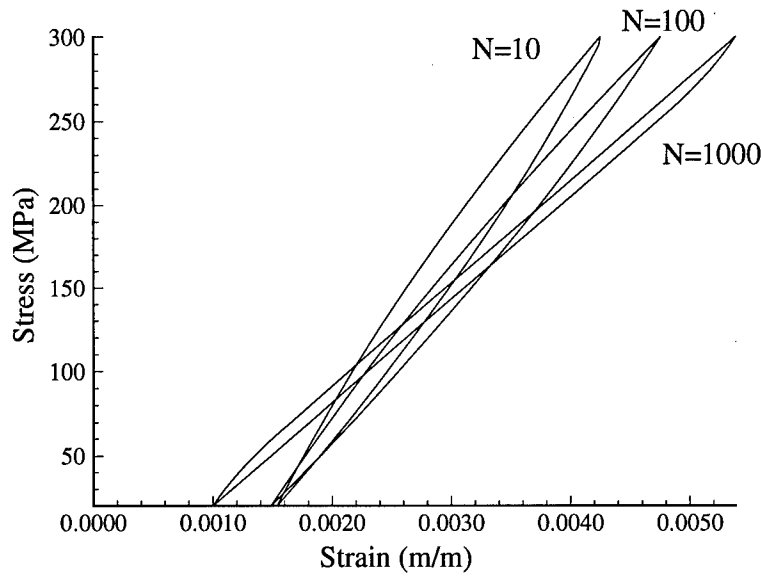
Figure 3.18   Stress-strain response of a ceramic matrix composite in which fiber
pull-out is not modeled.

eled according to Eq. (3.126). For the example shown, $\Delta\sigma(N)$ is arbitrarily cho-
sen. Appendices G and H outline the development of the stress $\Delta\sigma(N)$ for the
unidirectional and cross-ply laminates, respectively. The solutions are determined
analytically by introducing a region within the laminate which does not slip during
unloading. The latter accounts for the fact that upon unloading of the actual com-
posite, the fiber crack opening displacement does not vanish. As expected, $\Delta\sigma(N)$
is dependent on the maximum applied stress and the interface shear.

3.3.3.2   Fatigue Life Predictions.   The laminate is assumed to fail
when the energy available for fiber pull-out, U_p, exceeds the work required to pull a
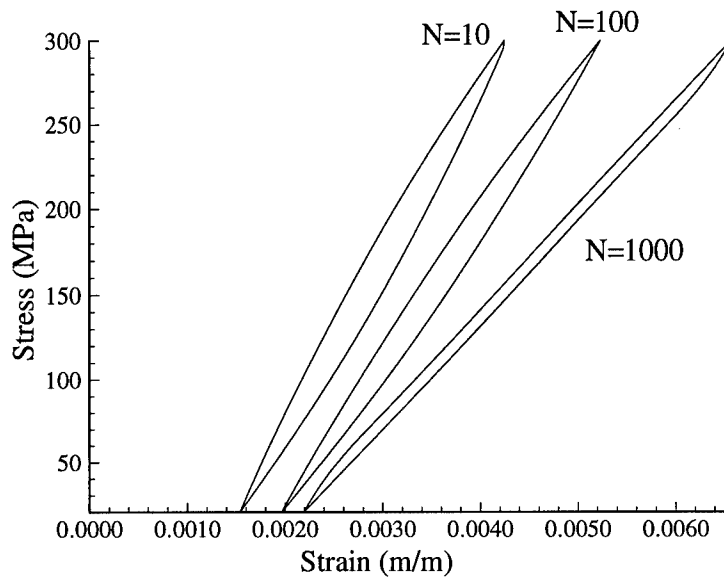
Figure 3.19   Stress-strain response of a ceramic matrix composite in which fiber pull-out is modeled.

fractured fiber completely from the matrix, W_p. In this study, the energy available for fiber pull-out, U_p, is defined as the additional fiber strain energy which results from the stress $\Delta\sigma(N)$, and W_p is given by reference 35.

This completes the development of the basics of the analysis methodology. Predicted results are compared with experimental data in chapters four and five. Quasi-static, repeated and cyclic loadings of unidirectional and cross-ply lay-ups are all considered.

IV. Unidirectional Behavior

With the theory in chapter three, the material stress-strain response of several unidirectional laminates is now investigated. Recall that based on the model development, the state of stress within a unidirectional laminate is defined by three components: the axial fiber stress, $\sigma_f(x)$; the axial matrix stress, $\sigma_m(x)$, and the shear stress which develops along the fiber/matrix interface, $\tau_i(x)$. These stresses are defined by the following equations which have been reproduced from chapter three.

$$\sigma_f(x) = A\cosh\left(\beta x\right) + B\sinh\left(\beta x\right) + \sigma_{f_o} \tag{3.41}$$

$$\sigma_m(x) = \frac{1}{v_m}\left\{\sigma - v_f\sigma_f(x)\right\} \tag{3.8}$$

$$\tau_i(x) = -\frac{r_f}{2}\frac{d\sigma_f(x)}{dx} \tag{3.10}$$

The parameters A and B in Eq. (3.41) depend on the composite's state of damage, and once this is determined the composite strain may be calculated from Eq. (3.6) as shown below.

$$\epsilon_c = \frac{1}{E_f L}\int_L \sigma_f(x)\ dx + (\alpha_f - \alpha_c)\Delta T \tag{3.6}$$

Hence, once the laminate properties and loading environment are known, the unidirectional stress-strain response may be determined from the above system of equations and the proposed failure criteria. For the current analysis, three composite systems are investigated. These are SiC/CAS, SiC/CAS-II and SiC/1723. The material property data for these systems are provided in Table 4.1. Note that in

Table 4.1 Material property data for SiC/CAS, SiC/CAS-II and SiC/1723 laminates.

	SiC/CAS [103]	SiC/CAS-II [75]	SiC/1723 [209]
E_1 (GPa)	139	127	145
E_2 (GPa)	120.5	109.5	90
v_f	0.38	0.35	0.45
r_f (μm)	7.5	7.3	6.25
α_f ($10^{-6}/^\circ$C)	3.1	3.1	3.1
α_m ($10^{-6}/^\circ$C)	4.5	4.5	4.36
ΔT ($^\circ$C)	-1000	-1000	-1100
τ_i (MPa)	20	15	20
τ_{ult} (MPa)	220	220	220
σ_{mc} (MPa)	100	120	220
σ_{cr} (MPa)	220	140 (210 exp.)	400
$\hat{m}$	2.0	6.5	4.0

addition to the material property data, the present failure criteria require that the laminate's critical composite stress (σ_{cr}) and the Weibull modulus ($\hat{m}$) be known. The critical composite stress is required to define the critical matrix strain energy, U_{cr_m}, which is used to determine the matrix crack densities under the CMSE failure criterion. In addition, recall that σ_{cr} is used as a bifurcation point for the current analysis (Fig. 3.1). For applied stresses less than the critical composite stress (e.g. $\sigma < \sigma_{cr}$), rule-of-mixtures equations are employed. For $\sigma \geq \sigma_{cr}$, the shear-lag formulation is invoked in order to account for the accumulation of matrix cracks within the composite structure. In reality, matrix cracking initiates at a much lower stress level[†]; however, since these matrix cracks ($\sigma < \sigma_{cr}$) do not dramatically influence the composite stress-strain response, the laminate can be modeled as if it is void of any damage.

In addition to the critical composite stress, σ_{cr}, the Weibull modulus, $\hat{m}$, is also required for the current analysis. In particular, $\hat{m}$ is used to determined the percentage of fractured fibers in the laminate. Both of these parameters, σ_{cr} and

---

[†]The stress corresponding to the initiation of matrix cracking is denoted by σ_{mc}.

$\hat{m}$, may be obtained from empirical data; however, they may also be estimated analytically as outlined in appendix I. The influence of the Weibull modulus, $\hat{m}$, on the predicted stress-strain behavior for a SiC/CAS composite system is illustrated in Fig. 4.1. The parameters σ_{cr} and $\hat{m}$ are listed in Table 4.1 for the three systems investigated.
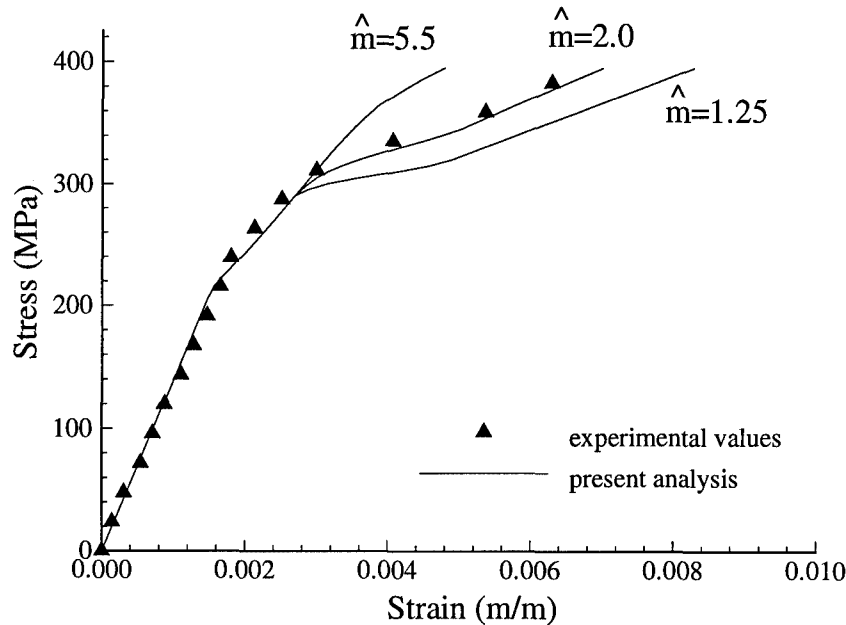
Figure 4.1   Stress-strain response for various levels of fiber failure. Results are shown for $\hat{m} = 1.25$, 2.0 and 5.5.

The remainder of this chapter investigates the material response of the unidirectional laminate under quasi-static, repeated and fatigue loadings. The damage mechanisms considered are matrix cracking, fiber/matrix interface debonding and slip, fiber fracture and fiber pull-out. The stress-strain response under monotonic tensile loading, and the fatigue life response (S-N relationship); modulus degradation, and stress-strain hysteresis under repeated and cyclic loadings obtained from the present analytical methodology are compared with their experimental counterparts. They are in a good agreement with one another.

4.1 Quasi-Static Loading

Predicted results for the three composite systems, SiC/CAS, SiC/CAS-II and SiC/1723, are compared with experimental data in Fig. 4.2. As evident in Fig. 4.2, the present analysis provides a very good representation of the experiments [75, 103, 209]. For the SiC/CAS system, for example, the predicted response matches especially well with the empirical data. For strains below 0.152%, the laminate stiffness is well approximated by the rule-of-mixtures analysis. Below this knee in the stress-strain curve, the amount of matrix cracking is insufficient to noticeably effect the material response. However, the presence of these cracks may still be important for time dependent effects since these fractures can expose the interface to the surrounding environment and permit unwanted oxidation of the interface. The matrix crack density increases to a saturation spacing of about 0.142 mm which is reached at 0.361% strain as shown in Fig. 4.2. Fiber fracture initiates at 0.259% strain and provides a critical fraction of D^*=0.42 at laminate failure ($\epsilon = 0.841\%$).
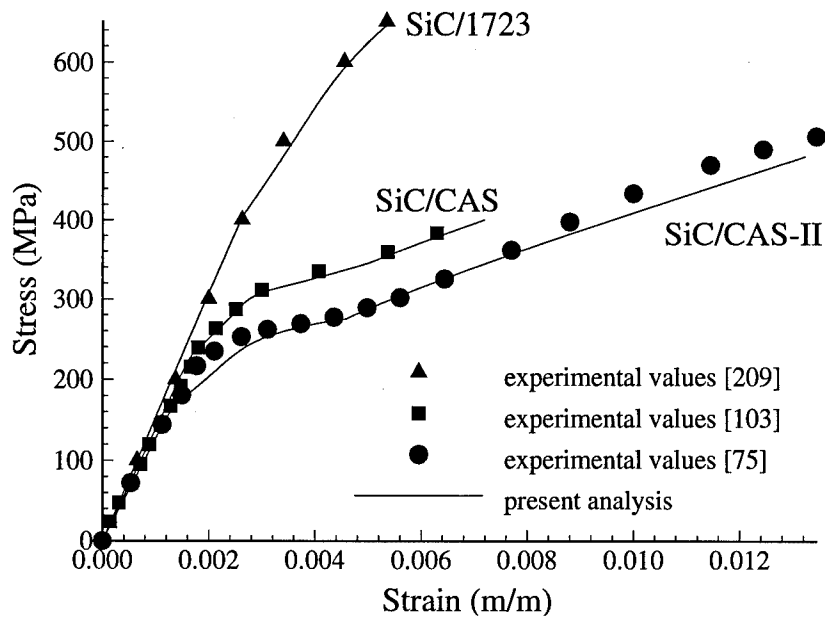
Figure 4.2   Unidirectional stress-strain response for several composite systems.

Note that the SiC/CAS-II results in Fig. 4.2 are generated with σ_{cr} defined as the stress at which matrix cracking initiates, σ_{mc}, rather than the laminate's proportional limit. This is done to illustrate the model's robustness to variations in σ_{cr}. Beyond the critical composite stress, the influence of other parameters such as the interface shear (τ_i and τ_{ult}) and fiber volume fraction on the material behavior is also of interest. Such data not only provide insight into the evolution of damages within CMCs, but also may be used to quantify these same parameters through empirical fits. The latter can be quite beneficial since the experimentally measured values of τ_i and τ_{ult}, for example, are questionable. As a result, numerical models are often used to estimate these parameters. Figures 4.3 through 4.5 illustrate the predicted sensitivity to variations in the interface shear stress, τ_i, the interface strength, τ_{ult}, and the fiber volume fraction, v_f. For each figure, the stress-strain response, crack density evolution, and debond progression are shown. The debond length is plotted in terms of the fiber diameter, i.e. $d/(2000 \cdot r_f)$.

As illustrated in Fig. 4.3, the extent of matrix cracking increases with rises in the interface shear stress. This is to be expected since the rate at which load is transferred between constituents also increases with τ_i, and more efficient load transfer reduces the shielding effect described in chapter two. In other words, the matrix crack density increases as the interface becomes stronger because the average matrix stress also increases. It is interesting to note that although the variation in the crack densities shown in Fig. 4.3 is rather significant, the stress-strain responses of the four conditions investigated are very similar. This results because of the corresponding changes in the debond lengths. Hence, an important consequence is that *when using empirical data to estimate the properties of the interface, it is insufficient to simply fit the macromechanical (stress-strain) data. For an accurate prediction, the state of microstructural damage must also be correctly modeled.* These are discussed in greater detail in appendix E.
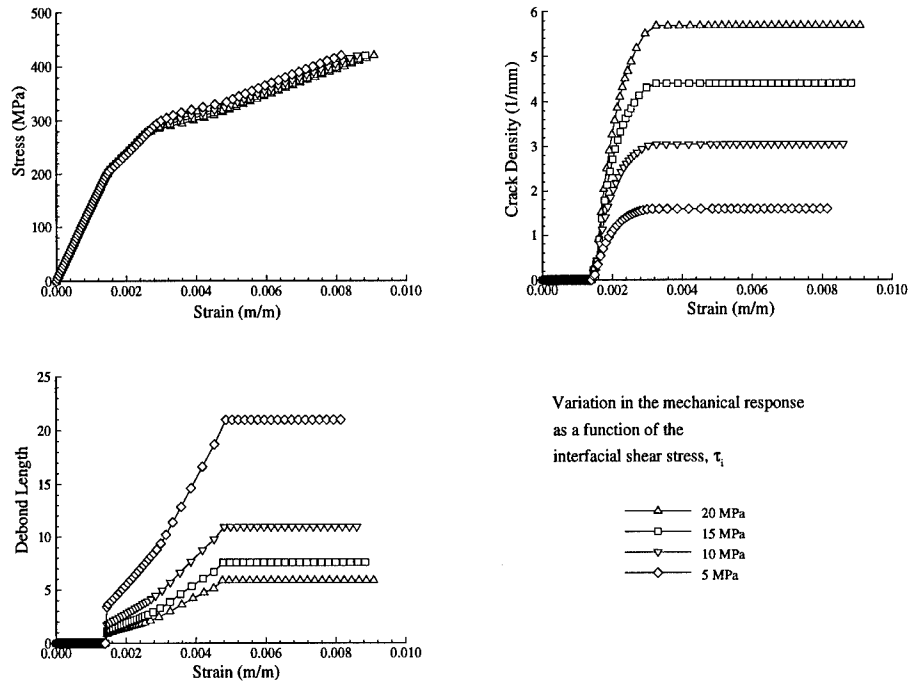
Figure 4.3   Stress-strain response and damage evolution for a unidirectional CMC as a function of the interface shear, τ_i.

As illustrated in Fig. 4.4, the interface shear strength, τ_{ult}, also impacts the evolution of damages within the composite. However, the effect is much less pronounced compared to τ_i. On the other hand, the damage progression is strongly dependent on fiber volume fraction (Fig. 4.5). This is expected since, as discussed in chapter two, the ability to dissipate energy and arrest crack growth is due solely to the presence of the fibers. The crack densities, in Fig. 4.5, increase with v_f since constituent load transfer again increases.
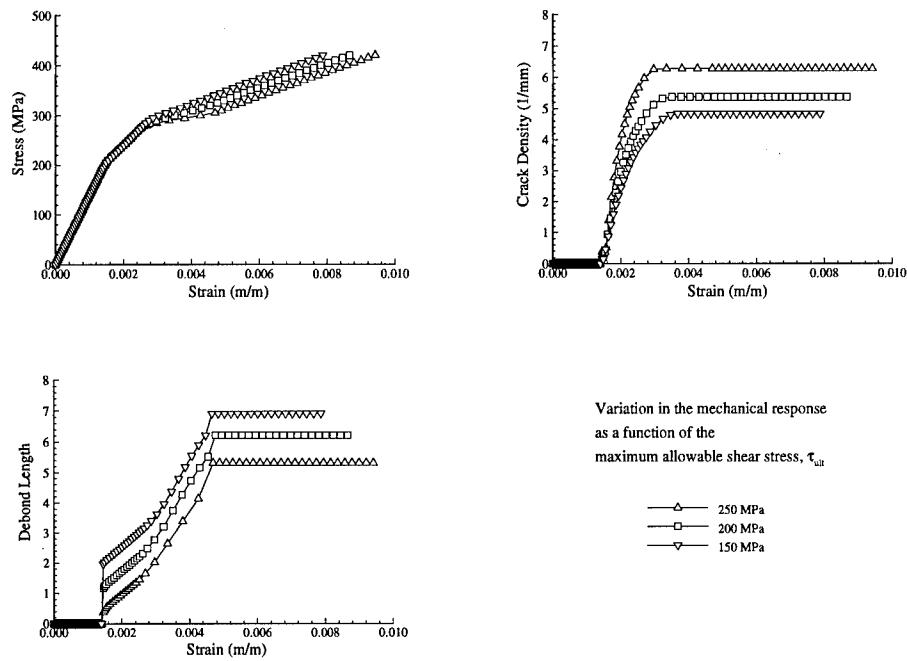
Figure 4.4 Influence of the maximum allowable shear, τ_{ult}, on the stress-strain response and damage evolution of a unidirectional CMC.
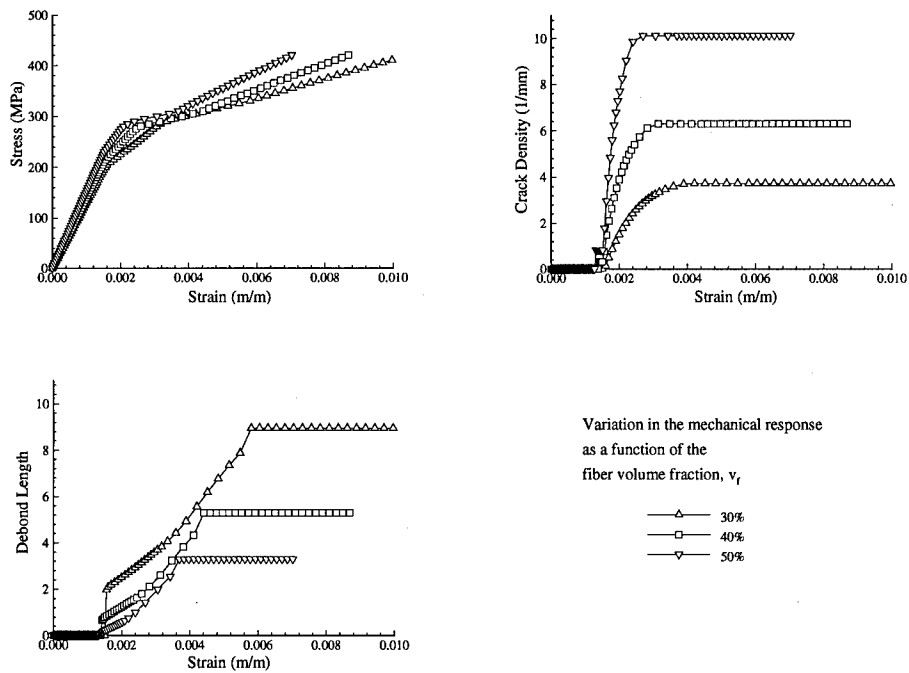
Figure 4.5 Impact of fiber volume fraction on material behavior.

4.2 Repeated Loading

Under conditions of repeated loading in which the applied load is cycled, stress-strain hysteresis develops due to the frictional sliding which occurs along any debonded regions. Hence numerically, the strain must be predicted during initial loading, unloading and subsequent reloading. For the first part, i.e. initial loading, this is quasi-static loading and hence the composite's behavior can be determined using the solution scheme of the previous section. In determining the actual hysteresis, i.e. unloading and subsequent reloading, the extent of frictional sliding must be determined. This derivation is provided in appendix C.

Several hysteresis loops are shown for a unidirectional SiC/CAS laminate in Fig. 4.6. As expected, the size of the loops, which characterizes the energy dissipated, increase with the applied stress. Unfortunately, few data are available for
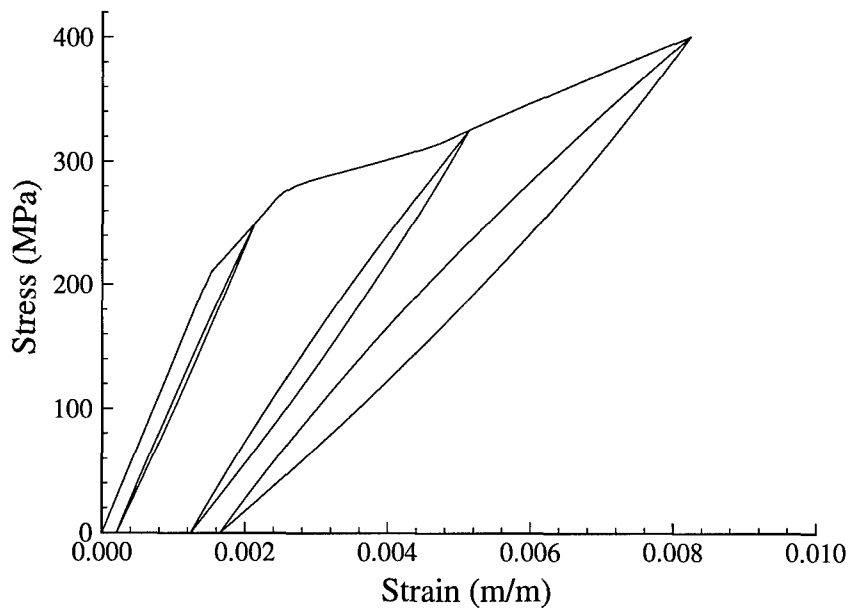
Figure 4.6   Repeated loading response of a unidirectional, SiC/CAS laminate. The maximum stress for the hysteresis loops shown are 250, 325, and 400 MPa.

unidirectional CMCs under conditions of repeated loading. In particular, only the data from Pryce and Smith was found by the author to be representative of this loading environment [152]. For the analysis, the material properties are taken as: $E_f = 190$ MPa, $E_m = 90$ MPa, $v_f = 0.34$, $r_f = 7.5$E-6 m, $\alpha_f = 3.3$E-6/°C, $\alpha_m = 4.6$E-6/°C, $\Delta T = -1200$°C, $\tau_i = 10$ MPa, and $\tau_{ult} = 220$ MPa. Furthermore, based upon the data reported by Pryce and Smith, σ_{cr} is selected as 125 MPa to match the proportional limit. A comparison of their experimental results with the present analysis is presented in Fig. 4.7. Although the present model's response is slightly stiffer, the salient features are present and the predicted residual strain after unloading is in good agreement with the empirical data. The fact that the linear (undamaged) portion of the 190 MPa test is stiffer than the empirical data may indicate that the material property data used is questionable. Further, the empirical data are obtained from a fatigued specimen; whereas, the predicted response assumes an initial undamaged laminate in both the 210 MPa and 225 MPa tests. The model stiffness can be relaxed by considering additional damages.

4.3 Cyclic Loading

The unidirectional fatigue response is characterized by a degradation in the interface shear stress, stress-strain hysteresis and strain ratchetting, modulus degradation, and S-N behavior. Each of these is now addressed.

4.3.1 Degradation in the interface shear.

Evans et al recently published experimental hysteresis data along with numerical estimates of $\tau_i(N)$ for a unidirectional SiC/CAS laminate subjected to tension-tension fatigue [54]. This variation in shear, $\tau_i(N)$, as provided by Evans et al is given by Eq. (4.1)

$$\tau_i(N) = \tau_{i_o} + \left(1 - \exp^{-\omega N^\lambda}\right)\left(\tau_{i_{min}} - \tau_{i_o}\right) \tag{4.1}$$
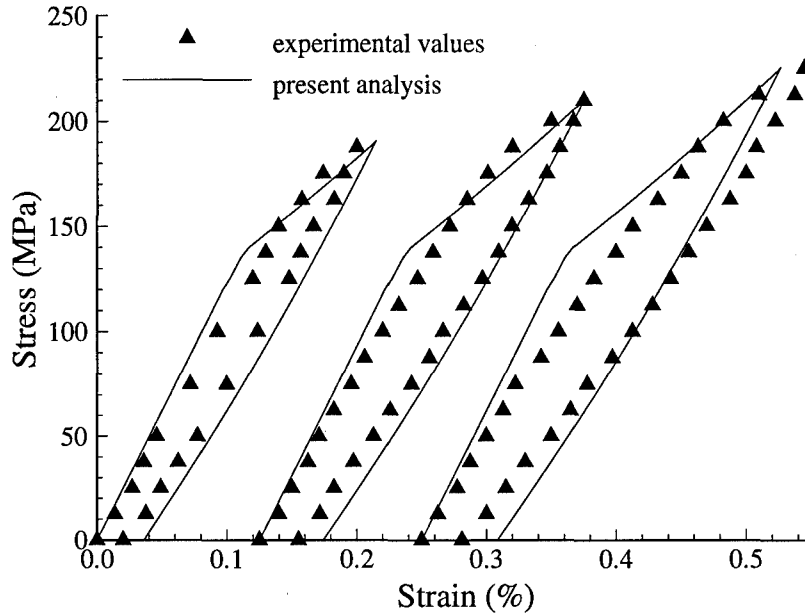
Figure 4.7   Repeated loading response of a unidirectional, SiC/CAS laminate at maximum applied loads of 190, 210 and 225 MPa. Note that the stress-strain curves for $\sigma_{max} = 210$ and 225 MPa have been shifted along the abscissa by 0.125 and 0.25, respectively, for clarity. The experimental data are from reference 152.

where τ_{i_o} is the initial shear stress (i.e. $\tau_i(N)$ at $N = 1$, before cycling). The quantity $\tau_{i_{min}}$ is the final steady-state shear during cycling, and ω and λ are empirical constants. Based upon the previous study [54], the numerical constants λ and ω are determined: λ=2.25 and ω=0.00275. A typical profile of Eq. (4.1) is illustrated in Fig. 4.8. An important consequence of Eq. (4.1) as presented by Evans *et al* is that the interface shear is assumed to degrade rapidly over the first one hundred or so cycles (Fig. 4.8). As illustrated in the following sections, this is somewhat inconsistent with the findings of the present study. Evans *et al* estimated the variation in the shear stress, $\tau_i(N)$, by fitting the size and shape of their predicted hysteresis loops with the experimental data; therefore, the accuracy of the data is unknown. In addition, the estimates are based upon data "confined to the parabolic range"
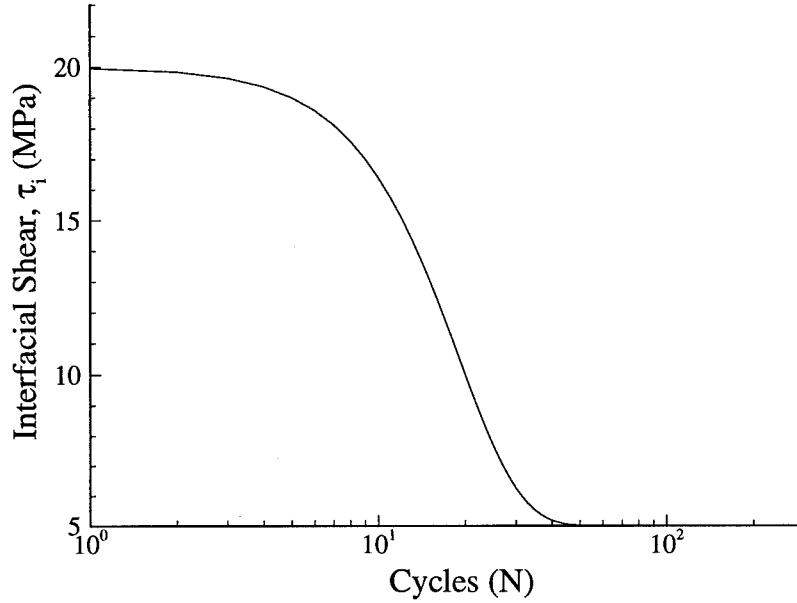
Figure 4.8   Assumed degradation in the interface shear stress, $\tau_i(N)$, during fatigue
loading.

of stress-strain hysteresis loops; whereas, the experimental hysteresis loops are ob-
served to change in shape from parabolic to linear [54]. These are not accounted
for in the determinations of $\tau_i(N)$, and therefore, the estimated range for the shear
degradation is likely to be an upper bound.

4.3.2   Stress-Strain Hysteresis and Strain Ratchetting.   As mentioned ear-
lier, the shear-lag formulation has no inherent means of capturing the extensive strain
ratchetting which occurs during fatigue testing. This ratchetting phenomenon results
from permanent slip of fractured fibers, and is accounted for with the superposition
of a constant stress, $\Delta\sigma(N)$, according to Eq. (4.2).

$$\sigma_f(x) = \frac{\sigma}{v_f(1-D)} + \Delta\sigma(N) - \frac{2\tau_i(N)}{r_f}\left(L/2 - x\right) \qquad (4.2)$$

4-11

Further, $\Delta\sigma(N)$ represents an approximation for the additional stress experienced by an undamaged bridging fiber when adjacent fibers fracture and slip according to a uniform distribution. Recall that an analytical solution for $\Delta\sigma(N)$ is determined by assuming that a portion of the shear-lag model remains permanently bonded. This permanently bonded region (PBR) represents areas where slip is obscured, and it is the assumption that the shear stress in this region is irreversible that leads to the solution for $\Delta\sigma(N)$. The derivation of $\Delta\sigma(N)$ is presented in appendix G with the final form of the expression being shown in Eq. (4.3).

$$\Delta\sigma(N) = \frac{v_m E_m + D v_f E_f}{v_f(1-D)E_1}\sigma_{max} - \frac{2\tau_i(N)}{r_f}L \qquad (4.3)$$

As expected, the extent of fiber pull-out is dependent on the maximum applied stress (σ_{max}), the interface resistance $[\tau_i(N)]$, and the composite's state of damage $(D, L$ and $d)$.

The irreversibility in shear is attributed to several physical mechanisms, including surface roughness and debris along the interface. During cycling, however, as the interface wears some slip reversal is likely, and should be considered in the analysis. Therefore, define $\phi_r(N) \in [0,1]$ such that the quantity $1-\phi_r(N)$ represents the percentage of the PBR which is allowed to unload elastically; then upon reformulating the problem, the additional fiber stress in Eq. (4.3) is modified according to

$$\Delta\sigma_r(N) = [1 - \phi_r(N)]\,\Delta\sigma(N) - \phi_r(N)\left[\frac{\tau_i(N)L}{r_f} + E_f(\alpha_f - \alpha_1)\Delta T\right]. \qquad (4.4)$$

In this manner, some additional degradation along the interface, separate from $\tau_i(N)$, is considered. Several solutions obtained using Eqs. (4.3) and (4.4) are now compared with their experimental counterparts as presented below.

Figure 4.9 shows the experimental hysteresis loops provided by Evans *et al* along with predicted loops from the present analysis. The predicted results in

Fig. 4.9 are determined with $\tau_{i_o} = 20$ MPa and $\tau_{i_{min}} = 5$ [54]. Note that because of the assumed form for the degradation in the interfacial shear stress, i.e. Eq. (4.1) and Fig. 4.8, the predicted response of the laminate will not change after (approximately) one-hundred cycles since no further damages or material degradation are assumed. Hence, the labels ($N = 1$, etc) indicating the number of fatigue cycles in Fig. 4.9, as well as in all subsequent stress-strain hysteresis plots correspond only to the empirical data. The fact that no additional composite degradation develops in the predicted fatigue response beyond one-hundred cycles is self-evident in the plots of the *normalized modulus versus cycles* and the S-N diagrams as illustrated later. Hence, the strong correlation between the predicted and experimental stress-strain hysteresis loops indicates that the assumed *extent*, not the *rate*, of interface degradation is probably representative of the physical system. Alternatively, if one disregards the assumed form of shear degradation, e.g. Eq. (4.1), the labels ($N = 1$, 5, etc) represent one means of estimating the rate of interface degradation.

Note that in Fig. 4.9, the present analysis captures the modulus and ratchetting behavior well; however, there is some error associated with the shape of the hysteresis loops during initial cycling. These results may be improved if the form of the degradation in interface shear is assumed other than Eq. (4.1). Also note that due to the present shear-lag assumptions, the predicted hysteresis loops will always be closed, whereas experimentally these may not be observed during initial cycling (Fig. 4.9).

Figure 4.10 illustrates several predicted and experimental hysteresis loops for a SiC/CAS-II composite system. The experimental data are from reference 76 in which estimates for τ_{i_o} and $\tau_{i_{min}}$ (15 and 3.5 MPa, respectively) are also provided. However, the actual variation of $\tau_i(N)$ during cycling is not determined [76], and therefore, $\tau_i(N)$ is again calculated using Eq. (4.1) with $\lambda = 2.25$ and $\omega = 0.00275$. Again, the present analytical results are in good agreement with their experimental counterparts.
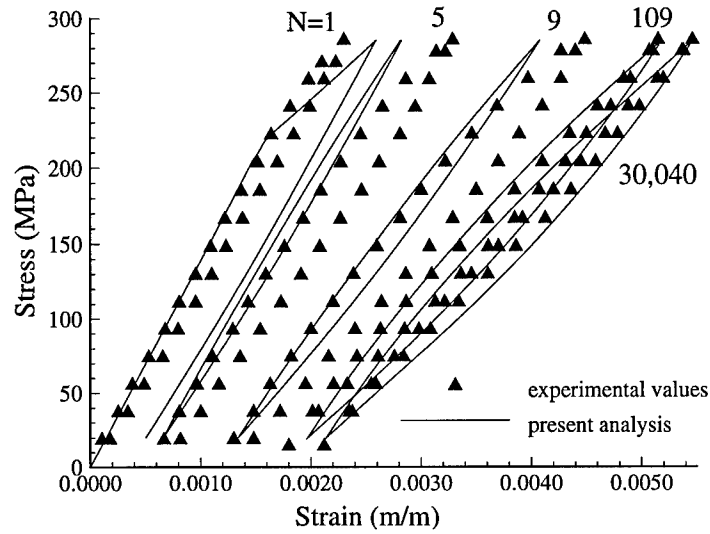
Figure 4.9 Predicted and experimental stress-strain hysteresis of a SiC/CAS laminate. For the experimental data, N=1, 5, 9, 109, 30040. The predicted results are generated with τ_{i_o}=20 MPa and $\tau_{i_{min}}$=5 MPa.
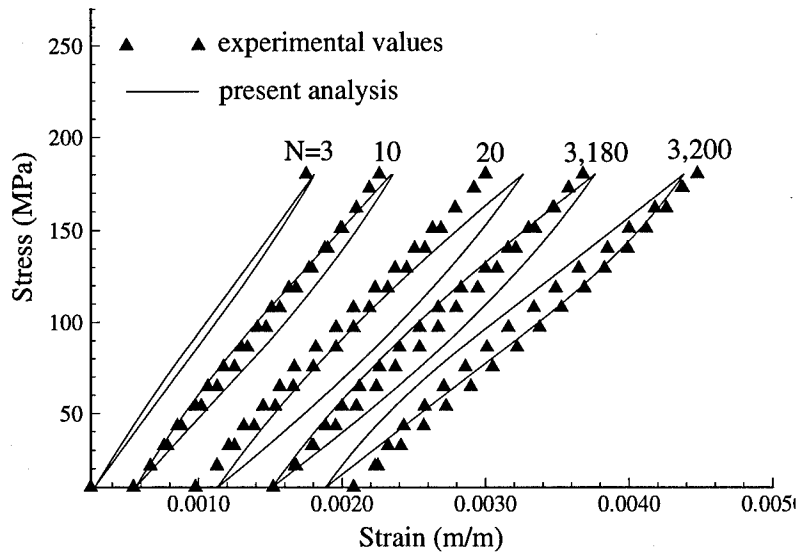
Figure 4.10 Predicted and experimental stress-strain hysteresis for a SiC/CAS-II laminate. N *is shown in thousands of cycles* for the experimental data. The predicted results are generated with τ_{i_o}=15 MPa and $\tau_{i_{min}}$=3.5 MPa. For clarity, the predicted response at N=50 is not shown.

4-14

Consider the variations in the hysteresis loops as τ_i varies. From Eq. (3.123), as τ_i vanishes, the shape of the hysteresis loops change from non-linear symmetric loops to more "cusped" or "S-shaped" curves. Furthermore, as the interface debonds [Eq. (3.124)], the loops form bi-linear or skewed parallelpipeds, and finally degenerate to zero width (linear line) as τ_i vanishes. These various shapes are also observed during experimental testing [100, 144]. Under the current approach, therefore, τ_i may be estimated by finding the best fit to empirical data. Based upon the results shown in Fig. 4.11, $\tau_{i_{min}} = 1.5$ MPa. These results were obtained for $\phi_r = 0.3$ [Eq. (4.4)]. Similar results are shown for SiC/CAS-II in Fig. 4.12.
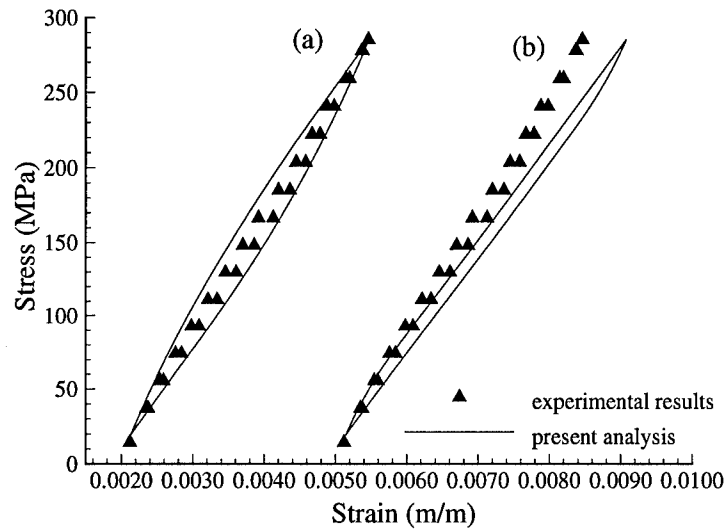
Figure 4.11 Predicted and experimental stress-strain hysteresis for a SiC/CAS system. N=30,040; τ_{i_o}=20 MPa and (a) $\tau_{i_{min}}$=5.0 MPa and ϕ_r=0.0, (b) $\tau_{i_{min}}$=1.5 MPa and ϕ_r=0.3. Note that the latter curve has been shifted along the abscissa by 0.003 for clarity.
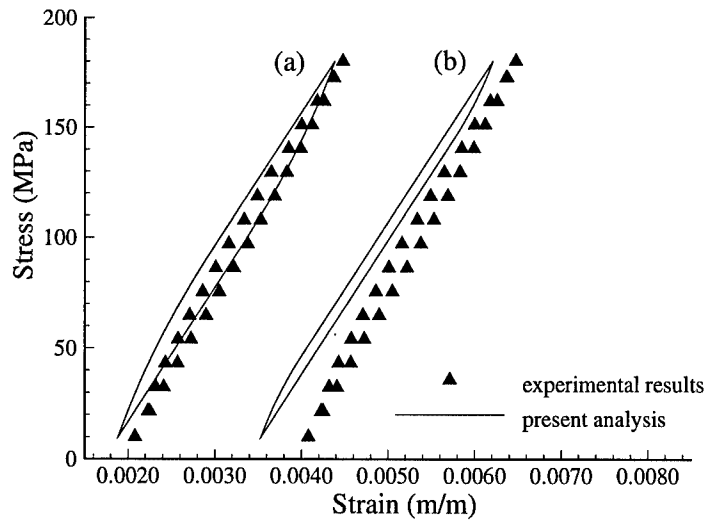
Figure 4.12 Stress-strain hysteresis (SiC/CAS-II). N=3.2E6; τ_{i_o}=15 MPa and (a) $\tau_{i_{min}}$=3.5 MPa and ϕ_r=0.0, (b) $\tau_{i_{min}}$=1.5 MPa and ϕ_r=0.3. Note that the latter curve has been shifted along the abscissa by 0.002 for clarity.

Several predictions for a SiC/CAS laminate are provided in Figs. 4.13 and 4.14. In both cases, the results obtained under the current analysis are in good agreement with the experimental data. The experimental data in Fig. 4.13 are from refer-
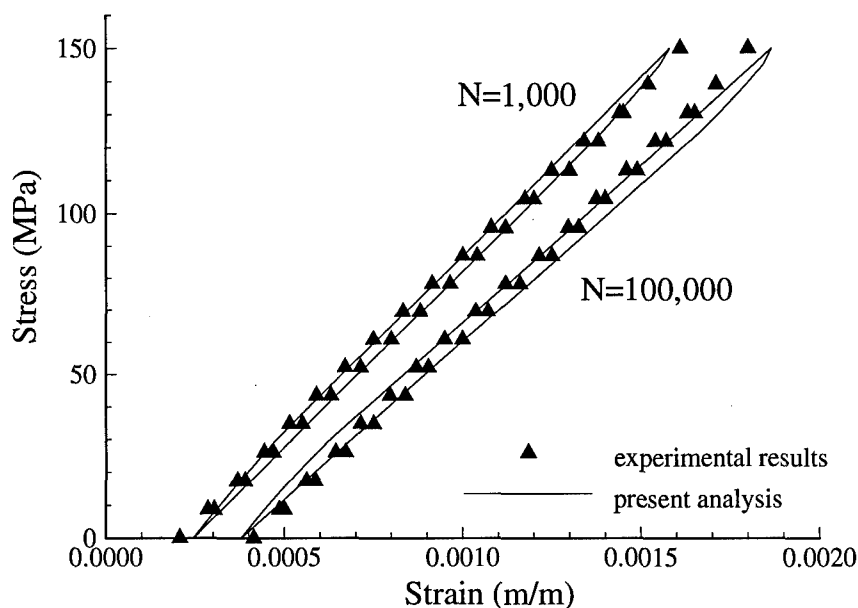
Figure 4.13   Stress-strain hysteresis at N=1,000 and 100,000 for a unidirectional SiC/CAS composite.

ence 153 and represent the laminate response at 1,000 and 100,000 cycles. The predicted results are for $\tau_i = 10.5$ and 5.0 MPa. In Fig. 4.14, the experimental data are from Opalski & Mall and Pryce & Smith [144,153]. The data from Opalski and Mall were obtained with $\sigma_{max} = 200$ MPa and $\mathcal{R}$=0.1 whereas the data from Pryce and Smith were generated with $\sigma_{max} = 200$ MPa and $\mathcal{R}$=0.0. The results shown in Fig. 4.14 are for N=10,000. Also, two stress-strain hysteresis loops from the current analysis are shown. These correspond to $\tau_i = 10$ and 5.5 MPa. The differences in the empirical data (Pryce & Smith and Opalski & Mall) may be attributed to the difference in the laminate properties between various batches of materials. In addition, whenever the composite is cycled at a peak stress near the critical composite stress
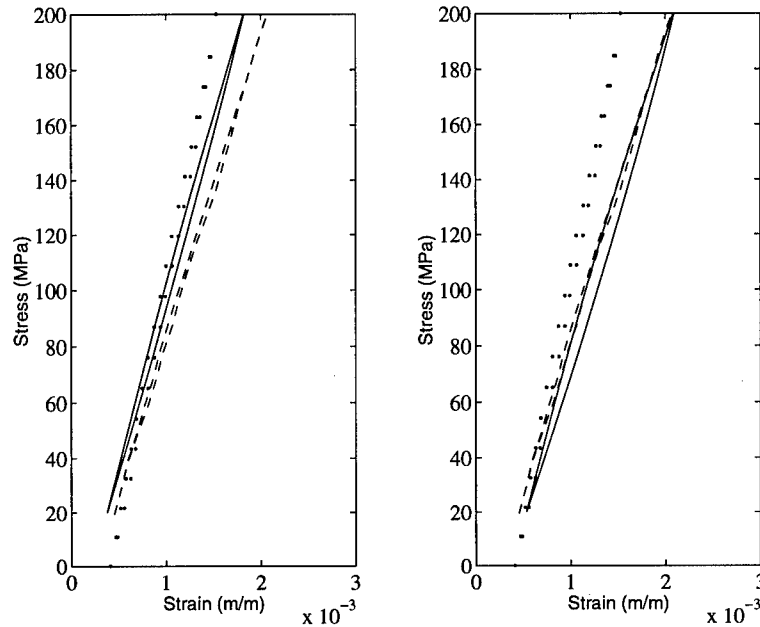
Figure 4.14   Stress-strain hysteresis of a SiC/CAS unidirectional laminate. The empirical data are from Opalski and Mall [144] (dashed line); and Pryce and Smith [157] (dotted line). N=10,000. The predicted response (solid line) is shown for $\tau_i = 10$ and 5.5 MPa.

(i.e. $\sigma_{max} \simeq \sigma_{cr}$), a large variation in the material response will exist due to the inherent differences and stochastic nature in the flaw distribution between different laminates. This is true even for laminates made from the same batch of constituents. As shown in Fig. 2.2, the matrix begins to break-up extremely rapidly at stresses near σ_{cr}. Hence, given two similar laminates; one a little stronger than the other, it is feasible that under loading to σ_{cr} one of the laminates may experience relatively substantial failure of the matrix whereas little damage may occur in the other. The exact reason for the discrepancy in the data in Fig. 4.14 is unknown.

4.3.3   Modulus Degradation.   Predicted and experimental variations in the modulus (in the longitudinal direction) resulting from the fatigue loading of SiC/1723 are shown in Fig. 4.15 for a maximum applied stress, σ_{max}, equal to 360 and 500 MPa. The predicted results are generated with $\tau_{i_{min}}$ =0.4 MPa which is determined

by fitting empirical S-N data for the same composite system. For $\sigma_{max} = 360$ MPa, no degradation in the modulus is predicted under the current investigation since this stress magnitude (360 MPa) is less than the critical composite stress, σ_{cr}, of 400 MPa. Recall that for $\sigma < \sigma_{cr}$, the laminate is assumed to be void of any damage. Overall, the agreement between the predicted degradation in the composite modulus in Fig. 4.15 and the empirical data is reasonable; however, the rapid decay in interface shear from Eq. (4.1) is again apparent as discussed previously. The modulus data in Fig. 4.15 are normalized by the initial modulus before cycling $(N = 1)$.[†]
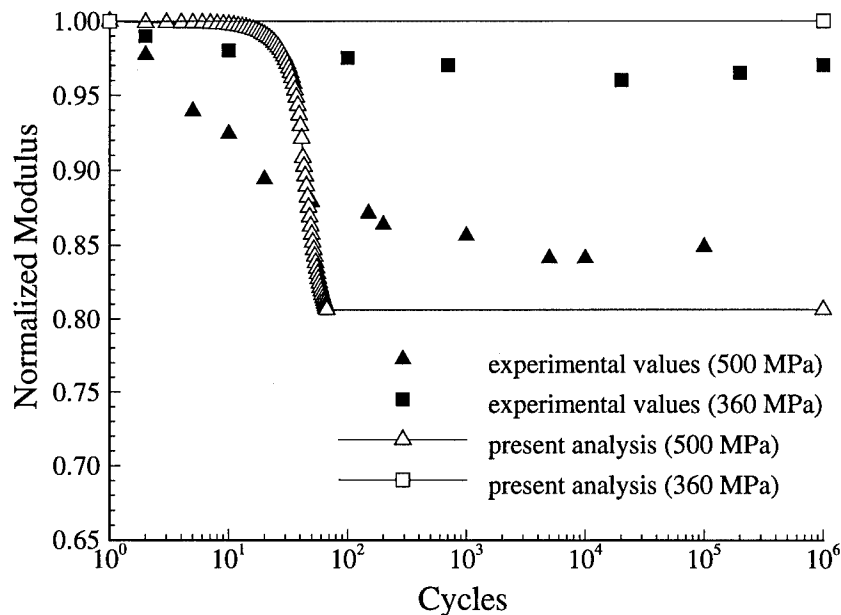
Figure 4.15   Normalized modulus versus fatigue cycles for a unidirectional SiC/1723 laminate.

4.3.4   S-N Behavior.   Figure 4.16 illustrates the S-N prediction for SiC/CAS composites based on the degradation in interface shear, $\tau_i(N)$ as expressed by Eq. (4.1)

[†]Note that along the abscissa in Fig. 4.15, the variable plotted is actually "cycles +1" since the first data point illustrated in this figure is the undamaged (normalized) laminate stiffness.

with $\tau_{i_{min}} = 5.0$ MPa. The predicted fatigue life is in a reasonable agreement with
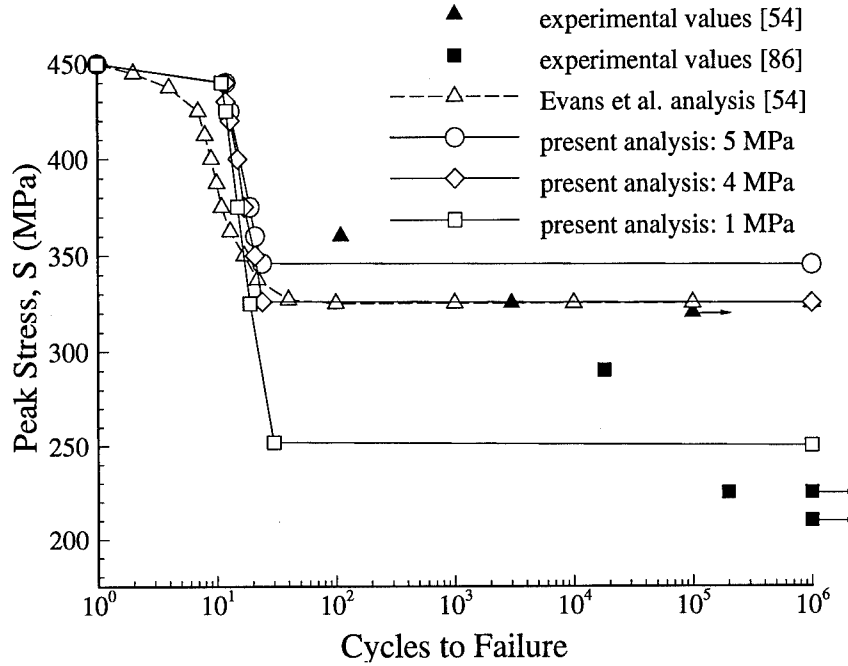
Figure 4.16   Fatigue life (S-N) diagram of a unidirectional, SiC/CAS laminate.

the experimental data of Evans *et al* [54]; however, it is likely that 5 MPa represents an upper bound for $\tau_{i_{min}}$ since this estimate is based upon data "confined to the parabolic range" of stress-strain hysteresis loops [54]. Evans *et al* observed changes in the shape of the experimental hysteresis loops from parabolic to linear during cycling, and this is not accounted for in their analysis of $\tau_i(N)$. This observed change in hysteresis could possibly result from a further decrease in $\tau_i(N)$. In support of this, if $\tau_{i_{min}}$ is chosen as 4.0 MPa, the empirical threshold stress of 325 MPa is obtained with the present analysis.

Karandikar [86] has also reported experimental fatigue life data for a SiC/CAS laminate under cyclic fatigue at room temperature, and these are shown in Fig. 4.16. If $\tau_i(N)$ is assumed to vary again as given by Eq. (4.1), however taking a minimum interface shear of $\tau_{i_{min}} = 1.0$ MPa but keeping λ and ω the same (i.e. $\lambda=2.25$ and $\omega=0.00275$), then the present analysis predicts a fatigue life which is in a reasonable

agreement with Karandikar's experimental data. When comparing the analytical and experimental S-N curves in Fig. 4.16, the reader should keep in mind the uncertainties in estimating $\tau_i(N)$, as well as the inherent scatter in the fatigue data especially in CMCs from different batches. In spite of these difficulties, however, the present analysis shows a promise to model fatigue responses of CMCs. Several estimates for $\tau_{i_{min}}$ are provided in Table 4.2 for a fatigued SiC/CAS system. The results in this table are based upon several micromechanics models [27,54,153].

Table 4.2   Minimum interface shear for a fatigued unidirectional SiC/CAS laminate. Estimates for $\tau_{i_{min}}$ are in units of MPa.

Evans et al [1]	Cho et al [2]	Current[3]	Pryce and Smith[4]
5.0	5.0 - 3.5	4.0	2

1. Empirical fit of hysteresis data *"confined to the parabolic range"* [54].
2. Based upon temperature and modulus data (partial frictional slip model) [27].
3. Best fit to empirical threshold stress.
4. Best agreement with experimental hysteresis loops [153].

The fact that the predicted cycles to failure for $\sigma > \sigma_{th}$ all occur at $N \leq 100$ is a result of the assumed rapid decay in the interface shear as given by Eq. (4.1).

$$\tau_i(N) = \tau_{i_o} + \left(1 - \exp^{-\omega N^\lambda}\right)\left(\tau_{i_{min}} - \tau_{i_o}\right) \qquad (4.1)$$

Assuming a more gradual reduction in shear should provide a closer match to the empirical data. In addition, Eq. (4.1) does not explicitly depend on the maximum applied stress, σ_{max}, nor the extent of composite damage. The reduction of interface shear should depend on σ_{max}, as well as the microstructural damage; however, by assuming the parameters λ and ω constant in Eq. (4.1), these effects have been neglected. Hence, in Fig. 4.16, the same *rate* of degradation in $\tau_i(N)$ is assumed for all values of peak stress (σ_{max}). The validity of this assumption is questionable since

the rate of decay in $\tau_i(N)$ (i.e. wear of the interface) is expected to increase with σ_{max} due to more severe deformations and microstructural damages. In general, this reduction would depend on the applied stress, σ, the residual thermal stresses, as well as the number of fatigue cycles, N. Alternately, a better estimate of $\tau_i(N)$ can be obtained from the empirical data.

Figure 4.17 compares the predicted fatigue life from the present analysis with the experimental counterpart for another CMC system, SiC/1723 [209]. Since no data on the specific variation of $\tau_i(N)$ is available for SiC/1723, the degradation in shear is determined from Eq. (4.1) with $\lambda = 2.25$ and $\omega = 0.00275$ but with different values of $\tau_{i_{min}}$. As shown in Fig. 4.17, a minimum interface shear of 0.4 MPa is found to provide the best fit to the empirical threshold stress of 440 MPa.
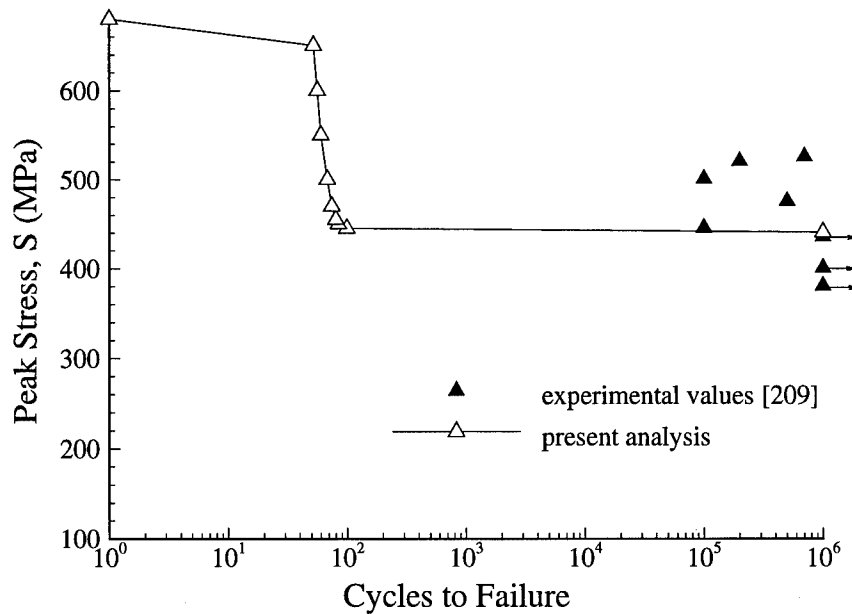
Figure 4.17   Fatigue life (S-N) diagram of a unidirectional, SiC/1723 laminate.

V. Cross-Ply Behavior

This chapter presents the predicted results for several cross-ply ceramic matrix composites under quasi-static, repeated and fatigue loadings. The present formulation considers a general damage state consisting of matrix cracking in both the transverse and longitudinal plies, as well as interface slip and debonding, fiber failure and fiber pull-out. The predicted results are compared with experimental data and are found to agree well with the data. The stress-strain response under monotonic tensile loading; hysteresis under repeated and cyclic loading and the S-N behavior are all investigated.

The state of stress in the cross-ply laminate is modeled using five components: the axial fiber stress in the 0° ply, $\sigma_f(x)$; the transverse ply stress, $\sigma_T(x)$; the axial matrix stress in the 0° ply, $\sigma_m(x)$; the interlaminar shear stress, $\tau(x)$, and the fiber/matrix interface shear stress in the 0° ply, $\tau_i(x)$. Under the current formulation, these stresses are given by the following equations as derived in chapter three.

$$\sigma_f(x) = c_3 \sinh(\beta x) + c_4 \cosh(\beta x) + \mathcal{T}\left\{c_1 \sinh(\lambda x) + c_2 \cosh(\lambda x)\right\}/\sigma_T^o + \sigma_f^o$$

(3.80)

$$\sigma_T(x) = c_1 \sinh(\lambda x) + c_2 \cosh(\lambda x) + \sigma_T^o$$

(3.78)

$$\sigma_m(x) = \frac{1}{v_m}\left\{\frac{b+d}{b}\sigma - \frac{d}{b}\sigma_T(x_{t_{|x}})\right\} - \frac{v_f}{v_m}\sigma_f(x)$$

(3.83)

$$\tau(x) = b\frac{d\sigma_L(x)}{dx} = -d\frac{d\sigma_T(x)}{dx}$$

(3.51)

$$\tau_i(x) = -\frac{r_f}{2}\frac{d\sigma_f(x)}{dx} \tag{3.10}$$

The constants in Eqs. (3.80) and (3.78) are dependent on the composite's state of damage, and once this is determined the composite strain may be calculated from Eq. (3.6). For the present cross-ply analysis, the behavior of several SiC/CAS and SiC/1723 laminates is investigated. The material property data for these systems are provided in Table 4.1. The cross-ply response under quasi-static, repeated and cyclic loading conditions is now investigated.

5.1 Quasi-Static Loading

Stress-strain responses for several cross-ply laminates, as predicted from the present analysis, are compared with their experimental counterparts [103] in Figs. 5.1 and 5.2.   Figure 5.1 provides the results for two cross-ply lay-ups, $[0_3/90_3/0_3]$ and
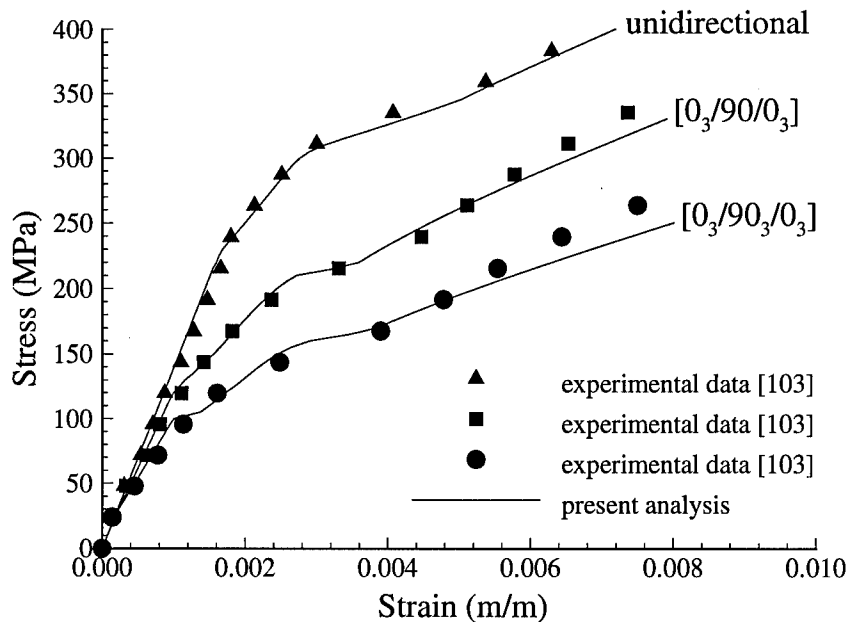
Figure 5.1   Stress-strain predictions from the current analysis along with experimental values [103]. Laminates shown are 0°, $[0_3/90/0_3]$ and $[0_3/90_3/0_3]$.
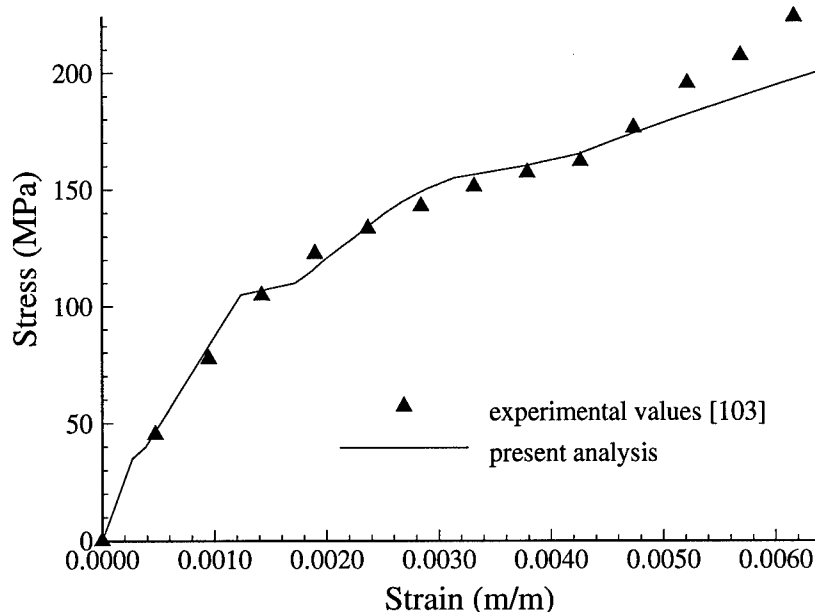
Figure 5.2   Predicted and experimental stress-strain response of a SiC/CAS laminate. The modeled ply lay-up is [0/90/0/90/0/90/0/90/0].

[$0_3/90/0_3$], along with the unidirectional laminate. The response for the [0/90/0/90/0/90/0/90/0] laminate is shown separately for clarity in Fig. 5.2. The material properties for the SiC/CAS composite are provided in Table 4.1. Other required data are given in Table 5.1. Also note that the [0/90/0/90/0/90/0/90/0] laminate is assumed to be of the symmetric form [$0_{2.5}/90_2$]$_s$ for the analysis. The results in Figs. 5.1 and 5.2 are obtained by choosing σ_{cr}^{90} and σ_{cr}^{0} from experimen-

Table 5.1   Assumed laminate properties

	b (mm)	d (mm)	σ_{cr}^{90} (MPa)	σ_{cr}^{0} (MPa)	$\hat{m}$
CAS [0/90]$_{2s}$	0.79	0.7	30	130	10.
CAS [$0_3/90/0_3$]	0.517	0.0862	30	130	5.0
CAS [$0_3/90_3/0_3$]	0.525	0.262	30	100	4.5
CAS [0/90/0/90/0/90/0/90/0]	0.9107	0.7281	30	110	5.0
1723 [(0/90)$_3$]$_s$	0.752	0.7	30	190	5.0

tal data in reference 103. For each laminate, the predicted stress-strain response is in good agreement with its experimental counterpart. Further, assuming the [0/90/0/90/0/90/0/90/0] laminate of the form $[(0_m/90_n)]_s$ still provides a reasonable prediction. The initiation of the transverse cracking occurs at 0.0165% strain while matrix cracking initiates at 0.27% strain. The laminate fails at 0.63% strain.

Several more stress-strain predictions for SiC/CAS cross-ply laminates are shown in Figs. 5.3 and 5.4. The points labeled 'a' through 'f' in Fig. 5.3 indicate
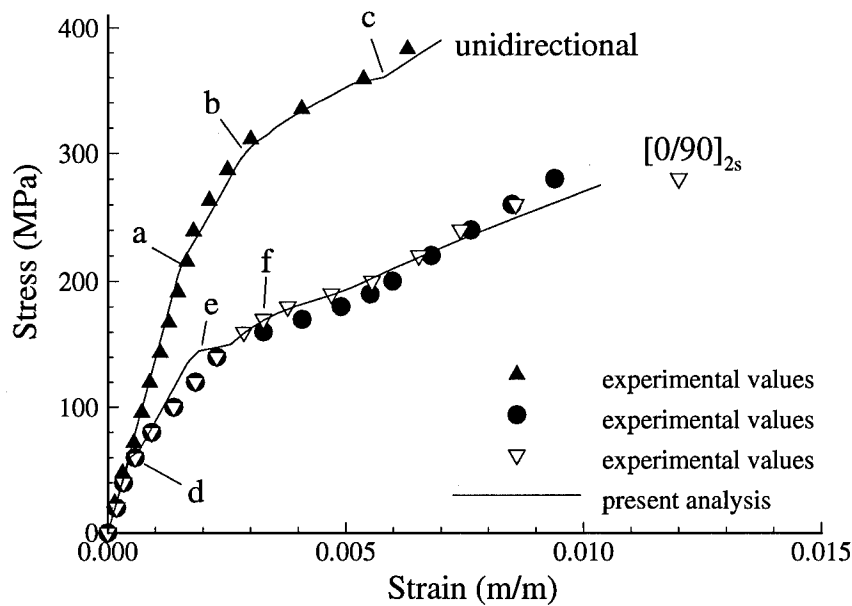
Figure 5.3   Stress-strain predictions of a $[(0/90)]_{2s}$, SiC/CAS laminate. The unidirectional response is also shown.

changes in the microstructural failure modes. Point 'a' corresponds to the unidirectional proportional limit and indicates the accumulation of sufficient matrix cracks to cause the stress-strain response to deviate from linearity. Point 'b' corresponds to crack saturation and the initiation of fiber failure; whereas, 'c' represents the point where the interface becomes completely debonded (i.e. $d = L/2$). The proportional limits for the cross-ply laminate (points 'd' and 'e') correspond to the accumulation

of transverse cracks in the 90° ply and the matrix cracks in the 0° ply, respectively. The influence of fiber fracture within the 0° ply of the cross-ply laminate becomes apparent at point 'f'. In Fig. 5.3, the material property data are taken from Table 4.1; however, in Fig. 5.4, $\tau_i = 14.4$ MPa and $\alpha_m = 5.0E-6$ /$^\circ$C in accordance with reference 147. Additionally, the thickness of the 0° ply for the $[0_3/90_2/0_3]$ laminate is assumed to be the average of the other two ($[0_3/90/0_3]$ and $[0_3/90_3/0_3]$) [197]. Two
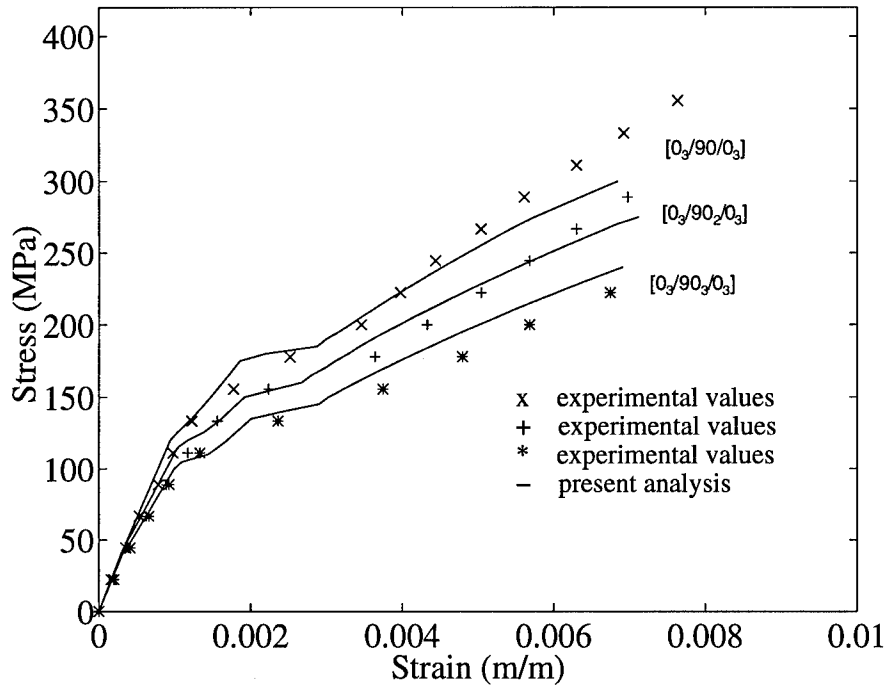
Figure 5.4   Stress-strain predictions for several cross-ply laminates. Experimental data are from reference 197. Three laminate configurations are shown: $[0_3/90/0_3]$ (x), $[0_3/90_2/0_3]$ (+) and $[0_3/90_3/0_3]$ (*). Note that some experimental data for the $[0_3/90_2/0_3]$ laminate are extrapolated.

sets of experimental data are provided in Fig. 5.3. These data are from Opalski and Gudiatis and were obtained from load and strain control tests, respectively [62,143].

The material behavior of a SiC/1723 cross-ply laminate is also predicted. Experimentally, the laminate lay-up is of the form $[(0/90)_3]_s$; however, numerically, the laminate is modeled as having the stacking sequence $[(0/90)]_{3s}$. The latter is required due to the assumed symmetry of the model. Again, there are no problems

in modeling the laminate in this manner as indicated by Fig. 5.5. The maximum stress obtained for the cross-ply laminate is 300 MPa. Figure 5.5 also shows the unidirectional prediction. In this case, the maximum stress is 700 MPa.
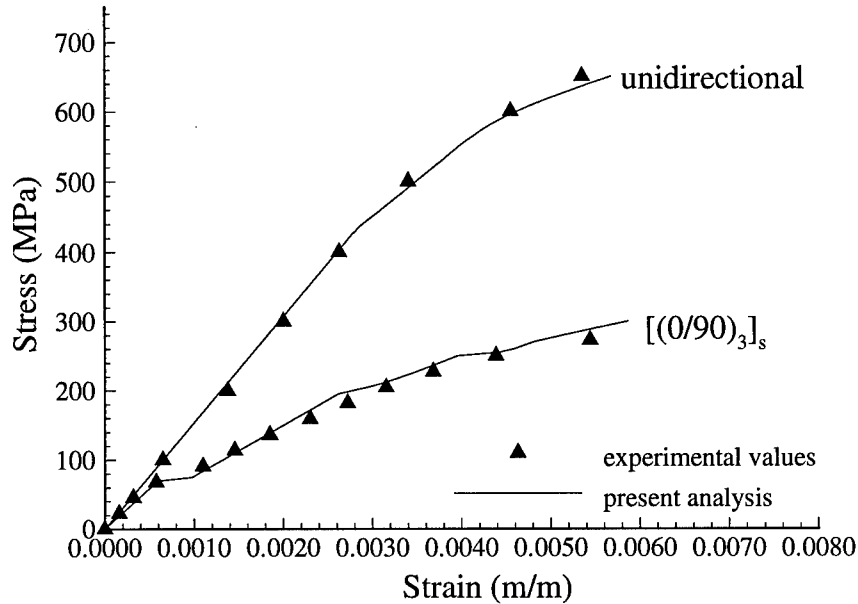
Figure 5.5   Stress-strain response of a unidirectional and $[(0/90)_3]_s$, SiC/1723 laminate.

5.1.1   Critical Strain Energies.

The critical strain energy for the 90° ply, U_{cr_T}, and the critical strain energy for the matrix in the 0° ply, U_{cr_m}, may be estimated by evaluating the energies associated with the appropriate proportional limits obtained from the cross-ply stress-strain curve $(\sigma_{cr}^{90}, \sigma_{cr}^{0})$.[†] In addition, the critical energies may also be estimated from the proportional limits of 90° and 0° laminates $(\sigma_{cr_{90}}, \sigma_{cr_0})$ [173]. The latter is desired since the stress-strain response for different cross-ply lay-ups may be predicted on the availability of $\sigma_{cr_{90}}$ and σ_{cr_0}.

[†]Reference Fig. 2.6 on page 2-16.

However, to obtain estimates for the cross-ply properties, σ_{cr}^{90} and σ_{cr}^{0}, from $\sigma_{cr_{90}}$ and σ_{cr_0} requires accounting for the effect of transverse cracks on matrix cracking within the $0°$ ply. If U_{cr_m} were to be determined from σ_{cr_0} then the actual proportional limit (σ_{cr}^{0}) for the cross-ply laminate will be overestimated since the influence of the transverse cracks on matrix cracking has not been accounted for in the analysis. Hence, the critical matrix and fiber strain energies (U_{cr_m}, U_{cr_f}) must be adjusted to account for the presence of transverse cracks in the $90°$ ply. A procedure for estimating these parameters is now provided.

Experiments have shown that the stress level associated with the onset of matrix cracking in the $0°$ ply of a cross-ply laminate is less than the stress level at which the cracking initiates in a $0°$ laminate [85, 86]. This behavior is expected due to the presence of the transverse cracks. Experimental data indicate that transverse cracks extend "a few fiber diameters" into the $0°$ ply and are therefore significant local stress risers [197]. Based upon empirical crack density data [85,86], the effect of transverse cracking on the initiation of matrix cracking may be estimated by simply shifting the *crack density versus $0°$ ply stress* curve (Fig. 5.1.1). The $0°$ ply stress is used since it is the local stress (and stress concentrations) in the $0°$ ply which control the crack progression in this ply rather than the applied laminate stress. The present analysis may be used to estimate the stress in the $0°$ ply.

Using the empirical data in references 85 and 86, the shift (i.e. the ratio $\sigma_{cr}^{o}/\sigma_{cr_o}$) is found to be equal to 0.7 for the three SiC/CAS laminates investigated in this study. These three laminates have lay-ups; $[0_3/90_3/0_3]$, $[0_3/90/0_3]$ and $[0/90/0/90/0/90/0/90/0]$. Since the shift is constant for all three laminates, the strain energies U_{cr_m} and U_{cr_f} are estimated using an adjusted critical stress of $\sigma_{cr}^{o} = 0.7\sigma_{cr_o}$ for all cases. The fact that this ratio is constant for all three cases seems to indicate that U_{cr_m} is a function of the orientation of the plies within the laminate only and not the number of plies or stacking sequence.
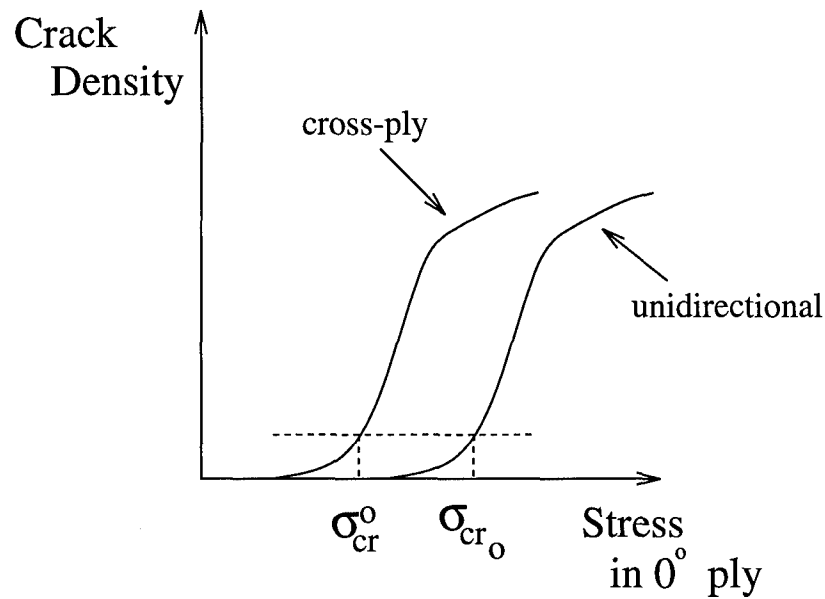
Figure 5.6   Schematic representation of *crack density versus 0° ply stress* for a uni-
directional and cross-ply laminate.

The predicted results for the $[0_3/90_3/0_3]$, $[0_3/90/0_3]$ and $[0/90/0/90/0/90/0/90/0]$
SiC/CAS laminates are shown in Figs. 5.7 and 5.8. The stress-strain curves are gen-
erated from the current analysis with $\sigma_{cr}^0 = 0.7\sigma_{cr_0}$. Again the results are in good
agreement with the empirical data. This agreement is noteworthy since different
cross-ply laminates' stress-strain responses are predicted from only lamina proper-
ties, i.e. the $90°$ ply and the $0°$ ply.
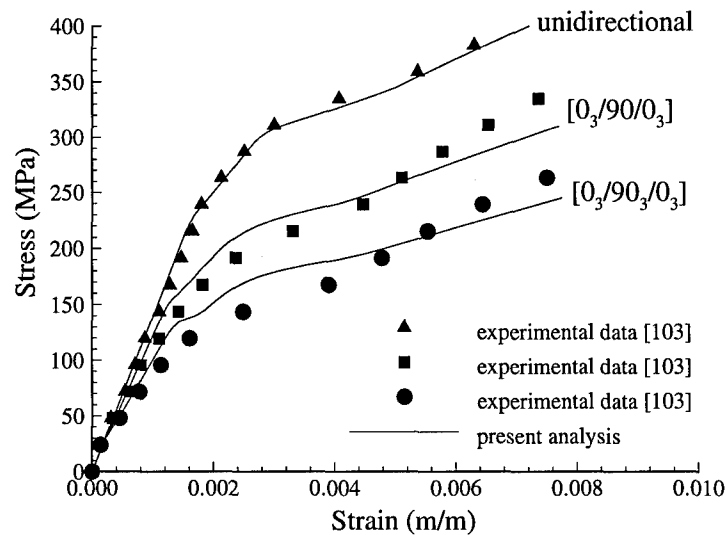
Figure 5.7   Stress-strain predictions from the current analysis along with exper-
              imental values [103].   Laminates shown are (a) 0°, $[0_3/90/0_3]$ and
              $[0_3/90_3/0_3]$ based upon $\sigma_{cr_{90}}$ and σ_{cr_0}.
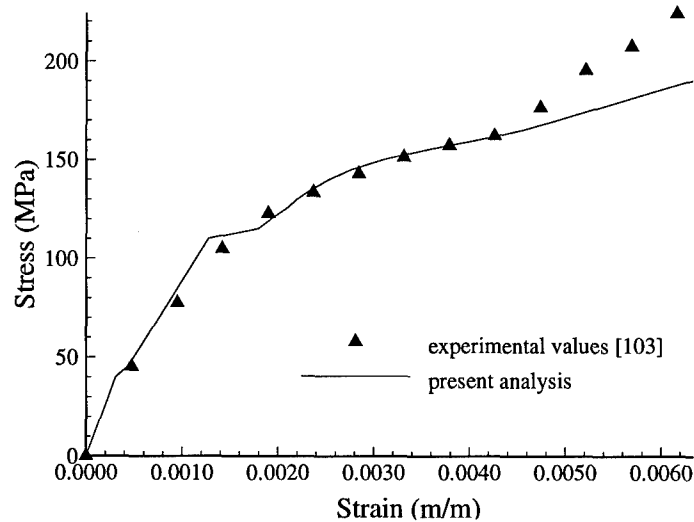
Figure 5.8   Predicted and experimental stress-strain response of a SiC/CAS
              laminate based upon $\sigma_{cr_{90}}$ and σ_{cr_0}.   The modeled ply lay-up is
              $[0/90/0/90/0/90/0/90/0]$.

5-9

5.2 Repeated Loading

Stress-strain curves for a $[0/90]_{2s}$, SiC/CAS laminate under loading and unloading conditions are shown in Fig. 5.9. The experimental data are from reference 143. The predicted response shown in Fig. 5.9 (a) is for the case when the cross-ply laminate is unloaded just after the onset of matrix cracking in the 0° ply. In Fig. 5.9 (b), the composite is unloaded after additional damage in the 0° ply has developed. In particular, the predicted response in Fig. 5.9 (a) is generated with a peak load of 140 MPa whereas loading in Fig. 5.9 (b) is allowed to continue up to a maximum applied stress of 180 MPa [143]. These results are obtained from the lamina properties, i.e. σ_{cr_0} and $\sigma_{cr_{90}}$. Figure 5.9 clearly demonstrates that the present analysis is capable of modeling the behavior of a cross-ply ceramic composite under repeated loading. For both cases, the predicted loading and unloading response is in good agreement with experimental data. Note that no attempt has been made to account for variations in material/lamina properties which may develop between various batches of materials.
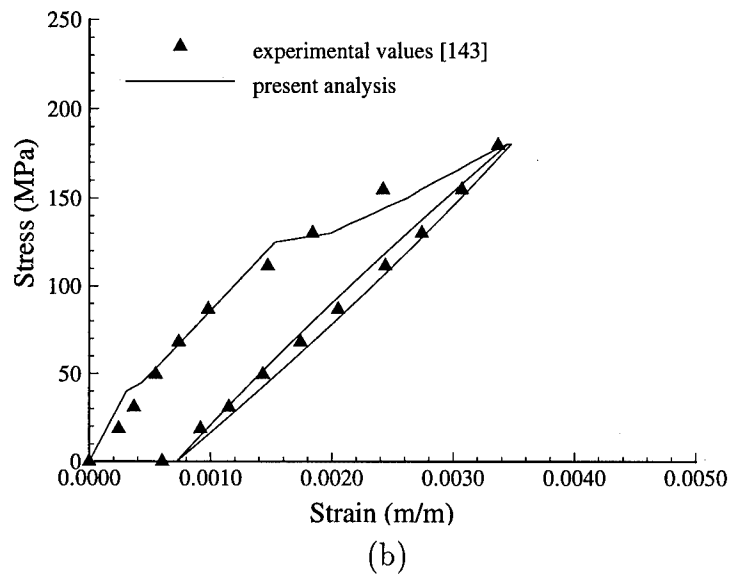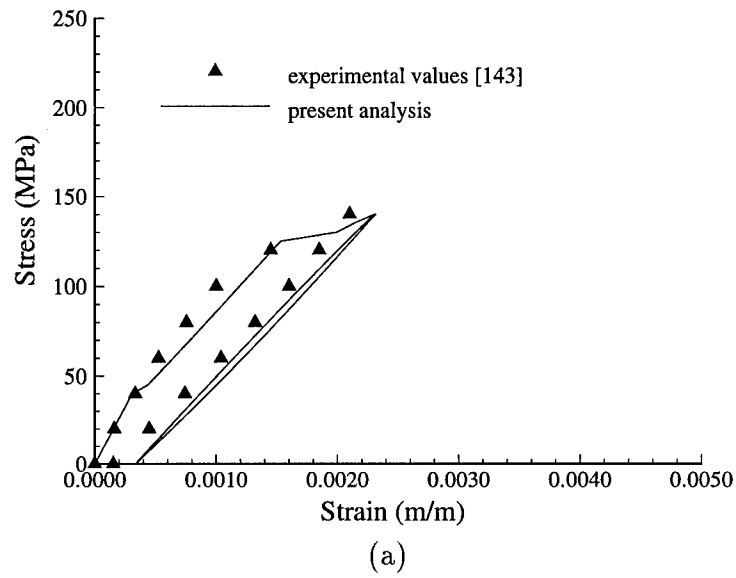
Figure 5.9 Stress-strain response of a $[(0/90)]_{2s}$, SiC/CAS laminate as predicted by the present analysis: (a) σ_{max}= 140 MPa, (b) σ_{max}= 180 MPa. $\mathcal{R}$=0.111.

Figure 5.10 illustrates the response of the same cross-ply laminate under repeated loading. The experimental data are from reference 4 and represent the cross-ply's behavior under three loading and unloading cycles. Initially, the composite is loaded to a maximum stress of 140 MPa and then unloaded to zero load. The same specimen is then reloaded to 175 MPa and again unloaded. Finally, the specimen is reloaded to a peak stress of 200 MPa after which the load is again removed. For clarity, the reloading portion of the stress-strain response is not presented. Again the predicted results match well with the empirical data. However, since the present analysis assumes that the interface shear stress remains constant during loading and unloading, the theory is not valid after several repeated loadings, especially under fatigue type of loading involving a large number of cycles. If a fatigue loading environment is to be considered, the degradation of the interface due to frictional wear, as well as the evolution of additional matrix cracks, fiber fractures and fiber pull-out must be considered as discussed in the next section.

Finally, the present analysis provides the cross-ply laminate's response when the fiber/matrix interface is partially bonded. However, once the interface completely debonds, the predicted residual or permanent strain (at $\sigma = 0$) remains constant. This phenomenon results from the simplified shear-lag theory and is illustrated in Fig. 5.11 which considers three loading cycles for a cross-ply, $[0_3/90_3/0_3]$, SiC/CAS laminate. The first hysteresis loop ($\sigma_{max} = 150$ MPa) occurs while the interface is still bonded. However, during the last two loading cycles, the maximum applied stress ($\sigma_{max} = 200$ and 250 MPa) is large enough to cause the interface to debond completely. The fact that the residual strain does not vary between the latter two hysteresis loops can be attributed to *not* modeling the fatigue specific damages such as the degradation of the fiber/matrix interface and fiber pull-out. These are, however, considered in the next section.
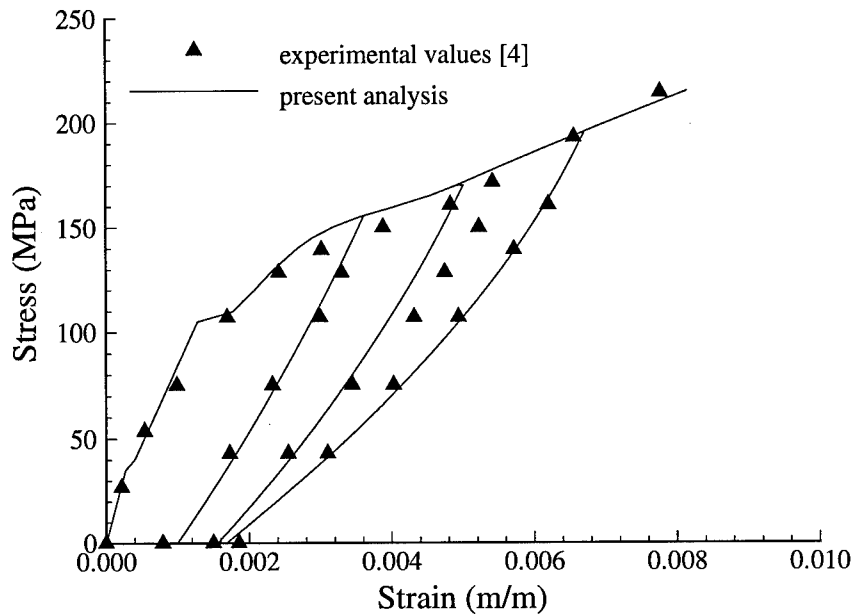
Figure 5.10   Repeated loading response of a $[(0/90)]_{2s}$, SiC/CAS laminate. Empirical data are from reference 4. For clarity, only the unloading portion of the response is illustrated. The reloading portion of the loading cycle is not shown.

5.3 Cyclic Loading

Under cyclic loading, additional damages can develop after the first loading cycle since the frictional resistance along the interface is allowed to decrease during each subsequent cycle. The latter is thought to result from wear of constituents due to the continuous frictional sliding along the interface. Moreover, as the interface wears, the ability of the fibers to transfer stress into the matrix and to reduce crack-tip stress intensities by providing closing tractions across the crack plane is reduced. This allows the formation of the additional (fatigue specific) damages which, in turn, produce the variations in the observed stress-strain response [172].

For the current investigation of cross-ply laminates, the degradation in the interface shear stress, $\tau_i(N)$, is again assumed to be given by Eq. (4.1) with λ=2.25 and ω=0.00275. Recall that this relation was proposed by Evans *et al* based upon their
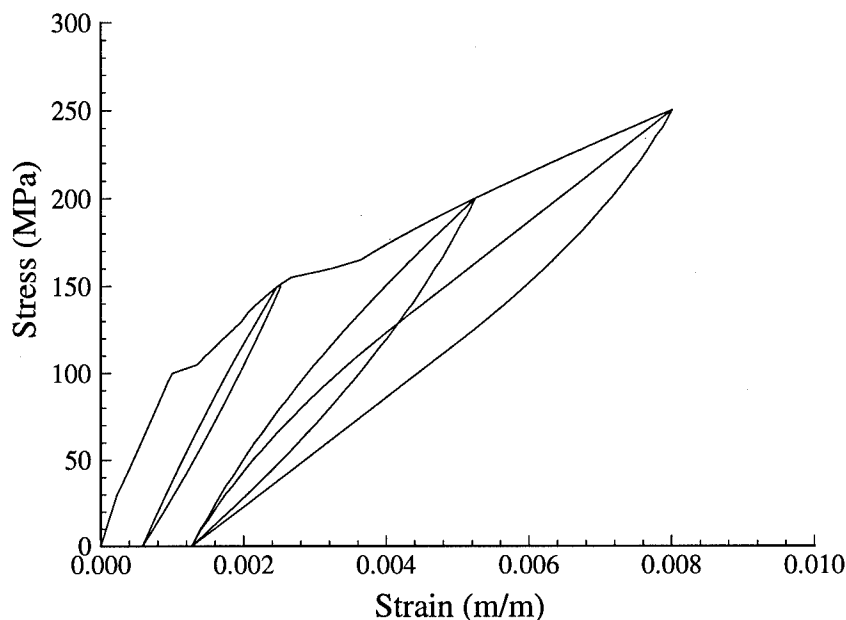
Figure 5.11   Repeated loading response of a $[0_3/90_3/0_3]$, SiC/CAS laminate.

investigation of *unidirectional* laminates [54]. The fact that Eq. (4.1) is now used for the investigation of different cross-ply laminates is one of not only convenience, but also necessity since alternate solutions are not available at this time. However, the degradation in shear can be determined by fitting the predicted results from the present study to empirical data, but this is not the current focus. Also, note that Eq. (4.1) is used for composite systems other than those originally proposed by Evans *et al*, e.g. SiC/1723.

The predicted results for cyclic loading are presented in three sections. The first section investigates the stress-strain hysteresis and strain ratchetting behavior of the cross-ply laminates. The final sections examine the modulus degradation and S-N behavior, respectively. As was observed with the unidirectional predictions, the assumed form of Eq. (4.1) causes the predicted results to differ from the experimental data; however, the two are still in relatively good agreement.

5.3.1 Stress-Strain Hysteresis and Strain Ratchetting. Stress-strain hysteresis and strain ratchetting are assumed to develop due to microstructural damages, e.g. fiber pull-out. These are accounted for by adjusting the fiber stress by a constant amount $\Delta\sigma(N)$ where $\Delta\sigma(N)$ is assumed to be the additional stress in an undamaged fiber when adjacent fibers fracture and pull-out (appendix H). As with the unidirectional analysis, the stress $\Delta\sigma(N)$ may be determined analytically by considering a permanently bonded region (PBR) along the fiber/matrix interface of the 0° ply. The PBR is assumed not to debond during loading nor slip during unloading. As expected, the maximum applied stress, σ_{max}, the interface resistance, $\tau_i(N)$, and the composite's state of damage, D, L and d, all effect the laminate's strain ratchetting behavior as illustrated in Eq. (5.1).

$$\Delta\sigma(N) = \frac{b+d}{b}\frac{1}{v_f(1-D)}\left\{\sigma_{max}-\sigma_{min}\right\} - \left\{\sigma^o_{f_{max}}-\sigma^o_{f_{min}}\right\} - \frac{2\tau_i(N)}{r_f}L$$
$$+\frac{d}{b}\frac{1}{\cosh\left(\lambda L_t/2\right)}\cdot\left\{\frac{1}{v_f(1-D)}\left[-\cosh\left(\lambda L_t/2\right)+\frac{1}{2}\cosh\left(\lambda x_{t}\big|_{x=-\gamma L/2}\right)\right.\right.$$
$$\left.\left.+\frac{1}{2}\cosh\left(\lambda x_{t}\big|_{x=\gamma L/2}\right)\right] - \frac{E_f}{E_1}\cosh\left(\lambda x_{t}\big|_{x=0}\right)\right\}\left\{\sigma^o_{T_{max}}-\sigma^o_{T_{min}}\right\} \qquad (5.1)$$

The reader may verify that in the absence of the 90° plies, Eq. (5.1) reduces to the unidirectional case [Eq. (4.3)].

Figures 5.12 and 5.13 show several predicted hysteresis loops along with their corresponding experimental data. The results shown in Fig. 5.12 are for $\sigma_{max}=160$ MPa and $\mathcal{R}=0.125$. In Fig. 5.13, $\sigma_{max}=180$ MPa and $\mathcal{R}=0.11$. These are consistent with the test conditions from Opalski [143]. Both sets of predicted data are generated using Eq. (4.1) with $\tau_{i_o}=20$ MPa and $\tau_{i_{min}}=1$ MPa. In both cases, the predicted results match well with the experimental data. Variations in both the size and shape of the hysteresis loops, as well as the strain ratchetting behavior are reasonably captured. The differences fall well within the expected range of empirical scatter. No further results of this type are provided due to the limited availability of experimental data.
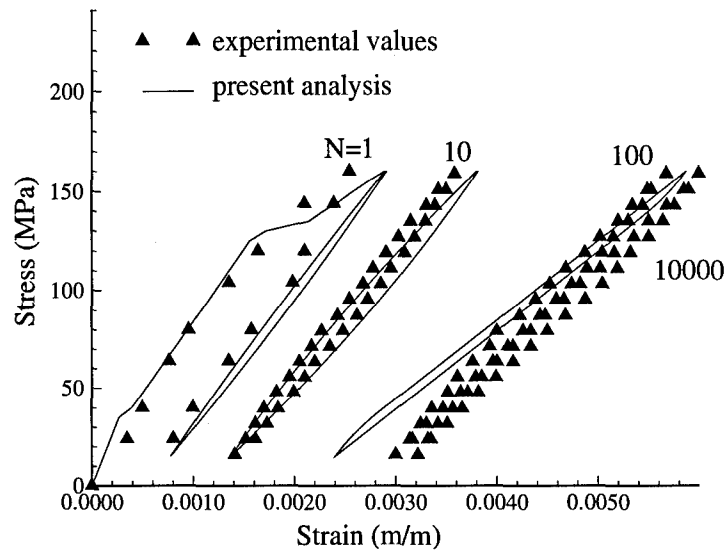
Figure 5.12   Stress-strain hysteresis for a $[0/90]_{2s}$, SiC/CAS ceramic composite. Experimental data are from Opalski [143]. $\sigma_{max} = 160$ MPa, $\mathcal{R}$=0.125. For the experimental data, $N = 1, 10, 100, 10000$.
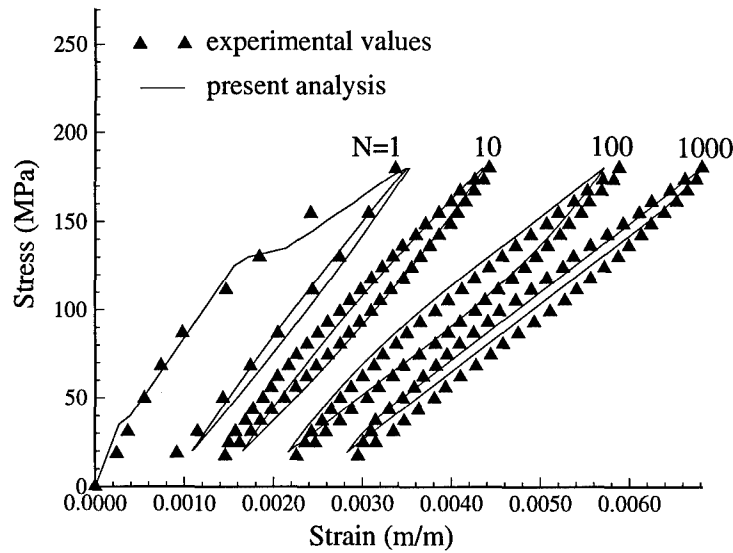
Figure 5.13   Stress-strain hysteresis for a $[0/90]_{2s}$, SiC/CAS ceramic composite. Experimental data are from Opalski [143]. $\sigma_{max} = 180$ MPa, $\mathcal{R}$=0.11. For the experimental data, $N = 1, 10, 100, 1000$.

5.3.2 Modulus Degradation. Several curves illustrating the degradation in the elastic modulus as a function of fatigue cycles are shown in Figs. 5.14 through 5.16.[†] The results shown in the first figure are for $\sigma_{max} = 160$ and 180 MPa, and correspond with the same loading conditions as in Figs. 5.12 and 5.13, respectively. Here,
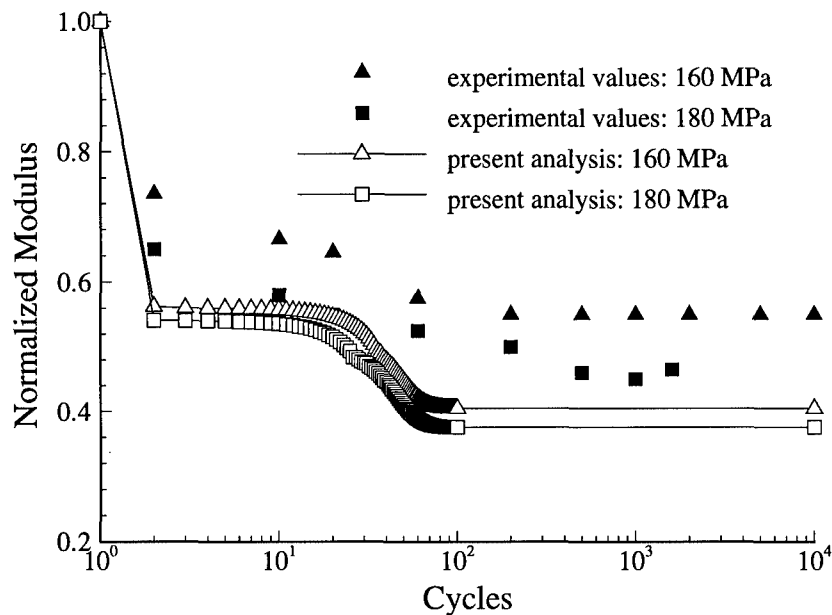
Figure 5.14   Laminate modulus versus fatigue cycles for a $[0/90]_{2s}$, SiC/CAS ceramic composite. Experimental data are from Opalski [143].

the elastic modulus is normalized with its initial value before cycling. In each case, the modulus substantially decreases during the first cycle due to the formation of microstructural damages, and further decreases in the modulus are dependent on the degradation of the shear, $\tau_i(N)$. In Fig. 5.14, the predicted modulus decreases to 56% of its initial value after the first cycle. As the interface wears with further cycling, the predicted modulus decreases to 40% of the undamaged magnitude. For $\sigma = 180$ MPa, the modulus initially decreases by 46% and continues to decline un-

_____

[†]Note that the abscissa in these figures actually plots the number of loading cycles plus one, i.e. cycles +1, since the first data point illustrated in each figure represents the undamaged (normalized) laminate stiffness.

til reaching 37.5% of its original value. For each case, the minimum interface shear $\tau_{i_{min}}$ is assumed to be 1 MPa. Moreover, the assumed rapid degradation in the shear, as predicted by Eq. (4.1), is self evident. Better correlation between the predicted results and experimental data could be obtained through appropriate selection of $\tau_i(N)$.

Similar results for a $[0_3/90/0_3]$ and $[0_3/90_3/0_3]$, SiC/CAS laminate are shown in Figs. 5.15 and 5.16. Again the predicted results are consistent with the published data; however, the assumed degradation in shear causes the predicted modulus to decline rapidly over the first one-hundred cycles. In all cases, the predicted results provide a conservative design estimate for the laminate behavior. For example, the initial decrease to 0.728 of the original modulus, E_{1_o}, for the $[0_3/90_3/0_3]$ laminate (Fig. 5.16) matches well with the published data [103]; however, the current analysis predicted the final degradation in the elastic modulus to 0.54 E_{1_o} whereas the experimental data show a decrease to only 0.61 E_{1_o}. The difference is due, in large part, to the assumption that the interface shear degrades to 1 MPa. If the shear stress is reduced to 2 or 3 MPa, a closer match between the predicted and experimental results would likely develop.
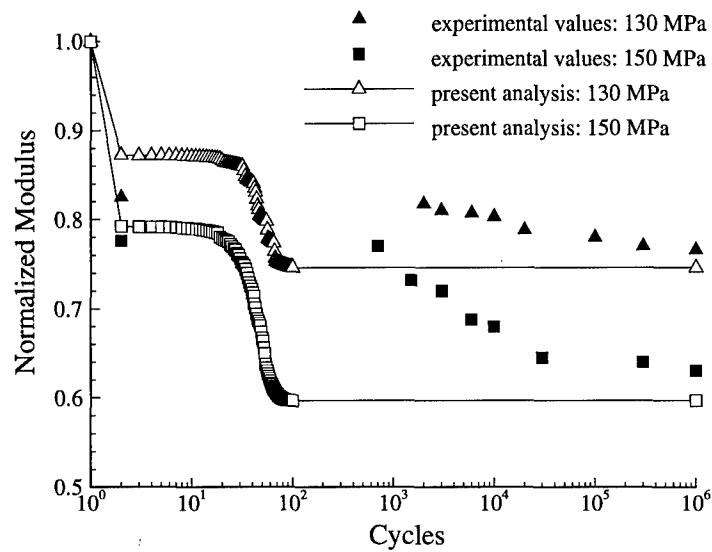
Figure 5.15   Laminate modulus versus fatigue cycles for a $[0_3/90/0_3]$, SiC/CAS ceramic composite.   Experimental data are from Kuo [103]. $\sigma_{max} = 150$ & 130 MPa.
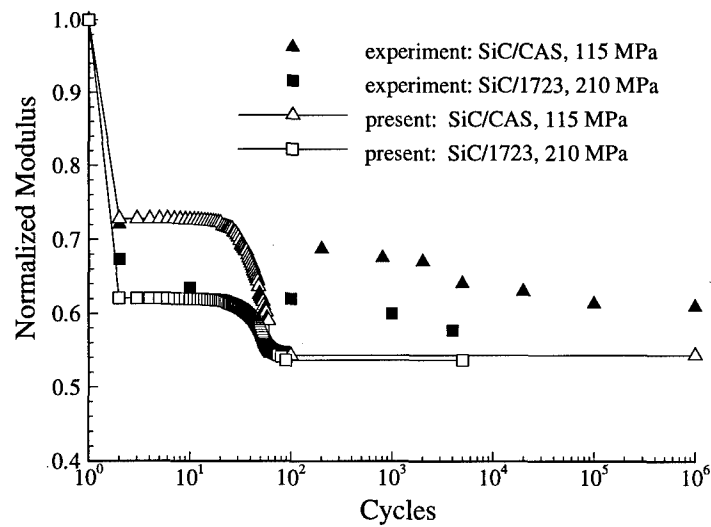
Figure 5.16   Laminate modulus versus fatigue cycles for a $[0_3/90_3/0_3]$, SiC/CAS ($\sigma_{max} = 115$ MPa) and a $[(0/90)_3]_s$, SiC/1723 ($\sigma_{max} = 210$ MPa) ceramic composite. Experimental data are from Kuo [103] and Zawada et al [209].

Finally, the degradation in the laminate modulus for a $[(0/90)_3]_s$, SiC/1723 ceramic composite is also shown in Fig. 5.16. The experimental data are from Zawada et al [209] and are shown for $\sigma_{max} = 210$ MPa. The elastic modulus decreases to 72.8% of the original stiffness during the first cycle. This decrease is due primarily to matrix cracking and interface debonding. Limited fiber failure is observed. In total, the modulus is predicted to decrease by 46% due to the damage formation and the degradation of the interface to 1 MPa. These are again consistent with the experimental data.

5.3.3 S-N Behavior. Figures 5.17 through 5.19 represent the predicted S-N behavior of the SiC/CAS laminates investigated by Kuo [103]. As shown in these figures, a minimum shear stress, $\tau_{i_{min}}$, of 1 MPa matches well with the empirical data. Furthermore, $\tau_{i_{min}} = 1$ MPa yields a conservative estimate for the fatigue limit. Similar results for the $[(0/90)_3]_s$, SiC/1723 laminate are shown in Fig. 5.20. As with the unidirectional results, the assumed rapid degradation in the interface shear, $\tau_i(N)$, is apparent in these figures. Furthermore, as expected the more the interface is allowed to wear, the farther the fatigue limit drops. This results since as the interface wears, i.e. $\tau_{i_{min}}$ decreases, fractured fibers slip/pull-out more easily from the matrix, and as the fibers slip, the likelihood of laminate failure increases.

As illustrated in Figs. 5.17 through 5.20, the interface shear stress is predicted to decrease to a minimum (steady-state) value somewhere between 1 and 5 MPa. In each of the referenced figures, this range for $\tau_{i_{min}}$ provides a good bounding envelop for the experimental data. As expected, the life expectancy of the laminate decreases as the interface shear drops from 5 to 1 MPa. The drop in the fatigue limit accompanying the decline in the shear stress is a bi-product of the additional decrease in $\tau_i(N)$ and its effect on the quantity $2\tau_i(N)L/r_f$ as it appears in Eq. (5.1). In addition, the decrease in $\tau_i(N)$ also permits the formation of additional damages due to less efficient load transfer between the constituents. In particular as $\tau_i(N)$
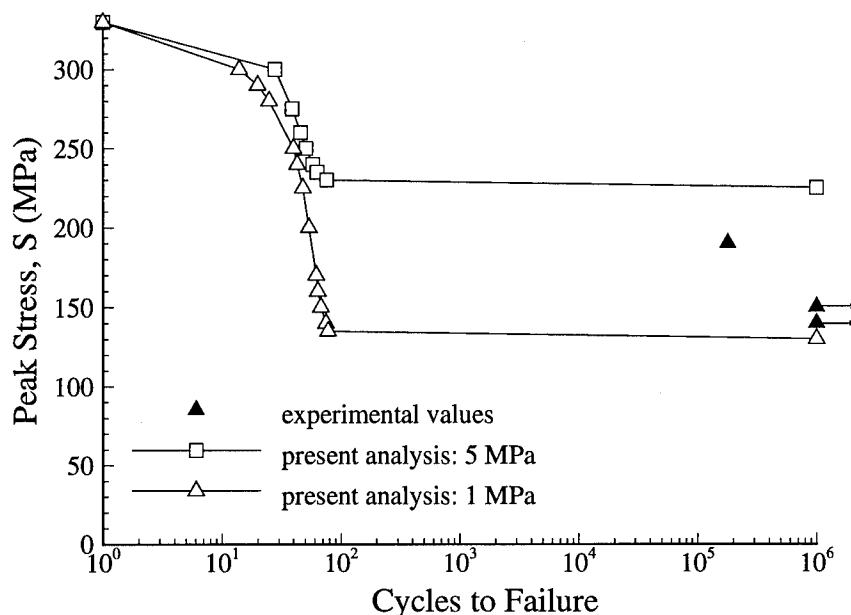
Figure 5.17   Peak stress versus cycles to failure for a $[0_3/90/0_3]$, SiC/CAS ceramic composite. Experimental data are from Kuo [103].

drops, the average stress in the fiber increases and correspondingly the probability of fiber fracture also increases.

The ability to predict the S-N behavior of CMC laminates, as illustrated in Figs. 5.17 through 5.20, is a significant accomplishment since under previous micromechanics analyses this could not be done with any degree of accuracy. The present formulation incorporates a number of microstructural mechanisms, e.g. matrix cracking, interface debonding, fiber fracture, frictional slip, fiber pull-out, strain ratchetting, stress-strain hysteresis, interface wear, etc, into a consistent, comprehensive and yet simple methodology which, as demonstrated by the results, does a good job in modeling the laminate behavior. It would be expected that if a more accurate representation for the degradation in interface shear, $\tau_i(N)$, could be obtained then the predicted results would likely improve. The alternative is to use the present analysis to determine $\tau_i(N)$ by fitting the empirical data. Each of the salient fatigue
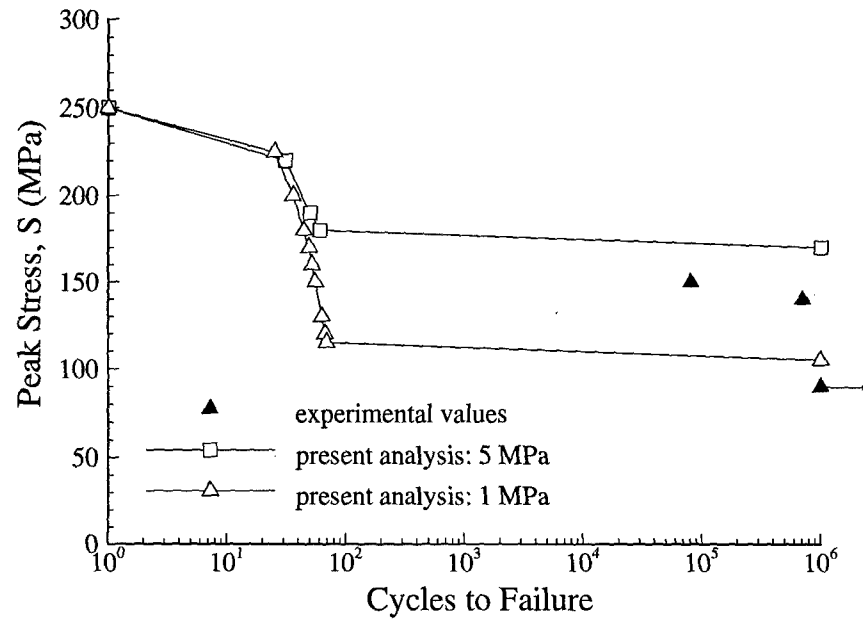
Figure 5.18 Peak stress versus cycles to failure for a $[0_3/90_3/0_3]$, SiC/CAS ceramic composite. Experimental data are from Kuo [103].

features (e.g. stress-strain hysteresis, strain ratchetting, modulus degradation and S-N behavior) could be selectively fit.
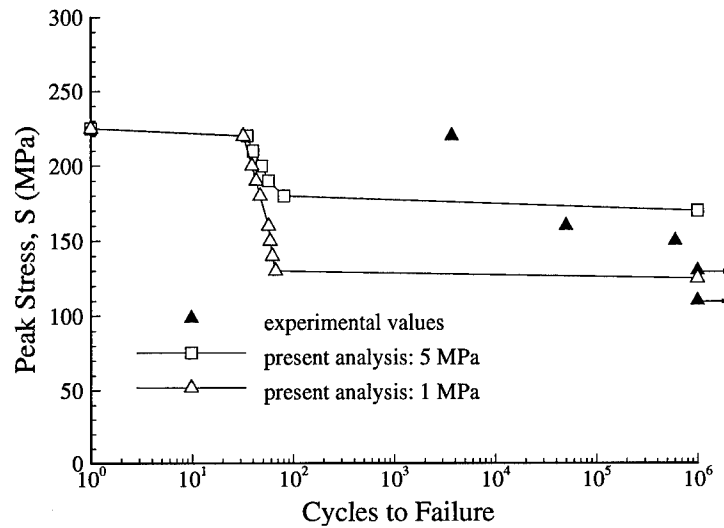
Figure 5.19   Peak stress versus cycles to failure for a [0/90/0/90/0/90/0/90/0], SiC/CAS ceramic composite. Experimental data are from Kuo [103].
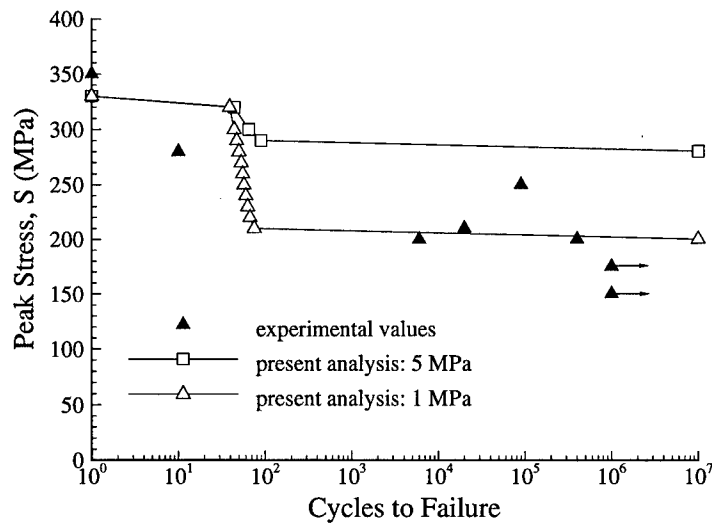
Figure 5.20   Peak stress versus cycles to failure for a [(0/90)$_3$]$_s$, SiC/1723 ceramic composite. Experimental data are from Zawada *et al* [209].

VI. Conclusions

Ceramic matrix composites exhibit a remarkable increase in strain-to-failure as compared with their monolithic counterparts. As such, this relatively new breed of composite is emerging as a viable material and structural candidate for a virtual plethora of industries. In particular, these advanced composites are ideally suited for aerospace and other high-temperature applications in which the thermal and wear properties of the ceramic matrix are of great benefit. The incorporation of the reinforcement phase into the brittle matrix almost serendipitously leads to microstructural mechanisms which reduce the propensity for catastrophic failure of the laminate. In practice, the ability of the reinforcing fibers to arrest the growth of dominant fractures via energy dissipation and the application of closing tractions to crack fronts has most notably increased the feasibility of employing these materials in environments dominated by severe thermal and mechanical fatigue loadings.

Under such conditions, however, extensive microstructural damages may develop due to the limited fracture toughness of the constituent materials. This, combined with the inherent complexities and stochastic nature of failure in brittle non-homogeneous media, makes the modeling of ceramic matrix composites quite difficult. However, it is worth noting that it is the formation of these damages which provided the ceramic composite with its large strain-to-failure, pseudo-ductility, and gradual non-catastrophic failure mode, and therefore, the formation of these damages is to be encouraged. Nonetheless, the ability to predict the evolution of the microstructural damages, as well as the resulting material response remains a worthwhile, albeit formidable, task since it is the only means of characterizing the composite's residual (strength and stiffness) properties.

Towards this end, the research accomplished under the current doctoral study includes the successful development and implementation of an analysis methodology for predicting the behavior of ceramic matrix composites under operating conditions

which produce the continuous progression of microstructural damages. In particular, the behavior of both unidirectional and cross-ply laminates under room-temperature quasi-static, repeated and cyclic loading conditions is investigated. Note that the present research represents a synthesis of existing theories, as originally proposed or appropriately modified for the current analysis, and new material generated by the author. For example, the formulation of the model used in the analysis of unidirectional laminates is rooted in shear-lag theory (section 3.1) but is modified by the author to consider damages other than matrix cracking as originally proposed [25]. This represents an area where existing work is modified/extended by the author. The model used in the analysis of cross-ply laminates, on the other hand, represents work accomplished as part of the current research. In all situations, the works accomplished by other researchers are appropriately referenced.

The solution technique is validated by comparing the predicted material stress-strain response of several composite materials and laminate lay-ups with the corresponding empirical data. A summary of the work done is presented in Table 6.1 which appears at the end of this chapter. This table should serve as a convenient "road map" as many of the tasks completed under the current research are cross-referenced according to the relevant chapters, sections, appendices and figures as they appear in this document. The table lists accomplishments for both the unidirectional and cross-ply studies. Furthermore, the work is categorized according to the *analysis* formulation and solution *validation*. The analysis consists in the development of the micromechanics models and failure criteria, whereas the solution validation high-lights areas where predicted and experimental test results are compared. The results are broken down by loading environment (e.g. static, fatigue); material (e.g. SiC/CAS, SiC/1723) and stacking sequence (e.g. $[0_3/90/0_3]$, $[0/90/0/90/0/90/0/90]$).

In short, the present formulation consists in the development of a micromechanics analysis (section 3.1) and set of failure criteria (section 3.2) for modeling the initi-

ation and evolution of various damages inherent to brittle composites. These include matrix cracking in 0° and 90° plies (section 3.2.1), fiber/matrix interface debonding (section 3.2.2), fiber fracture (section 3.2.3) and fiber pull-out (section 3.3.2). In addition, frictional slip along fiber/matrix interfaces is necessary for repeated and fatigue loadings. Therefore, formulations of the extent of frictional sliding for a partially bonded and fully debonded interface is accomplished (appendix C). In previous studies, only the fully debonded case was considered. In addition, analyses required to capture the continuous development of permanent strain, as experienced under fatigue loading conditions, are developed (appendices G and H).

The stress-strain and strain-displacement relations for the current analysis are derived from a one-dimensional shear-lag formulation. For unidirectional laminates, the work originally presented by Kuo and Chou [106], which was formulated to model the material behavior with the two damage modes of matrix cracking and interface debonding, is extended to consider fiber fracture, frictional slip and fiber pull-out (section 3.1.2). These allow not only for a more accurate prediction of the material response under quasi-static loading, as originally proposed, but also the present analysis is well suited for modeling the stress-strain hysteresis and strain ratchetting behavior associated with repeated and fatigue loadings. For the cross-ply laminates, a new model is formulated which considers a generalized state of damage in which any relative configuration between matrix cracking of 0° and 90° plies is permitted (section 3.1.3). In the previous study, this had been limited to only a few special configurations [106]. In both cases, unidirectional and cross-ply laminates, the present shear-lag models prove adequate for modeling the material response provided an equivalent state of damage can be derived. Moreover, these models provide a convenient vehicle to relate the macromechanical behavior with specific micromechanical mechanisms (chapters four and five). In particular, matrix cracking, interface debonding and fiber fracture are well characterized and can be associated with the salient features of the material response curves. The monotonic

loading response (sections 4.1 and 5.1), stress-strain hysteresis, strain ratchetting, modulus degradation and S-N behavior under cyclic loading (sections 4.3 and 5.3) all compare well with experimental data.

The failure criteria developed in the current analysis are formulated to be amenable to a variety of solution techniques. Moreover, the dependence of these criteria on empirical data is minimized. Closed-form solutions are provided for estimating the instantaneous matrix crack density (appendix E) and interface debond length whereas the extent of fiber fracture is determined using a Weibull failure distribution in which the statistical modulus is based upon empirical data (appendix F). For consistency throughout the analysis, the failure criteria governing fiber fracture, matrix cracking and transverse cracking are all based on corresponding *critical strain energies*, U_{cr_f}, U_{cr_m} and U_{cr_T} (section 3.2). Moreover, for the cross-ply laminates, these energies can be calculated based upon the energies of the unidirectional laminate and the relative crack density evolution of these two laminate systems (section 5.1.1). This permits the material response of a large number of composite systems and laminate geometries to be modeled based only on the most basic laminate properties (appendix I).

The proposed micromechanics model and failure criteria are quite effective in modeling the behavior of unidirectional laminates under quasi-static loadings (section 4.1). As is illustrated in Figs. 4.1 and 4.2, the present shear-lag analysis does a nice job of predicting the changes in the composite's (elastic) modulus due to the initiation and progression of damages. Furthermore, the evolution of matrix cracks and interface debonds is captured well with the *critical matrix strain energy* (CMSE) and maximum stress criteria. As expected, however, the break-up of the fibers produces a more dramatic decline in the composite modulus than the two damage modes of matrix cracking and interface debonding. Fortunately, the proposed Weibull distribution is sufficient for accounting for large variations in the evolutions of fiber fractures. In theory, a range of behaviors can be modeled based solely on

the Weibull modulus, $\hat{m}$. Moreover, the estimated range is consistent with previous findings (appendix F) [37]. The final composite modulus is observed to approach a magnitude of $v_f E_f (1 - D)$.

The behavior of unidirectional laminates under repeated (section 4.2) and fatigue loadings (section 4.3) is also well characterized. Under repeated loadings, the modulus degradation (section 4.3.3) and the stress-strain hysteresis (section 4.3.2) is consistent with the expected behavior - at least while the interface remains bonded. Once the interface fully debonds, the predicted permanent (residual) strain upon unloading fails to increase as observed experimentally. Under fatigue loadings, this problem becomes worse since the predicted residual strain decreases as the interface wears. The latter is a result of the simplifying assumptions associated with the micromechanics model. To correct this behavior, the constituent stresses are modified to account for fracture and pull-out of fibers which is thought to be the catalyst for the aforementioned phenomenon (appendix G). With the incorporation of these damage mechanisms, both the hysteresis and strain ratchetting behavior of unidirectional CMCs are successfully modeled up to several millions of cycles (Fig. 4.10). The analysis, as presented herein, is also a viable means for estimating the interface shear resistance and bonding strength. This is significant since there exists some uncertainty regarding the empirical data. Finally, the predicted fatigue life and S-N behavior for various unidirectional laminates is found to be consistent with previous results [54]; however, as expected, the analysis shows a strong dependency on the (assumed) interface wear.

The proposed model for the cross-ply laminate also does a good job in predicting the material behavior of the CMCs (chapter five). All relevant damage modes appear to be adequately handled. The quasi-static stress-strain analysis, however, does require that the critical composites stresses for the 0° and 90° plies be determined (section 5.1). This is accomplished within the current study by choosing the critical stresses based upon experimental data or through approximations based

upon properties of the unidirectional laminate (section 5.1.1). Analytical solutions also exist (appendix I). For repeated and fatigue loading conditions, the hysteresis and strain ratchetting mechanisms are consistent with the experimental data once fiber fracture and pull-out are adequately modeled (section 5.3.1). The other salient features associated with the fatigue response of cross-ply laminates, e.g. modulus degradation and S-N behavior, are also predicted with reasonable accuracy (sections 5.3.2 and 5.3.3). However, once again it is clear that the residual properties of the interface govern, in large part, the global composite response. This is to be expected since it is the chemical bonding and residual thermal stresses along the fiber/matrix interface which dictate everything from the initiation and evolution of microstructural damages and the corresponding energy dissipating mechanisms to the macromechanical stress-strain and hysteresis behavior, as well as the fatigue life of the laminate itself.

And indeed, the material behavior predicted under the current analysis is found to be strongly dependent on the assumed interface properties, e.g. the frictional resistance of the interface, τ_i, and the ultimate shear strength of the interface, τ_{ult}. This dependence results in the matrix cracking and interface debonding failure modes being highly coupled (appendix E). Moreover, the (assumed) degradation in shear during fatigue loadings is found to significantly influence the predicted behavior of the laminate (sections 4.3 and 5.3). In particular, the assumed rapid decline in $\tau_i(N)$ as modeled with Eq. (4.1) is quite apparent in the predicted (elastic) modulus degradation and S-N behavior for both the unidirectional and cross-ply laminates. However, the final steady-state interface shear predicted by the current analysis is consistent with estimates from previous studies. For example, the frictional resistance along the interface of the unidirectional SiC/CAS laminate is predicted to fall from 20 MPa to around 5 MPa during fatigue cycling. This is consistent with the current literature [54]. Also, the present analysis estimates an interface bond strength of about 200 MPa which is in agreement with previous work [113].

Under the current research, the model and failure criteria are chosen to allow for analysis of complex loading (i.e. fatigue). And, in fact, the analysis methodology is successfully employed to consider many of the nuances associated with fatigue loading environments. Also, since the failure criteria proposed under the current analysis do not restrict the location where new cracks form, a more gradual progression of damages than otherwise determined with previous criteria is found. As a result, the analysis matches the empirical trends more accurately. Finally, the proposed approach is found to be robust to variations in the critical composite stress and with the assumed stacking sequence of the $0^o/90^0$ plies in the cross-ply laminates. These make the current analysis a viable approach for modeling a variety of CMC unidirectional and cross-ply laminates under different loading conditions.

Table 6.1   Accomplishments of the Present Study

<u>Unidirectional Laminate</u>

- Analysis

  - Model Formulation

    * Quasi-static loading

Chapter	Section	Appendix	Figure
1, **3**	1.3, 2.4, **3.1.2**, B.2	A, B, I	2.7, 3.1, **3.7**, **B.3**, I.3

    * Repeated loading

Chapter	Section	Appendix	Figure
1, **3**	2.2.3, **3.3.2**	**C**	2.4, C.1

    * Cyclic loading

Chapter	Section	Appendix	Figure
1, **3**	2.2.3, **3.3.3**, A.6.2	**C**, G	2.5, G.2, G.3

      · Stress-strain hysteresis

Chapter	Section	Appendix	Figure
1, **3**	A.6.2.2, B.3	A, B, **C**, D	2.5, B.4

      · Modulus degradation

Chapter	Section	Appendix	Figure
1, **3**	A.6.2.1, B.3	A, B	B.4

      · Strain ratchetting

Chapter	Section	Appendix	Figure
1, **3**	**3.3.3.1**, A.6.2.3, B.3	A, B, **G**	2.5, 3.18, 3.19, B.4

      · S-N behavior

Chapter	Section	Appendix	Figure
1, **3**	**3.3.3.2**, A.6.2.4, B.3	A	2.5, B.4, B.5

  - Failure Criteria

    * Matrix cracking

Chapter	Section	Appendix	Figure
1, **3**	**3.2.1**, E.1, E.3	**E**, I	3.13, E.6, E.8, E.11, E.14

    * Interfacial debonding

Chapter	Section	Appendix	Figure
1, **3**	**3.2.2**, F.5	F	3.14, C.2

    * Fiber fracture

Chapter	Section	Appendix	Figure
1, **3**	**3.2.3**, F.2	**F**, I	4.1, 4.2

- Validation

  - Quasi-static loading

Chapter	Section	Appendix	Figure
4	**4.1**	E	4.2, 4.3

  - Repeated loading

Chapter	Section	Appendix	Figure
4	**4.2**	C	4.6, 4.7, C.3

  - Cyclic loading

Chapter	Section	Figure
4	**4.3**	4.9-4.17

    * Stress-strain hysteresis

Chapter	Section	Figure
4	**4.3.2**	4.6, 4.9-4.14

    * Modulus degradation

Chapter	Section	Figure
4	**4.3.3**	4.7, 4.9-4.14, **4.15**

    * Strain ratchetting

Chapter	Section	Figure
4	**4.3.2**	4.7, 4.9-4.14

    * S-N behavior

Chapter	Section	Figure
4	**4.3.4**	4.16, 4.17

  - Ceramic composite systems

    * SiC/CAS

Chapter	Section	Figure
4	4.1-4.3	4.1-4.11, 4.13, 4.14, 4.16

    * SiC/CAS-II

Chapter	Section	Figure
4	4.1-4.3	4.2, 4.10, 4.12

    * SiC/1723

Chapter	Section	Figure
4	4.1-4.3	4.2, 4.15, 4.17

- Analysis

  - Model Formulation

    * Quasi-static loading

Chapter	Section	Appendix	Figure
1, **3**	1.3, 2.4, **3.1.3**	I	2.8, 3.8-3.10, I.3

    * Repeated loading

Chapter	Section	Appendix	Figure
1, **3**	1.3, 2.2.3, **3.1.3**, C.2.2	**C**	2.4

    * Cyclic loading

Chapter	Section	Appendix	Figure
1, **3**	1.3, 2.2.3, **3.1.3**	C, H	2.5

      · Stress-strain hysteresis

Chapter	Section	Appendix	Figure
1, **3**	A.6.2.2, B.3	A, B, **C**, D	2.5, B.4

      · Modulus degradation

Chapter	Section	Appendix	Figure
1, **3**	A.6.2.1, B.3	A, B	B.4

      · Strain ratchetting

Chapter	Section	Appendix	Figure
1, **3**	**3.3.3.1**, A.6.2.3, B.3	A, B, **H**	2.5, 3.18, 3.19, B.4

      · S-N behavior

Chapter	Section	Appendix	Figure
1, **3**	**3.3.3.2**, A.6.2.4, B.3	A	2.5, B.4, B.5

  - Failure Criteria

    * Matrix cracking

Chapter	Section	Appendix	Figure
1, **3**	**3.2.1**, E.1, E.3	**E**, I	3.13, E.6, E.8, E.11, E.14

    * Interfacial debonding

Chapter	Section	Appendix	Figure
1, **3**	**3.2.2**, F.5	F	3.14, C.2

    * Fiber fracture

Chapter	Section	Appendix	Figure
1, **3**	**3.2.3**, F.2	**F**, I	4.1, 4.2

- Validation

  - Quasi-static loading

Chapter	Section	Figure
5	**5.1**	3.11, 3.12, 5.1-5.5, 5.7, 5.8

  - Repeated loading

Chapter	Section	Figure
5	**5.2**	5.9-5.11

  - Cyclic loading

Chapter	Section	Figure
5	**5.3**	5.12-5.22

    * Stress-strain hysteresis

Chapter	Section	Figure
5	**5.3.1**	5.9, 5.11-5.13

    * Modulus degradation

Chapter	Section	Figure
5	**5.3.2**	5.14-5.16

    * Strain ratchetting

Chapter	Section	Figure
5	**5.3.1**	5.9, 5.11-5.13

    * S-N behavior

Chapter	Section	Figure
5	**5.3.3**	5.19-5.20

  - Ceramic composite systems

    * SiC/CAS

      · $[0_3/90/0_3]$

Chapter	Section	Figure
5	5.1, 5.3	5.1, 5.4, 5.7, 5.15, 5.17

      · $[0_3/90_2/0_3]$

Chapter	Section	Figure
5	5.1	5.4

      · $[0_3/90_3/0_3]$

Chapter	Section	Figure
5	5.1-5.3	5.1, 5.4, 5.7, 5.11, 5.16, 5.18

      · $[0/90/0/90/0/90/0/90/0]$

Chapter	Section	Figure
5	5.1, 5.3	5.2, 5.8, 5.19

· $[0/90]_{2s}$

Chapter	Section	Figure
5	5.1-5.3	5.3, 5.9, 5.10, 5.12-5.14

* SiC/1723

· $[(0/90)_3]_s$

Chapter	Section	Figure
5	5.1, 5.3	5.3, 5.16, 5.20

VII. Recommendations

This chapter provides several suggestions for further work in the present topic area. The majority of recommendations are natural extensions of the current doctoral research.

7.1   General Recommendations

It is clear that the development of a *fundamental* theory which can be used to analyze the behavior of a ceramic matrix composite of arbitrary ply orientation and under all possible (multi-axial) loading conditions would be of great utility. Moreover, the present research is presented as a first step in this direction; however, there is still much to be done. Two natural extensions of the current work include the investigation of thermal/mechanical fatigue loading and the behavior of off-axis lamina under uniaxial loading. If successfully completed, multiple dimensions, instead of the one-dimensional shear-lag analysis, should then be considered and finally, a general state of loading may be incorporated in the analysis.

As mentioned, the current analysis investigates the behavior of CMCs under room temperature conditions. Incorporating temperature effects, whether due to isothermal or thermal/mechanical fatigue will most likely require some modifications to the current analysis in order to account for time/temperature dependent material properties, as well as the oxidation effects along the fiber/matrix interface [23, 29, 30, 51, 101, 108, 192]. In general, the latter can be handled by allowing the interface parameters τ_i and τ_{ult} to be time and temperature dependent. Furthermore, because of the assumed critical matrix strain energy criteria, the degradation in the composite constituents due to time, temperature and fatigue may be modeled via adjustments in the critical strain energies, i.e. $U_{cr_m}(t,\ \Delta T,\ N)$ and $U_{cr_f}(t,\ \Delta T,\ N)$[†] [42, 74, 95, 165, 190, 204]. This would permit the development of additional damages. Empirical

---

[†]t: time

or semi-empirical relations would most likely need to be developed. Also, when varying ply orientation, the critical energies may become a function of the fiber angle, θ, e.g. $U_{cr_m}(\theta)$. Hopefully, the critical strain energies for off-axis plies could be estimated much in the same manner as presented in chapter five of this document for the cross-ply laminates. That is, the critical energies for multi-angled laminates are a function of the critical energy of the unidirectional lamina, e.g. $\sigma_{cr}^{45} = \varrho \cdot \sigma_{cr}^{0}$ where $0 \leq \varrho \leq 1$. Analysis of two-dimensional woven composites might also be considered [105].

Because of the failure criteria used in the current analysis, the present model formulation may be extended to consider a multi-dimensional unit-cell in which the off-axis (transverse) behavior of the laminate may be included. This would permit the examination of multi-axial loading, as well as the incorporation of Poisson's effects into the analysis. Some work in this area has been accomplished and, in particular, the development of transverse strain in a unidirectional laminate has been successfully modeled. Such data are also important for investigating *longitudinal splitting* in ceramic matrix composites. The analysis is similar to that derived by Robertson and Mall for metal matrix composites [159]. The micromechanics solution can then be embedded into classical laminate plate and finite element schemes to consider the behavior of a general ceramic matrix *component* under arbitrary conditions of loading [1, 2, 136, 160].

7.2 Estimation of Interface Properties

The variables τ_i, τ_{ult} and $\tau_i(N)$ are influential parameters and appear in most failure criteria and constitutive laws governing the behavior of ceramic matrix composites and, therefore, accurate representations of these parameters are critical for the majority of numerical analyses. Unfortunately, empirical estimates of the interface (frictional) resistance (τ_i); the ultimate shear strength (τ_{ult}), and the degradation of the interface shear [$\tau_i(N)$] are difficult to obtain and are unreliable. As a result,

many numerical models have been used to approximate these parameters, including estimates based on empirical fits of stress-strain, stress-strain hysteresis, elastic modulus, strain ratchetting, and S-N data. The current model may also be used to estimate the interface properties by matching the experimental data. It is important to recognize that both the macromechanical (e.g. stress-strain) and micromechanical (e.g. crack density evolution) aspects of the composite behavior must be matched. As presented earlier and in appendix B, assessing the interface properties based on the macromechanical response only may prove inaccurate.

Another assumption employed in the current analysis is that the frictional resistance within any debonded regions is independent of location or the loading environment. In general, the frictional resistance will vary along the length of the composite. Moreover, the interface shear, τ_i, will depend on the loading direction (e.g. Poisson's effects) and the relief of thermal stresses across the fiber/matrix interface. The latter results from the development of constituent damages. For the current analysis, the interface shear, τ_i, is assumed to be a known lamina property, eliminating the need for further definition according to Eq. (7.1).

$$\tau_i = \mu_i \sigma_i^{th} \qquad (7.1)$$

In general, the interface stress, σ_i^{th}, may be estimated from the Lamé solution for thick concentric cylinders under uniform pressure loadings [188]. For each fiber/matrix cross-section, the pressure might depend on the thermal mismatch and the Poisson contractions. The latter changes sign with the loading direction.

The size and shape of the stress-strain hysteresis loops is of interest not only as an indicator of damage, but also in regards to energy dissipation and heat transfer. Kotil *et al* devised a numerical model for investigating the development of hysteresis along purely frictional interfaces [100]. It is recommended that a similar study be undertaken with the current analysis. By comparing predicted hysteresis with

experimental observations, much insight into the progression of debonding, d, and the degradation in interface shear, $\tau_i(N)$, can be obtained. Furthermore, the energy dissipated per unit volume, which is given by the area within the hysteresis loop, may be a reasonable indicator for the fatigue life of a given laminate [144].

The shape of the stress-strain hysteresis response for a ceramic matrix composite typically undergoes a variety of observable changes. Initially, during the first few cycles, the loops are typically "open" owing to variations in the frictional sliding and the formation of damages. As loading continues and damages evolve (and reach steady-state), the hysteresis loops close. Moreover, the shape of the loops are, on average, initially symmetric about a linear tangent drawn from one tip of the loop to the other (i.e. maximum strain to residual strain). However, at some point, believed to correspond with the onset of fiber failure, the symmetry is lost. The hysteresis loops then become "cusped" or "S-shaped" in appearance. The latter is typical of frictional joints under uniform pressure [60], indicating a *structural*, not material response. This may indicate complete debonding of the constituents.

The size (width) of the stress-strain hysteresis loop may also vary extensively during the fatigue cycling. In general, the loop width increases during the initial cycles due to the development of microstructural damages. Eventually, as the interface wears, the loop width may decrease. In some cases, the width vanishes and the response becomes essentially a linear line. Each of these configurations may be generated from the current analysis. Hence a detailed comparison of the origins of hysteresis might prove appropriate.

7.3 Damage Progression

The evolution of transverse and matrix cracks is fairly easy, albeit tedious, to obtain. Unfortunately, the same is not true with interface debonds and fiber fractures. Currently, there is no accurate procedure for measuring these damages.

To date, the best approach seems to be acoustic emissions; however, the confidence in identifying specific causes of "a.e. hits" is low.

The initiation and evolution of fiber fractures could possibly be determined more accurately by a series of tests in which a laminate is tested, and then immersed in a chemical solution which dissolves the matrix, but leaves the fibers intact. Such procedures have been used to determine the fiber volume fraction of a given composite. Once the matrix is removed, the fiber fractures could be counted. Of course, such a procedure is quite tedious especially since a large number of tests would be required to get a time-history representation of the fiber fracture process. Furthermore, the variability between specimens would introduce some uncertainty. Edge replication techniques for estimating the number of fracture fibers are questionable since the surface fibers are likely to be damaged during specimen preparation. In addition, the load carried by surface fibers will likely differ than for those in the interior since the fiber boundary conditions might be significantly different (e.g. surface fibers have a free boundary).

Estimating the extent of debonding presents even more problems due to the subtle nature of this failure mode. As a result, therefore, the debonding process will most likely need to be estimated numerically. If accurate assessments of matrix and fiber fractures can be obtained, it is reasonable to assume that any additional material compliance results from interface debonding. Furthermore, stress-strain hysteresis, frictional heating, and strain ratchetting could all be used to confirm the results.

7.4 Transverse Ply Stresses

Recall that the shear-lag formulation for the cross-ply laminate assumes that the stress in the transverse ply, $\sigma_t(x)$, is not altered by matrix cracks within the $0°$ plies. The validity of this assumption needs further examination. An alternative method is to superimpose known solutions. Unfortunately, satisfying the boundary

condition of all three entities (90° ply, fiber of the 0° ply and matrix of the 0° ply) is so difficult that it makes such a procedure impractical for a general damage state. Instead Eq. (7.2) is offered as an alternate solution.

$$\sigma_T(x) = \left\{ \left(\frac{F(x)}{2} \right) \left[\frac{1}{\sigma_{T_1}(x)} + \frac{1}{\sigma_{T_2}(x)} \right] \right\}^{-1} \qquad (7.2)$$

where $\sigma_{T_1}(x)$ and $\sigma_{T_2}(x)$ are solutions to known configurations and $F(x)$ is a function which ensures equilibrium is satisfied. The most obvious advantage of this approach is that the zero boundary condition along any fracture planes are satisfied. Further, if $\sigma_{T_1}(x) = \sigma_{T_2}(x)$, then $\sigma_T(x) = \sigma_{T_1}(x) = \sigma_{T_2}(x)$. An investigation which assumed that $\sigma_{T_1}(x)$ was the transverse stress which develops in a representative volume element (RVE) with only matrix cracks, and $\sigma_{T_2}(x)$ was the solution in a RVE with only transverse cracks ($L_T = L$) showed some improvement in modeling a RVE with co-planer transverse and matrix cracks. Further study is recommended. Alternatively, the solution from Nairn could be employed [138].

The constituent and lamina stresses are both dependent on the shear-lag parameters, β and λ, for the present analysis. Moreover, the formulation of these parameters is dependent on the assumed form of the two-dimensional constituent/lamina displacements (reference chapter three). Many relationships for these parameters have been presented in the literature. A few of which are provided below. Clearly, the problem will be dependent of the choice of β and λ, and therefore each of the relationships might be investigated.

The shear-lag parameter for the unidirectional analysis, β, was derived by Kuo & Chou and Daniel *et al* [40,106]. Daniel *et al* assumed that the shear stresses varied linearly in the fiber and by ($c_1/r^2 + c_2$) in the matrix where r is the radial coordinate and c_1 and c_2 are constant. Kuo and Chou also had a linear distribution within the fiber but the variation within the matrix was found to vary as $c_1(c_2/r + c_3 r)$ where c_1, c_2, and c_3 are again constant. The respective shear-lag parameters are shown

below for Kuo & Chou and Daniel *et al*, respectively.

$$\beta^2 = \frac{8}{r_f{}^2} \frac{E_1}{E_f E_m v_m} \left[\frac{1}{G_f} + \frac{1}{G_m} \left(\frac{2}{v_m{}^2} \ln \frac{1}{v_f} - 3 - 2\frac{v_f}{v_m} \right) \right]^{-1} \qquad (3.48)$$

$$\beta^2 = \frac{2E_1}{v_m r_f E_f E_m} \left\{ \frac{r_f}{4G_f} + \frac{1}{G_m} \left(\frac{2}{3} \frac{v_f(r_f - R)}{(1 - v_f)^2} (4 + (r_f/R) + v_f) + \frac{r_f(1 + v_f)}{1 - v_f} \right) \right\}^{-1} \qquad (7.3)$$

Both parameters are based only upon the basic constituent properties and the laminate geometry.

Several expressions for λ have also been proposed. Some of these are given below [112, 118, 168].

$$\lambda^2 = \frac{G_o}{d_o} \frac{dE_1 + dE_2}{dbE_1 E_2} \qquad (7.4)$$

$$\lambda^2 = \frac{3G(bE_1 + dE_2)}{bd^2 E_1 E_2} \qquad (7.5)$$

$$\lambda^2 = \frac{3G_{13} G_{23}}{(bG_{23} + dG_{13})} \frac{(bE_1 + dE_2)}{bd E_1 E_2} \qquad (7.6)$$

For the current analysis,

$$\lambda^2 = \mathcal{H}_x \frac{E_c}{E_1 E_2} \frac{b + d}{bd}. \qquad (3.76)$$

For the above equations, G_o and d_o are the shear modulus and the thickness of an assumed interlaminar shear region [118], and G is the shear modulus of the transverse ply.

7.5 *Computer Code/Numerical Algorithms*

When developing the Fortran code, limited foresight was given to computational efficiency, and therefore one area for improvement lies in the reformulation of the computer code itself. The procedures for calling subroutines; passing variable, and looping are areas for possible improvement. The largest gain in efficiency,

however, will most likely come from the reformulation of the numerical/convergence algorithms used in conjunction with the failure criteria. For example, in the cross-ply analysis, the transverse crack spacing, L_t; the matrix crack spacing, L, and the debond lengths, d_l and d_r, must all be determined simultaneously. Furthermore, the solutions are coupled. Several CPU run times are shown in Table 7.1. Results are shown for a Sparc 10. For the unidirectional laminate, $\sigma_{max} = 280$ MPa and $\mathcal{R}$=0.0714. The CMC material is SiC/CAS. The results in Table 7.1 for the cross-ply laminate are for a $[0_3/90/0_3]$, SiC/CAS laminate with σ_{max}=250 MPa and $\mathcal{R}$=0.08.

Table 7.1   CPU run time (sec) for various loading cycles (N)

	unidirectional				cross-ply		
N	1	10	20	50	1	10	20	50
sec	6.9	9.8	12.3	19.0	74.2	342.5	641.9	1548.5

Currently, only rudimentary convergence algorithms are employed. It is possible that better techniques exist. Under the present formulation, at any stress increment, n, an initial guess for a damage parameter, say $p \in \{L_t,\ L,\ d_l,\ d_r\}$, is obtained based upon the previous trends, e.g. $p_n = p_{n-1} + \Delta p_{n-1}$. Convergence is then sought based upon the specific failure criteria. For example, under the maximum stress criterion for debonding, the parameter p is adjusted according to the relative magnitude of the maximum interface shear stress to the interface shear strength according to

$$p_i = p_{i-1} + \mathcal{V}_i \left(\frac{\tau_{i_{max_i}} - \tau_{ult}}{\tau_{ult}} \right), \tag{7.7}$$

whereas under the critical matrix strain energy criterion

$$p_i = p_{i-1} + \mathcal{V}_i \left(\frac{U_{m_i} - U_{cr_m}}{U_{cr_m}} \right). \tag{7.8}$$

The variable $\mathcal{V}$ is an adjustable parameter to speed the rate of convergence. The slip distances y_l, y_r, z_l and z_r are also determined in a similar manner.

Separate from the convergence schemes, a few numerical integration algorithms are used. These appear in the cross-ply analysis and are used to determine the constituent strain energies, U_f and U_m, and the laminate strain, ϵ. Currently *Newton-Cotes* formulae are employed with no apparent problems. However, the resulting error has not been calculated. Moreover, alternate solutions might be sought.

Appendix A. Fracture in Brittle Non-Homogeneous Media

This appendix details the fracture processes associated with ceramic matrix composites, including discussions on fracture in brittle homogeneous materials; toughening mechanisms associated with fiber-reinforcement, and the role of the fiber/matrix interface on the progression of damages and load transfer. Also several failure criteria common to brittle composites are reviewed. The purpose of the latter is to provide a general introduction to some of the more traditional failure criteria, as well as to make apparent some of the advantages and disadvantages of these classical solutions. In addition, the discussion should familiarize the reader with some of the basics on model formulation. In doing so, this appendix acknowledges that even though thorough understanding of fracture in brittle materials is important, the main objective of this study is to capture the residual *laminate* properties (e.g. residual strength and modulus) which are defined by the *macromechanical* behavior observed in the stress-strain response. The specific details of a single fracture propagating around a bi-material interface are not the focus of the current investigation; rather only to determine an equivalent damage state which yields the desired laminate response.

A.1 Introduction

Monolithic ceramics may be toughened with the incorporation of small diameter reinforcing fibers which maintain some assemblage of integrity in the ceramic despite the evolution of multiple cracks within the ceramic matrix [140, 169]. The fibers aid in load transfer, reduce crack-tip stress intensities by producing closing tractions across crack planes, and also induce energy dissipating mechanisms which reduce the propensity for the creation of additional damages (chapter two). These effects are what provide ceramic matrix composites (CMCs) with their exceptional toughness and non-catastrophic failure mode. Moreover, the characteristics of the interface influence the ability of the fibers to transfer load and dissipate energy. If

the constituents are strongly adhered, stresses are readily transferred between the constituents such that the probability of fiber fracture is enhanced as large crack-tip stresses are transferred to the fiber. Weaker interfaces (e.g. frictional) reduce the latter effect, but also decrease the utility of the fibers. The interface strength can be optimized to maximize toughness. This appendix examines both toughening and interface design in CMCs. First, however, fracture in ceramics and ceramic composites is investigated. The purpose is to familiarize the reader on not only the reasons for why cracks propagate so readily through ceramic materials, but also on what can be done to prevent it.

A.2   Fracture of Ceramic Materials

Figure A.1 illustrates a penny-shaped crack within a homogeneous linear-elastic medium. The well-known expression for the stresses in the vicinity of the crack tip
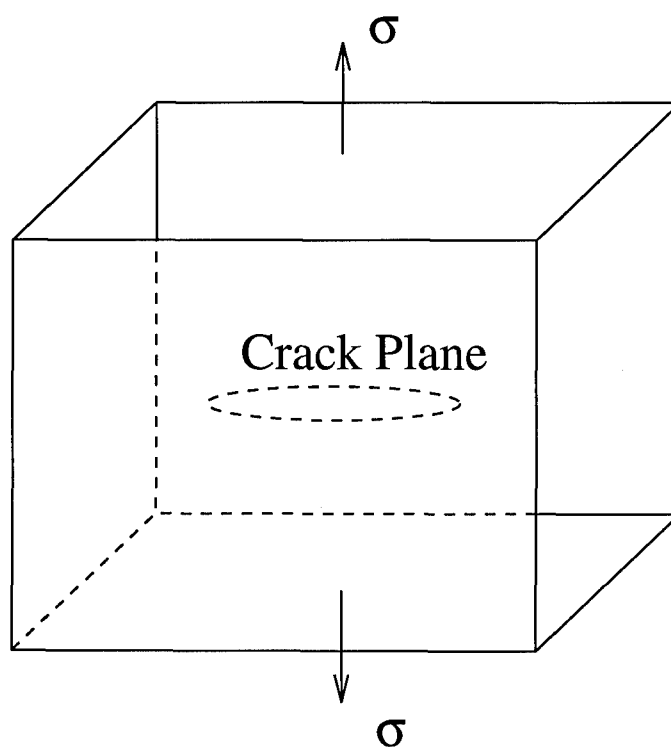
Figure A.1   Penny-shaped crack in a homogeneous medium.

is given by Eq. (A.1) where r and θ are the radial and circumferential directions illustrated in Fig. A.2.

$$\sigma_{ij} = \frac{K}{\sqrt{2\pi r}} f_{ij}(\theta) \qquad (A.1)$$

The parameter K is the crack-tip *stress intensity factor*, and $f_{ij}(\theta)$ is a function of the angle θ and is typically dependent on the material geometry and loading condition. For a stress-free crack in an infinite plate, for example, $K = \sigma_\infty \sqrt{\pi a}$ where σ_∞ is the far-field applied stress and a is the crack length. For a material free of any prominent fractures, a is the average microstructural flaw size.
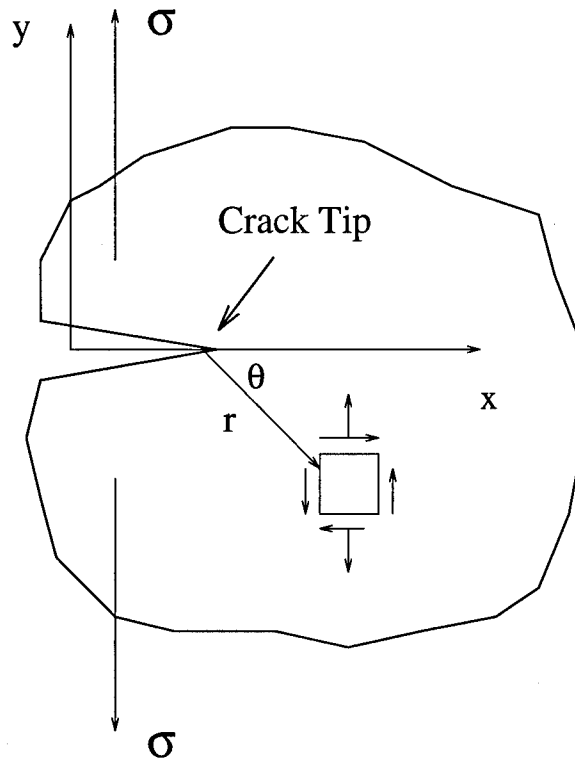
Figure A.2   Crack-tip stresses in an arbitrary body.

For linear-elastic materials, fracture occurs when the stress intensity factor K attains a critical value K_I^c which is the *mode I fracture toughness* of the material. That is, *crack growth occurs when* $K \geq K_I^c$. For conditions of plane strain, K_I^c is a material constant and is dependent on the surface energy, γ_m, associated with the

molecular bonding in the material of interest. In particular,

$$(K_1^c)^2 = \frac{E g_m^c}{1 - \nu^2} \qquad (A.2)$$

where $g_m^c = 2\gamma_m$. The parameter g_m^c is known as the *critical strain energy release rate* and has units of N/m. Hence, in accordance with Eq. (A.2), the fracture criterion in Eq. (A.1) also be expressed in terms of energy, i.e.

$$\sigma_{ij} = \sqrt{\frac{E g_m}{2(1 - \nu^2)\pi r}} f_{ij}(\theta) \qquad (A.3)$$

where $g_m = K^2/E$. As before, crack growth occurs whenever $g_m \geq g_m^c$. The variable g_m is the crack-tip *energy release rate*, and in general varies with loading and the fracture geometry. As with K_1^c, g_m^c is a material constant.

The subscript 1 in K_1^c indicates that the crack propagation results from a pure mode I opening (Fig. A.3). In general, the motion of the crack surface relative to the loading axis can be described by three orthogonal components of a global system of coordinates. In practice, therefore, K is divided into three cracking modes which are then superimposed to describe a general state of fracture. Stresses normal to the crack plane produce mode I *opening*; in-plane shear results in mode II *sliding*, and out-of-plane shear yields mode III *tearing* (Fig. A.3). Deformations resulting from application of more than one mode are referred to as *mixed mode*. For the present analysis, only mode I deformations are considered. As a result, all crack growth is orthogonal to the loading axis.

Cracks propagate readily in ceramic materials because of their low fracture toughness, K_1^c. In fact, K_1^c for a ceramic is typically much smaller (by an order magnitude or more) then for say a ductile metal. As an example, K_1^c for a silicon carbide ceramic falls between 2 and 5 MPa/$\sqrt{m}$. This is compared to 50 MPa/$\sqrt{m}$ for a low carbon steel, and 100-300 MPa/$\sqrt{m}$ for copper and aluminum [25]. Furthermore, because of the low fracture toughness of ceramic materials, once a crack

Mode 1	Mode 2	Mode 3
Opening mode	Sliding mode	Tearing mode
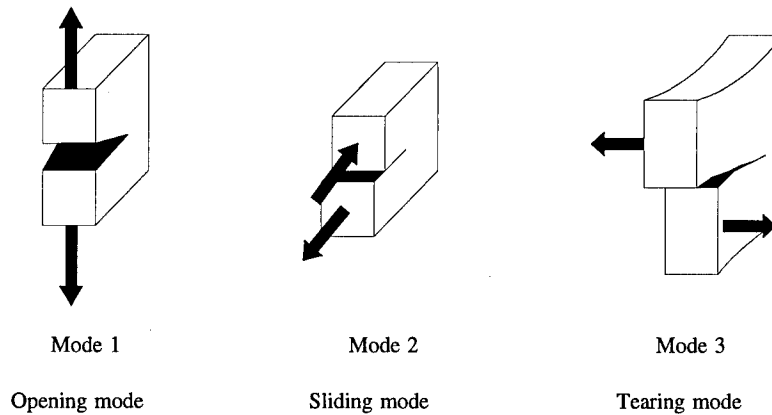
Figure A.3   Crack displacement modes.

begins to propagate, the stress intensity at the crack tip remains larger than the material fracture toughness (i.e. $K > K_I^c$) and the crack continues to grow. In most metals, on the other hand, local plasticity effects tend to lower the stress intensity factor such that $K < K_I^c$ and the crack propagation ceases. Hence, the fracture process in brittle materials may also be improved by either reducing the crack-tip stress intensity, K, or by increasing the material fracture toughness, K_I^c. Both avenues continue to be aggressively pursued. The latter is accomplished through the reduction of material imperfections and is associated with improvements in the manufacturing process. Fiber reinforcement, on the other hand, reduces the impact of the matrix failure. One consequence, however, is that multiple fractures form within the composite matrix prior to laminate failure.

Unlike polymer based (PMCs) or metal-matrix composites (MMCs) in which the progression of damages has been fairly well characterized, fracture in brittle com-

posites is a less mature area, stochastic in nature, and sensitive to many parameters (material imperfections, stress concentrations, etc). Microstructural damages can, of course, develop within PMCs and MMCs, however, neither PMCs nor MMCs are dominated by the deluge of critical microstructural flaws as with ceramic composites. For CMCs, the ratio of the fiber modulus to the matrix modulus for CMCs is typically of order one, compared to 10 or 100 for PMCs and MMCs. In addition, the functionality of the fiber in CMCs is fundamentally different than with these other types of composites. For example, the reinforcing fibers in CMCs are not the main load bearing member. Instead, bridging fibers maintain the integrity of the composite in spite of extensive matrix cracking. The additional toughening allows CMCs to be used for a number of applications.

Because of their thermal and wear properties, CMCs are ideal materials for components such as dies and tool bits, seals, nozzles, grinding wheels, and brakes. However, CMCs are also finding their way into many diverse industries. For example, ceramic composites are not only used in aircraft structures, rocket nozzles, and turbine engines, but also in armor plating, missile radomes, pressure sensors, and even artificial teeth and heart valves; [73] proving that CMCs are viable candidates for a wide range of applications over large temperature regimes. In addition, as with most composites, CMCs offer the promise of providing significant weight savings for many structural components. Automotive engines, for example, could not only be designed to run hotter, but also to be lighter in weight. This could result in a significant savings in the specific fuel consumption. However, as with many advanced materials, design and manufacturing cost is an important consideration [191].

The market size for aerospace and defense related applications of ceramic composites is projected to approach five hundred million dollars a year by the year 2000 [187]. The United States government has already invested approximately a quarter of a billion dollars in research and development of ceramic matrix composites over the period of 1979 to 1989 [128]. However, a survey conducted by the

Department of Defense (DOD) Ceramics Information Analysis Center (CIAC) concluded that although the funds appeared to have been invested wisely, the life of CMC components when subjected to fatigue loadings could not be adequately predicted due to the lack of available models [148]. The objective, in many cases, is to model the macromechanical behavior of the composite material with emphasis on accurate predictions of the residual strength, stiffness, and life cycle. Hence, modeling the laminate's stress-strain response is desired. This, however, calls for an estimate laminate's damage progression, and therefore, some focus of the laminate's micromechanical behavior is in order.

Prior to laminate failure, as damage forms within the composite, the material's compliance gradually increases. This produces the non-linear stress-strain behavior observed during experiments (Fig. A.4). The increased compliance can be estimated from simple one-dimensional models if the average number of cracks can be determined [115]. Unfortunately, the most common technique of estimating the crack
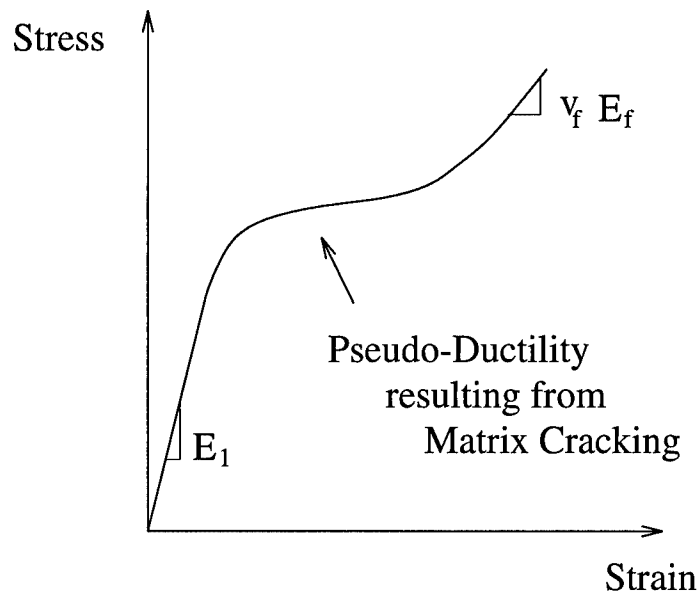
Figure A.4   Stress-strain response of a ceramic matrix composite.

density is to manually count the cracks. This is accomplished by examining acetate replicas of the composite surface obtained during experimental tests of the laminate.

This typically involves interrupting the test and pressing a piece of acetate on one face of the composite to obtain a reproduction of the composite surface. The tests are usually stopped during a tensile portion of the loading cycle so that the crack openings are more apparent. The acetate replica is examined under a microscope and the average crack density is estimated by manually counting the cracks. This can be quite a tedious process especially to get a time history representation of the crack density progression since the process must be accomplished a number of times. Other problems with this approach are that the representative damage is limited to only the surface damage appearing on the outer edge of the specimen, and that discrepancies in the data may result if different techniques are used to count the cracks. For example, how long does a fracture need to be before it constitutes a matrix crack? Also, even if the matrix crack density can be determined, the number of fiber fractures and the extent of interface debonding are almost impossible to determine. This is not only because of the relative size of the crack openings, but also because for these damage modes, in particular, the extent of damage is likely to differ significantly from the surface damage captured on the replica. For these reasons, estimating or verifying the extent of damage within brittle composites is certainly an inexact science.

There are, of course, alternate techniques for gathering crack density data [13, 48, 98, 193, 199]. For example, the information may be obtained optically using a highly magnified lens [199]. In addition, since matrix breaks are audible, the crack density may be estimated using acoustic sensors [193]. In some cases, acoustic emissions have been used to gather information on matrix cracking, fiber fracture and even interface debonding. The various damage modes can be differentiated by the strength (i.e. decibel level) of the the emission.

A.3 Toughening Mechanisms

In order to appreciate the details of the stress-strain (macroscopic) response, a better understanding of the fracture and toughening mechanisms which dictate the shape of the curve is required. These are now reviewed, and should provide some insight into the requirements and potential difficulties in modeling the rather benign response illustrated in Fig. A.4.

In the early 1900's, Griffith investigated the fracture characteristics of brittle materials [61]. He is best known for the development of an energy equilibrium criterion which states that *crack propagation will occur in a brittle homogeneous material if the energy released upon crack growth is sufficient to provide all the energy required for crack growth* [43]. An important consequence is that crack growth may be slowed or even arrested if energy used to propagate the fracture can be dissipated.

The Griffith criterion has been recently shown to be applicable to brittle non-homogeneous materials [129]. This has led to a better understanding of multiple matrix cracking in CMCs. As matrix cracks advance toward and envelop embedded fibers, a number of events can take place. For example, if the fiber and matrix are physically (i.e. chemically) bonded to one another, the large stress fields near the crack tip can cause the constituents to debond. Since this debonding process reduces the energy available to propagate the main fracture, *interface debonding contributes positively toward toughening of the composite.* If the interface debonds and the fiber remains intact such that the fiber continues to bridge the crack plane, energy will be dissipated as the matrix slides along the fiber since the crack opening displacement must increase in order for the crack front to advance. This *frictional sliding also contributes toward toughening.* In fact, frictional heating within debonded regions is one of the primary toughening mechanisms. Hence, it is advantageous to have the fiber continue to bridge the crack plane since this not only increases the heat loss, but also as mentioned earlier, bridging fibers provide closing tractions which tend to

reduce the crack-tip stress intensities [127]. However, the fibers do not always bridge the crack plane.

Consider a single crack as it propagates across the laminate microstructure (Fig. A.5). As a crack advances toward a fiber, the fiber may break, pull out, or
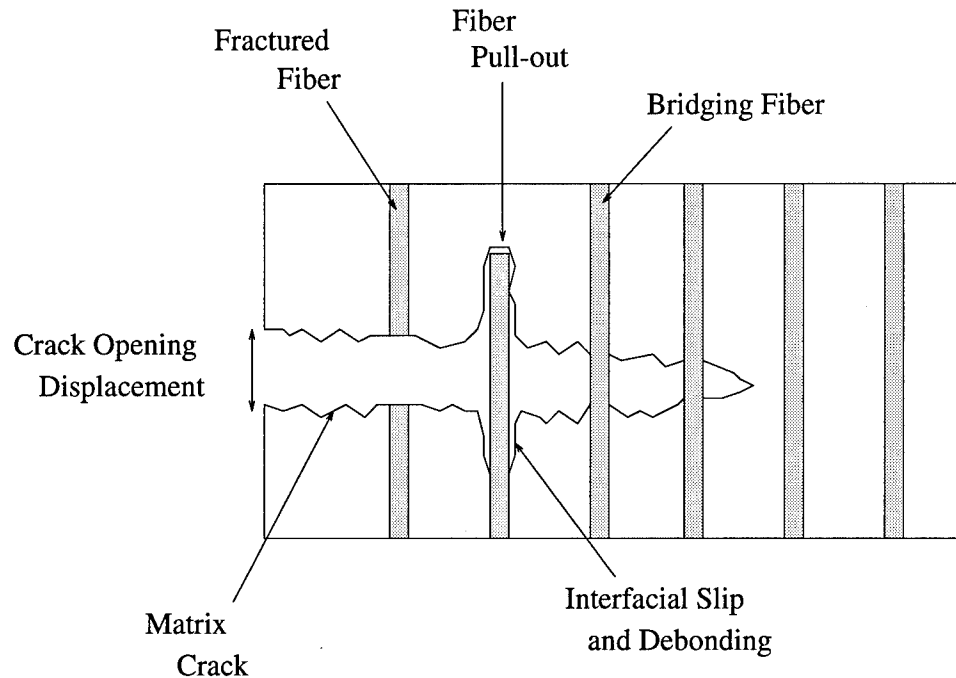
Figure A.5   Failure mechanisms within ceramic matrix composites.

continue to bridge the matrix. Which of these events takes place is largely dependent on the "strength" of the fiber/matrix interface. If the interface is too tight, the large crack-tip stresses are easily transferred to the fiber and the crack propagates through the fiber (i.e. fiber fracture). If, on the other hand, the interface is loose, the fiber may debond and pull free from the matrix. In general, this process (fiber pull-out) may be a large contributor to the material's toughness due to potentially large frictional forces; however, if the interface is too weak little energy is dissipated since the frictional sliding is negligible. In both cases (extremely weak or strong interfaces), no appreciable improvement in the mechanical properties of the composite is realized. Fiber failure, for example, releases only a small amount of energy equal to the stored

elastic energy in the fiber. Further, after pull-out or failure, the fiber no longer effectively contributes to the strength of the ceramic.

If the interface is properly designed, the percentage of fibers which continue to bridge the crack plane can be enhanced. This promotes toughness through load transfer and continued frictional energy losses. Hence, "tuning" the interface strength though proper design and manufacturing is a very important area of research in composite engineering. Furthermore, because of this ability to tune material properties, such as in the case with CMCs, there has been a fundamental change over the past thirty years in how material engineering is approached. In the past, materials were simply *applied* to structural components. Today, through improved understanding of material science, advanced materials are able to be *designed* for specific applications. Ceramic matrix composites represent an excellent example of the change in philosophy. Tuning the strength of the interface in order to obtain the desired lamina properties is covered in the next section.

A.4   Interface Design

Design of composite materials not only includes optimizing the *laminate* by adjusting the interlaminar properties (e.g. ply orientation, stacking sequence), but also includes the optimization of *lamina* properties. Hence, improvements in both the strength and failure characteristics of the individual plies are desired and can be accomplished, in large part, by controlling the properties along the fiber/matrix interface. The latter is accomplished primarily by two techniques: (1) by adjusting the residual stresses across the plane of the interface and (2) through the application of interface coatings.

During processing, residual thermal stresses develop normal to the interface due to the mismatch in the coefficients of thermal expansion between the fiber and matrix. For most CMCs, the thermal coefficient of the matrix is greater than that

A-11

of the fiber (i.e. $\alpha_m > \alpha_f$). This creates a residual compressive stress across the interface which can be adjusted to optimize the frictional energy dissipation.

An alternate means of adjusting the strength of the interface is through the use of different interface coatings. During processing, a chemical reaction occurs between the constituents which forms a thin (10 nm) carbon layer which helps to weaken the interface [87]. Manufacturers often add coatings to the fiber to enhance the result [80, 114, 120, 122]. Carbon and silicon carbide are common coatings used in the design of CMCs. Unfortunately, the application of the coating is a complex procedure since the carbon *interphase* can oxidize and form a continuous silica layer under elevated temperatures [5]. This reaction can result in an undesirable increase in the interface strength which has been found to decrease the composite toughness by up to two-thirds [6]. If properly designed, however, the effects of oxidation can be reduced [30, 131, 166].

Although the strength of the interface is somewhat easy to control, quantifying the strength of the interface can be quite difficult. Typically, two parameters are used: the maximum interface shear strength associated with bonded fiber/matrix regions, τ_{ult}, and the interface shear within debonded regions, τ_i. The latter is assumed to be constant along the debonded region, and governed by Coulomb friction according to

$$\tau_i = \mu_i \sigma_i^{th} \tag{A.4}$$

where μ_i is the friction coefficient between the fiber and matrix, and σ_i^{th} is the residual thermal stress across the interface.

There has been an extensive amount of research devoted to characterizing the parameters τ_{ult} and τ_i. Both experimental [55, 92, 93, 99, 135] and numerical [31, 37, 54, 55, 78, 121, 186] studies have been conducted. The most common experimental techniques are single-fiber *push-in* and *pull-out* tests; however, there is some question of the utility of such tests since these techniques induced unwarranted Poisson's

effects and also fail to account for crack-tip stress fields [167]. The numerical studies typically involve fitting empirical data. Since the interface controls so many of the characteristics of the CMC, a number of approaches are possible. The interface stresses τ_{ult} and τ_i can be estimated, for example, through curve fits of empirical crack density or stress-strain data [37], or by matching the shape and location of hysteresis curves [54] or the fatigue life diagrams (e.g. S-N behavior, modulus degradation) [176]. In general, each of the predominant damage modes, matrix cracking, interface debonding and fiber failure, is dependent on the interface properties. Several failure criteria governing the initiation and evolution of matrix cracks are now considered.

A.5 Existing Failure Criteria for Matrix Cracking

Two dominant failure criteria are present in the literature: maximum stress (strain) theories and the more traditional fracture mechanics approaches. The latter category including both the energy balance techniques (discrete solutions) of Aveston, Cooper and Kelly [8], as well as the stress intensity solutions (continuum solutions) similar to those proposed by Marshal, Cox and Evans [127]. The solutions from Aveston, Cooper & Kelly, and Marshal, Cox & Evans are typically referred to as the ACK and MCE theories, respectively. The theories presented in this section are divided into two categories: those which employ a maximum stress criterion and those using more traditional fracture mechanics approaches. However, as illustrated by the ACK solution, there can be some overlap between the two fields.

A.5.1 Maximum Stress Criterion.
The maximum stress criterion assumes that a new matrix crack will form whenever the matrix stress exceeds the ultimate strength of the matrix, $\sigma_{m_{ult}}$. Furthermore, the matrix strength is assumed to be single-valued and a known material property. Since under the micromechanics approach, the matrix cracks are assumed to be uniformly spaced throughout the composites, the maximum matrix stress is guaranteed to exist at the mid-spans of the existing cracks. Hence, new cracks form at locations equal-distance from adjacent

crack, and as such the composite's crack density doubles with their formation. For the unit-cell shown in Fig. A.6, for example, a matrix crack is assumed to form at a the axial coordinate $x = 0$ whenever, the peak stress at this location, σ_1, exceeds the matrix strength, i.e.

$$\sigma_1 \geq \sigma_{m_{ult}}. \tag{A.5}$$

Equation (A.5) is the failure criterion.
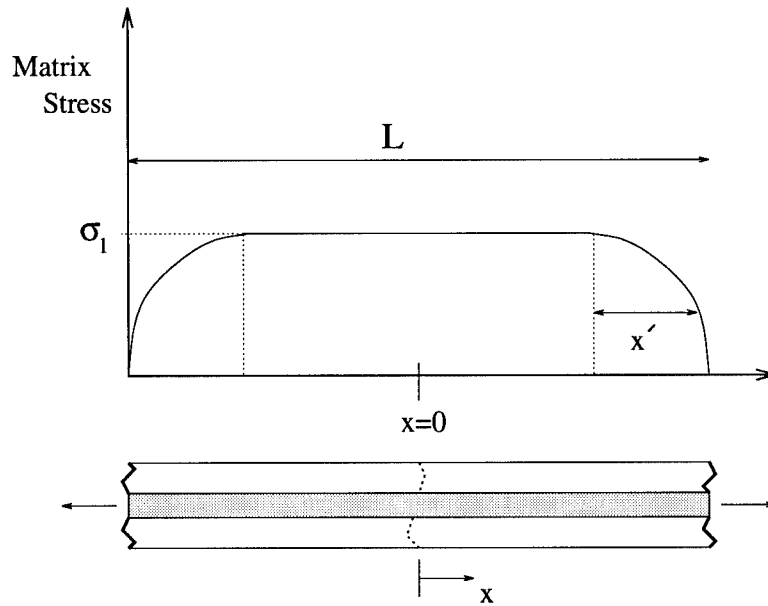
Figure A.6   Distribution of the matrix stress in a one-dimensional unit-cell.

For a moment, define some parameter x' which characterizes the distance it takes the stress in the matrix to go from zero along the plane of the matrix crack to a peak value of σ_1 [Fig. A.6]. If x' is small compared to the average crack spacing L, then once Eq. (A.5) is satisfied at $x = 0$ such that a matrix crack is allowed to form at this location, it is likely that Eq. (A.5) will be satisfied at a number of locations (e.g. $L/4$, $L/8$, etc) and that an extensive amount of matrix cracking will occur instantaneously. This concept is illustrated in Fig. A.7.

First assume that matrix crack spacing is L, and that the matrix stress distribution is as given by Fig. A.7 (a). In addition, assume that σ_1 is such that the

A-14
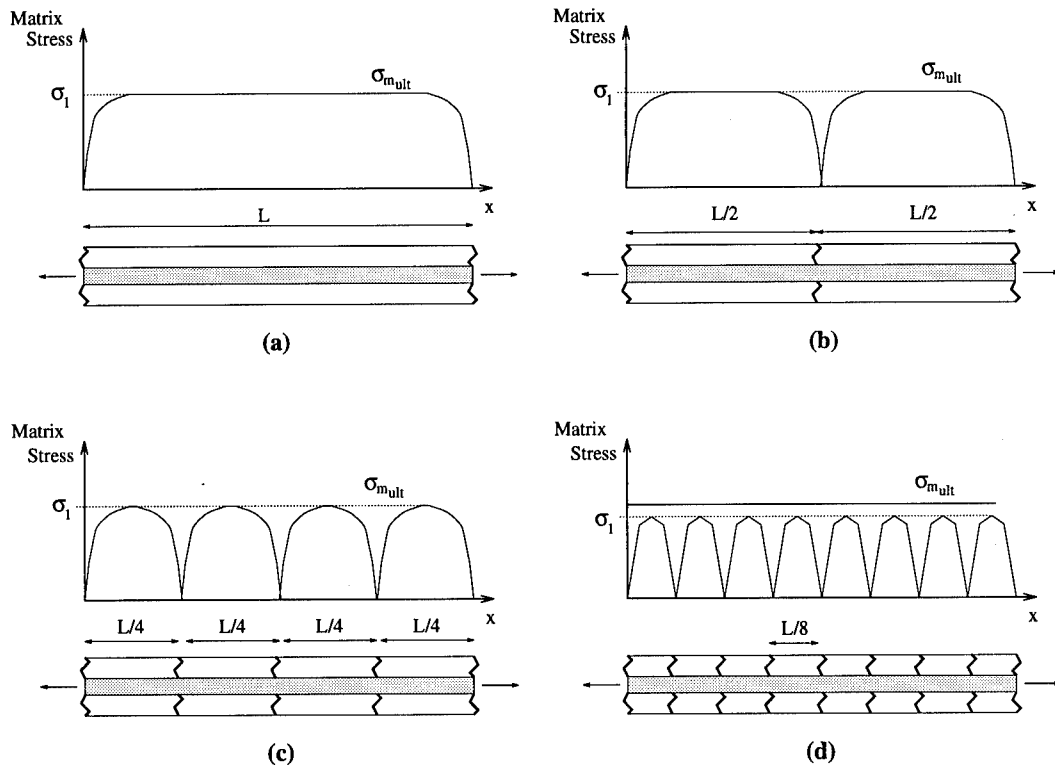
Figure A.7 Evolution of matrix cracks as predicted from a maximum stress criterion.

failure criterion is satisfied (i.e. $\sigma_1 = \sigma_{m_{ult}}$), and therefore, allows a new crack to form at the mid-spans of the existing cracks. Now consider the redistribution of stresses within the matrix [Fig. A.7 (b)]. Note that since x' is small compared to L, the stress in the matrix again reaches a peak value of σ_1, and therefore in accordance with Eq. (A.5), additional cracks are assumed to form [Fig. A.7 (c)]. This procedure would be repeated until Eq. (A.5) is no longer satisfied [Fig. A.7 (d)]. Note that Figs. A.7 (a) through (d) are assumed to occur instantaneously, and at the same level applied stress. This is one of the drawbacks of the maximum stress criterion: an extensive amount of cracking occurs at a single applied stress. Hence, the maximum stress criterion is not likely to capture the gradual evolution of matrix cracking observed experimentally. This results in a "stepped" stress-strain prediction rather

than a gradual non-linear deviation. A sketch of a *crack density versus applied stress* prediction and *stress-strain response* are illustrated in Fig. A.8.
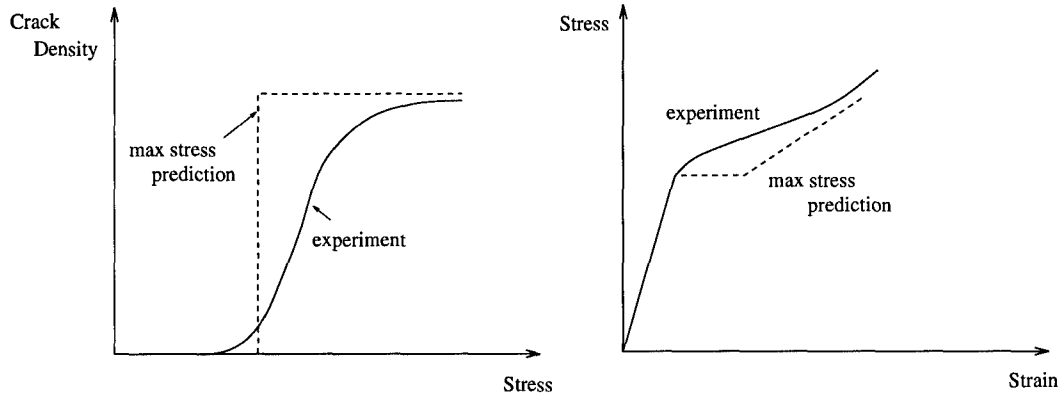
Figure A.8   Crack density and stress-strain evolutions based on a maximum stress criterion.

Aveston, Cooper and Kelly (ACK).   The maximum stress criterion was first applied to ceramic matrix composites by Aveston, Cooper and Kelly (ACK) [8]. Their analysis considers a unit-cell similar to that in Fig. 2.11 in which the fiber/matrix interface is assumed to be purely frictional; having a constant interface shear stress. Failure of the matrix is assumed governed by a single-valued matrix stress (strain), and the matrix cracks are assumed to be infinitely long and uniformly spaced. No fiber damage is considered. Thermal effects are also neglected.

The failure criterion employed by ACK assumes that matrix cracking occurs whenever the stress in the matrix, $\sigma_m(x)$, exceeds the ultimate strength of the matrix, $\sigma_{m_{ult}}$, i.e.

$$\sigma_m(x) \geq \sigma_{m_{ult}}. \tag{A.6}$$

Since the laminate is initially assumed to be free of any damage, the matrix stress $\sigma_m(x)$ has the same magnitude at all points in the unit-cell. Hence, once Eq. (A.6) is satisfied at a single point, it is satisfied everywhere. This results in an extensive amount of matrix cracking occurring instantaneously as previously discussed. In

A-16

addition, it should now be clear that $\sigma_{cr} = \sigma_{mc}$ and $L = L_{init} = L_{sat}$. Both parameters σ_{cr} and L_{sat} are determined by ACK. The formulation for L_{sat} is now presented whereas the derivation for σ_{cr} is presented in section 2.6.2.1 since it falls under the fracture mechanics approach.

For the analysis, consider the unit-cell shown in Fig. A.9, and assume that the applied stress is just sufficient to cause the fracture to form, i.e.

$$\sigma = \frac{E_1}{E_m}\sigma_{m_{ult}}. \tag{A.7}$$

It is known that along the plane of the matrix crack, the stress in the matrix vanishes at the free boundary and the fiber is forced to carry the entire load. Away from the crack plane, the load is redistributed between the constituents. Furthermore, in the ACK model the interface shear has been assumed constant such that the stress transfer is linear (Fig. A.9). The parameter x' represents the stress transfer distance or, equivalently, the distance over which the fiber/matrix constituents slip.[†]
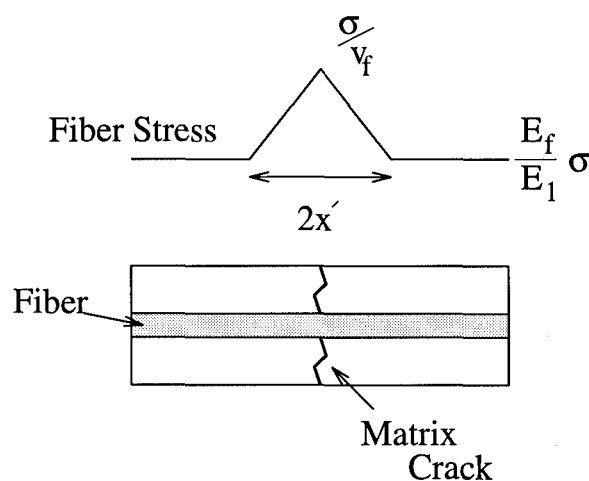
Figure A.9   Fiber stress near a matrix crack for a completely debonded interface.

[†]The *stress transfer distance* is the distance over which the presence of the matrix crack is felt. In particular, it is the distance away from a crack plane required for the matrix stress to return to its undamaged magnitude.

The *additional stress* in the fiber due to the presence of the fracture will vary from zero to a maximum of

$$\frac{\sigma}{v_f} - \frac{E_f}{E_m}\sigma = \frac{v_m}{v_f}\sigma_{m_{ult}} \qquad (A.8)$$

and the *additional strain* in the fiber due to the crack is

$$\bar{\epsilon}_f = \frac{\hat{a}}{2}\epsilon_{m_{ult}} \qquad (A.9)$$

where $\hat{a} = \{v_m E_m\}/\{v_f E_f\}$ and $\epsilon_{m_{ult}} = \sigma_{m_{ult}}/E_m$. Further, when multiple matrix cracks exist, the final crack spacing must satisfy

$$x' \leq L_{sat} < 2x' \qquad (A.10)$$

since upon completion of matrix cracking, the maximum stress in the matrix must be less than $\sigma_{m_{ult}}$. The matrix stress distributions for $L_{sat} = 2x'$ and $L_{sat} = x'$ are shown in Fig. A.10. In Fig. A.10 (a), the crack spacing is sufficient to allow the strain
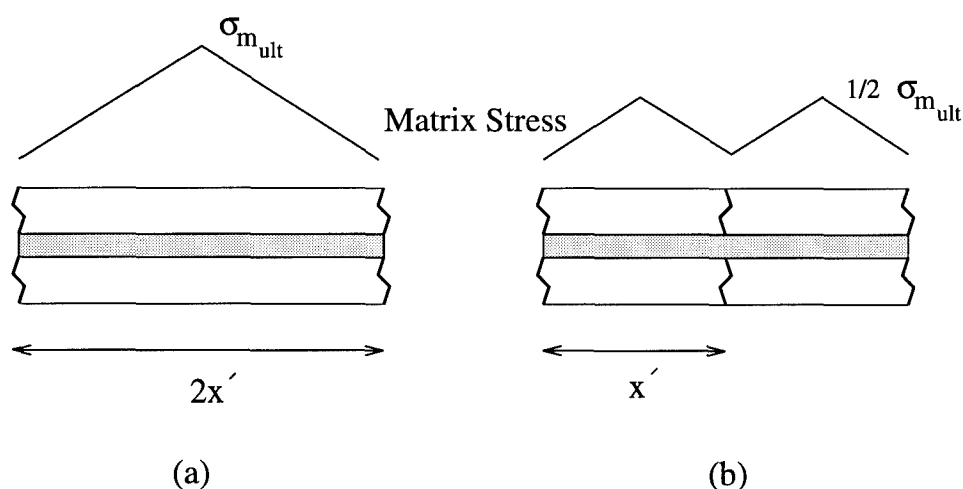
Figure A.10   Matrix stress for a completely debonded interface: limiting cases.

in the matrix to reach the strength of the material. Hence for this case, Eq. (A.6) is satisfied and additional matrix cracking would be allowed such that $L_{sat} = x'$. This

is the limiting case. From statistical theory, the final crack spacing can be expected to be $1.337x'$ [37].

From Fig. A.9, equilibrium along the plane of the crack requires

$$\sigma = v_f \left[\frac{\sigma}{v_f} - \frac{2\tau_i}{r_f} x' \right] + v_m \sigma_{m_{ult}}. \tag{A.11}$$

Hence, from Eq. (A.8),

$$x' = \frac{r_f}{2\tau_i} \frac{v_m}{v_f} \frac{E_m}{E_1} \sigma. \tag{A.12}$$

Finally, the additional strain in the fiber due to the matrix cracking is

$$\bar{\epsilon}_f = \frac{1}{2E_f} \frac{v_m}{v_f} E_m \epsilon_{m_{ult}} \qquad \text{for} \quad L_{sat} = 2x' \tag{A.13}$$

and

$$\bar{\epsilon}_f = \frac{1}{2E_f} \frac{3}{4} \frac{v_m}{v_f} \sigma_{m_{ult}} \qquad \text{for} \quad L_{sat} = x'. \tag{A.14}$$

Therefore, from Eq. (A.10), the additional fiber strain resulting from failure of the matrix can be shown to satisfy

$$\frac{3}{4} \hat{a} \epsilon_{m_{ult}} \leq \bar{\epsilon}_f < \frac{\hat{a}}{2} \epsilon_{m_{ult}}. \tag{A.15}$$

Since all matrix cracking has occurred at a single stress, the resulting stress-strain response is characterized by a *single step* as illustrated in Fig. A.11. Initially, the stress-strain response exhibits a stiffness of E_1. However, when the applied stress has a magnitude of $E_m \epsilon_{m_{ult}}$, matrix cracking occurs. This results in a single jump in strain satisfying Eq. (A.15). Beyond this stress, the stress-strain response is again linear; however since the matrix has failed so extensively, the composite stiffness approaches $v_f E_f$.
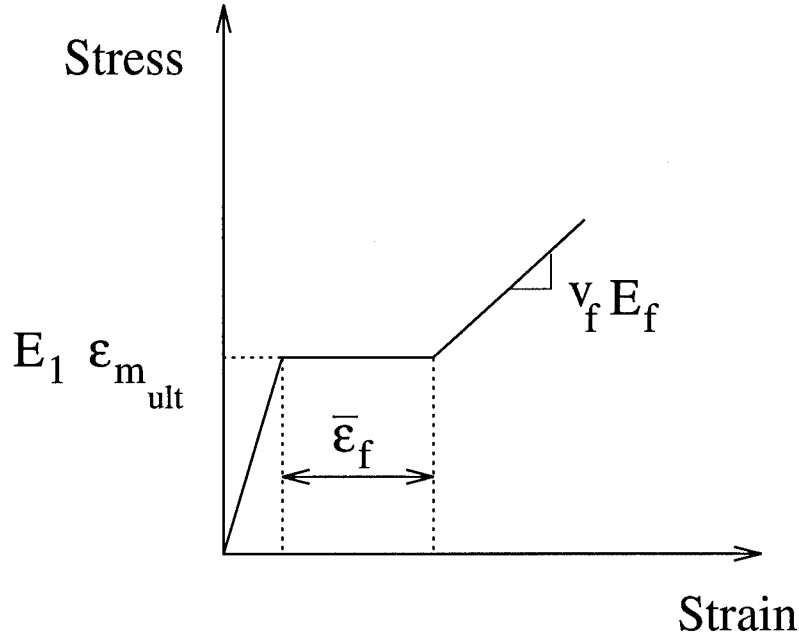
Figure A.11   Stress-strain prediction when matrix cracking is predicted from a maximum stress criterion.

Lee and Daniel.   Another model which employs a maximum stress criterion and provides closed-form solutions for the average matrix crack spacing was presented by Lee and Daniel [113]. Their model is based on a modified shear-lag technique and considered matrix cracking in a *partially bonded* unit-cell. Residual thermal stress fields are also considered in the analysis. As with the ACK model, the matrix is assumed to fail whenever the stress in the matrix exceeds the strength of the matrix material. Since thermal stresses are considered, the matrix is assumed to fail when

$$\sigma \geq \frac{E_1}{E_m} \left(\sigma_{m_{ult}} - \sigma_m^{th} \right) \tag{A.16}$$

where σ_m^{th} is the residual thermal stress in the matrix. In addition, for the shear-lag formulation presented by Lee and Daniel, the stress in the matrix is given by

$$\sigma_m(x) = \left(\frac{E_m}{E_1} \sigma + \sigma_m^{th} \right) \left\{ 1 - \frac{\cosh\left[\alpha\left(L/2 - x\right)\right]}{\cosh\left(\alpha L/2\right)} \right\} \tag{A.17}$$

where α is the shear-lag constant as derived under their formulation [113]. Furthermore, the instantaneous average crack spacing can be determined by assuming that new matrix cracks form at the mid-spans of existing cracks whenever Eq. (A.16) is satisfied. This yields

$$L = \frac{2}{\alpha} \cosh^{-1} \left\{ \frac{E_m \sigma + E_1 \sigma_m^{th}}{E_m \sigma + E_1 (\sigma_m^{th} - \sigma_{m_{ult}})} \right\}. \qquad (A.18)$$

Unfortunately, just as with the ACK model, Eq. (A.18) predicts a very rapid saturation of matrix cracking, and once again, the resulting stress-strain response is of a stepped fashion (Fig. A.11). Neither approach (ACK or Lee and Daniel) is able to capture the gradual evolution of matrix cracking observed experimentally. Moreover, the correct procedure for considering brittle fracture is through the use of the *critical energy release rate* and, therefore, a number of fracture mechanics solutions have been formulated [8, 20, 37, 54, 127, 129, 196, 201, 213]. Several of these solutions are reviewed below.

A.5.2 Fracture Mechanics Solutions. Because fracture mechanics approaches generally focus on conditions required to propagate a single fracture, they are not, in general, suited for modeling the initiation and growth of multiple cracks as required in the current analysis. The solutions are, however, well suited for investigating the salient characteristics of fracture, as well as determining which material and laminate parameters influence the matrix failure. Such approaches also provide estimates for the critical composite stress (σ_{cr}) and final crack densities (L_{sat}). In order to capture the behavior of multiple cracking, however, additional factors such as the statistical distribution of flaws and the interactions of adjacent cracks need to be considered.

The models reviewed in this section are presented in three subsections. The first two subsections (*Discrete Models* and *Continuum Models*) present established fracture mechanics solutions which can be used to estimate σ_{cr} and L_{sat}. The dis-

crete models are labeled as such since they consider each discrete fiber as a separate entity. The continuum models, on the other hand, consider an effective distribution of closing tractions to account for the influence of bridging fibers. Hence, the functionality of an individual fiber is lost in the collective. In the final subsection, *Evolution of Matrix Cracking*, the nucleation and growth of matrix cracks for $\sigma > \sigma_{cr}$ is discussed.

A.5.2.1 Discrete Models. The conditions for the *onset* of matrix cracking can be determined by ensuring the formation of the cracks is energetically consistent. This requires that the energies before and after crack formation must satisfy

$$\Delta U - \Delta W + g_m + W_{fr} = 0 \qquad (A.19)$$

where ΔW is the work done by the external load during crack formation, W_{fr} is the frictional energy dissipated through interface sliding; g_m is the strain energy release rate available for matrix cracking, and ΔU is the total change in strain energy. Formulations which employ Eq. (A.19) will be referred to as the *energy balance solutions*. The most famous of which is the model presented by Aveston, Cooper and Kelly (ACK) in which the energies within a simple unit-cell are considered [8].

Aveston, Cooper and Kelly. In conjunction with the maximum stress criterion presented in section 2.6.1, the original ACK analysis also examined the *energetics of multiple fracture* in brittle composites. The purpose was to explain why multiple cracking occurred in composites and how a quick estimate of the strain to the onset of multiple cracking could be obtained. In doing so, the analysis also showed the effects of various material parameters on the matrix cracking. Several important results are obtained. The first is that under the assumptions of the discrete

model, the strain energy release rate available for matrix cracking is

$$g_m = \frac{\sigma^3 E_m^2 v_m^2 r_f}{6 E_f v_f^2 \tau_i E_1^2}. \tag{A.20}$$

Further, equating g_m to the matrix fracture energy, $v_m g_m^c$, leads to a solution for the initial matrix cracking stress

$$\sigma_{cr} = \left\{ \frac{6 E_f v_f^2 \tau_i E_1^2 g_m^c}{E_m^2 v_m r_f} \right\}^{1/3}. \tag{A.21}$$

Note that Eq. (A.21) is a *lower bound* for σ_{cr} since variations in g_m due to flaw size and location have been neglected. In addition, the crack length was assumed "long" (infinite), and therefore, independent of the crack-tip stress intensity. Solutions which consider incremental increase in the crack size are presented in the next section. The following is a summary of the ACK analysis and is presented in a format analogous to the review appearing in reference 129

Figure A.12 illustrates the discrete model to be considered. The fiber/matrix interface is assumed to be completely debonded, and the interface slip is governed by a constant interface shear, τ_i. The length of the fiber is assumed to be twice the slip length, i.e. $2x'$. Again, the parameter x' is the slip length needed to recover to the pre-cracked stress state as defined in section 2.6.1. The stress T represents the maximum fiber stress and occurs along the plane of the matrix crack (i.e. $x = x'$). This stress has a magnitude of σ/v_f. If ϵ is defined as σ/E_1 then $T = E_1 \epsilon / v_f$. The crack opening displacement is $2U$, and the far-field constituent stresses are

$$\sigma_{f_o} = \frac{E_f}{E_1} \sigma = E_f \epsilon, \tag{A.22}$$

$$\sigma_{m_o} = \frac{E_m}{E_1} \sigma = E_m \epsilon \tag{A.23}$$
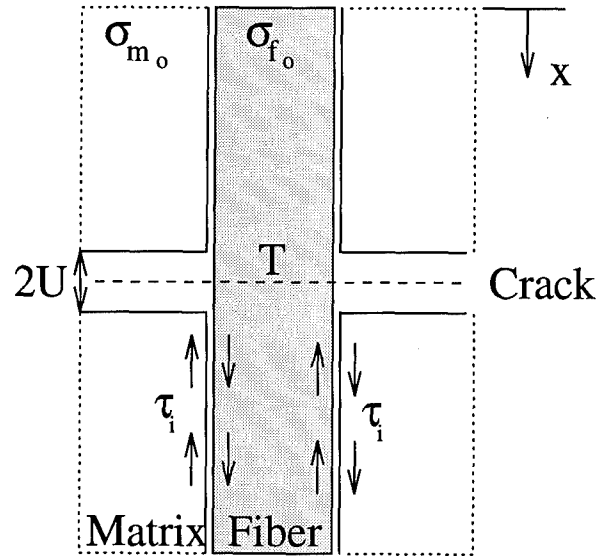
Figure A.12   Discrete fiber model.

since thermal stresses are neglected in the original ACK analysis. In addition, since the interface shear, τ_i, is assumed constant, the constituent stresses near the fracture are given by

$$\sigma_f(x) = \sigma_{f_o} + \frac{2\tau_i}{r_f}x, \qquad (A.24)$$

$$\sigma_m(x) = \sigma_{m_o} - \frac{v_f}{v_m}\frac{2\tau_i}{r_f}x. \qquad (A.25)$$

Now, if $u_f(x)$ and $u_m(x)$ represent the displacements in the fiber and matrix such that

$$\sigma_f(x) = E_f\frac{\partial u_f(x)}{dx}, \qquad (A.26)$$

$$\sigma_m(x) = E_m\frac{\partial u_m(x)}{dx} \qquad (A.27)$$

then

$$u_f(x) = \epsilon x + \frac{\tau_i}{E_f r_f}x^2 \quad \text{for } 0 < x < x', \qquad (A.28)$$

$$u_m(x) = \epsilon x + \frac{v_f}{v_m}\frac{\tau_i}{E_m r_f}x^2 \quad \text{for } 0 < x < x'. \qquad (A.29)$$

Further, the crack opening displacement is given by $2\left[u_f(x') - u_m(x')\right]$ which implies

$$U = \frac{r_f v_m E_m}{4\tau_i v_f^2 E_f} E_1 \epsilon = \frac{r_f v_m E_m}{4\tau_i E_1 E_f} T^2. \qquad (A.30)$$

Let p be the effective closing traction created from the bridging fiber. Then for the discrete model, $p = v_f T$. Further, from Eq. (A.30)

$$p = \overline{\lambda}\sqrt{u} \qquad (A.31)$$

where $u = E_1\, U/2\pi$ and $\overline{\lambda} = 2v_f\left\{\dfrac{2\pi\tau_i}{r_f}\dfrac{E_f}{v_m E_m}\right\}^{1/2}$. It will be shown later that the effective traction under the continuum approach is of the same form as Eq. (A.31).

With the model now established, the energy terms in Eq. (A.19) can now be established. The additional work performed by the external tractions during crack formation is

$$\Delta W = 2\sigma\left\{u_f(x) - \epsilon x'\right\} = \frac{r_f}{2\tau_i} E_f E_1 \left(\frac{v_m E_m}{v_f E_f}\right)^2 \epsilon^3. \qquad (A.32)$$

The change in the strain energy per unit area is

$$\Delta U = \frac{v_f}{E_f}\int_0^{x'} \sigma_f^2(x)\, dx + \frac{v_m}{E_m}\int_0^{x'}\sigma_m^2(x)\, dx - E_1\epsilon^2 x' = \frac{r_f E_f E_1}{6\tau_i}\left(\frac{v_m E_m}{v_f E_f}\right)^2 \epsilon^3. \ (A.33)$$

Finally, the work done (per unit area) by the frictional forces along the fiber / matrix interface is

$$W_{fr} = \frac{4v_f}{r_f}\tau_i \int_o^{x'} u_f(x) - u_m(x)\, dx = \frac{r_f E_f E_1}{6\tau_i}\left(\frac{v_m E_m}{v_f E_f}\right)^2 \epsilon^3. \qquad (A.34)$$

Substituting Eqs. (A.32), (A.33) and (A.34) into Eq. (A.19) yields Eq. (A.20). Equations (A.10) and (A.21) follow directly.

Zok and Spearing. Zok and Spearing presented an analysis similar to ACK in which the same energy balance approach was considered for the

two damaged configurations illustrated in Fig. A.13 [213]. As with the ACK analysis,
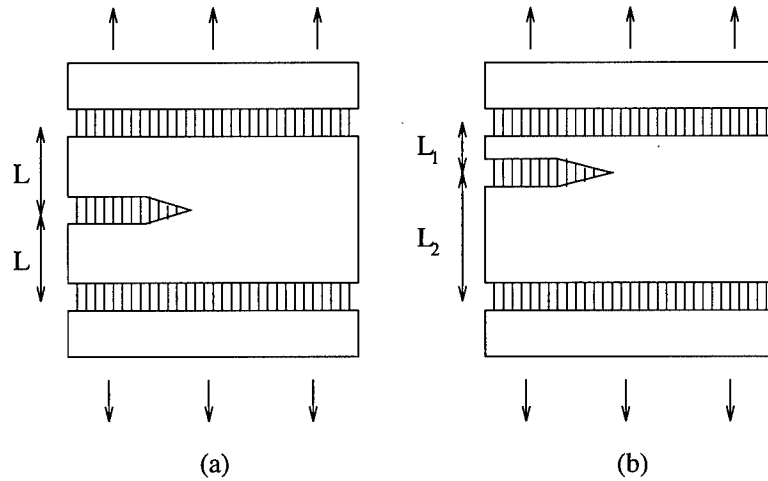
Figure A.13   Schematic diagrams of (a) periodic matrix cracks and (b) random matrix cracks.

the interface was assumed to be debonded and the matrix cracks were assumed to extend throughout the entire laminate cross-section. However, this time a reduction in the matrix stress due to the interactions of adjacent cracks was included in the analysis.

As the matrix fails, the crack spacing decreases. Eventually, the spacing may be insufficient to permit a full recovery of matrix stress and this reduces the opportunity for continued cracking. This phenomenon is sometimes referred to as a *shielding* or *screening* effect. Zok and Spearing considered the influence of both periodic and random crack spacing on the shielding aspects of brittle composites. For brevity however, only the results for the first configuration (periodic cracks) are presented.

Shielding results when $x' \geq L$ such that the stress in the matrix does not fully recover (Fig. A.14). Two cases need to be considered: $1 \leq L/x' \leq 2$ and $0 \leq L/x' \leq 1$. In the first case, the existing cracks do not interfere with one another (i.e. the matrix stress fully recovers), however, with the formation of a new crack, the spacing is insufficient to permit the matrix stresses to recover. For $0 \leq L/x' \leq 1$, the pre-existing cracks screen one another even prior to the formation of the new
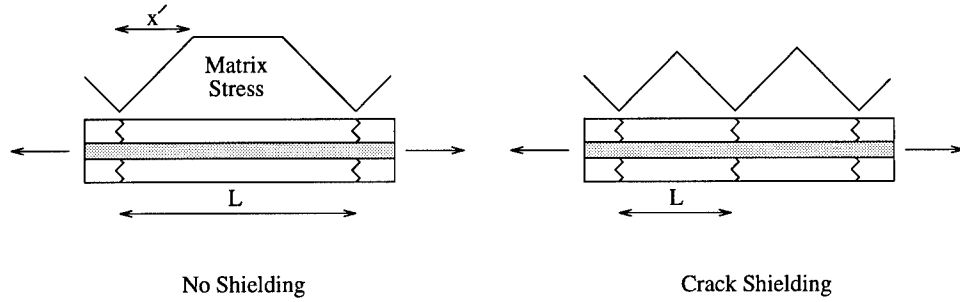
Figure A.14 Shielding (screening) effect resulting from a sufficiently small crack spacing.

crack. The net effect of the screening is that the strain energy release rate, g_m, varies with L/x'. The formulation follows directly from Eq. (A.19), but is somewhat more involved than the ACK solution since the constituent stresses are a function of the crack spacing in Zok and Spearing's analysis. The crack-tip strain energy release rate is found to vary as

$$\frac{g_m}{g_m^c} = 1 - 4\left(1 - \frac{L}{2x'}\right)^3 \quad \text{for } 1 \leq L/x' \leq 2, \qquad (A.35)$$

$$\frac{g_m}{g_m^c} = 4\left(\frac{L}{2x'}\right)^3 \quad \text{for } 0 \leq L/x' \leq 1. \qquad (A.36)$$

This variation is illustrated in Fig. A.15. An important result of this analysis is that crack saturation does not occur instantly (i.e. $\sigma_{sat} \neq \sigma_{cr}$) as a result of the shielding effect. The final cracking spacing and saturation stress are found to be $L_{sat} = 1.26x'$ and $\sigma_{sat} = 1.26\sigma_{cr}$ [213]. Hence, *shielding slows matrix cracking by reducing crack-tip stress intensities*. This phenomenon was shown to be more prevalent under random crack spacing [Fig. A.13 (b)].

A.5.2.2 Continuum Models. For mathematical purposes, it is convenient to "smooth the mechanical effect of the discrete system of unbroken fibers
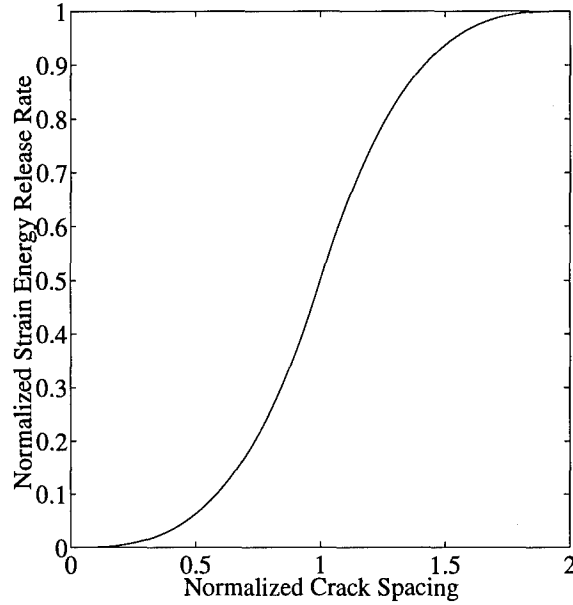
Figure A.15   Variation in the crack-tip strain energy release rate, g_m/g_m^c, as a function of the crack spacing L/x', for periodic matrix cracking.

that cross the crack and assume that the displacement distribution is everywhere single-valued and smoothly varying." [129]. This is the idea behind the continuum approach in which the net effect of the bridging fibers is modeled as a continuous distribution of closing tractions (Fig. A.16). In the review of the ACK model presented earlier, it was shown for the discrete model that the closing tractions, $p(x)$, were proportional to the crack opening displacement, $u(x)$ [Eq. (A.31)]. For the continuum model, the relationship between these two parameters is

$$u(x) = \frac{2}{\pi^2} \int_x^a \frac{t}{\sqrt{t^2 - x^2}} \left\{ \int_0^t \frac{\sigma_\infty - p(\zeta)}{\sqrt{t^2 - \zeta^2}} \, d\zeta \right\} \, dt \qquad (A.37)$$

where a is the crack length. The later result was obtained from reference 129. The corresponding stress intensity factor as determined under the formulation presented by McCartney [129] is

$$K = \sigma_\infty \sqrt{\pi a} \mathcal{Y} \quad \text{where} \quad \mathcal{Y} = \frac{2}{\pi} \int_0^1 \frac{1 - P(X)}{\sqrt{1 - X^2}} \, dX \qquad (A.38)$$

A-28
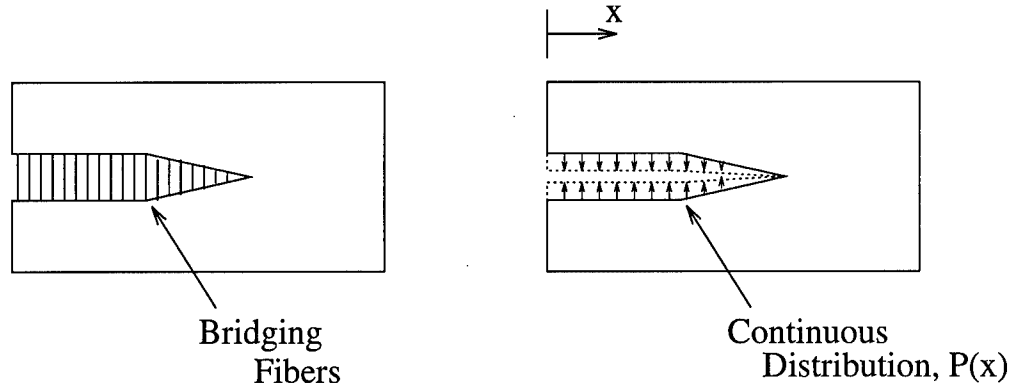
Figure A.16   Continuum model

where $P(X)$ is a normalized effective closing distribution such that when $P(X) = 0$ (i.e. no fibers bridge the crack plane), $K = \sigma_\infty \sqrt{\pi a}$. The latter is recognized as the solution for a stress-free crack in an infinite plate as presented earlier. For $P(X) > 0$, K decreases from this fundamental solution. Hence, as was observed with the screening effects of adjacent cracks, *bridging fibers reduce crack-tip stress intensities by providing forces which reduce the crack opening displacements* [127,129,196] These forces, typically referred to as closing tractions, can be effectively modeled using a continuous single-valued distribution, $p(x)$. At the onset of crack propagation, therefore, the energy release rate at the crack tip is given by

$$g_m = g_m^c - \int_a p(x) \, da. \tag{A.39}$$

The models presented by Marshall, Cox & Evans (MCE) [127] and McCartney [129] represent the classical solutions in this area (continuum models). Such models are referred to as *stress intensity solutions* as opposed to the *energy balance solutions* presented earlier. An important consequence of the MCE analysis is that for crack lengths larger than some characteristic flaw size, c_o, the crack-tip stress intensity factor is independent of crack length. Thus, for $a \geq c_o$, the ACK solution [Eq. (A.21)]

is valid. The characteristic length may be estimated by Eq. (A.40) [37].

$$c_o \simeq \frac{1}{2}(g_m^c)^{(1/3)} \cdot \left[\frac{v_m r_f E_1 \sqrt{E_m}}{v_f^2 \tau_i E_f}\right]^{2/3} \tag{A.40}$$

In addition,

$$\frac{\sigma_{cr}}{\sigma^*} = 1 + \frac{1}{8}\left(\frac{a}{c_o}\right)^{-3/4} \tag{A.41}$$

where σ^* is the original ACK solution.

As illustrated in the preceding sections, there are a number of solutions which yield estimates for the critical composite stress, σ_{cr}. Perhaps the most referenced of these are those presented by Aveston, Cooper & Kelly (ACK) [8], Marshall, Cox & Evans (MCE) [127] and Budiansky, Hutchinson & Evans (BHE) [20]. The ACK and MCE models have been examined in the above discussion. The BHE model considers *steady-state* crack growth under which it is assumed that the stress at the crack front remains unchanged during incremental crack growth, and that the upstream and downstream stress states, far ahead of and behind the crack front, do not change [20]. The crack growth model is shown in Fig. A.17. where P_u and P_d
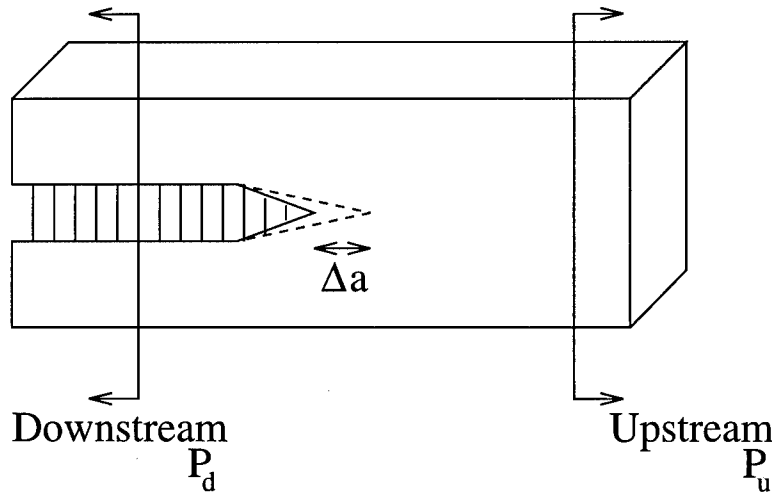
Figure A.17   Crack growth model.

are the upstream and downstream potential energies per unit cross-sectional area.

Moreover, in order for the crack to advance an incremental distance which produces a net increase in the crack area of Δa, the following must hold.

$$(P_u - P_d)\Delta a = \Delta U \qquad (A.42)$$

Equation (A.42) is now the energy balance failure criterion where ΔU is the potential energy loss during crack advancement. From the Betti-Maxwell theorem of reciprocal displacements, it follows that

$$g_m = \frac{v_f}{2v_m\pi r_f^2}\int_V (\sigma_u - \sigma_d):(\epsilon_u - \epsilon_d)\ dV. \qquad (A.43)$$

From here, σ_{cr} is estimated by setting $g_m = v_m g_m^c$.

In analogy to BHE, Weitsman and Zhu [201] formulated a criterion for the formation of a new matrix crack which compared the energy levels of two discrete (upstream and downstream) states. Rather than considering incremental growth a single crack (BHE), however, Weitsman and Zhu considered two damaged states of uniform crack spacing. "State I" was assumed to have a crack density of $1/L$ and the crack density of "State II" was twice this amount. The failure criterion was again that $\Delta U = v_m g_m^c$. Their solution is important to the present work since it is the only known *analytic* criterion which has a finite stress range over which matrix cracking is predicted. That is to say, the Weitsman and Zhu criterion does capture some evolution of matrix cracking. Unfortunately, the criterion offered only a slight improvement over the previous analyses. The solution presented by Weitsman and Zhu is presented in greater detail in the chapter three.

A.5.2.3 Evolution of Matrix Cracking. Under the traditional fracture mechanics approach, in order to capture the gradual evolution of matrix cracking which is observed experimentally, the *shielding* and *stochastic* behavior of matrix failure must be accounted for in the analysis. The shielding effect was discussed

earlier in chapter two, and results from crack interactions once the matrix crack density becomes sufficiently large. This interaction can reduce the driving force for the propagation of additional cracks. In addition to this phenomenon, matrix cracking is governed by statistical relations which relate the size and spatial distribution of matrix flaws to their relative propagation stress. These relations have been well publicized by William Curtin [37].

Curtin. As mentioned in the previous section, for relatively large cracks (e.g. $a > c_o$), the stress required to propagate the fracture is independent of the flaw size [127]. The propagation stress is given by Eq. (A.21). Hence, if all flaws inherent to the matrix are larger than c_o, the statistical analysis becomes trivial. However, experimentally, the evolution of cracking occurs over a finite stress range. Hence, the statistical aspects of failure may be important. For flaws smaller than the critical length determined by MCE, the stress required to propagate the flaw is greater than that predicted by Eq. (A.21). It follows that if a distribution of flaw sizes is incorporated in the analysis, then the matrix strength will also be characterized by some distribution.

Curtin proposed modeling the crack progression using a 3-parameter Weibull strength distribution [37]. In particular, the matrix strength distribution, $\Phi(\sigma, V)$, was taken as

$$\Phi(\sigma, V) = \frac{V}{V_o} \left(\frac{\sigma - \sigma^*}{\sigma_o} \right)^m \tag{A.44}$$

where m is the Weibull modulus, σ_o is a scale parameter and σ^* is the minimum stress for crack formation. These parameters may be chosen to match the empirical data. V is the material volume, and V_o is a characteristic volume which contains one flaw smaller than c^* where

$$\sigma_o = \sigma^* + \frac{1}{8} \left(\frac{c^*}{c_o} \right)^{-3/4}. \tag{A.45}$$

Evans, Zok and McMeeking. As a final note, the work accomplished by Evans, Zok and McMeeking [54] serves as a comprehensive overview of the matrix cracking process. Reference 54 discusses the initiation and evolution of matrix cracking for both unidirectional and cross-ply laminates. Quasi-static and fatigue loading are also considered. In addition, the effects of shielding, as well as the statistic aspects of failure are addressed. A simple approximation for determining the average crack spacing is also provided, and is shown below.

$$L = L_{sat} \left\{ \frac{\sigma_{sat}/\sigma_{mc} - 1}{\sigma/\sigma_{mc} - 1} \right\} \tag{A.46}$$

A.6 Additional Comments

This section investigates some of the simplifying assumptions employed in the current model formulation, as well as several assumptions used in the development of the failure criteria. In addition, some general observations on the fatigue response of brittle composites are presented.

A.6.1 Micromechanics/Shear-lag Assumptions. In order to simplify the analysis, a number of assumptions are made on the geometric arrangement of the constituents and the configuration of the damages. In doing so, the analysis is reduced to one dimension; however, a host of effects and the true nature of fracture in CMCs is lost. For example, it is to be expected that because of the dominating role of the fiber/matrix interface, the Poisson's effects near the bi-material regions may be rather significant in determining the laminate response. The Poisson's effects may prove especially important in debonded regions where the stress transfer is dependent on the frictional resistance of the fiber/matrix constituents. This is particularly the case when repeated and cyclic loadings are considered and in which the "direction" of the Poisson's effects vary. The effect may be rather pronounced and manifests as large variations in the shape of the stress-strain hysteresis loops predicted under the analysis.

The concentric cylinder models used in the present analysis assume that the distribution of fibers in the composite matrix are uniform. From Fig. 2.10, this is most certainly not the case [177]. To investigate the effects of the relative fiber spacing on the strength of the brittle laminate, Weitsman and Beltzer recently introduced an eccentric shear-lag model in which the fiber spacing in an extended representative volume element can be given some eccentricity [200]. The analysis found that traditional models may significantly underestimate the loading effect near fractured fibers, and as such the validity of current statistical failure distributions is questionable. Furthermore, the accuracy of "dry" bundle tests for estimating the evolutions of fiber fractures in *in-situ* composites is also in debate.

The assumptions used in the shear-lag derivation are also only gross approximations. More accurate solutions do exist; however, because of their complexity, the applicability of such models is limited [137, 139]. Each problem will require an assessment and trade-off between the accuracy of the assumed stress fields and the ease of implementation. The primary assumption of the shear-lag model is that the interface shear stress in bonded regions is proportional to the difference in the average displacements between the constituents. The assumption, plus the approximate nature of the assumed constituent displacements, calls into question the accuracy of this approach. However, as presented in this document and in other literature, the shear-lag formulation is suitable for modeling polymer-based, metal matrix and ceramic matrix composites under a number of loading conditions [133].

A.6.2 Fatigue Loading. The fatigue behavior of ceramic matrix composites can be characterized by four predominate features: modulus, stress-strain hysteresis, strain ratchetting, and S-N behavior. Each of these are useful for defining the material behavior. Unfortunately, due to the variability in material batches, testing methods, and stochastic failure processes, the salient features/empirical trends may vary, sometimes significantly, between the data reported in the literature. Moreover, due to the uncertainties in the failure mechanism, the observed phenomenon

can be difficult to explain. This section briefly summarizes some of the observations/discrepancies reported for the four characteristics: modulus, stress-strain hysteresis, strain ratchetting, and S-N behavior.

A.6.2.1 Modulus. During fatigue loadings where the applied stress is greater than the critical composite stress (i.e. $\sigma \geq \sigma_{cr}$), the laminate's modulus, E_c, decreases due to the formation of damages [76,210]. The damages progress on a cycle by cycle basis in which the modulus approaches a magnitude of $v_f E_f$ as the matrix cracks and the fibers debond. Once the matrix cracks saturate, the degradation in the elastic modulus is a result of the interface debonding which continues due to Poisson's effects and changes in the stress intensity factor at the debond crack tip [184]. Note also that E_c may decrease below the stated limit, e.g. $v_f(1 - D)E_f$, as fibers fracture and pull-out. The reduction in the modulus is a function of the loading environment[†], interface shear[‡] and the laminate's composition. Zawada *et al* observed a gradual degradation in the modulus over the first 10,000 cycles [210]. Pryce and Smith reported a much quicker degradation [153].

With extensive cycling, a slight recovery ($\approx 5 - 10\%$) in E_c may be observed [153, 210]. This could result from an increase in the interface shear, $\tau_i(N)$, due to long term exposure to the environmental conditions. In particular, the humidity level is believed to be the main contributor. Also, debris along the interface may produce some mechanical interlocking which reduces the interface sliding. Finally, as the matrix cracks and the interface debonds, the fibers are permitted to realign; perhaps into a stiffer orientation. Note that as the modulus increases, the fiber strain decreases, and in turn, the interface slip and stress-strain hysteresis also decrease. Cycling below the critical composite stress can increase the residual strength of the laminate by decreasing the crack-tip stresses [210].

[†]Maximum applied stress, atmospheric conditions, temperature, strain rate, loading frequency, stress ratio, etc. [74,95,165,190,210].

[‡]The degradation in $\tau_i(N)$ may be modeled as presented in chapter four or by some alternate form, e.g. $\tau_i(N) = \tau_{i_o} N^{-t}$ [54,163].

A.6.2.2 Stress-Strain Hysteresis. Stress-strain hysteresis results from frictional sliding along the fiber/matrix interface. The shape of the stress-strain loop and the width of the loop can both vary during cycling. In general, the *shape* of the hysteresis loop is non-linear when the state of interface sliding is changing (partially bonded) and linear when the constituents are fully sliding (debonded) [178]. Furthermore, the loop *width* may remain the same, decrease, or increase with cycling [100]. All possibilities exist due to the competing nature of the frictional sliding. For a constant slip distance, the larger the frictional force (i.e. large τ_i), the wider the hysteresis loop due to an increase in energy dissipated. However, as $\tau_i(N)$ declines, the slip distance also decreases which, in turn, reduces the energy dissipated and hysteresis. Pryce and Smith observed that for $\sigma > \sigma_{cr}$, the hysteresis width decreases with cycling, and for $\sigma \approx \sigma_{cr}$, the width remains fairly constant over the fatigue life [153]. Holmes & Cho and Rouby & Reynauld reported increases in the loop width with cycling [76, 163].

A.6.2.3 Strain Ratchetting. Strain ratchetting occurs when fibers fail and pull-out from the matrix. It has been observed that strain ratchetting is a time dependent phenomenon due to variations in τ_{ult} and τ_i resulting from oxidation embrittlement [153]. Furthermore, the fatigue specific damages and time-dependent matrix cracking which occurs, increases the rate of fiber fracture since the fibers are forced to carry a greater share of the applied load. In a similar manner, the slippage process itself may be a catalyst for increases in the matrix crack density, and ultimately the fiber crack density, due to the surface roughness of the constituents [153]. Also, additional fiber fractures form as microscopic flaws grow under fatigue loading and eventually obtain a critical size.

A.6.2.4 S-N Behavior. The fatigue life of a composite is typically defined as one million cycles. The maximum stress for which the composite does *not* fail over the prescribed fatigue life is known as the *fatigue limit*. For ceramic matrix

composites, it is generally observed that the fatigue limit is close to the critical composite stress of the laminate [151,210]. However, based upon some unpublished work by Holmes,[†] for long duration cyclic tests ($> 10^7$), the fatigue limit can be far below, on the order of 40%, σ_{cr}. This reinforces the time dependency of failure in these materials (e.g. oxidation embrittlement). Moreover, the reduction in the fatigue life at high loading frequency may be a consequence of additional interface damages caused by large temperature rises.

[†]University of Michigan, Ann Arbor.

Appendix B. Theory of Micromechanics

This appendix provides an introduction to the modeling of ceramic matrix composites via the theory of micromechanics. For brevity, unidirectional laminates are emphasized. *Rule-of-mixtures* equations are reviewed for the case of an undamaged laminate, and an introduction to shear-lag theory is presented for when damage is considered. Also, this appendix includes a review of the solution methodology employed in the current study.

B.1 Rule-of-Mixtures Theory

Under the geometric constraints outlined in chapter two, the behavior of a unidirectional laminate can be modeled using a simplified unit-cell consisting of a single fiber and surrounding matrix. If the composite is void of any damage, the strain in the constituents is assumed to be equal and to define the composite strain, i.e.

$$\epsilon_c = \epsilon_f = \epsilon_m. \tag{B.1}$$

Moreover, the total strain is a combination of the mechanical and thermal strains:

$$\epsilon_c = \frac{\sigma}{E_1} + \alpha_1 \Delta T,$$
$$\epsilon_f = \frac{\sigma_{f_o}}{E_f} + \alpha_f \Delta T, \tag{B.2}$$
$$\epsilon_m = \frac{\sigma_{m_o}}{E_m} + \alpha_m \Delta T.$$

The subscripts $f, m, 1, 2$ and c denote the fiber, matrix, axial direction, transverse direction, and composite, respectively. The parameter E is Young's modulus; α is the coefficient of thermal expansion.

Substituting Eq. (B.2) into Eq. (B.1), it may be shown that

$$\sigma_{f_o} = \frac{E_f}{E_1}\sigma + E_f(\alpha_1 - \alpha_f)\Delta T, \qquad (3.47)$$

$$\sigma_{m_o} = \frac{E_m}{E_1}\sigma + E_m(\alpha_1 - \alpha_m)\Delta T. \qquad (3.46)$$

Hence, the constituent stresses are assumed to be constant over the length of the unit-cell as illustrated in Fig. B.1.
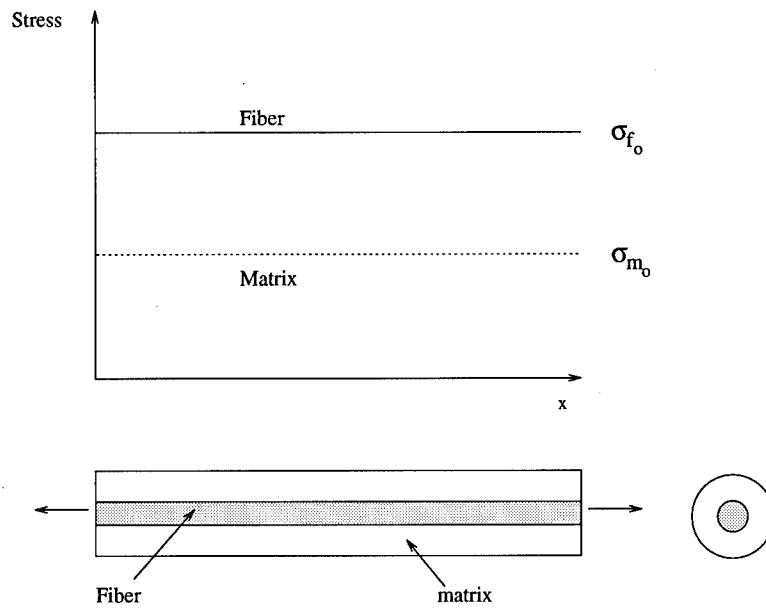
Figure B.1   Constituent stresses, based upon micromechanics theory, for an undamaged laminate.

The equilibrium relation may be determined by noting that any applied *load*, P, may be expressed as the sum of the loads on the individual constituents, i.e.

$$P = P_f + P_m. \qquad (B.3)$$

From which, equilibrium is determined by dividing by the composite area as illustrated below.

$$\begin{aligned} \sigma &= \frac{P}{A_c} \\ &= \frac{P}{A_f}\frac{A_f}{A_c} + \frac{P}{A_m}\frac{A_m}{A_c} \\ &= v_f \sigma_{f_o} + v_m \sigma_{m_o} \end{aligned} \tag{B.4}$$

Furthermore in differentiating Eq. (B.4) with respect to ϵ_c, it follows that

$$E_1 = v_f E_f + v_m E_m \tag{3.4}$$

since the constituents are assumed linear-elastic. The following relationships also hold [25].

$$E_2 = \left\{ \frac{v_f}{E_f} + \frac{v_m}{E_m} \right\}^{-1} \tag{3.5}$$

$$\alpha_1 = \frac{v_f E_f \alpha_f + v_m E_m \alpha_m}{E_1} \tag{B.5}$$

$$\alpha_2 = v_f \alpha_f + v_m \alpha_m \tag{B.6}$$

$$G_{12} = G_m \left\{ \frac{v_m G_m + (1 + v_f) G_f}{(1 + v_f) G_m + v_m G_f} \right\} \tag{B.7}$$

$$G_{23} = G_m \left\{ \frac{(\alpha + \beta_m v_f)(1 + \rho v_f^3) - 3 v_f v_m^2 \beta_m^2}{(\alpha - v_f)(1 + \rho v_f^3) - 3 v_f v_m^2 \beta_m^2} \right\} \tag{B.8}$$

where

$$\alpha = \frac{\gamma + \beta_m}{\gamma - 1} \qquad \beta_m = \frac{1}{3 - 4v_m} \qquad \beta_f = \frac{1}{3 - v_f}$$

$$\rho = \frac{\beta_m - \gamma \beta_f}{1 + \gamma \beta_f} \qquad \gamma = \frac{G_f}{G_m}$$

The parameters G_f and G_m are the shear moduli for the fiber and matrix, respectively. Similarly, v_f and v_m are the corresponding Poisson's ratios. For the cross-ply

laminate,

$$\alpha_c = \frac{bE_1\alpha_1 + dE_2\alpha_2}{bE_1 + dE_2} \tag{B.9}$$

where b and d are the half-thicknesses of the 0° and 90° plies.

B.2   Introduction to Shear-lag Theory

One-dimensional shear-lag models typically assume that the state of stress in a bi-material composite can be defined by the normal (axial) stresses in the constituents and the shear stress which develops at the interface of the two materials. For the system of materials, a and b, shown in Fig. B.2, these correspond to $\sigma_a(\eta)$, $\sigma_b(\eta)$ and $\tau_i(\eta)$. Note that the unmodified shear-lag theory is limited to the anal-
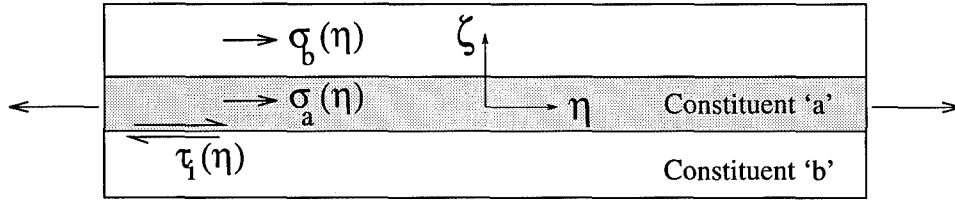
Figure B.2   Bi-material representative volume element (RVE).

ysis of two constituent systems with uniaxial loadings (e.g. η direction). Further, equilibrium requires that the following two relations hold.

$$\sigma = \frac{V_a}{V_a + V_b}\sigma_a(\eta) + \frac{V_b}{V_a + V_b}\sigma_b(\eta) \tag{B.10}$$

$$\tau_i(\eta) = \mp\delta_a\frac{d\sigma_a(\eta)}{d\eta} = \pm\delta_b\frac{d\sigma_b(\eta)}{d\eta} \tag{B.11}$$

where V denotes the constituent volume and δ is of unit *length* and depends on the RVE cross-sectional area. The unit-cell is assumed to span a pair of matrix cracks. Note that Eqs. (B.10) and (B.11) constitute only two equations for the three unknown stresses. The final relation is obtained from the shear-lag formulation which assumes that the *rate* of stress transfer between the constituents is proportional to

the average constituent displacements according to Eq. (B.12); where it has been recognized that the stress transfer rate is also proportional to the interface shear [Eq. (B.11)].

$$\tau_i(\eta) = \pm \mathcal{H} \left\{ \bar{u}_a(\eta) - \bar{u}_b(\eta) \right\} \tag{B.12}$$

The *sign* in Eq. (B.12), $\pm$, is dependent on which entity, a or b, is the main loading bearing member.

Equation (B.12) represents an additional relation for the analysis; however, several unknowns are also introduced. In particular, the shear-lag parameter, $\mathcal{H}$, and the constituent displacements, $\bar{u}_a(\eta)$ and $\bar{u}_b(\eta)$, must be determined. The latter requiring the introduction of an assumed set of in-plane constituent shear stresses, $\tau(\eta, \zeta)$. These shears are not to be confused with the interface shear stress, $\tau_i(\eta)$; rather $\tau(\eta, \zeta)$ describes in-plane warping of the constituents. Note however that since the shear-lag stresses [$\sigma_f(\eta)$, $\sigma_m(\eta)$ and $\tau_i(\eta)$] are based on the *average* displacements, cross-sections of the RVE are assumed to remain plane under deformation. The solution is formulated in this manner to reduce the problem to a single dimension. It is worth noting that several of the shear-lag models differ only in the assumed form of the constituent shear stresses, $\tau(\eta, \zeta)$. Furthermore, given $\tau(\eta, \zeta)$, the average displacements may be determined from the *assumed* problem kinematics, e.g.

$$\bar{u}(\eta) = \int_A \int_\zeta \tau(\eta, \zeta)/(AG) \, d\zeta \, dA \tag{B.13}$$

where A is the cross-sectional area of the unit-cell under consideration. Equation (B.13) represents the reduction in the problem to one dimension.

It turns out that in its present form, Eq. (B.12) is not independent of Eq. (B.11) due to the assumed kinematic relation, and therefore, an insufficient number of equations still exists to solve the problem. However, in differentiating Eq. (B.12), the desired solution is obtained. In particular, by differentiating Eq. (B.12) and employing Eqs. (B.10) and (B.11) and the proper kinematic relations, the following

relation is obtained.

$$\delta_a \frac{d^2\sigma_a(\eta)}{d\eta^2} - \Lambda_1\sigma_a = \mathcal{H}\left\{\Lambda_2\sigma - (\alpha_a - \alpha_b)\Delta T\right\} \qquad \text{(B.14)}$$

where $\Lambda_1 = |\mathcal{H}|\left\{V_aE_a + V_bE_b\right\}/\left\{V_bE_aE_b\right\}$ and $\Lambda_2 = (V_a + V_b)/(E_bV_b)$. The latter is recognized as the inverse of the volume fraction of constituent b (i.e. $\Lambda_2 = 1/v_b$). Equation (B.14) represents a second-order linear differential equation with constant coefficients and whose solution yields one of the desired axial stresses. The two boundary conditions for Eq. (B.14) are dependent on the damage configuration within the composite. Typical boundary conditions are that the axial stresses must vanish at the free boundaries (i.e. a matrix crack), and that the interface shear vanishes along planes of symmetry. Finally, Eqs. (B.10), (B.11), (B.12) and (B.14) constitute four equations in four unknowns: $\sigma_a(\eta)$, $\sigma_b(\eta)$, $\tau_i(\eta)$ and $\mathcal{H}$. Hence, the state of stress is now completely defined.

Under the current formulation, the two-dimensional constituent[†] shear stresses are assumed to be of the form shown in Eq. (B.15).

$$\tau(\eta,\ \zeta) = \begin{cases} \delta_1 \cdot (\zeta + \delta_2) \cdot \tau_i(\eta) & \text{for constituent 'a'} \\ \delta_3 \cdot (\delta_4/\zeta - \zeta + \delta_5) \cdot \tau_i(\eta) & \text{for constituent 'b'} \end{cases} \qquad \text{(B.15)}$$

The constants δ_i are dependent on the initial laminate geometry. Moreover, the separation of variables is required for Eq. (B.13). The final stresses for the unidirectional laminate are given in Eq. (B.16). These are the same as presented by Kuo and Chou [106], but have been modified to account for fiber fracture. For brevity the stresses in the cross-ply laminate are not shown, but can be found in chapter

---

[†]Note that the term *constituent* is used loosely in this text since it refers to not only the fiber and matrix of the unidirectional laminate, but also the 90° ply and the 0° ply of the cross-ply laminate. Refer to chapter three for more detail.

three.

$$\sigma_f(\eta) = \begin{cases} \sigma_{f_o} + \mathcal{G} \cosh(\beta\eta) / \cosh(\beta[L/2-d]) & \text{bonded region} \\ \dfrac{\sigma}{v_f(1-D)} - \dfrac{2\tau_i}{r_f}(L/2 - |x|) & \text{debonded region} \end{cases}$$

$$\sigma_m(\eta) = \begin{cases} \dfrac{v_f}{v_m}\{\mathcal{G}\cosh(\beta\eta)/\cosh(\beta[L/2-d])\} & \text{bonded region} \\ \dfrac{v_f}{v_m}\dfrac{2\tau_i}{r_f}(L/2-|\eta|) & \text{debonded region} \end{cases}$$

$$\tau_i(\eta) = \begin{cases} -\dfrac{r_f}{2}\mathcal{G}\sinh(\beta\eta)/\cosh(\beta[L/2-d]) & \text{bonded region} \\ \tau_i & \text{debonded region} \end{cases} \quad\text{(B.16)}$$

where

$$\mathcal{G} = \left\{\frac{\sigma}{v_f(1-D)} - \sigma_{f_o} - \frac{2\tau_i}{r_f}d\right\} \quad\text{(B.17)}$$

The variable β is the shear-lag constant [106]; L is the crack spacing; d is the debond length, and τ_i is the frictional shear resistance in regions of fiber/matrix debonding. τ_i is assumed constant.

From the above development, the composite stress-strain response is completely described by the Hookean relation given in Eq. (B.18)

$$\sigma = E_1\,\epsilon_c \quad\text{(B.18)}$$

where σ is the applied stress and ϵ_c is the strain of the composite. Since the applied load is assumed to be aligned with the fibers in this case, E_1 represents the laminate stiffness, i.e. $E_1 = E_c$. In addition, for an intact fiber, the composite strain is defined as the average strain in the fiber. Hence,

$$\epsilon_c = \frac{1}{E_f L}\int_L \sigma_f(x)\,dx + (\alpha_f - \alpha_c)\Delta T \quad\text{(3.6)}$$

where x is the axial coordinate defined along the fiber axis.

B.3   Methodology

The methodology employed in the current study for modeling the CMC behavior under quasi-static and fatigue loadings is illustrated in Figs. B.3 and B.4. The solution algorithm is detailed in Fig. B.3 while Fig. B.4 provides a general overview of the mechanisms which must be considered in the fatigue analysis. Note that both rule-of-mixtures and shear-lag formulae are employed for analysis purposes.
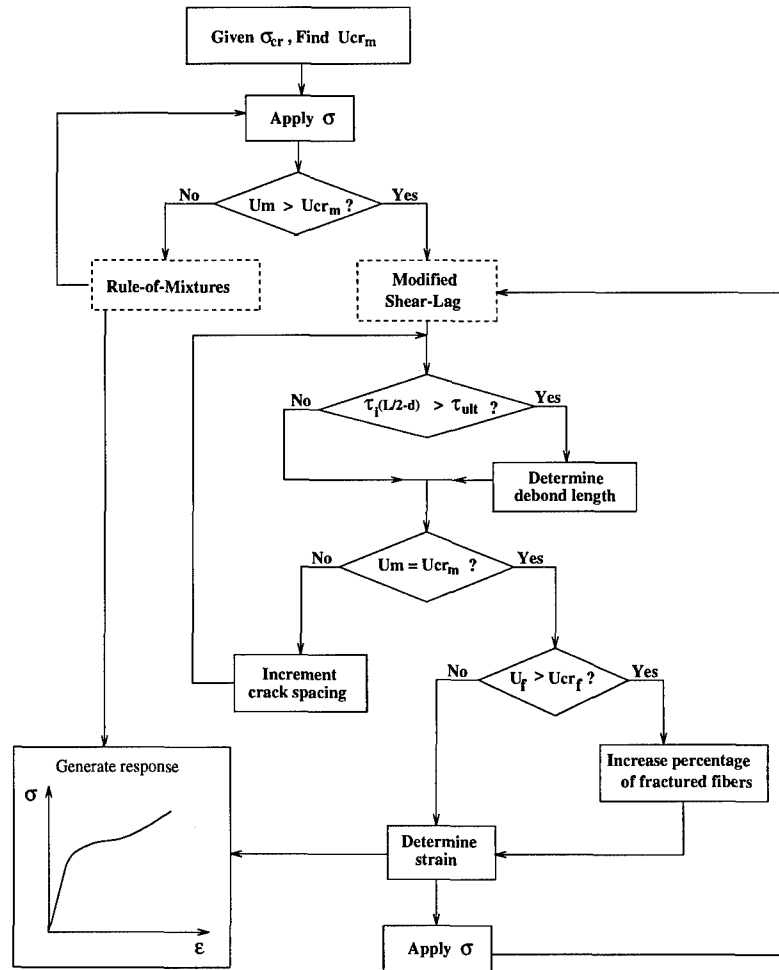
Figure B.3   Flow chart outlining the current approach used in generating the stress-strain response for a ceramic matrix composite in which matrix cracking, interface debonding and fiber fracture are considered.
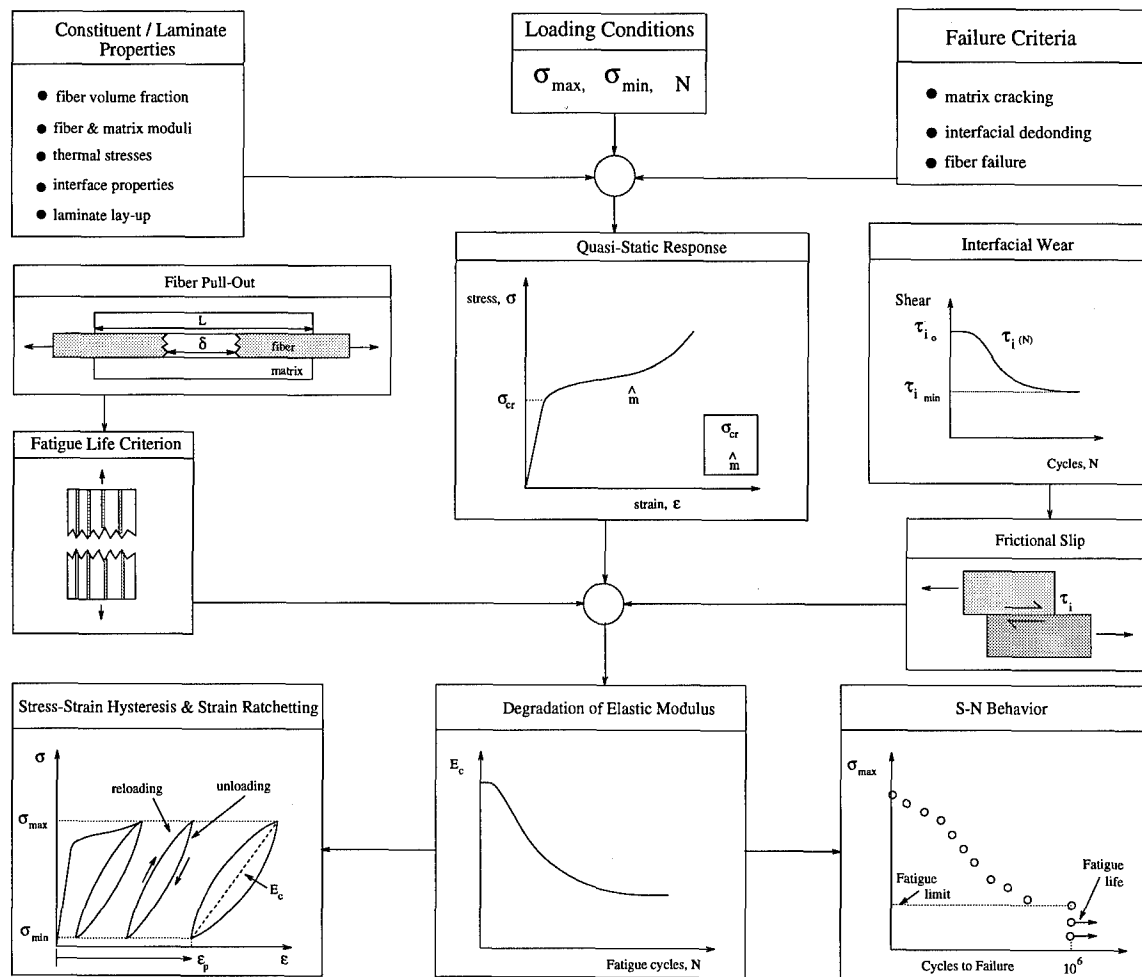
Figure B.4   Fatigue methodology

The fatigue behavior of a ceramic composite can be characterized by several salient features: stress-strain hysteresis, modulus degradation, strain ratchetting, and S-N behavior. Each of these are illustrated in Fig. 2.5. *Stress-strain hysteresis* refers to the size (e.g. width) and shape of the loading and unloading laminate response which (numerically) describes a closed loop within the stress-strain response (Fig. 2.5). The hysteresis is caused primarily by frictional sliding of the fiber/matrix constituents in regions where the interface has debonded and, moreover, the area enclosed by the loop represents the energy dissipated during the fatigue cycle. Hence, the hysteresis loop is a good indicator for the magnitude of the interface shear stress [100]. Similarly, decreases in the composite *modulus* are representative of the formation of damages within the laminate microstructure. In particular, *strain ratchetting*, which denotes the continuous evolution in residual/permanent strain, ϵ_p, results primarily from permanent slip of broken fibers. Finally, *S-N plots* define the expected fatigue life (and fatigue limit) of a given composite and are generated by plotting the maximum applied stress versus the maximum number of loading cycles to laminate failure. As is common throughout the literature, the *fatigue limit* is defined as the maximum allowable applied stress for which the laminate does not fail over a standard fatigue life, defined here as one-million cycles.

Figure B.4 illustrates the analysis methodology employed in the current analysis for modeling the fatigue behavior of the cross-ply laminates. The analysis calls for *a priori* knowledge of the constituent and laminate properties, as well as the loading conditions. Moreover, the principle mechanism contributing to the fatigue response must be included in the analysis. For the present study, the major contributors to the fatigue behavior are assumed to include the formation of damages (matrix cracking, interface debonding, and fiber fracture); frictional slip along the interface; the degradation in interface shear, and fiber pull-out which is the primary mechanism for strain ratchetting. In addition to these phenomena, a means for predicting laminate failure is required.

As before, σ_{cr} and $\hat{m}$ must first be obtained from a monotonic tensile test before the fatigue behavior can be determined. In addition, the degradation of interface shear, $\tau_i(N)$, during fatigue is required. Given σ_{cr}, $\hat{m}$ and $\tau_i(N)$, the stress-strain hysteresis and fatigue life may be predicted. Alternatively, $\tau_i(N)$ may be estimated by fitting empirical ϵ_p, hysteresis, and/or S-N data. This is desirable since the degradation in interface shear is difficult to measure experimentally, and therefore, such empirical data are unavailable at this time. Under the current analysis, the laminate is assumed to fail when the energy available for pulling the fibers out of the matrix, U_p, exceeds the work required to do so, W_p.

Appendix C. Origin of Hysteresis

During unloading and subsequent reloading, hysteresis in the stress-strain relationship will develop as a result of energy dissipated through frictional sliding between the constituents of ceramic composites [47, 149, 189]. Hysteresis developing from a completely debonded interface in the shear-lag formulation has been well documented [153]. For a partially debonded interface in the present shear-lag formulation, the analysis becomes slightly more complicated. This appendix develops the unloading (and subsequent reloading) behavior of a partially debonded interface based upon the shear-lag assumptions. Before presenting the analysis for the partially debonded interface, the same is presented for a completely debonded interface as a first step [153].

C.1 Completely debonded interface

The mechanics of frictional slip for a completely debonded interface is well described by Pryce and Smith [153]. The fiber is forced to carry the entire load along the plane of the matrix crack. Within this plane, the fiber obtains a maximum stress value of σ/v_f. Away from the crack plane, the additional load is transferred back into the matrix via interface shear stresses. Since the interface shear is assumed constant, the rate of transfer of stresses between constituents also remains constant. Provided the crack spacing is sufficient, the stress transfer will take place over a distance x' at which point the constituent stresses will return to their original rule-of-mixture values [153]. Since the rate of transfer of stresses is directly proportional to τ_i, x' may be determined. Pryce and Smith found x' to be

$$x' = \frac{r_f}{2\tau_i} \left[\frac{v_m}{v_f} \frac{E_m}{E_1} \sigma - \sigma_f^{th} \right] \tag{C.1}$$

where σ_f^{th} is the residual thermal stress in the fiber. Further, it may be shown from simple strength of material calculations that if the matrix is to remain stress free

along the plane of the matrix crack, then for any applied load, frictional sliding, i.e. relative displacement of points on opposite sides of the interface, will occur over the entire distance x'. Note that slip will not occur in reality until the interface shear stress exceeds some limiting or threshold value. However, in the shear-lag model the problem has been reduced to one dimension (i.e. constituent's shear stresses are neglected), and if the normal matrix stress is forced to be zero at the boundary, slip will occur for any stress value.

Upon unloading the interface shear now resists slip in the opposite direction (counterslip). Such slip again starts near the plane of the matrix crack where the constituent interactions first occur, and results mathematically in a *sign* change in τ_i over a given distance y (Fig. C.1). Further the maximum distance over which counterslip may occur is exactly one-half of the original slip distance (i.e. $y_{max} = x'/2$). This is a common phenomenon associated with frictional joints [132]. The magnitude of the shear stress resisting the counterslip is often assumed equal to the original shear stress [8, 153]. Realistically, this will not be the case especially when one considers Poisson's effects. Whichever is the case, as long as the magnitude of the shear is known, y may be easily determined since both the stresses at the boundaries and the rate of transfer of stress are known. Based upon Pryce and Smith's work, the resulting form is as shown below.

$$y = \frac{1}{2} \left\{ x' - \frac{r_f}{2\tau_i} \left[\frac{v_m}{v_f} \frac{E_m}{E_1} \sigma - \sigma_f^{th} \right] \right\} \tag{C.2}$$

Equation (C.2) assumes that the magnitude of the shear stresses are equal in areas of slip and counterslip.

Upon reloading slip must once again occur near the crack plane to ensure a stress free boundary in the matrix. This slip is assumed to occur over a distance z which is given by Eq. (C.3). Figure C.1 illustrates typical fiber stress distributions at the peak applied stress, σ_{max}; after unloading to σ_1 ($< \sigma_{max}$), and after reloading
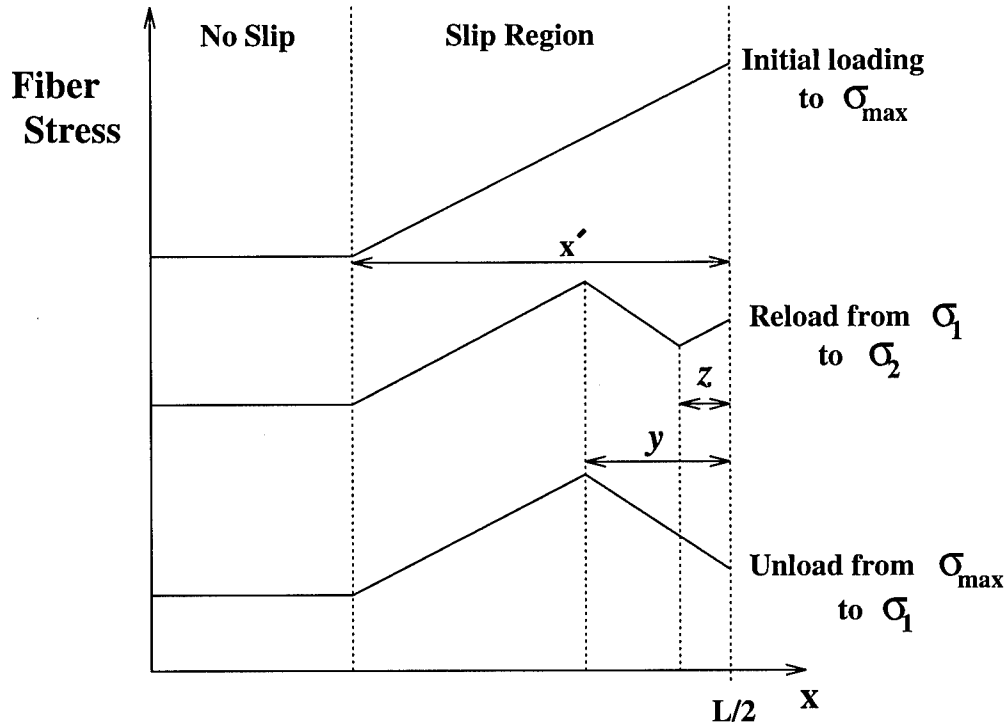
Figure C.1   Fiber stress distributions for a completely debonded interface with frictional sliding during loading (σ_{max}), unloading (σ_1) and subsequent reloading (σ_2).

to σ_2 ($< \sigma_{max}, > \sigma_1$). The main feature, to be noted, is that slip (counterslip) will occur over a given distance required to satisfy equilibrium and continuity of stresses and that the remaining portion simply unloads (or reloads) elastically.

$$z = y - \frac{1}{2}\left\{ x' - \frac{r_f}{2\tau_i}\left[\frac{v_m}{v_f}\frac{E_m}{E_1}\sigma - \sigma_f^{th} \right] \right\} \qquad (C.3)$$

C.2   Partially debonded interface

The above argument is also applicable to a partially debonded interface. However due to the shear within the bonded region, the relative magnitude of slip (counterslip) will differ from the previous case. Figure C.2 shows the constituent normal stresses and interface shear stresses for a partially debonded interface. Note that

within the debonded region ($x \in [L/2 - d, L/2]$) the shear stress is constant and yields a linear transfer of constituent stresses.
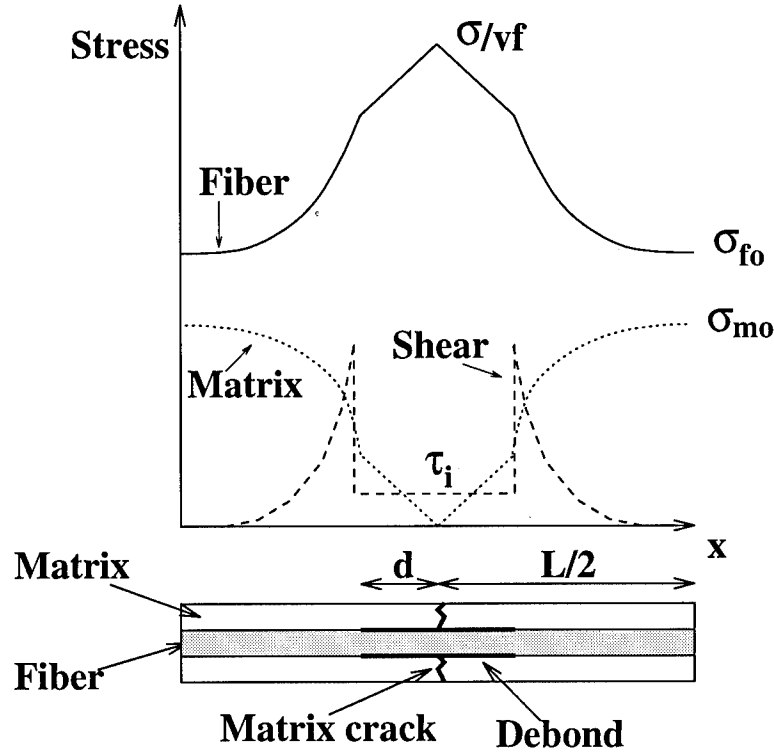
Figure C.2 Constituent stress distributions near a matrix crack for a partially debonded interface. The interface shear stress, $\tau_i(x)$, is also shown.

Clearly, based upon the formulation used in the development of the debond length with $\tau_i < \tau_{ult}$, slip extends throughout the entire debonded region. Upon unloading from a peak value of σ_{max}, counterslip will again occur near the plane of the matrix crack over a distance y. To simply use the existing shear-lag equations at the new stress level ($\sigma < \sigma_{max}$) would incorrectly assume that a portion of the model within the bonded region has *not unloaded elastically* $\{\epsilon_m(x_o) \neq \epsilon_f(x_o); \quad x_o \in [0, L/2 - d]\}$ while unloading in surrounding regions has been elastic. In theory, what must occur is that there will be a reversal of slip near the plane of the matrix crack and the remaining areas must unload elastically. However, due to the large shear

stresses within the bonded region, counterslip may occur over the entire debond length. But since slip cannot occur in the bonded region, the maximum counter slip distance is equal to the debond length, i.e. $y_{max} = d$.

Upon reloading (to σ_2), slip again occurs near the crack plane over a distance z. Three cases need to be considered here. For $y < d$, z is determined by ensuring τ_i evaluated at $x = L/2 - d$ equals τ_{ult}. For $y = d$ and $z < d$, z is again determined such that reloading within the bonded region is elastic and where $|\tau_i(x)|$ at $x = L/2 - d$ is still constant but now $< \tau_{ult}$. The resulting fiber stresses may be determined by letting $y = d$ in the previous equations. For $y > d$ and $z > d$, the original shear-lag equations are again valid.

C.2.1 Unidirectional Laminate. Since τ_i has been assumed constant in the present analysis, as is typical of most studies [8,106,113], the extent of interface slip during loading and unloading may be determined analytically [132,153,174]. For the unloading portion of the cycle, the counterslip distance y may be calculated from Eq. (3.45) by noting that the magnitude of the interface shear, $\tau_i(x)$, at $x = L/2 - d$ remains equal to τ_{ult} since the deformations within the bonded region are know to be elastic. The analysis results in the following expression for y.

$$y = \frac{1}{2}\left\{ d - \frac{1}{2}r_f \frac{v_m}{v_f}\frac{\sigma_{m_o}}{\tau_i} + \frac{1}{\beta \tanh \beta(L/2 - d)}\frac{\tau_{ult}}{\tau_i} \right\} \tag{C.4}$$

Furthermore, the stresses within the fiber may be shown to be defined by the following set of equations.

$$\sigma_f(x) = \sigma_{f_o} + \frac{\cosh(\beta x)}{\cosh[\beta(L/2 - d)]}\left(\frac{v_m}{v_f}\sigma_{m_o} - \frac{2\tau_i}{r_f}(d - 2y) \right) \quad x \in \left[0, \frac{L}{2} - d\right] \tag{C.5}$$

$$\sigma_f(x) = \frac{\sigma}{v_f} + \frac{2\tau_i}{r_f}\left(x + 2y - \frac{L}{2} \right) \quad x \in \left[\frac{L}{2} - d, \frac{L}{2} - y\right] \tag{C.6}$$

$$\sigma_f(x) = \frac{\sigma}{v_f} + \frac{2\tau_i}{r_f}\left(\frac{L}{2} - x \right) \quad x \in \left[\frac{L}{2} - y, \frac{L}{2}\right] \tag{C.7}$$

Since slip cannot occur within the bonded region, the maximum counterslip distance is equal to the debond length, i.e. $y_{max} = d$.

Upon reloading, slip again occurs near the crack plane; this time over a distance z. Three cases need to be considered here. For $y < d$, z is again determined by ensuring $\tau_i(x)$ evaluated at $x = L/2 - d$ equals τ_{ult}. This results in the following.

$$z = y - \frac{1}{2}\left\{ d - \frac{1}{2}r_f \frac{v_m}{v_f}\frac{\sigma_{m_o}}{\tau_i} + \frac{1}{\beta \tanh \beta(L/2 - d)}\frac{\tau_{ult}}{\tau_i} \right\} \qquad \text{(C.8)}$$

In addition, the fiber stress for this case is given by Eqs. (C.9) through (C.12).

$$\sigma_f(x) = \sigma_{f_o} + \frac{\cosh(\beta x)}{\cosh[\beta(L/2 - d)]}\left(\frac{v_m}{v_f}\sigma_{m_o} + \frac{2\tau_i}{r_f}[2(y - z) - d] \right) \quad x \in \left[0, \frac{L}{2} - d\right] \qquad \text{(C.9)}$$

$$\sigma_f(x) = \frac{\sigma}{v_f} + \frac{2\tau_i}{r_f}\left(x + 2(y - z) - \frac{L}{2} \right) \quad x \in \left[\frac{L}{2} - d, \frac{L}{2} - y\right] \qquad \text{(C.10)}$$

$$\sigma_f(x) = \frac{\sigma}{v_f} + \frac{2\tau_i}{r_f}\left(\frac{L}{2} - 2z - x \right) \quad x \in \left[\frac{L}{2} - y, \frac{L}{2} - z\right] \qquad \text{(C.11)}$$

$$\sigma_f(x) = \frac{\sigma}{v_f} - \frac{2\tau_i}{r_f}\left(\frac{L}{2} - x \right) \quad x \in \left[\frac{L}{2} - z, \frac{L}{2}\right] \qquad \text{(C.12)}$$

For $y = d$ and $z < d$, the deformations within the bonded region is still elastic; however, $|\tau_i(x = L/2 - d)| < \tau_{ult}$. The maximum existing shear may be determined from Eq. (C.4) by letting $y = d$ and solving for τ_{ult}. Moreover, the resulting fiber stresses may be determined from Eqs. (C.9) through (C.12) with $y = d$. Figure C.3 represents a sequence of normal (axial) fiber stress distributions during unloading and reloading for both $y_{max} < d$ and $y_{max} = d$. Note that in both cases, hysteresis will develop during unloading and reloading.

For $y > d$ and $z > d$, the original shear-lag equations [Eq. (3.45)] are again valid, and more importantly the state of stress and composite damage is *exactly* the same as if the unloading never occurred. This is why under the assumed conditions of repeated loading, the stress-strain response of coupons cycled to the same maximum
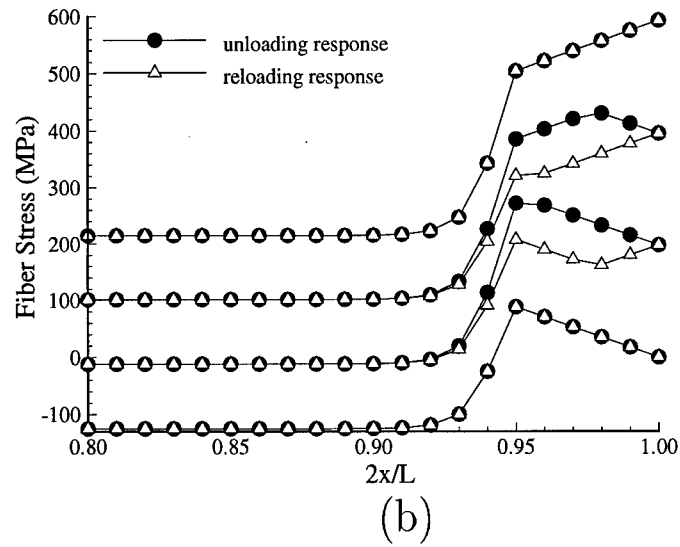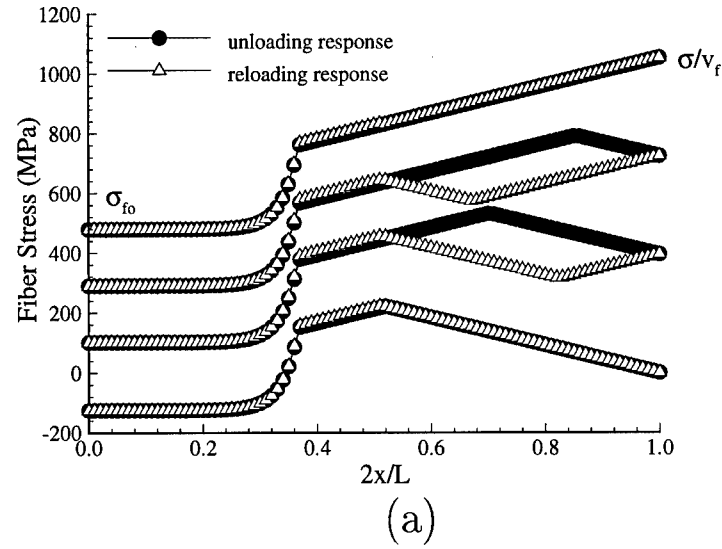
Figure C.3 A time history representation of the normal fiber stress during un-
loading and subsequent reloading of a damaged composite where $x \in$
$[0, L/2]$. In the above figures, matrix cracks are assumed to exist at
abscissa values of ± 1. Hence, for the figures shown, the fiber stress at
$x = 0$ has a magnitude equivalent to σ_{f_o}. (a) $y_{max} < d$ and $\sigma = 400$,
275, 150 and 0 MPa. (b) $y_{max} = d$ and $\sigma = 225$, 150, 75 and 0 MPa.

stress remain constant. In addition, the fatigue behavior and fatigue specific damages cannot be modeled under the present conditions. Eqs. (C.4) and (C.8) are valid under the assumption that the interface is partially bonded, once the interface debonds fully (i.e. $d = L/2$), the analysis must be re-evaluated as follows.

Once the interface completely debonds, the slip distances y and z can be obtained by ensuring that the constituent displacement remain elastic in regions where slip has not occurred. Furthermore, for the current shear-lag formulation, the constituent stresses for the fiber and matrix, $\sigma_f(x)$ and $\sigma_m(x)$, are given by Eqs. (C.13) through (C.16) under the conditions of complete debonding and unloading.

$$\sigma_f(x) = \frac{\sigma}{v_f(1-D)} + \frac{2\tau_i}{r_f}(x + 2y - L/2) \qquad \text{for} \quad x \in [0, L/2 - y] \qquad \text{(C.13)}$$

$$\sigma_f(x) = \frac{\sigma}{v_f(1-D)} + \frac{2\tau_i}{r_f}(L/2 - x) \qquad \text{for} \quad x \in [L/2 - y, L/2] \qquad \text{(C.14)}$$

$$\sigma_m(x) = -\frac{v_f}{v_m}\frac{2\tau_i}{r_f}(x + 2y - L/2) \qquad \text{for} \quad x \in [0, L/2 - y] \qquad \text{(C.15)}$$

$$\sigma_m(x) = -\frac{v_f}{v_m}\frac{2\tau_i}{r_f}(L/2 - x) \qquad \text{for} \quad x \in [L/2 - y, L/2] \qquad \text{(C.16)}$$

Equations (C.17) and (C.18) represent the change in constituent strains for a partial unloading from σ_{max} to σ.

$$\Delta\epsilon_f = \frac{2}{E_f L}\int_o^{L/2-y}\left\{\sigma_f(x)_{\substack{|\sigma=\sigma_{max}\\y=0}} - \sigma_f(x)_{\substack{|\sigma=\sigma\\y\neq0}}\right\}dx \qquad \text{(C.17)}$$

$$\Delta\epsilon_m = \frac{2}{E_m L}\int_o^{L/2-y}\left\{\sigma_m(x)_{\substack{|\sigma=\sigma_{max}\\y=0}} - \sigma_m(x)_{\substack{|\sigma=\sigma\\y\neq0}}\right\}dx \qquad \text{(C.18)}$$

Based upon these results, the criterion for determining the slip distance for a completely debonded interface becomes

$$\Delta\epsilon_m - \Delta\epsilon_f = 0. \qquad \text{(C.19)}$$

When considering Eqs. (C.13) through (C.19), y is determined to be

$$y = \begin{cases} \dfrac{1}{4} \left\{ \dfrac{(\sigma_{max} - \sigma)}{\tau_i} \dfrac{E_m}{E_1} \dfrac{v_m}{v_f} \dfrac{r_f}{(1 - D)} \right\} & \text{for} \quad y < L/2 \\ L/2 & \text{for} \quad y \geq L/2. \end{cases} \tag{C.20}$$

The reader may verify that Eq. (C.20) is equivalent to Eq. (C.2). During reloading of the unit-cell, Eq. (C.19) may once again be applied. This time, the slip distance z, is found to obey the following equations.

$$z = \begin{cases} \dfrac{1}{4} \left\{ \dfrac{(\sigma - \sigma_{min})}{\tau_i} \dfrac{E_m}{E_1} \dfrac{v_m}{v_f} \dfrac{r_f}{(1 - D)} \right\} & \text{for} \quad z < L/2 \\ L/2 & \text{for} \quad z \geq L/2 \end{cases} \tag{C.21}$$

Hence, Eqs. (C.20) and (C.21) are used when the interface is purely frictional. A known phenomenon associated with frictional joints is that during unloading, the maximum counterslip distance is equal to exactly one-half of the original slip distance [60, 132]. However, for a partially bonded interface, this restriction is no longer true [174] (reference appendix D). It is somewhat convenient to express the slip distance in relation to the debond length (e.g. y/d and z/d). Denoting this ratio by $\mathcal{D}$, it may be shown that for a *partially bonded* interface,

$$\mathcal{D} = \begin{cases} \dfrac{1}{2} \left(1 - \dfrac{v_m \sigma_{m_o} r_f}{2 v_f \tau_i d} + \dfrac{\tau_{ult}}{\tau_i \beta d \tanh[\beta(L/2 - d)]} \right) & \text{unloading} \\ \mathcal{D}_u - \dfrac{1}{2} \left(1 - \dfrac{v_m \sigma_{m_o} r_f}{2 v_f \tau_i d} + \dfrac{\tau_{ult}}{\tau_i \beta d \tanh[\beta(L/2 - d)]} \right) & \text{reloading.} \end{cases} \tag{3.123}$$

where $\mathcal{D}_u$ is $\mathcal{D}$ at $\sigma = \sigma_{min}$ (unloaded), and for a *completely debonded* interface,

$$\mathcal{D} = \begin{cases} \dfrac{1}{2} \left(\dfrac{v_m E_m r_f}{v_f (1 - D) E_1 L} \dfrac{\sigma_{max} - \sigma}{\tau_i} \right) & \text{unloading} \\ \dfrac{1}{2} \left(\dfrac{v_m E_m r_f}{v_f (1 - D) E_1 L} \dfrac{\sigma - \sigma_{min}}{\tau_i} \right) & \text{reloading.} \end{cases} \tag{3.124}$$

Before presenting results for repeated loading conditions, note that Eqs. (C.4) and (C.8) can be used to approximate the slip distances for a completely debonded interface. For example, during unloading, Eq. (C.4) can be used to estimate y by considering the limits as the interface debonds ($d \to L/2$) and the interface strength (which is a function of the bonding energy) vanishes ($\tau_{ult} \to 0$), i.e.

$$\lim_{d \to \frac{L}{2}} \lim_{\tau_{ult} \to 0} \left(\frac{1}{2} \left\{ d - \frac{1}{2} r_f \frac{v_m}{v_f} \frac{\sigma_{m_o}}{\tau_i} + \frac{1}{\beta \tanh \beta (L/2 - d)} \frac{\tau_{ult}}{\tau_i} \right\} \right) \qquad (C.22)$$

or

$$y = \frac{1}{2} \left\{ d - \frac{1}{2} r_f \frac{v_m}{v_f} \frac{\sigma_{m_o}}{\tau_i} + C \right\} \qquad (C.23)$$

where the constant C is obtained by ensuring y vanishes at $\sigma = \sigma_{max}$. Equation (C.23) does not (mathematically) follow from Eq. (C.22); however, it does provide a convenient link between Eqs. (C.4) and (C.20).

C.2.2 Cross-Ply Laminate. The frictional sliding which occurs along the fiber/matrix interface during cyclic or repeated loading conditions determines in large part the stress-strain and stress-strain hysteresis behavior of a ceramic matrix composite. For a cross-ply laminate, the interface debonding and slip within the 0° plies is assumed to be the sole contributor to the hysteresis phenomenon. Furthermore, interface slip occurs between the constituents over the entire debonded region, and the extent of the slip is governed by the frictional resistance along their common interface. During unloading, the constituents slip in the opposite direction over a discrete region, y. As shown in chapter four, the extent of counterslip may be determined from equilibrium and displacement continuity relations. For the cross-ply composite, y is found to be

$$y_i = \frac{1}{2} \left\{ d_i - \frac{1}{2} \frac{r_f}{\tau_i} \left[\frac{1}{v_f} \left(\frac{b+d}{b}\sigma - \frac{d}{b}\sigma_T(x_{t_{|x=\frac{L}{2}}}) \right) - \mathcal{T}\frac{\cosh\left(\lambda x_{t_{|x=\phi_i}}\right)}{\cosh(\lambda L_t/2)} - \sigma_f^o \right. \right.$$

$$\left. + \frac{\mathcal{T}\lambda}{\beta} \frac{\sinh\left(\lambda x_{t_{|x=\phi_j}}\right) - \cosh(\phi_l - \phi_r)\sinh\left(\lambda x_{t_{|x=\phi_i}}\right)}{\sinh(\phi_l - \phi_r)\cosh(\lambda L_t/2)} \right]$$

$$\left. - \frac{\tau_{ult}}{\beta\tau_i}\left(\frac{1}{\tanh(\phi_l - \phi_r)} + \frac{1}{\sinh(\phi_l - \phi_r)} \right) \right\} \qquad (C.24)$$

where $\phi_i = \beta\left(\mp L/2 \pm d_i\right)$ and $j = r$ (right) if $i = l$ (left) or $j = l$ if $i = r$. Recall within the cross-ply analysis, the fiber stress is not symmetric and therefore there exists a left counterslip distance, y_l and a right counterslip distance, y_r. The reader may verify that if a symmetric damage configuration exists within the representative volume element (e.g. $\phi_i = -\phi_j$ and $x_{t_{|x=\phi_i}} = -x_{t_{|x=-\phi_j}}$) and if $\sigma_T(x) \simeq \sigma_T^o$ with d and σ_T^o vanishing then Eq. (C.24) reduces to the unidirectional counterslip distance [Eq. (C.4)].

During reloading, the frictional resistance will again reverse near the plane of the matrix crack; this time over a distance z. It may be shown that

$$z_i = y_i - \frac{1}{2} \left\{ d_i - \frac{1}{2} \frac{r_f}{\tau_i} \left[\frac{1}{v_f} \left(\frac{b+d}{b}\sigma - \frac{d}{b}\sigma_T(x_{t_{|x=\frac{L}{2}}}) \right) - \mathcal{T}\frac{\cosh\left(\lambda x_{t_{|x=\phi_i}}\right)}{\cosh(\lambda L_t/2)} - \sigma_f^o \right. \right.$$

$$\left. + \frac{\mathcal{T}\lambda}{\beta} \frac{\sinh\left(\lambda x_{t_{|x=\phi_j}}\right) - \cosh(\phi_l - \phi_r)\sinh\left(\lambda x_{t_{|x=\phi_i}}\right)}{\sinh(\phi_l - \phi_r)\cosh(\lambda L_t/2)} \right]$$

$$\left. - \frac{\tau_{ult}}{\beta\tau_i}\left(\frac{1}{\tanh(\phi_l - \phi_r)} + \frac{1}{\sinh(\phi_l - \phi_r)} \right) \right\}. \qquad (C.25)$$

Once again, with the proper assumptions, Eq. (C.25) reduces to the unidirectional case [Eq. (C.8)]. Given y and z, the fiber stress may be easily obtained, and are

provided below. During unloading,

$$\overline{\{(-L/2)\}} + \frac{2\tau_i}{r_f}(L/2 + x) \quad \text{for } x \in [-L/2, \ -L/2 + y_l], \quad \text{(C.26)}$$

$$\overline{\{(-L/2)\}} + \frac{2\tau_i}{r_f}(2y_l - L/2 - x) \quad \text{for } x \in [-L/2 + y_l, \ -L/2 + d_l], \quad \text{(C.27)}$$

$$\sigma_f(x) = c_3 \sinh(\beta x) + c_4 \cosh(\beta x)$$
$$+ \frac{\mathcal{T} \cosh\left(\lambda x_{t_{|x=x}}\right)}{\cosh\left(\lambda L_t/2\right)} + \sigma_f^o \quad \text{for } x \in [-L/2 + d_l, \ L/2 - d_r], \quad \text{(C.28)}$$

$$\overline{\{(L/2)\}} + \frac{2\tau_i}{r_f}(2y_r - L/2 + x) \quad \text{for } x \in [L/2 - d_r, \ L/2 - y_r], \quad \text{(C.29)}$$

$$\overline{\{(L/2)\}} + \frac{2\tau_i}{r_f}(L/2 - x) \quad \text{for } x \in [L/2 - y_r, \ L/2] \quad \text{(C.30)}$$

where

$$\overline{\{(-L/2)\}} \doteq \frac{1}{v_f(1-D)}\left\{\frac{b+d}{b}\sigma - \frac{d}{b}\sigma_T\left(x_{t_{|x=-L/2}}\right)\right\} \quad \text{(C.31)}$$

and

$$\overline{\{(L/2)\}} \doteq \frac{1}{v_f(1-D)}\left\{\frac{b+d}{b}\sigma - \frac{d}{b}\sigma_T\left(x_{t_{|x=L/2}}\right)\right\}. \quad \text{(C.32)}$$

For the subsequent reloading,

$$\overline{\{(-L/2)\}} - \frac{2\tau_i}{r_f}(L/2 + x) \quad \text{for } x \in [-L/2, \ -L/2 + z_l], \quad \text{(C.33)}$$

$$\overline{\{(-L/2)\}} + \frac{2\tau_i}{r_f}(L/2 + x - 2z_l) \quad \text{for } x \in [-L/2 + z_l, \ -L/2 + y_l], \quad \text{(C.34)}$$

$$\overline{\{(-L/2)\}} + \frac{2\tau_i}{r_f}(2\{y_l - z_l\} - L/2 - x) \quad \text{for } x \in [-L/2 + y_l, \ -L/2 + d_l], \quad \text{(C.35)}$$

$$\sigma_f(x) = c_3 \sinh(\beta x) + c_4 \cosh(\beta x)$$
$$+ \frac{\mathcal{T} \cosh\left(\lambda x_{t_{|x=x}}\right)}{\cosh\left(\lambda L_t/2\right)} + \sigma_f^o \quad \text{for } x \in [-L/2 + d_l, \ L/2 - d_r], \quad \text{(C.36)}$$

C-12

$$\overline{\{(L/2)\}} + \frac{2\tau_i}{r_f} \left(2\{y_r - z_r\} - L/2 + x \right) \quad \text{for} \ \ x \in [L/2 - d_r, \ L/2 - y_r], \quad \text{(C.37)}$$

$$\overline{\{(L/2)\}} + \frac{2\tau_i}{r_f} \left(L/2 - 2z_r - x \right) \quad \text{for} \ \ x \in [L/2 - y_r, \ L/2 - z_r], \quad \text{(C.38)}$$

$$\overline{\{(L/2)\}} + \frac{2\tau_i}{r_f} \left(L/2 - x \right) \quad \text{for} \ \ x \in [L/2 - z_r, \ L/2]. \quad \text{(C.39)}$$

For repeated loading, once the composite is reloaded to σ_{max}, both y and z vanish. Hence, the predicted strain at $\sigma = \sigma_{max}$ is independent of the loading history. Additional damage mechanisms need to be considered if the material response under fatigue loading is to be modeled.

If the fiber/matrix interface is completely debonded then the slip distances y and z may again be determined by ensuring that the constituent displacements are elastic in regions where slip has not occurred, i.e.

$$\Delta\epsilon_m - \Delta\epsilon_f = 0 \quad \text{(C.19)}$$

and where Eqs. (C.17) and (C.18) are still applicable. The axial fiber stress is shown below in Eqs. (C.40) through (C.49) for the unloading and reloading conditions. The axial matrix stress is determined from equilibrium [Eqs. (3.52) and (3.53)]. The axial fiber stress in the 0° ply of a cross-ply laminate with a fully debonded interface during unloading is

$$\sigma_f(x) = \overline{\{(-L/2)\}} + \frac{2\tau_i}{r_f} \left(L/2 + x \right) \quad \text{for} \ \ x \in [-L/2, \ -L/2 + y_l], \quad \text{(C.40)}$$

$$\sigma_f(x) = \overline{\{(-L/2)\}} + \frac{2\tau_i}{r_f} \left(2y_l - L/2 - x \right) \quad \text{for} \ \ x \in [-L/2 + y_l, \ 0], \quad \text{(C.41)}$$

$$\sigma_f(x) = \overline{\{(L/2)\}} + \frac{2\tau_i}{r_f} \left(x + 2y_r - L/2 \right) \quad \text{for} \ \ x \in [0, \ L/2 - y_r], \quad \text{(C.42)}$$

$$\sigma_f(x) = \overline{\{(L/2)\}} + \frac{2\tau_i}{r_f} \left(L/2 - x \right) \quad \text{for} \ \ x \in [L/2 - y_r, \ L/2], \quad \text{(C.43)}$$

and during reloading, these stresses become

$$\sigma_f(x) = \overline{\{(-L/2)\}} - \frac{2\tau_i}{r_f}\left(L/2 + x\right) \qquad \text{for} \quad x \in \left[-L/2,\; -L/2 + z_l\right], \qquad \text{(C.44)}$$

$$\sigma_f(x) = \overline{\{(-L/2)\}} + \frac{2\tau_i}{r_f}\left(L/2 - 2z_l + x\right) \qquad \text{for} \quad x \in \left[-L/2 + z_l,\; -L/2 + y_l\right], \qquad \text{(C.45)}$$

$$\sigma_f(x) = \overline{\{(-L/2)\}} + \frac{2\tau_i}{r_f}\left(2\left(y_l - z_l\right) - L/2 - x\right) \qquad \text{for} \quad x \in \left[-L/2 + y_l,\; 0\right], \qquad \text{(C.46)}$$

$$\sigma_f(x) = \overline{\{(L/2)\}} + \frac{2\tau_i}{r_f}\left(2\left(y_r - z_r\right) - L/2 + x\right) \qquad \text{for} \quad x \in \left[0,\; L/2 - y_r\right], \qquad \text{(C.47)}$$

$$\sigma_f(x) = \overline{\{(L/2)\}} + \frac{2\tau_i}{r_f}\left(L/2 - 2z_r - x\right) \qquad \text{for} \quad x \in \left[L/2 - y_r,\; L/2 + z_r\right], \qquad \text{(C.48)}$$

$$\sigma_f(x) = \overline{\{(L/2)\}} - \frac{2\tau_i}{r_f}\left(L/2 - x\right) \qquad \text{for} \quad x \in \left[L/2 - z_r,\; L/2\right]. \qquad \text{(C.49)}$$

Appendix D. Sliding Along Frictional and Non-Frictional Interfaces

The following presentation illustrates that for a purely frictional interface in which the shear stress is assumed constant, the maximum counterslip distance which may develop during unloading is exactly one-half of the original slip distance. For non-frictional interfaces, the counterslip distance may be larger. Note that the development presented in this appendix is intended to be neither mathematically rigorous nor descriptive of the problem mechanics of a composite interface; rather is thought to be an interesting treatise.

The development assumes that one-quarter of the representative volume element can be modeled as an infinite sequence of frictional blocks and linear springs (Fig. D.1). The lower series of blocks in Fig. D.1 represent the fiber region. These blocks are numbered $1, 2 \ldots n$. Similarly the upper blocks represent the matrix and are numbered $n + 1, n + 2 \ldots 2n - 1$. The spring stiffnesses are A and B for the matrix and fiber respectively. The shear stresses which develop along the interface for each pair of blocks (matrix and fiber) are denoted $\tau_1, \tau_2 \ldots \tau_{n-1}$. Relative displacements $(\bar{x}_1, \bar{x}_2 \cdots \bar{x}_{2n-1})$ are given by (fixed) local coordinates $(x_1, x_2 \cdots x_{2n-1})$. From symmetry, $\bar{x}_1, \bar{x}_{n+1}$ and τ_1 are all zero. In addition, the composite interface is assumed to be completely debonded.

As the applied load, F, is increased from zero, individual pairs of blocks will displace with no relative slip initially between them. For this condition, the interface shear stresses are given by

$$
\tau_k = \begin{cases} 0 & \text{for} \quad k = 1, 2 \ldots n - 2 \\ KF & \text{for} \quad k = n - 1 \end{cases} \tag{D.1}
$$

where $K = A/(A + B)$. Eventually τ_{n-1} will exceed the ultimate frictional resistance of the blocks, τ_{ult}. At this point, blocks $n - 1$ and $2n - 1$ slip and the shear stresses
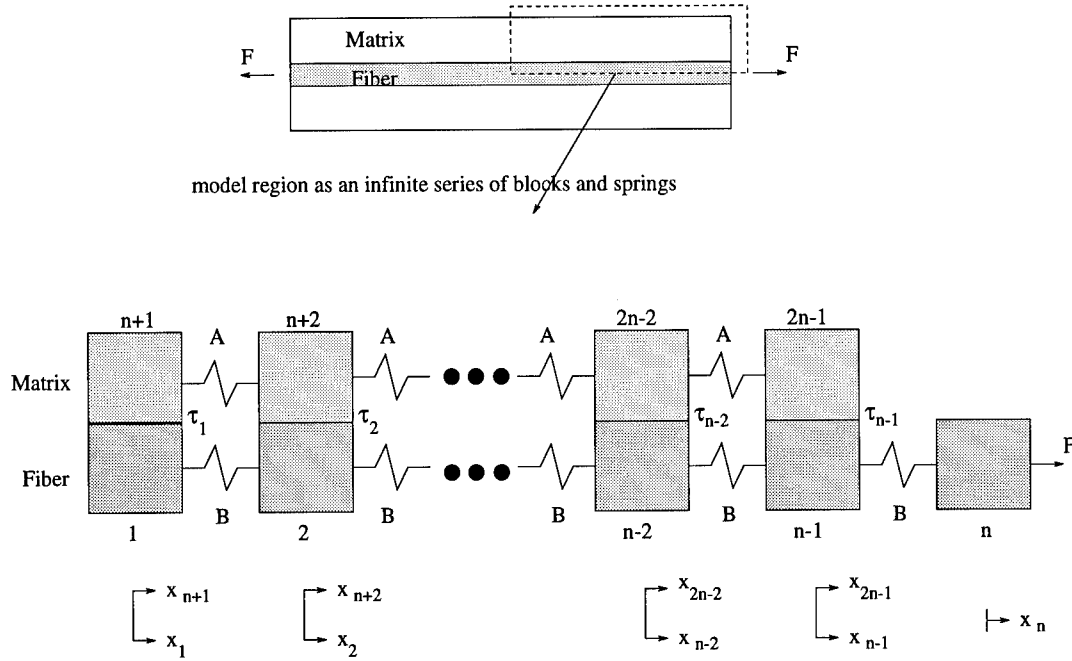
Figure D.1   Representative model using an infinite number of frictional blocks and
linear springs.

become

$$
\tau_k = \begin{cases} 0 & \text{for} \quad k = 1, 2 \ldots n - 3 \\ KF - \tau_{ult} & \text{for} \quad k = n - 2 \\ \tau_{ult} & \text{for} \quad k = n - 1 \end{cases}
\qquad (D.2)
$$

when the second pair of blocks $[n - 2$ and $2(n - 1)]$ slip, the shear becomes

$$
\tau_k = \begin{cases} 0 & \text{for} \quad k = 1, 2 \ldots n - 4 \\ KF - 2\tau_{ult} & \text{for} \quad k = n - 3 \\ \tau_{ult} & \text{for} \quad k = n - 2, n - 1 \end{cases}
\qquad (D.3)
$$

and so on.

The corresponding block displacements are given by the following:

$$
\begin{Bmatrix}
\bar{x}_1 \\
\bar{x}_2 \\
\vdots \\
\bar{x}_{n-3} \\
\bar{x}_{n-2} \\
\bar{x}_{n-1} \\
\bar{x}_n \\
\bar{x}_{n+1} \\
\bar{x}_{n+2} \\
\vdots \\
\bar{x}_{2n-3} \\
\bar{x}_{2n-2} \\
\bar{x}_{2n-1}
\end{Bmatrix}
=
\begin{Bmatrix}
0 \\
\frac{1}{B}\left[F - \sum_{i=2}^{n-1}\tau_i\right] \\
\vdots \\
\frac{1}{B}\left[(n-4)F - (n-5)\sum_{i=n-4}^{n-1}\tau_i - (n-6)\tau_{n-5} - \cdots - 2\tau_3 - \tau_2\right] \\
\frac{1}{B}\left[(n-3)F - (n-4)\sum_{i=n-3}^{n-1}\tau_i - (n-5)\tau_{n-4} - \cdots - 2\tau_3 - \tau_2\right] \\
\frac{1}{B}\left[(n-2)F - (n-3)\sum_{i=n-2}^{n-1}\tau_i - (n-4)\tau_{n-3} - \cdots - 2\tau_3 - \tau_2\right] \\
\frac{1}{B}\left[(n-1)F - (n-2)\tau_{n-1} - (n-3)\tau_{n-2} - \cdots - 2\tau_3 - \tau_2\right] \\
0 \\
\frac{1}{A}\sum_{i=2}^{n-1}\tau_i \\
\vdots \\
\frac{1}{A}\left[(n-4)\sum_{i=n-3}^{n-1}\tau_i + (n-5)\tau_{n-4} + \cdots + 2\tau_3 + \tau_2\right] \\
\frac{1}{A}\left[(n-3)\sum_{i=n-2}^{n-1}\tau_i + (n-4)\tau_{n-3} + \cdots + 2\tau_3 + \tau_2\right] \\
\frac{1}{A}\left[(n-2)\tau_{n-1} + (n-3)\tau_{n-2} + \cdots + 2\tau_3 + \tau_2\right]
\end{Bmatrix}.
$$

In order to ensure that maximum slip and counterslip occur, a load sufficient to cause $\tau_2 = \tau_{ult}$ will be applied. That is, at the maximum applied load, F_{max}, all but the last two pair of blocks (1 & $n+1$ and 2 & $n+2$) are assumed to slip. Further, blocks 1 & $n+1$ can never slip and for any load greater than F_{max}, blocks 2 & $n+2$ will slip. This requires $F_{max} = (n-2)\tau_{ult}/K$. Now define, $\bar{y}_i \equiv \bar{x}_{i_{max}} - \bar{x}_i$ where $\bar{x}_{i_{max}}$ is the maximum displacement for the ith block (i.e. displacement at F_{max}). Let $\bar{y}_{i_{max}}$ denote $\bar{x}_{i_{max}} - \bar{x}_i$ evaluated at zero load. Further note that maximum counterslip will occur between blocks $n-1$ and $2n-1$. Let ψ represent the (maximum) ratio of the final slip distance (ie. at zero load) over the original slip distance (ie. at F_{max})

for these blocks. That is

$$\psi = \frac{\text{original slip distance} - \text{counterslip distance}}{\text{original slip distance}} \qquad (D.4)$$

or

$$\psi = \frac{\left(\bar{x}_{n-1_{max}} - \bar{y}_{n-1_{max}}\right) - \left(\bar{x}_{2n-1_{max}} - \bar{y}_{2n-1_{max}}\right)}{\bar{x}_{n-1_{max}} - \bar{x}_{2n-1_{max}}}. \qquad (D.5)$$

Substituting in the proper displacements, it can be shown that

$$\psi = \frac{\displaystyle\sum_{k=n/2}^{2(n-1)} k - \sum_{j=1}^{n/2-1} j}{\displaystyle\sum_{i=1}^{n-3} i - \frac{(n-2)(n-3) + K}{(BK)^2}}. \qquad (D.6)$$

For K greater than 0.05, the limit of ψ as $n \to \infty$ is 1/2. Hence the maximum reversal of slip is one-half of the original slip distance. As expected, ψ vanishes for A or B zero. For ceramic matrix composites, $K \in (0.3, 0.5)$.

A partially bonded interface may be modeled by restricting slip between a pair of blocks and allowing the shear to exceed τ_{ult}. For the special case of $n = 6$, $K = .32$, and $\tau_2 = 2\tau_{ult}$, ψ was found to be 1/3. Similarly, with $\tau_2 = 10\tau_{ult}$, $\psi = 0.05$ and with $\tau_2 = 10000\tau_{ult}$, $\psi = 0.00005$. Hence it may be surmised that for a partially debonded interface $\psi \in [0, 1]$ whereas for a completely debonded interface $\psi \in [1/2, 1]$. Although admittedly not a proof, the preceding analysis has given some support to the original hypothesis that the maximum counterslip for a completely debonded interface is exactly one-half of the original slip distance whereas counterslip may extend over the entire slip distance for a partially debonded interface.

Appendix E. Critical Matrix Strain Energy (CMSE) Failure

Criterion

This appendix examines, in detail, the *critical matrix strain energy* (CMSE) criterion used within the present study to determine the evolution of matrix cracking in ceramic matrix composites as initially presented in chapter three. In summary, the instantaneous crack spacing, L, is determined by ensuring that the matrix strain energy remains constant once it obtains some critical value. Mathematically, this criterion is represented by Eq. (3.117) where the left hand side is the instantaneous matrix strain energy; U_{cr_m} is the critical matrix strain energy, and σ_{cr} is the critical composite stress.

$$U_{m_o} + U_m(L) = U_{cr_m} \qquad \text{for all} \quad \sigma \geq \sigma_{cr} \qquad (3.117)$$

Under the current analysis, the initial crack spacing, L_{init}, must be estimated by means other than Eq. (3.117) since for $\sigma = \sigma_{cr}$ multiple solutions exists. In fact, computationally, an infinite number of solutions exists. As such, a technique for estimating L_{init} is presented in this appendix. Also, a detailed discussion of how the matrix strain energy varies with loading; interface debonding and matrix cracking is provided. In particular, several *matrix strain energy versus crack density* plots are presented. These plots portray a unique representation for the CMSE criterion in which bounding limits for the crack density and expected trends in the predicted crack density evolution can be obtained. Following this presentation, the CMSE criterion is compared with more traditional fracture mechanics approaches. Advantages and limitations of both techniques are provided. In the final section, the models sensitivity to several material parameters (e.g. σ_{cr}, τ_i and τ_{ult}) is investigated. First, however, an introduction to the CMSE criterion is presented.

E.1 Development of the Critical Matrix Strain Energy

In previous analytical studies, two failure criteria for predicting matrix cracking have been widely used: maximum stress (or strain) theories [28, 37, 113], and classical fracture mechanics approaches [20, 130, 196]. The latter includes both the energy balance formulation as originally proposed by ACK [8], and the classical stress intensity factor approach [127]. Although the simplicity of the maximum stress criterion is appealing, it typically results in rapid saturation of matrix cracking with small increases in loading. That is, the evolution of matrix cracking occurs over a very narrow stress range. This results in a "stepped" stress-strain response which is not seen in experiments of CMCs [193].

Classical fracture mechanics approaches have yielded an extensive amount of information on the mechanics of matrix cracking. These may be used to determine closed-form solutions for the matrix crack spacing [20,179,201]. In addition, several of these approaches provide lower bounds for the *initial* matrix cracking stress as well as estimates for the saturated crack spacings (i.e. upper bounds) [8,20,127,130,179,196]. One approach presented by Weitsman and Zhu [201] employs a matrix cracking criterion analogous to Budiansky *et al* [20] to determine the crack densities for a unit-cell similar to the one used in the present study (Fig. 3.7). Their analysis involves comparison of the energies associated with two damage configurations ("state I" and "state II", Fig. E.1), under constant stress, and assumes the additional matrix cracks (state II versus state I) develop once the available energy (shown as shaded region in Fig. E.1) is sufficient for the crack formation. The crack density of state II is assumed twice that of state I.

With the current shear-lag formulation, this cracking criterion is represented by Eq. (E.1).

$$(W - U)_I = (W - U)_{II} + \Delta A_m g_m^c + \Delta A_{db} g_{db}^c \qquad \text{(E.1)}$$
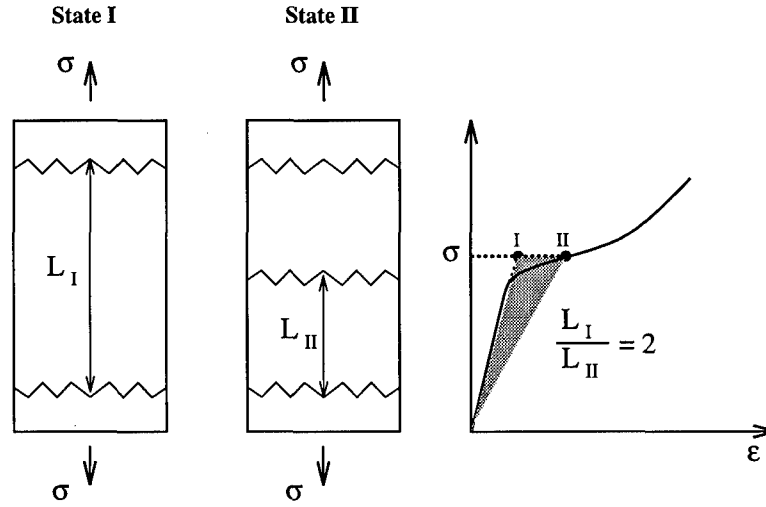
Figure E.1   Matrix cracking criterion based upon a classical fracture mechanics approach.

where W and U are the work and energy terms appropriate to the assumed damage laminates, and the areas associated with the newly formed matrix cracks and debonds are denoted by ΔA_m and ΔA_{db}, respectively. The terms g_m^c and g_{db}^c are the critical strain energy release rates for matrix cracking and debonding, respectively.

Note that the work term (W) includes both the work of the external tractions (W_T) and the work of the frictional forces along any debonded regions (W_{fr}) [Eq. (E.2)].

$$W = W_T - W_{fr} \tag{E.2}$$

or more specifically,

$$W = \frac{\sigma\epsilon}{v_m} - \frac{4v_f\tau_i}{v_m r_f L\mathcal{H}} \int_{L/2-d}^{L/2} \tau_i(x)\ dx. \tag{E.3}$$

Additionally, the total strain energy (U) includes components from the fiber (U_f), matrix (U_m) and (bonded) interface (U_i) [Eq. (E.4)].

$$U = U_f + U_m + U_i \tag{E.4}$$

For the present shear-lag model, these energies are

$$U = \frac{1}{L} \int_0^{L/2} \left\{ \frac{v_f}{v_m} \frac{\sigma_f^2(x)}{E_f} + \frac{\sigma_m^2(x)}{E_m} + \frac{2v_f}{r_f v_m \mathcal{H}} \tau_i^2(x) \right\} dx. \qquad (E.5)$$

Finally, note that from Eq. (E.1), the critical energy release rates g_m^c and g_{db}^c are required to predict the instantaneous crack spacing, L. Unfortunately, some uncertainty regarding the magnitude of these parameters for CMCs exists [37]. Estimates for g_m^c range from the monolithic (matrix) value to far less [37, 201]. The fracture energy associated with debonding is even more difficult to quantify.

Weitsman and Zhu [201] considered several values of g_m^c ranging from 44 N/m to 5 N/m in their analysis of a unidirectional laminate of a CMC system, silicon carbide fibers reinforced in a calcium-aluminosilicate matrix (SiC/CAS). In addition, they assumed that the fiber/matrix interface was *not* bonded ($g_{db}^c = 0.0$). In the present study, the same CMC system is investigated and the critical energy release rate for matrix cracking (g_m^c) is initially assumed to range from 50 to 20 N/m. 50 N/m is the measured value for unreinforced CAS and the value of 20 N/m is based upon work by Curtin [37]. As in the previous study [201], no toughness is associated with the fiber/matrix interface (i.e. $g_{db}^c = 0.0$).

The *stress-strain* and *crack density versus applied stress* response for the unidirectional SiC/CAS laminate are shown in Figs. E.2 and E.3 for several values of g_m^c. These results are computed from the present shear-lag formulation and the cracking criterion in Eq. (E.1). Note that in order to compare this criterion of matrix cracking [Eq. (E.1)] with empirical data, as well as the proposed approach, Eq. (E.1) is implemented in the analysis at $\sigma = 200$ MPa with an initial crack density of 0.747 $1/mm$. The stress level of 200 MPa corresponds to the laminate's proportional limit, σ_{cr}, and the crack density value of 0.747 $1/mm$ is based upon experimental data at this load level [103]. Weitsman and Zhu employed an initial crack spacing of 30,000 r_f at

zero load. However, under the present study, the composite is assumed undamaged for stresses below the proportional limit.
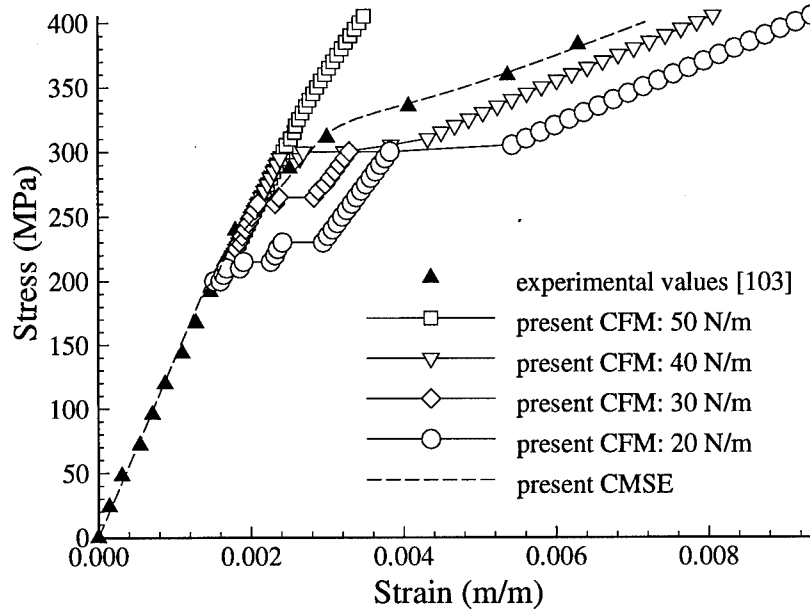
Figure E.2 Stress-strain response of a unidirectional SiC/CAS laminate. Experimental data are from reference 103. Predicted results determined using the current micromechanics model and a classical fracture mechanics (CFM) cracking criterion with g_m^c = 50, 40, 30, and 20 N/m and the *critical matrix strain energy* (CMSE) criterion.

As illustrated in Fig. E.3, little matrix cracking is predicted with a critical energy release rate, g_m^c, of 50 N/m. More specifically, the failure criterion [Eq. (E.1)] is only satisfied once before the ultimate strength of the composite (425 MPa) is reached; thus allowing the crack density to double from 0.747 to 1.494 $1/mm$ (Fig. E.3). The limited matrix cracking causes the predicted stress-strain response to be a fairly linear relationship, as expected (Fig. E.2). On the other hand, for g_m^c=20 N/m, extensive matrix cracking is predicted. However, as in the case of maximum stress theory [113], the evolution of the matrix cracks occurs over a narrow stress range (Fig. E.3), and results in a stepped stress-strain response (Fig. E.2).
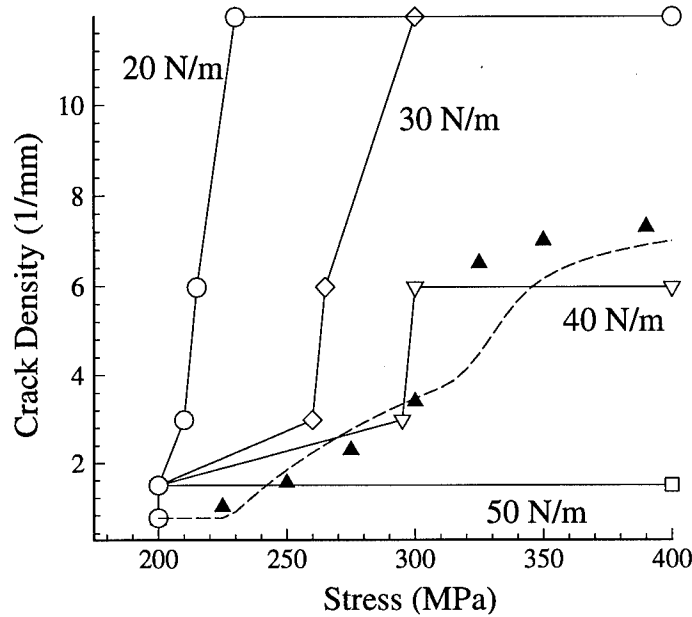
Figure E.3   Crack density versus applied stress for a unidirectional SiC/CAS lami-
nate. Experimental data are from reference 103. Predicted results de-
termined using the current micromechanics model and a classical frac-
ture mechanics (CFM) cracking criterion with $g_m^c = 50, 40, 30,$ and 20
N/m and the *critical matrix strain energy* (CMSE) criterion.

The range over which crack densities are predicted is greater for $g_m^c = 30$ and 40 N/m
than in the other cases ($g_m^c = 20$ and 50 N/m); however, the continuous progression
of damage as observed in experiments is not captured with this damage criterion of
matrix cracking (Figs. E.2 and E.3).

The analytical results in Figs. E.2 and E.3 may be improved if other factors (e.g.
flaw size, crack location and environmental effects) are considered [179]. However,
consideration of these factors further complicates the modeling process especially
for fatigue involving thousands or millions of cycles. Therefore within the scope of
the present study, where a simplified matrix cracking criterion is sought for both
monotonic and cycling loading conditions, an alternate solution is desired.

E-6

The fracture mechanics solutions shown in Figs. E.2 and E.3 are generated under the assumption that the crack density doubles each time the failure criteria [Eq. (E.1)] is satisfied (i.e. $L_I/L_{II} = 2$) [201]. In order to examine the effect of this assumption on the development of crack densities, the previous analysis [201] may be modified to consider a more continuous progression of crack growth by allowing the ratio L_I/L_{II} to be arbitrary. To avoid violating the steady-state assumptions of the continuum approach [20,127], "state I" is assumed to remain fixed at a reference state chosen in the present study at the critical composite stress, σ_{cr} (Fig. E.4). With this modification, Eq. (E.1) becomes

$$(W - U)_{cr} = (W - U)_{II} + \Delta A_m g_m^c + \Delta A_{db} g_{db}^c. \tag{E.6}$$

This approach is computationally less efficient since the external work in Eq. (E.6)
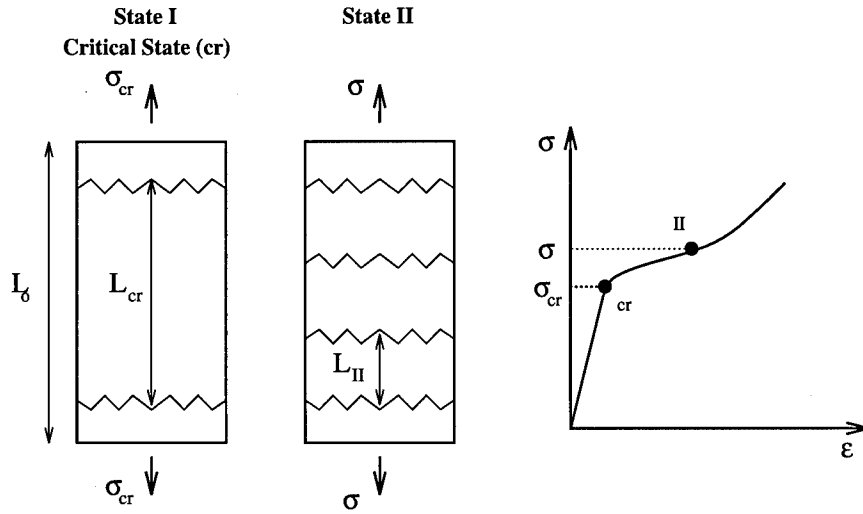
Figure E.4   Incremental crack growth model.

must be determined numerically. Additionally, this approach may initially violate the assumptions of the continuum approach if $L_{II} \simeq L_{cr}$ [127]. However, given an initial damage configuration (L, d) at σ_{cr} and the appropriate critical strain energy release rates (g_m^c, g_{db}^c), the matrix crack spacing may be determined analytically at any stress

level from Eq. (E.6). Crack density and stress-strain solutions are determined in this manner; however, no improvement over the previous analysis [201] is found. The progression of matrix cracking is again found to occur over a very narrow stress range which results in a stepped stress-strain response as is observed with the previous cracking criterion [Eq. (E.1), Fig. E.2].

With only limited success from the fracture mechanics approach [Eqs. (E.1) and (E.6)], empirical crack density data is next used to examine how the work and energy terms associated with the external work, frictional dissipation, matrix cracking and interface debonding [Eqs. (E.2) and (E.4)] vary during loading with the current shear-lag formulation. Such data are useful in understanding how energy is dissipated and redistributed between the constituents during the formation of damage. Further, the non-dimensional quantities represent a convenient way of monitoring these variations by normalizing the instantaneous value by their magnitude at the critical stress, σ_{cr}. These parameters, W_T/W_{cr_T}, $W_{fr}/W_{cr_{fr}}$, U_m/U_{cr_m}, U_f/U_{cr_f}, and U_i/U_{cr_i}, are plotted as functions of the applied stress for a SiC/CAS composite in Fig. E.5. The results in this figure are generated using empirical crack density data from reference 86. It is interesting to note that in Fig. E.5 the normalized matrix strain energy, U_m/U_{cr_m}, remains fairly constant throughout the loading process once damage initiates (i.e. $\sigma \geq \sigma_{cr}$). Readers should keep in mind that there are several factors which could influence this variation of U_m/U_{cr_m}, such as scatter in empirical matrix crack density, fiber/matrix debonding, etc. Underestimating the extent of debonding will cause the magnitude of U_m/U_{cr_m} to be overestimated, or vice versa.

Based upon the above findings, a simple matrix cracking criterion is proposed which assumes that for any loading beyond the critical stress, the matrix strain energy remains constant to a critical value [174,175]. This damage criterion is referred to as the *critical matrix strain energy* (CMSE) approach, and has proved successful in modeling both the nonlinear laminate stress-strain response, as well as the continuous progression in matrix cracking [174,175]. In general, the CMSE criterion
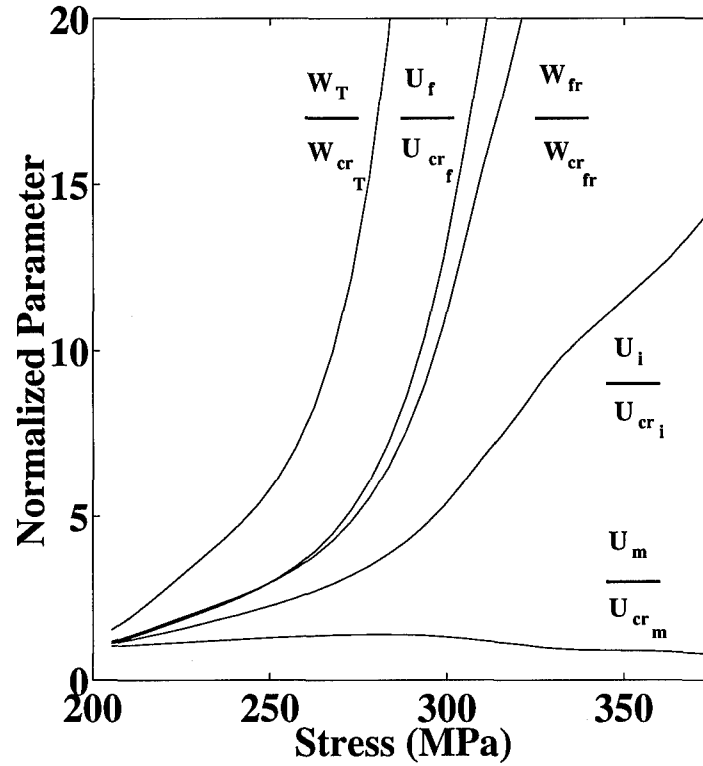
Figure E.5 Variations in the work and energy terms due to microstructural damages.

states that matrix cracking at any stress level σ; with the average crack spacing of L and having a fiber/matrix debond length d (Fig. 3.7) will occur when the matrix strain energy is equal to its critical value, U_{cr_m}, i.e.

$$U_{m_o} + U_m(L) = U_{cr_m}. \qquad (3.117)$$

The *critical matrix strain energy*, U_{cr_m}, is defined as the strain energy in the matrix at the critical composite stress, σ_{cr}.

In Eq. (3.117), U_{m_o} is the matrix strain energy which would exist if the composite was undamaged, i.e.

$$U_{m_o} = \frac{1}{2} A_m L \frac{\sigma_{m_o}^2}{E_m}, \qquad (E.7)$$

E-9

and the term $U_m(L)$ accounts for the decline in the matrix strain energy due to the presence of the microstructural damages. Also note that since the matrix strain energy is defined by Eq. (E.8), the left hand side of Eq. (3.117) can be determined using Eqs. (3.45) and (E.8).

$$U_m = \frac{1}{2E_m} \int_{A_m} \int_{-L/2}^{L/2} \sigma_m^2(x) \, dx \, dA_m \tag{E.8}$$

Performing the math, the instantaneous matrix strain energy is found to be

$$U_m = \frac{A_m}{v_m{}^2 r_f{}^2 \beta E_m} \Big\{ (H + 4\beta d/3) \, (\tau_i v_f d)^2 + (\beta(L/2 - d) + H/4 - 2G) \cdot$$
$$(v_m r_f \sigma_{m_o})^2 - d \, r_f v_m v_f \tau_i \sigma_{m_o}(H - 4G) \Big\} \tag{E.9}$$

where $G = \tanh[\beta(L/2 - d)]$ and

$$H = \frac{\beta(L - 2d) + \sinh[\beta(L - 2d)]}{\cosh[\beta(L/2 - d)]^2}. \tag{E.10}$$

An important computational note is that as $\beta L \to \infty$, $G \to 1$ and $H \to 2$. Furthermore, as $d \to L/2$, both G and H vanish. Also note that for the current CMSE criterion, the volumetric matrix strain energy is considered rather than the matrix strain energy *density*, i.e. per unit volume, as in the previous case [201].

Under the CMSE criterion, by letting U_m in Eq. (E.9) equal U_{cr_m}, the average crack spacing can be determined for any applied stress. However because of the non-linear nature of Eq. (E.9), L is determined iteratively. In particular, at each σ, an initial guess for the crack spacing is made according to

$$L_{n+1} = L_n - (L_{n-1} - L_n). \tag{E.11}$$

After the initial guess, if Eq. (3.117) is not satisfied, the solution is updated itera-tively, with index i, until the criterion is satisfied [Eq. (E.12)].

$$L_{i+1} = L_i + \mathcal{V}_i \left(\frac{U_{m_i} - U_{cr_m}}{U_{cr_m}} \right) \qquad \text{(E.12)}$$

where $\mathcal{V}$ is a dynamic variable tuned to speed the rate of convergence.

Accounting for matrix failure in this manner allows for a more accurate repre-sentation of the *average* instantaneous crack spacing as compared to other existing (analytical) failure criteria. For example, consider the evolution of matrix cracking and the representative models shown in Fig. E.6. Since no restriction is placed on

Composite Unit-Cell
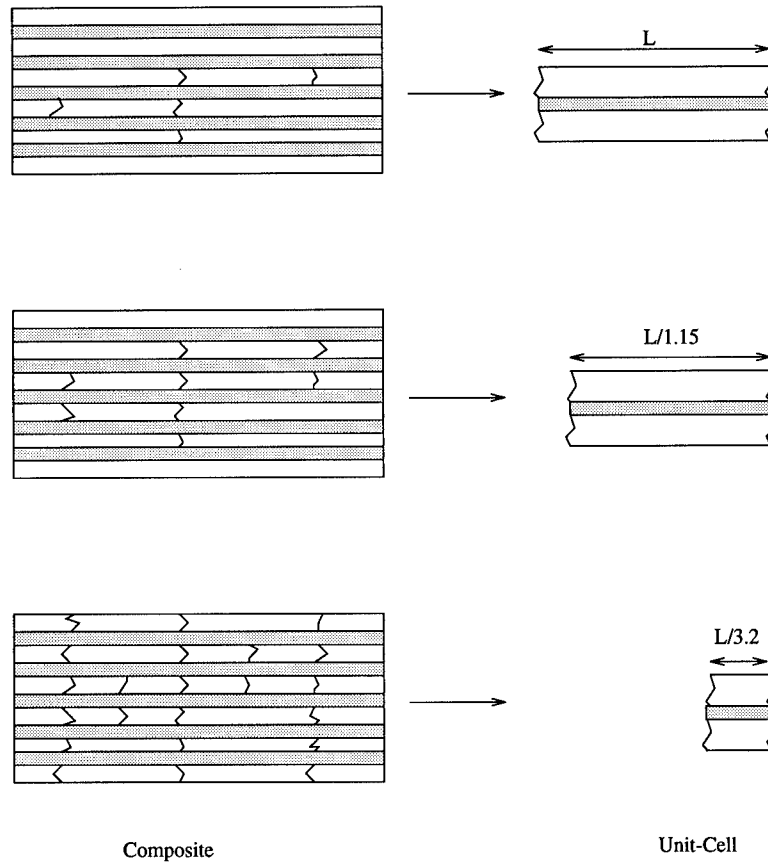
Figure E.6 Unit-cell representation of the *average* matrix crack spacing as predicted by the CMSE criterion.

the location where new matrix cracks must form under the CMSE approach, an infi-

nite number of crack configurations are possible. On the other hand, for the criteria set forth by Daniel *et al* [40] and Zhu and Weitsman [212], the representative model decreases in size only discretely since the respective failure criterion assume that the crack density doubles whenever the criterion is satisfied (Fig. E.7). Therefore, for the composite damages illustrated in Figs. E.6 and E.7, the present CMSE solution is able to more accurately model the *continuous* evolution in matrix cracking (Fig. E.6) whereas, the other approaches are only able to capture discrete steps (Fig. E.7).

Composite   Unit-Cell
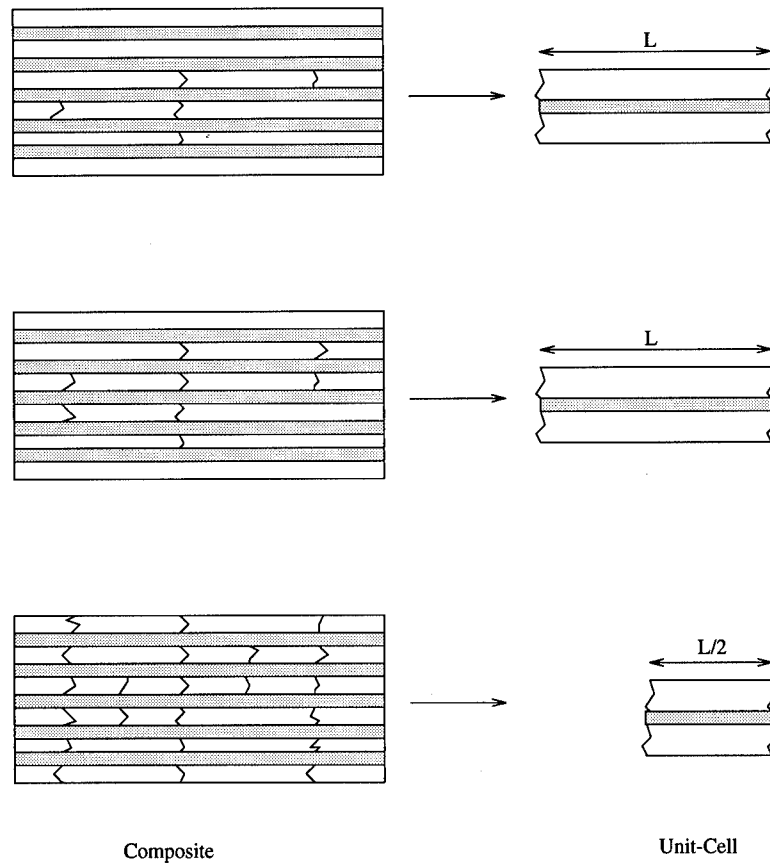
Figure E.7   Unit-cell representation of the *average* matrix crack spacing as predicted by criteria which assume that the crack density doubles whenever the criteria are satisfied.

Since the volume of the shear-lag model varies with matrix cracking, care must be taken to ensure that equivalent volumes (Fig. E.1) are considered when applying Eq. (3.117). The *stress-strain* and *crack density versus applied stress* plots

resulting from the present shear-lag approach using this criterion of matrix cracking [Eq. (3.117)] are shown in Figs E.2 and E.3, and they are in good agreement with their experimental counterparts. Further, they show a great improvement over their counterparts obtained from matrix cracking criterion based on the fracture mechanics approach, Eq. (E.1). Also the predicted stress-strain relationship does not result in a stepped response as in the previous analytical case.

Equation (3.117) has proven to be an effective technique for estimating the instantaneous crack density in unidirectional composites. As is evident from Fig. E.3, results from the CMSE method are in very good agreement with their experimental counterparts. For this reason, the critical matrix strain energy criterion is employed also in the analysis of cross-ply laminates. That is, crack propagation in the transverse plies is assumed to be governed by a critical energy as shown by Eq. (3.118).

$$U_{T_o} + U_T(L_t) = U_{cr_T} \qquad (3.118)$$

where U_{T_o} is the rule-of-mixtures (transverse ply) strain energy for an undamaged laminate and $U_T(L_t)$ accounts for the transfer of energy upon damage formation. The critical strain energy is U_{cr_T} and is assumed to be a material constant. The parameter L_t is the average crack spacing of the transverse plies.

Moreover, prior to the development of any damage of the 0° plies, the strain energy in the 90° plies due to transverse cracking is found to be

$$U_T = \frac{1}{2} d L_t E_2 \left(\frac{\sigma_T^o}{E_2} \right)^2 \left\{ 1 + \frac{4}{\lambda L_t} \left[\frac{1}{8} \frac{\lambda L_t + \sinh(\lambda L_t)}{[\cosh(\lambda L_t/2)]^2} - \tanh\left(\lambda L_t/2 \right) \right] \right\}. \qquad (E.13)$$

Note that Eq. (E.13) is of the same form as Eq. (3.118), i.e. $U_T = U_T^o + U_T(L_t)$. Once damages form within the 0° plies, the strain energies are determined numerically from Eqs. (E.14) through (E.16).

$$U_T = \frac{1}{2} \left(1 + \frac{L - L_t}{L_t} \right) d \int_{-L_t/2}^{L_t/2} \frac{\sigma_T^2(x_t)}{E_2} \, dx \qquad (E.14)$$

E-13

$$U_m = \frac{1}{2} v_m b \int_{-L/2}^{L/2} \frac{\sigma_m^2(x)}{E_m} \, dx \qquad (E.15)$$

$$U_f = \frac{1}{2} v_f b \int_{-L/2}^{L/2} \frac{\sigma_f^2(x)}{E_f} \, dx \qquad (E.16)$$

Note that the current *critical matrix strain energy* approach is fundamentally different than the traditional fracture mechanics approach. This has many advantages. For example, the CMSE approach eliminates dependence on parameters g_m^c and g_{db}^c which are difficult to evaluate. Further, no consideration to variations in flaw size and crack location is required. With the proposed approach, only the critical composite stress, σ_{cr}, is required to determine the average crack spacing analytically. In addition, interface debonding and fiber failure are easily incorporated into the solution scheme. For the current analysis, transverse cracking is governed by a critical strain energy limit in the 90° ply, U_{cr_T}; matrix cracking by U_{cr_m} and fiber failure, as discussed in appendix F, is governed by its own critical energy U_{cr_f}.

E.2 Estimation of the Initial Crack Density

For the present study, the stress-strain response is predicted using two independent algorithms. For applied stresses below the critical composite stress (i.e. $\sigma < \sigma_{cr}$), the rule-of-mixtures (ROM) solution is employed. For $\sigma \geq \sigma_{cr}$, the shear-lag analysis is used in order to account for laminate damage. In dividing the solution algorithm into two schemes, ROM and shear-lag, the analysis code becomes more efficient since crack density data for $\sigma \leq \sigma_{cr}$ (i.e. left of point 'c' shown in Fig. E.8) does not need to be estimated. However, the initial crack spacing, L_{init}, at $\sigma = \sigma_{cr}$ must be determined for the CMSE failure criterion.

To better understand how L_{init} is calculated, recall that the instantaneous matrix strain energy, $U_m(L)$, can be written in terms of the undamaged strain energy, U_{m_o}, plus an additional term which accounts for the fact that energy is transferred between the constituents because of existing damage. Experimentally, the energy
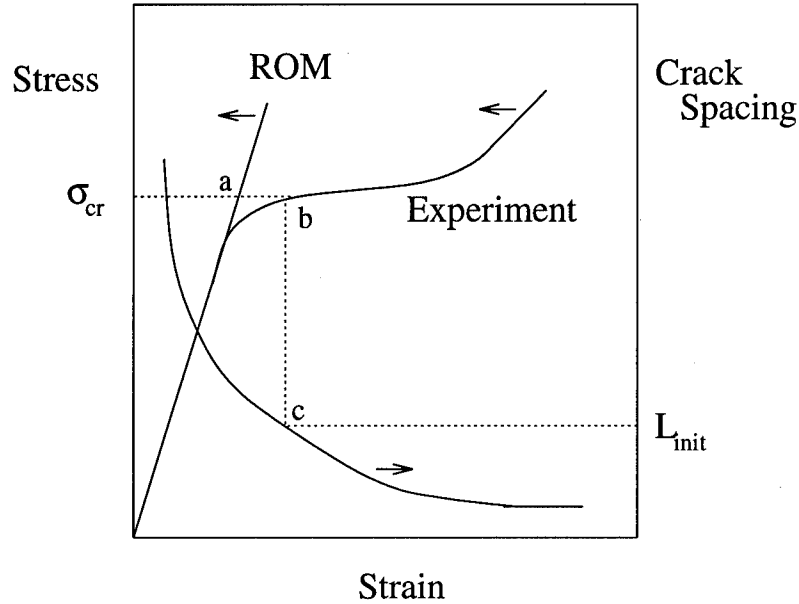
Figure E.8 Typical stress-strain and crack density development within a brittle fiber-reinforced composite. A rule-of-mixtures stress-strain approximation is also shown.

transfer manifests as a deviation in the composite's stress-strain response from its linear ROM approximation (Fig. E.8). Numerically, of course, the energy transfer can be monitored directly. For example, Fig. E.9 shows the deviation in the matrix strain energy at σ_{cr} for various crack spacings. The strain energies have been normalized by the undamaged matrix strain energy U_{m_o}; hence, the ordinate value of 1.0 represents critical matrix strain energy, U_{cr_m} if $\sigma = \sigma_{cr}$.

For the current analysis, the initial crack spacing is chosen such that the strain energy of the damaged configuration is "close" to the strain energy in the undamaged configuration U_{m_o}. For example, for a deviation of three percent (i.e. $U_{cr_m} = 0.97\ U_{m_o}$), the predicted crack density matches well with the empirical data presented by Kuo for a SiC/CAS system [103]. In both cases, the crack density is determined to be 0.747 $1/mm$ for $\sigma_{cr} = 200$ MPa. For the present study, a constant deviation of one percent, $U_{cr_m} = 0.99\ U_{m_o}$, is used for all cases. Under this condition, the initial crack density is determined to be 0.26 $1/mm$ for the SiC/CAS

laminate (Fig. E.9). By limiting the deviation in the matrix strain energy, the
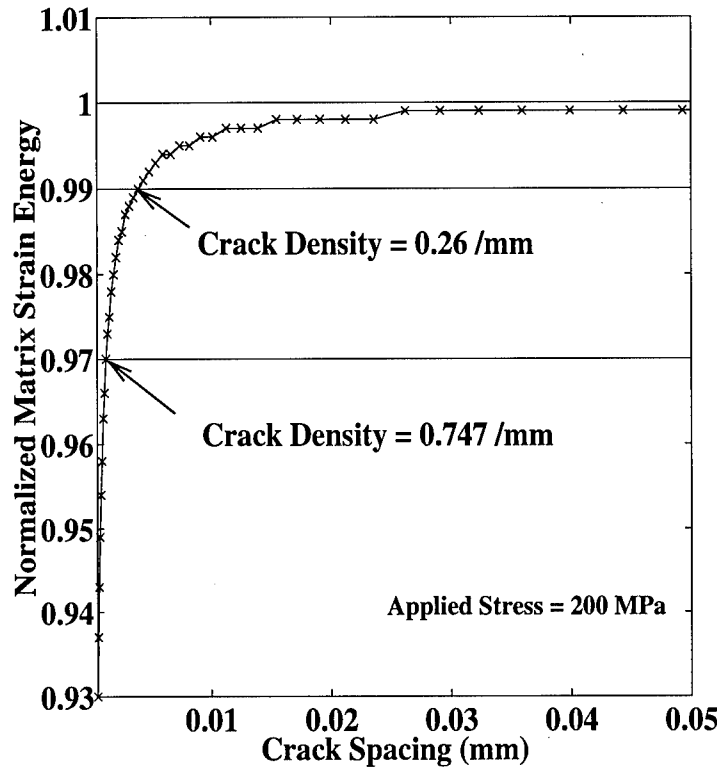
Figure E.9   Deviation, away from the *critical matrix strain energy*, in the matrix strain energy as a function of crack spacing. The plot is for a constant critical stress value of 200 MPa.

stepped appearance[†] of the stress-strain response is reduced. The change in the initial crack density between the two cases (0.26 $1/mm$ versus 0.747 $1/mm$) has only a slight effect on the composite response (Fig. E.10).

Once the initial crack spacing, L_{init}, is determined, the instantaneous crack spacing at any stress level follows directly, and efficiently, from Eq. (3.117). Hence, under the current CMSE criterion, any energy placed into the system via loading is transferred to the fibers though the formation of new matrix cracks, the propagation of existing cracks, and fiber/matrix debonding.

[†]The "stepped" appearance results from the transition from the rule-of-mixtures analysis to the shear-lag analysis. The size of the step is represented by the horizontal spacing between points 'a' and 'b' in Fig. E.8.
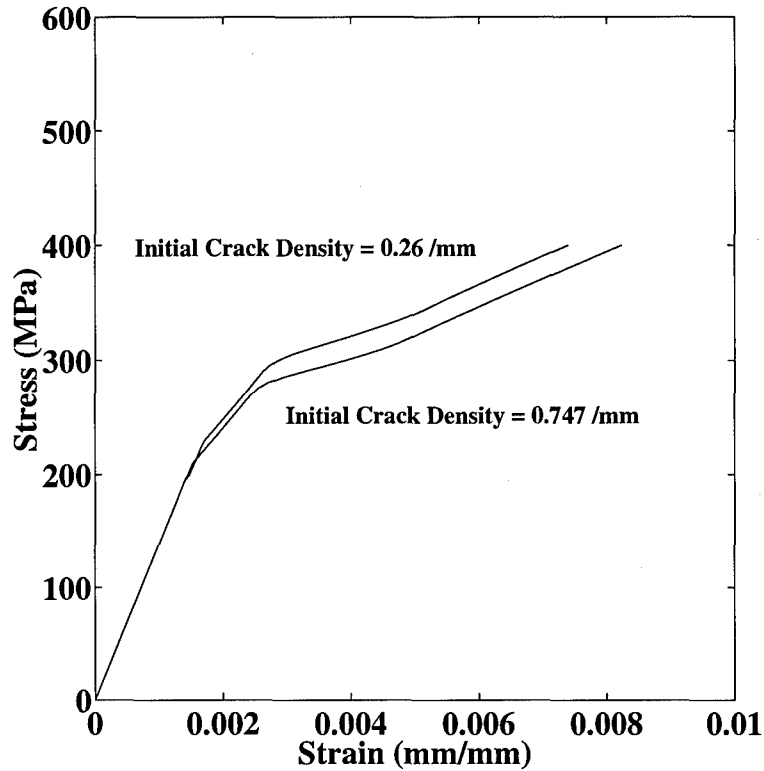
Figure E.10   Stress-strain predictions for a unidirectional SiC/CAS laminate. The initial crack density of 0.26 $1/mm$ corresponds to $U_{cr_m} = 0.99\ U_{m_o}$ and the initial crack density of 0.747 $1/mm$ corresponds to $U_{cr_m} = 0.97\ U_{m_o}$.

E.3   The CMSE Criterion and Its Relation to Variations in the Matrix Strain Energy

A convenient format for representing the *critical matrix strain energy* (CMSE) failure criterion is found in plotting the *matrix strain energy versus crack density* for various levels of applied stress. The range for the applied stress is reasonably chosen as $\sigma_{cr} \le \sigma \le \sigma_{ult}$. A typical plot is illustrated in Fig. E.11. The *broom shaped* appearance of Fig. E.11 proves to be an important representation for the CMSE criterion. In particular, the intersection of the *broom bristles* and the (dashed) horizontal line in Fig. E.11 provides information on the expected evolution of the crack densities predicted by the CMSE criterion. In addition, the *bounding limits* of
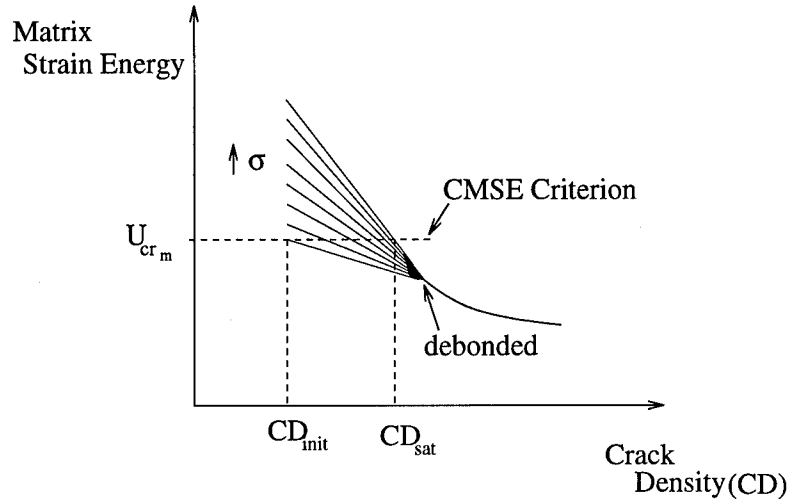
Figure E.11   Matrix strain energy versus cracks density at various levels of applied stress. The CMSE failure criterion is represented by the horizontal dashed line.

the crack densities are easily obtained. In Fig. E.11, the crack density (CD) limits, for example, are denoted CD_{init} and CD_{sat} for σ_{cr} and σ_{sat}, respectively. Note that once the interface completely debonds, the matrix stress, and consequently the matrix strain energy, is independent of the applied load. The matrix stress for a completely debonded interface has been derived many times for the one-dimensional micromechanics model [153]. For the shear-lag model, the interface is not only assumed to be completely debonded, but also to have slipped completely. This is a reasonable assumption under the maximum stress debonding criterion used in the present study. Under these conditions, the matrix strain energy is

$$U_m = \frac{1}{6E_m}\left(\frac{v_f\tau_i}{v_m r_f}\right)^2 L^2 = \frac{1}{6E_m}\left(\frac{v_f\tau_i}{v_m r_f}\right)^2\left(\frac{1}{CD}\right)^2. \qquad (E.17)$$

The reader will note that Eq. (E.17) is independent of the applied stress, σ.

The utility of the *broom plots* is that even though the broom moves around as input conditions change, the crack densities which will be predicted by the CMSE criterion are always defined by where the broom intersects the line $U_m/U_{cr_m}=1.0$.

E-18

Hence, in theory, the broom plots are an effective method for investigating the impact of different input parameters on matrix cracking. In addition, these plots point out the expected limitations of the CMSE failure criterion. These are discussed later in this section

In general, the shape and location of the broom is dependent on the laminate's composition and residual properties (e.g. fiber volume fraction, interface strength, and residual thermal stresses). However, since matrix cracking is coupled with the other damage modes, the salient features of the broom are also dependent on the extent of debonding and fiber failure. The remainder of this section investigates the influence of debonding on matrix cracking. As would be expected, the two modes are highly coupled.

Figure E.12 illustrates the dependence of matrix cracking on interface debonding. In particular, four plots are generated: $d = L/2$, $d = 16\ r_f$, $d = 8\ r_f$ and $d = 0$. For each plot, the debond length is held constant. For convenience, the ratio U_m/U_{cr_m} is plotted against L_{sat}/L where L_{sat} is the bounding limit obtained from the classical ACK analysis, i.e.

$$L_{sat} = 1.337 \frac{r_f}{2\tau_i} \frac{v_m}{v_f} \frac{E_m}{E_1} \sigma_{cr}. \qquad (E.18)$$

Clearly, from Fig. E.12, the crack densities predicted by the CMSE criterion change dramatically with debonding. Two cases of particular interest occur when the interface is completely debonded (i.e. $d = L/2$) and when it is fully bonded (i.e. $d = 0$). These are now considered.

The first case considered is for a completely debonded interface, $d = L/2$. The broom plot for this situation in given by the first (upper left) plot in Fig. E.12. Note, that in this case, the CMSE criterion is satisfied at only two points: $L = L_{init}$ and $L = L_{sat}$. By definition, these correspond to the conditions $\sigma = \sigma_{cr}$ and $\sigma = \sigma_{sat}$, respectively. In addition, because of how U_{cr_m} is defined, the first point,
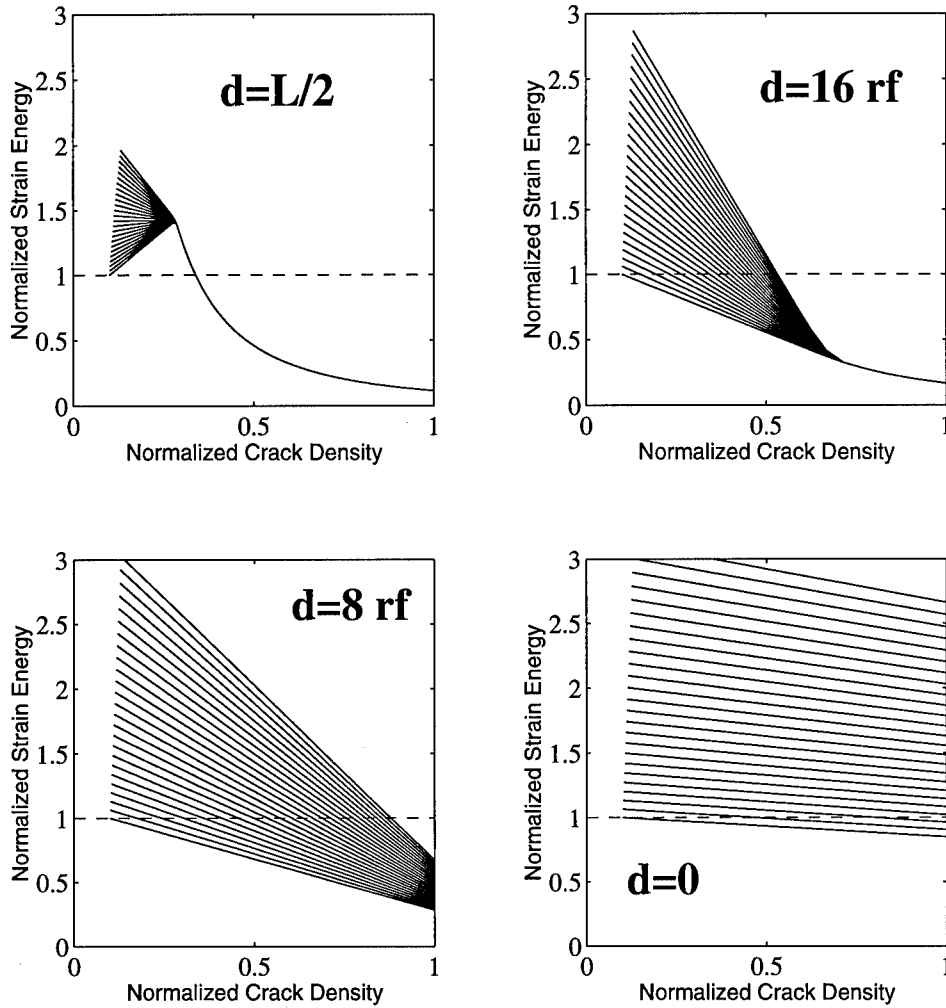
Figure E.12   Broom plots for $d = L/2$, $d = 16\ r_f$, $d = 8\ r_f$ and $d = 0$. In each case, the debond length is held constant.

$(U_m(L) = U_{cr_m}$, $L = L_{init})$, is always a solution. Based on the shape of the broom plot in Fig. E.12, it is apparent that for an incremental increase in applied stress, the predicted crack density will jump from CD_{init} to CD_{sat}. Hence, an extensive amount of matrix cracking occurs instantaneously. This is the same as the classical solution for a debonded interface as formulated by Aveston, Cooper and Kelly (ACK) [8].

The other limiting solution is obtained when the interface is fully bonded (i.e. $d = 0$). The broom plot for this configuration is given by the last (lower right) plot in Fig. E.12. It is clear from this figure that an extensive amount of cracking will

be predicted. This is to be expected since for a bonded interface the applied load is readily transferred between the constituents, and therefore, the stress in the matrix increases much faster than in the debonded case. Hence, the final crack densities for a fully bonded interface can be expected to be much larger than for a completely debonded interface. The same argument can be made for a fully debonded interface with a high interface shear strength, τ_i, versus a debonded interface with low interface shear. The fact that the broom bristles are approaching horizontal indicates that for a completely bonded interface, the evolution of matrix cracking is again very rapid. That is, large decreases in the crack spacing can be expected for incremental rises in stress. In contrast to these two limiting cases ($d = L/2$ and $d = 0$), the CMSE crack density evolution for a partially bonded interface (second and third plots in Fig. E.12) are well defined and representative of empirical trends.

Unfortunately, Fig. E.12 does not provide a complete picture for how the crack densities will evolve under the current formulation since the debond length will vary with loading. Recall, that for each of the four plots in Fig. E.12, the debond length is held constant. Figure E.13 shows several broom plots which are generated using different debonding criteria. As expected, debonding plays a large role in the crack density evolution.

For the upper left plot in Fig. E.13, the debond length is held constant at each applied stress level, but is allowed to increase as the applied stress increases. The formula used in determining d is shown in Eq. (E.19) where Γ_d is a constant which varies linearly with σ and has end conditions: $\Gamma_d = 0$ for $\sigma = \sigma_{cr}$ and $\Gamma_d = 1$ for $\sigma = \sigma_{sat}$.

$$d = \Gamma_d \sigma L / (2\sigma_{cr}) \qquad (E.19)$$

The second plot (upper right) in Fig. E.13 is generated using a debond criterion which assumes that the ratio d/L remains constant and *independent of the applied stress*. In particular, it is assumed that $d = L/100$, independent of σ. For the third case (lower left), the ratio of d/L is again held constant at each stress level, but this
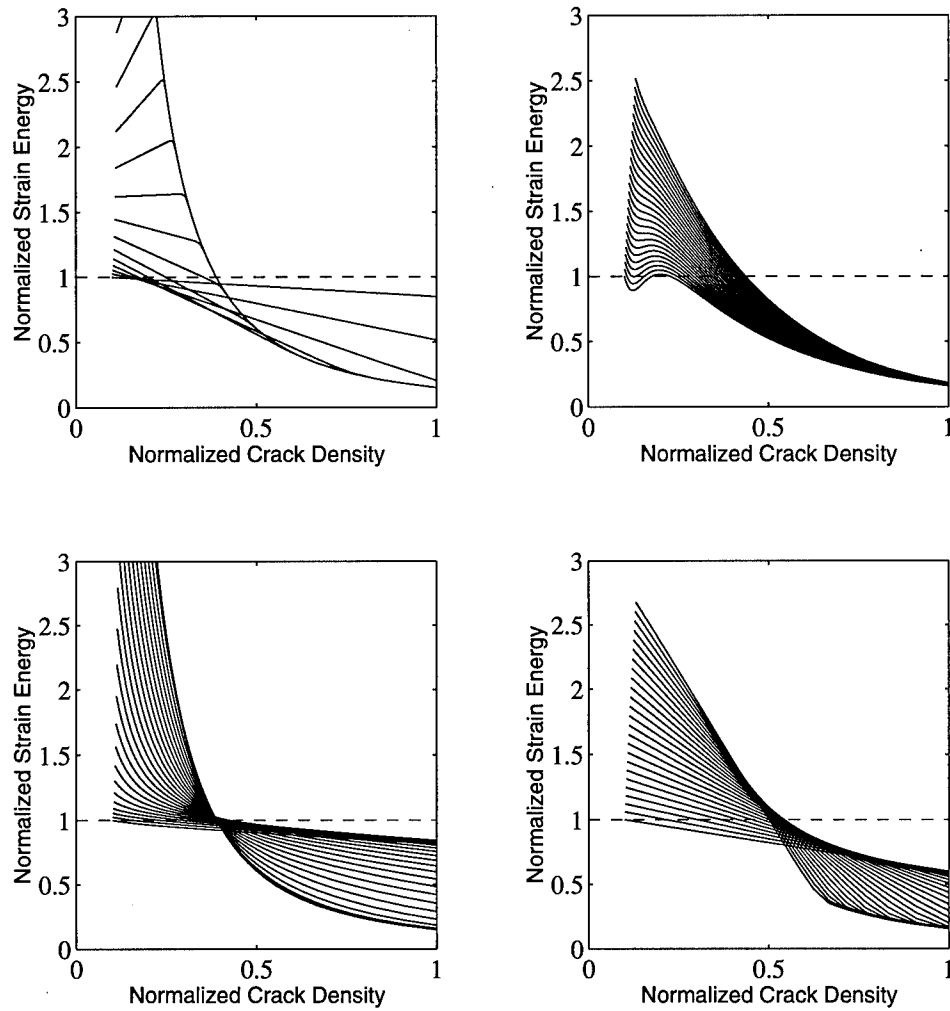
Figure E.13 Normalized *matrix strain energy versus crack density* for several
debond criteria.

time, the ratio is assumed to increase with the applied load (e.g. for $\sigma = 200$ MPa,
$0 \leq 2d/L \leq 0.01$, for $\sigma = 205$ MPa, $0.01 \leq 2d/L \leq 0.05$, etc). The last plot in
Fig. E.13 is generated using a simple maximum stress debonding criterion similar to
the one used in the current analysis, however, the solution is limited to one step in
the Newton iteration scheme.

Even though the broom plots provide information for the *evolution* of matrix cracking,[†] as predicted by the CMSE criterion, the manner in which the information is presented is somewhat inconvenient. The best approach for examining such data is, of course, simply to plot the predicted crack density versus the applied stress plots. Such results for various levels of debonding are shown in Fig. E.14. For each
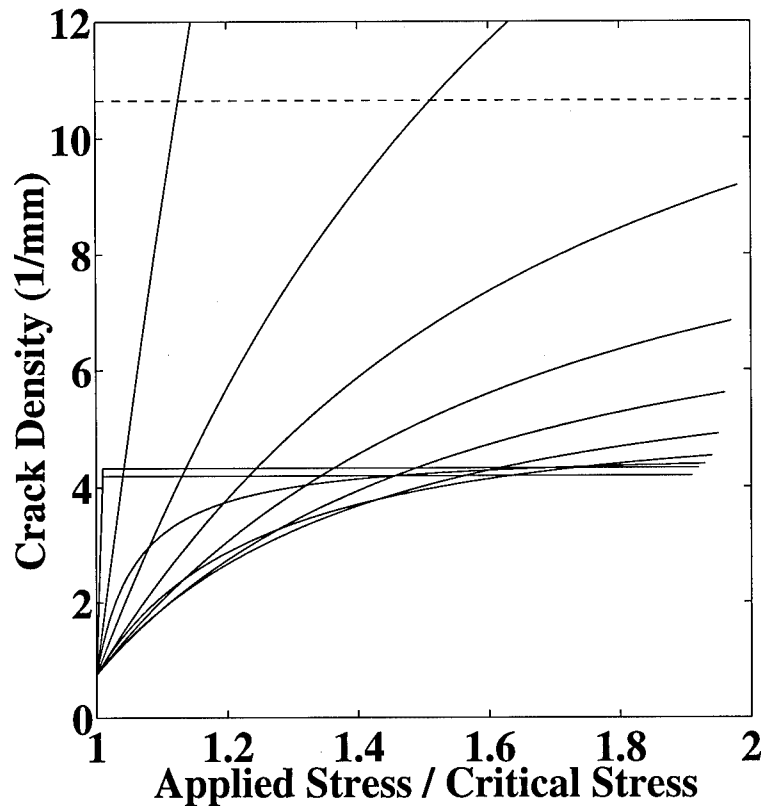
Figure E.14   Crack density versus normalized stress as predicted by the CMSE criterion in which the debond length is held constant. Several curves are shown for different levels of debonding. The dashed line represents the ACK solution for $g_m^c = 45 \ N/m$.

prediction, the debond length is assumed constant. Note that the predicted crack

---

[†]The distance between the adjacent bristles along the line $U_m/U_{cr_m} = 1.0$ characterizes the *rate* at which crack growth occurs. The closer the bristles, the less rapid is the crack growth, and the opposite is also true. As an example, for the case of $d = 0$ in Fig. E.12, the distance between the bristles for which the CMSE criterion is satisfied is relatively large. Hence, an extensive amount of cracking occurs for a small increase in stress.

densities for the two limiting cases, $d = 0$ and $d = L/2$ are consistent with the previous results (Fig. E.12). In both cases, the matrix cracks evolve quickly, and further the final crack density (CD_{sat}) is much larger for the bonded interface due to the efficient stress transfer.

It is interesting to note that the crack density predictions in Fig. E.14 define a *fan* which forms as the solution for $d = 0$ is pivoted around the point (σ_{cr}, CD_{init}). The bottom of the fan is defined in the limit as d approaches $L/2$. Moreover, the completely debonded solution defines a minimum saturated crack density for the CMSE criterion. As the bonded solution is pivoted, once the saturated crack density obtains this limit, the crack density solution bends upon itself,[†] and eventually becomes the unit-step response associated with a completely debonded interface.

The fan defines an envelope for the crack densities in which almost any path can be predicted due to the coupling between the cracking and debonding modes. In addition, the span of the envelop can be narrowed since it is reasonable to expect some debonding. The bounding envelop, as predicted, could provide a design engineer with reasonable estimates for the expected crack densities. Also, such plots are a convenient way of comparing various failure criterion. In this light, the following section examines the CMSE criterion and its relation to more traditional fracture mechanics approaches.

E.4   CMSE and Its Relation to Other Failure Theories

As discussed in chapter two, fracture within ceramic matrix composites is governed by the relation between the crack-tip energy release rate, g_m, and the critical energy release rate, g_m^c. The former is a function of the crack-tip stress fields, and the latter is an inherent property of the composite. In general, a given fracture will propagate under the condition that $g_m \geq g_m^c$. Hence, given some distribution of

---

[†]The phrase *bends upon itself* is intended in indicate that the initial slope of the *crack density versus stress* curve is increasing, and is indicative of an interface which is completely debonded, but for which interface slip occurs along only a portion of the debonded region (i.e. $x' < L/2$) [179].

matrix flaws, the evolution of cracking can be accurately predicted if g_m is known at each fracture. Unfortunately, predicting the energy release rate in a brittle composite with multiple crack fronts in far from trivial. Several fracture mechanics solutions have been presented; however, their implementation has been limited due to the inherent complexities associated with the analysis. The purpose of this section is to compare and contrast the CMSE criterion with some of the fracture mechanics solutions. In doing so, the utility of the CMSE criterion should become apparent. Also, the CMSE criterion is shown to be reasonable and consistent with the more traditional criterion.

A good comparison for the CMSE criterion is the energy balance solution introduced by Weitsman and Zhu [201]. Both solutions are analytic, and under reasonable conditions, predict a finite stress range over which matrix cracking occurs. Bounding envelops for the CMSE criterion and the energy criterion employed by Weitsman and Zhu (WZ) [201] are provided in Fig. E.15. The results shown in this figure are for a SiC/CAS composite system and are generated by varying the critical strain energy release rate, g_m^c, in the WZ analysis, and the debond length under the CMSE criterion. The critical strain energy release rate is varied between 20 and 50 N/m. In addition, for the WZ criterion, variable debonding and fiber fracture are permitted. For the CMSE results, the debond length is held constant and a minimum debond length of a few fiber diameters is assumed.

As mentioned, the difficulty with the fracture mechanics approaches lies in trying to determine the energy release rate, g_m. Even under the simplest of loading conditions (e.g. uniaxial tension), the shielding and statistical influences associated with multiple fractures, as discussed in chapter two, make determination of g_m difficult. To remedy the problem, statistical fits of empirical data are sometimes used [179]. Bounding envelopes for a statistical model presented by Spearing and Zok are illustrated in Fig. E.16 [179]. The results are again shown for a SiC/CAS composite; however, unfortunately insufficient data are presented in the article to
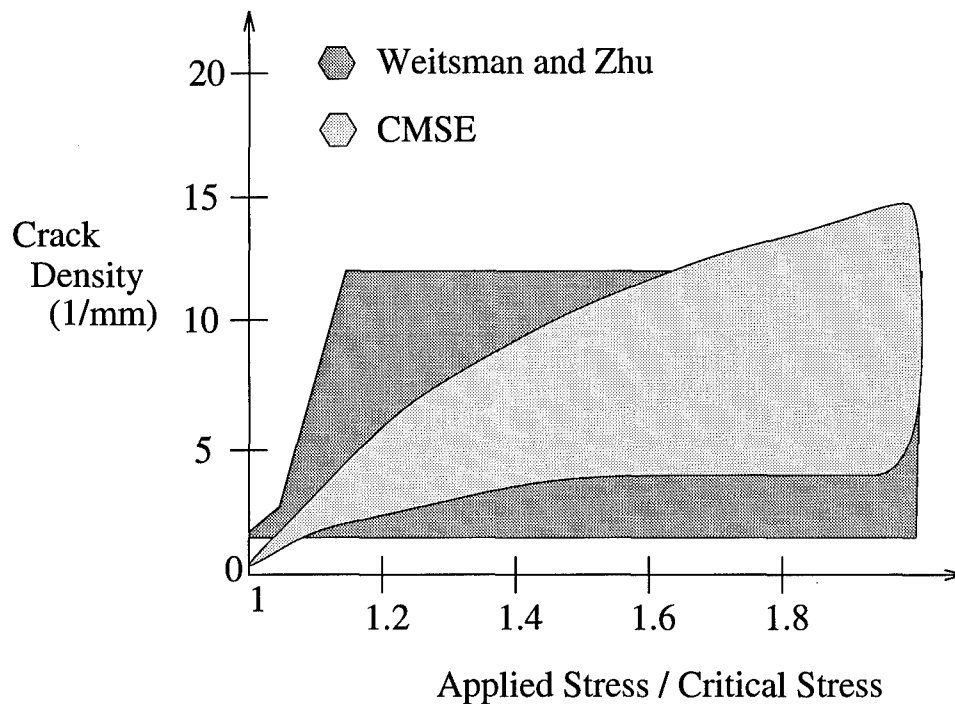
Figure E.15   Crack density (bounding) envelopes for the Weitsman and Zhu energy
criterion and the current CMSE failure criterion.

determine the exact range of crack densities predicted. The expected range of crack

densities are shown for the Weibull modulus equal to 4 and 10. As would be expected,

the empirical models are more representative of the experimental data.

Due to the statistical aspects of fracture in brittle composites, it is reasonable

to expected that the strain energy release rate, g_m, required to propagate a fracture

will increase during loading [171]. This results since more energy is required to

initiate growth in very small flaws as opposed to rather large microcracks which

may exist [127]. In addition, Zok and Spearing illustrated that the strain energy

release rate must also increase due to the shielding effects associated with small

crack spacings.

The strain energy release rate can be estimated by comparing the energy states

before and after the formation of damage. Equation (E.20) represents this result

where "state I" and "state II" represent the damage configurations before and after
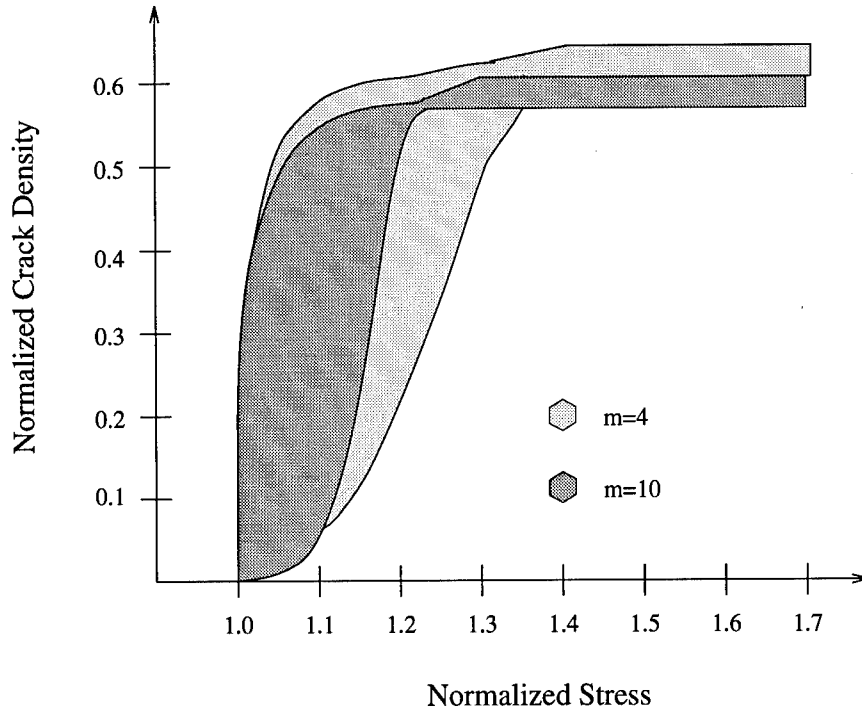
Figure E.16   Crack density bounds based upon a statistical model. The parameter m is the Weibull modulus.

crack formation.

$$g_m = \frac{1}{v_m} \frac{L_I L_{II}}{L_I - L_{II}} \left\{ \Delta W - \Delta U - \Delta W_{fr} - \frac{4v_f g_{db}}{r_f L_I L_{II}} \left(L_I d_{II} - L_{II} d_I \right) \right\} \qquad \text{(E.20)}$$

The terms in Eq. (E.20) are defined in chapter two. For the current shear-lag analysis, the energy associated with debonding, g_{bd}, is neglected; however, a study by Kuo suggests that $g_{db}/g_m \leq 0.3$ for SiC/CAS composites [103]. Also, note that g_m may be determined by assuming that state I is fixed at a given stress and damage configuration, or else by allowing the state definition to vary with these parameters. In the latter case, the work terms become trivial, i.e. $\Delta W = \sigma(\epsilon_{II} - \epsilon_I)$, and numerical integration can be avoided. However, care must be taken not to violate the inherent assumptions used in formulating Eq. (E.20).[†]

[†]The energy balance relation in Eq. (E.20) implicitly implies that large increments in crack growth are required under the assumption that $da = \Delta a$.

The change in the strain energy release rate, as predicted from the current CMSE failure criterion, is illustrated in Figs. E.17 and E.18. The results in Fig. E.17 are shown for when state I is assumed to vary; whereas the results in Fig. E.18 assume that state I is fixed. In both cases, solutions for a range of debond lengths are presented. Also, note that the strain energy release rate is normalized by the critical energy release rate, g_m^c, which is taken as 50 N/m. For both figures, g_m
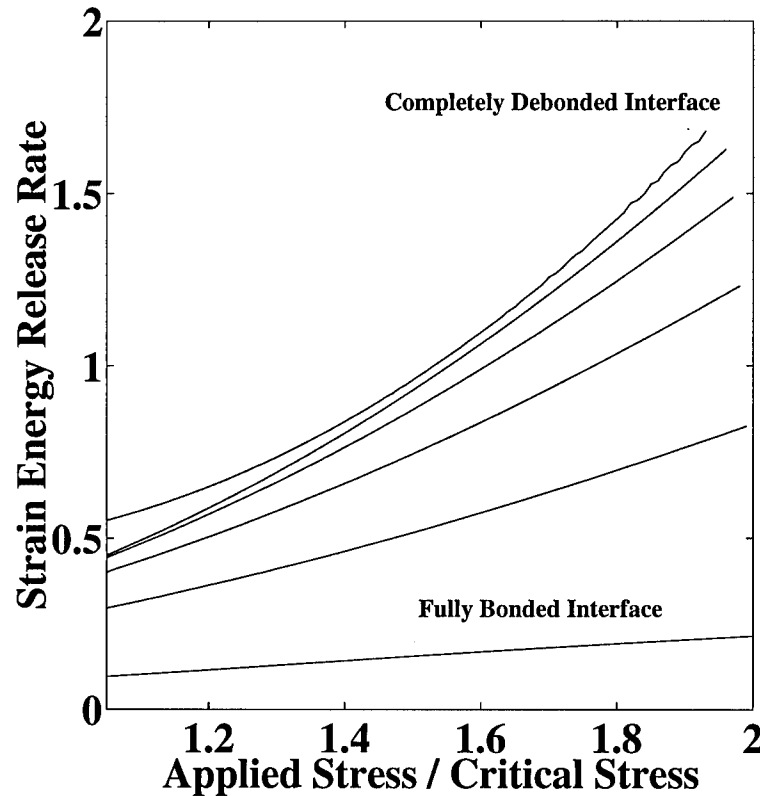
Figure E.17   Strain energy release rate versus applied stress.

increases with the applied stress, as expected. In addition, from Fig. E.18, the strain energy release rate can be expected to range between 0.3 g_m^c and 0.75 g_m^c. This is consistent with experimental data [37]. As a special case, when using Eq. (E.20) with the empirical data from Kuo, g_m is found to vary almost linearly over this same range [103]. Under the WZ criterion, g_m is assumed constant.
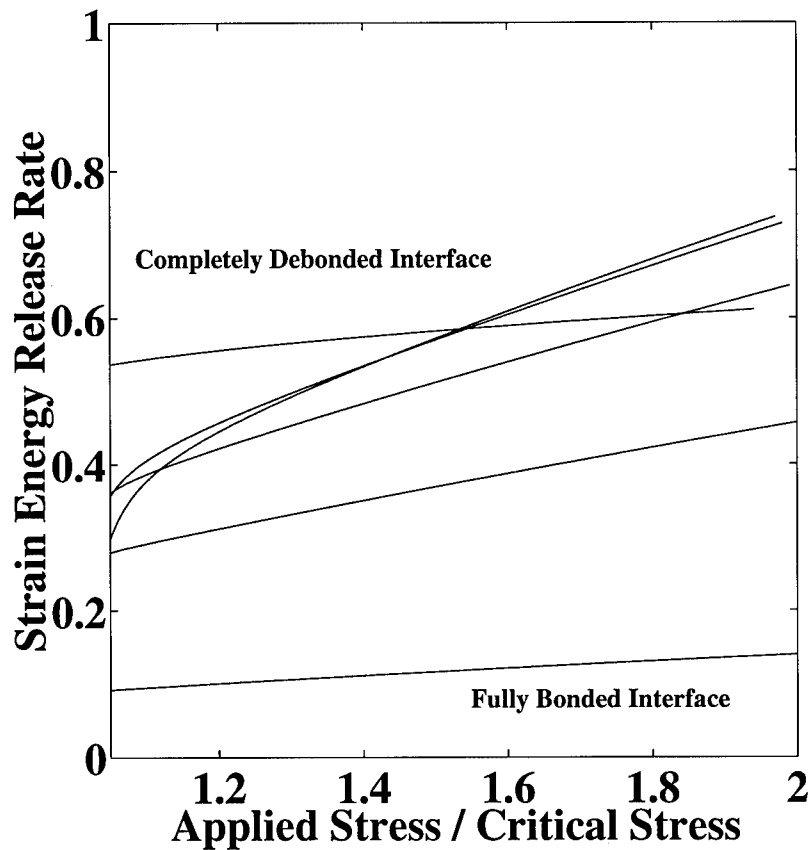
Figure E.18   Strain energy release rate versus applied stress with state I fixed.

A final comment on the WZ criterion is also in order. Recall, that each time the energy failure criterion is satisfied the crack density doubles. This results by design since the crack ratio, L_I/L_{II}, appearing in Eq. (E.20) is assumed to have magnitude 2.0. To examine the impact of this assumption on the evolution of crack densities, the energy criterion in Eq. (E.20) is now investigated for arbitrary crack ratios.

When applying the WZ criterion with $g_m^c = 45\ N/m$, the predicted range of crack densities is in tolerable accord with the empirical data; however, the predicted evolution fits the empirical data only in piecewise steps (Fig. E.19). The gradual evolution of matrix cracking, as observed experimentally, is not captured. At first glance, it is reasonable to suspect that the discrete steps results from the assumed

doubling in crack density. To investigate, the crack density is now predicted under conditions of arbitrary crack ratios, L_I/L_{II}. In performing the analysis, it is found that the predicted crack densities do *not* change for $1.05 \leq L_I/L_{II} \leq 2.0$. Ratios below 1.05 are not examined since Eq. (E.20) becomes singular as $L_{II} \to L_I$. The fact that the crack densities are independent of the ratio of L_I/L_{II} results from the fact that the magnitude of g_m is for all intensive purposes independent of L when d, g_{db} and σ are assumed fixed. This is also the reason for the stepped stress-strain responses predicted by the energy balance solutions. The change in the predicted matrix strain energy, normalized by U_{cr_m}, is shown in Fig. E.20 for crack ratios of $L_I/L_{II} = 1.1$ and $L_I/L_{II} = 2.0$. The latter is the WZ criterion.

The vertical drops in Fig. E.20 represent solutions to Eq. (E.20); hence, each drop represents a change in the crack density. Clearly, the crack density progression is very similar for the two cases, and therefore, the assumed crack ratio of $L_I/L_{II} = 2.0$ is *not* believed to be the reason for the discrete or piecewise crack density predictions presented by Weitsman and Zhu. In general, matrix cracking under the energy criterion represented in Eq. (E.20) is dependent on three parameters: g_m^c, d and g_{db} in which d is a function of L and σ. Unfortunately, Eq. (E.20) is *extremely sensitive* to these parameters. Moreover, since the material constants g_m^c and g_{db} are unknown, it is difficult to justify any solution from Eq. (E.20). Hence, in the authors opinion, the CMSE criterion is currently the best *analytical* approach for predicting the evolution of matrix cracks.
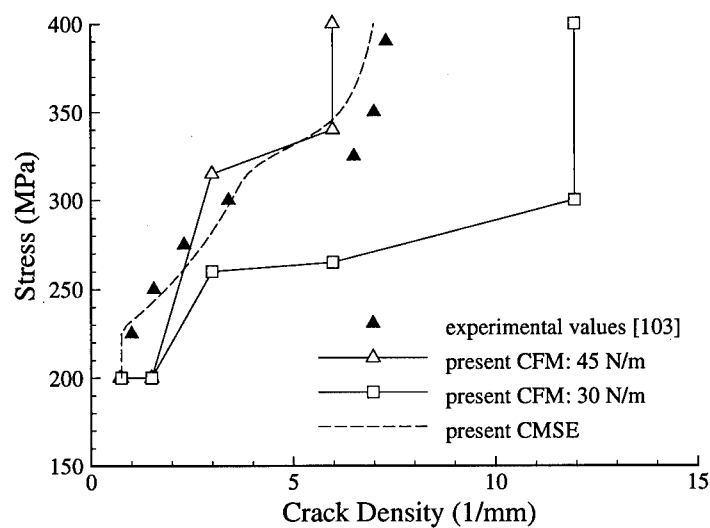
Figure E.19 Applied stress versus crack density as predicted by the current analysis and a classical fracture mechanics (CFM) failure criterion and the current *critical matrix strain energy* (CMSE) criterion.
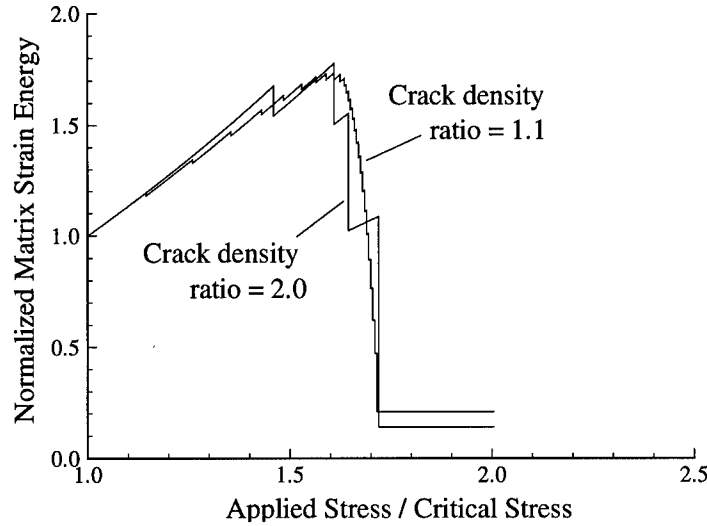
Figure E.20 Normalized matrix strain energy versus normalized stress based upon the fracture criterion presented by Weitsman and Zhu [201].

E.5 Sensitivity Analysis

For unidirectional composites, the nonlinear material response is due, in large part, to the relative magnitudes of the crack spacing, L, and debond length, d, rather than matrix cracking or interface debonding alone. Uncertainties in material properties which influence L and d may therefore be significant sources of error. In light of this, the critical composite stress, σ_{cr}, the ultimate interface shear strength, τ_{ult}, and the interface frictional shear stress, τ_i, are investigated since they are deemed the most important parameters for the present closed-form analysis. The interface parameters (τ_{ult} and τ_i) are difficult to measure experimentally and a wide scatter of data is reported in the literature (due in part to the use of various interface coatings and curing processes) [12]. Further, although σ_{cr} may be easily determined from experimental data, its influence on the proposed model is unknown. In an attempt to better characterize the cracking and debonding modes, fiber failure is not considered.

E-32

It is known from experiments that matrix cracking initiates at a stress level often far below the proportional limit [103]. However since this crack density is low, its influence is negligible. Hence within the present algorithm, it is not necessary to capture the initiation of matrix cracking but rather only the crack density corresponding to the start of non-linear behavior is required. In the present formulation, the deviation of the stress-strain curve is caused by the damage term $U_m(L)$ in the CMSE relation

$$U_{m_o} + U_m(L) = U_{cr_m}. \tag{3.117}$$

If the critical stress is chosen inappropriately low, the desired initial crack spacing which is predicted should tend to be large such that $U_m(L)$ is negligible. If not, the predicted response would incorrectly become non-linear at this stress level. It's effect, as desired, manifests itself as both a continued linear stress-strain prediction, as well as an initial horizontal "step" on the crack density versus applied stress plots (i.e. no increase in crack density). The latter requiring $U_m(L)$ to remain negligible until the "correct" σ_{cr} is obtained. If the critical stress is chosen too large, the initial crack spacing becomes excessively small; resulting in an inappropriately large disparity in strain (at σ_{cr}) between the rule-of-mixtures subroutine and the shear-lag subroutine. However since σ_{cr} was chosen large anyway, it would be desirable if the jump in strain placed the predicted response back on the correct path.

A series of computed normalized crack density [normalized by $100\,(r_f/L)$] versus applied stress plots are provided in Figs. E.21, E.22 and E.23. These figures indicate the influence of σ_{cr}, τ_{ult} and τ_i on matrix cracking for the current analysis.
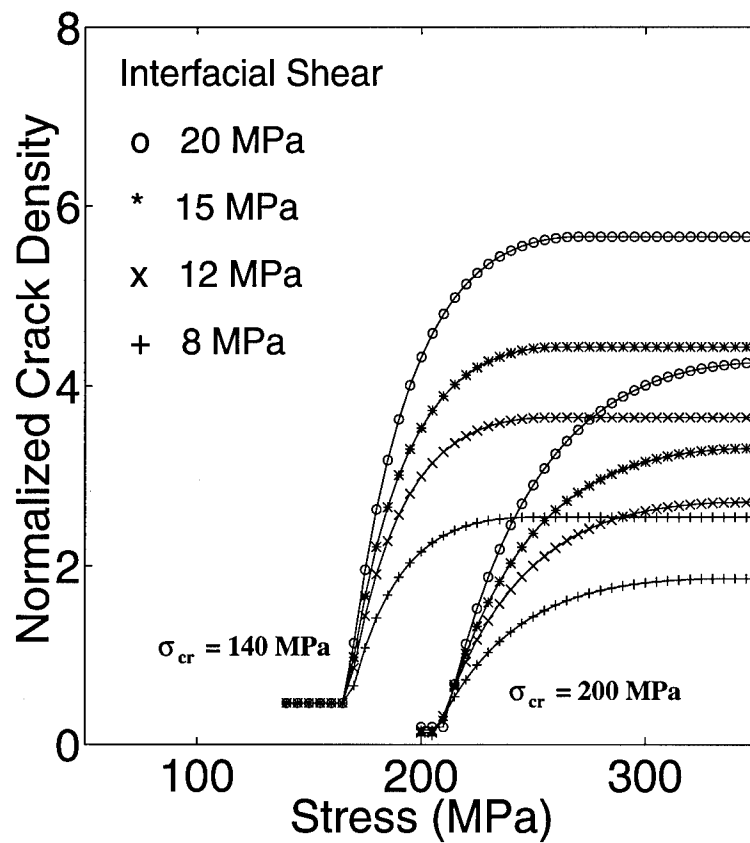
Figure E.21 Influence of τ_i on the crack density progression during loading. Data is shown for both $\sigma_{cr} = 140$ MPa and $\sigma_{cr} = 200$ MPa.
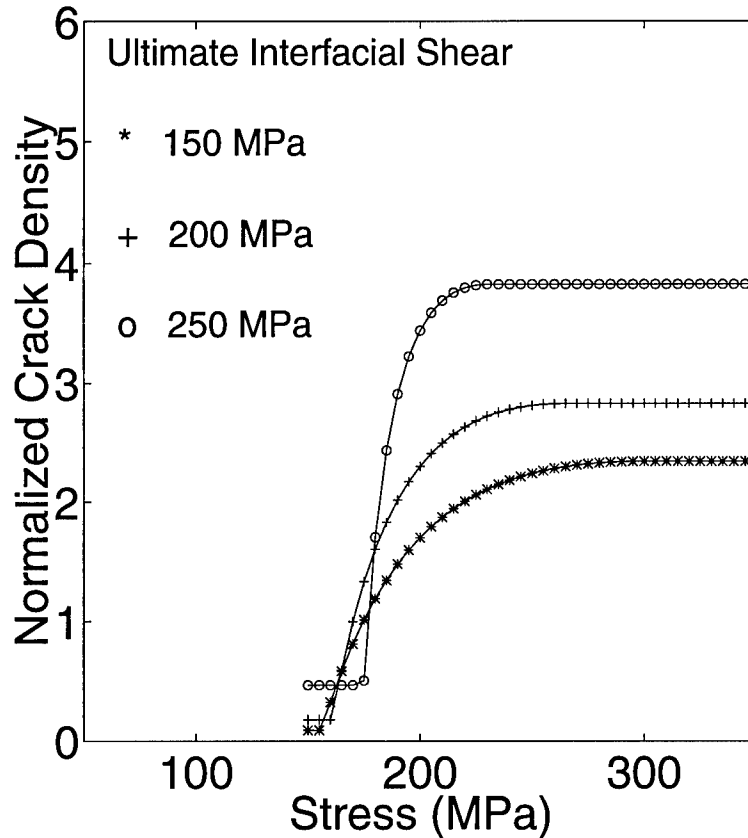
Figure E.22   Influence of τ_{ult} on the crack density progression during loading.

The influence of the frictional interface shear stress and the critical composite stress on the crack density progression within the laminate is shown in Fig. E.21. The stress at which crack saturation is reached appears to be independent of τ_i; however, variations in τ_{ult} cause crack saturation to be achieved more sharply with increasing value of τ_{ult} or gradually with decreasing value of τ_{ult}. That is, as τ_{ult} increases, the stress differential, $\sigma_{sat} - \sigma_{cr}$, from crack initiation (σ_{cr}) to crack saturation (σ_{sat}) decreases. Clearly, σ_{cr}, τ_i and τ_{ult} may be estimated by fitting a set of empirical crack density data. For example, choosing $\sigma_{cr} = 200$ MPa, $\tau_i = 35$ MPa, and $\tau_{ult} = 220$ MPa provides a good fit to the empirical data provided by Kuo [103] (Fig. E.23). Of course, these parameters should not be arbitrarily selected to match existing data, but rather should be obtained based upon physical evidence (push-

out tests, stress-strain response, etc). Based upon published data, τ_i is probably closer to 10 MPa [103]. The crack densities for $\tau_i = 10$ MPa are also shown in Fig. E.23. Interestingly enough, even though the crack density curve for $\tau_i = 10$ MPa seems to have significant error (i.e. doesn't match empirical crack densities), the resulting stress-strain responses for $\tau_i = 10$ and 35 MPa (Fig. E.24) are quite similar. This again results from the fact that the stress-strain response is dependent on the relative magnitudes of L and d rather than their exact values. Hence for the purpose of predicting the composites stress-strain response, it is not required to exactly match empirical crack density data. Of course doing so may provide insight into the progression of interface debonding and/or variations in interface shear stresses.
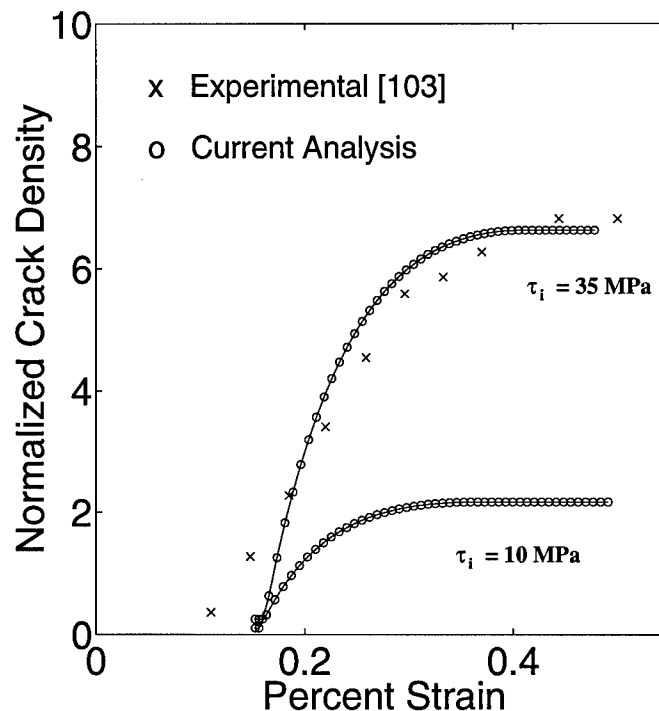
Figure E.23 Normalized crack density versus strain. Empirical data are from reference 103.
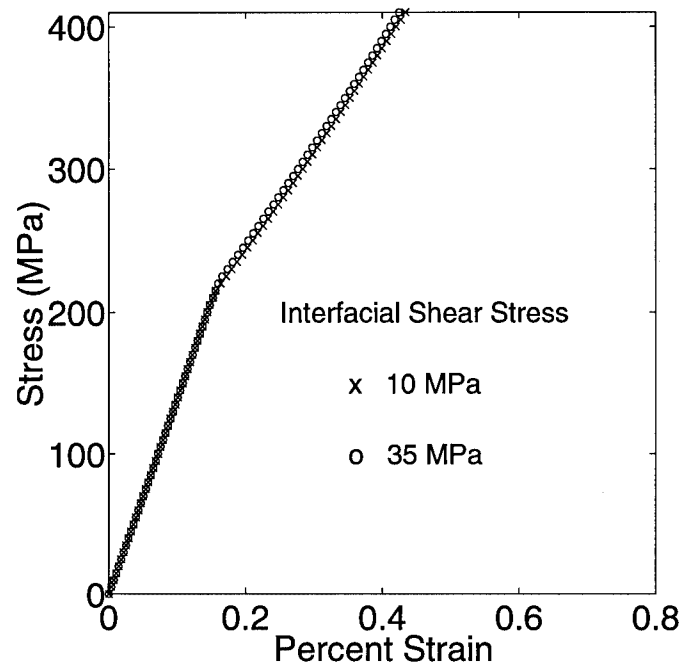
Figure E.24   Stress-strain predictions for $\tau_i = 10$ MPa and $\tau_i = 35$ MPa.

Figures E.23 and E.24 indicate that even though the crack densities decreased significantly for $\tau_i = 10$ MPa, the debond length appears to have increased enough such that the resulting stress-strain response remained approximately equivalent to the original case ($\tau_i = 35$ MPa). Similarly, relatively large changes in σ_{cr} also result in small changes in material response curves. For example, Fig. E.25 shows that for a 60 MPa variation in σ_{cr} the maximum (stress) difference in the predicted stress-strain curves for any value of strain is only around 20 MPa. As this variation decreases, the error quickly vanishes, and as such the present algorithm is surprisingly robust to variations in the critical composite stress. Based upon these results, a series of parametric studies may be developed which will yield information on not only τ_i and τ_{ult} but also upon the progression of interface debonding during loading. As mentioned, if σ_{cr} is chosen small, $U_m(L)$ should be negligible; at least until the "correct" proportional limit is reached. Again this would show up as an initial horizontal step in the crack density curves; minimal debonding, as well as a continued linear response in the stress-strain plots.
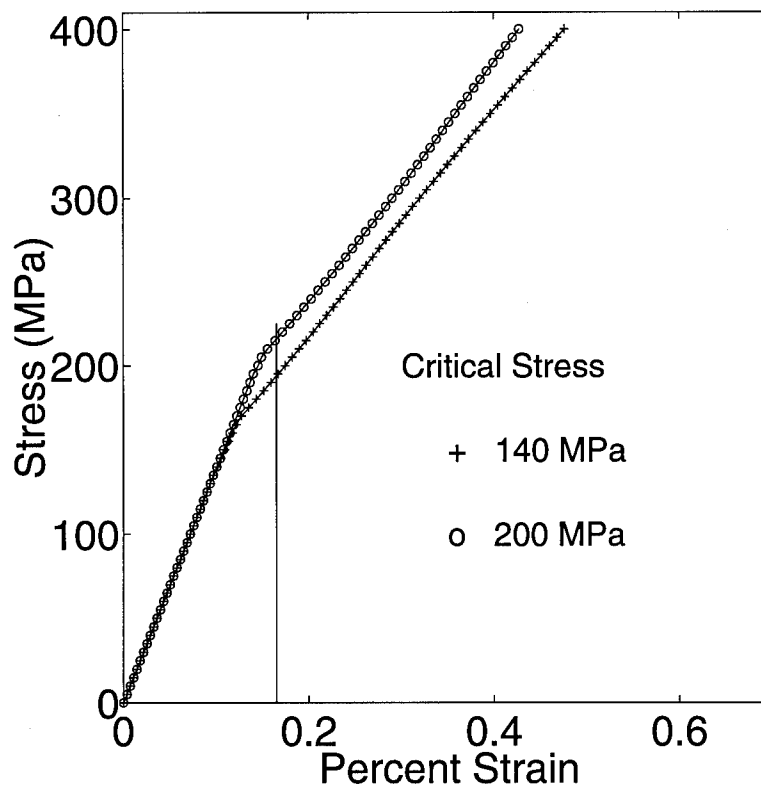
Figure E.25 Stress-strain response for critical stress values of $\sigma_{cr} = 140$ MPa and $\sigma_{cr} = 200$ MPa. For a strain value of 0.00165 (vertical line), the difference in stress is approximately 20 MPa.

Appendix F. Fiber Fracture in Ceramic Matrix Composites

The percentage of fracture fibers, D, in ceramic matrix composites is typically determined using some type of statistical failure criterion. The most common approach is to use a two-parameter Weibull distribution of the form

$$D = 1 - \exp\left[-L\left(\frac{\sigma}{\alpha}\right)^{\beta}\right] \tag{F.1}$$

where α and β are constants which are determined from dry bundle tests of fibers (*ex-situ*). Such tests are difficult to perform, and have resulted in a wide scatter of reported data. In addition, the variation between *ex-situ* and *in-situ* values is unknown. To avoid these problems, a fiber fracture criterion independent of any empirical constants is sought. This appendix outlines two approaches considered in the present study. The first solution is an attempt to find D analytically using a discrete approximation. Unfortunately, the solution overestimates the percentage of fractured fibers under the current strain energy approach. As a result, a statistical approach is adopted. The analytical criterion, as initially developed, is presented in the first section of this appendix. After this presentation, the statistical model is briefly revisited.[†] The appendix concludes with some final comments on Weibull statistics and the present critical energy approach. Some brief comments on fiber/matrix debonding are also included as an aside.

F.1 Fiber Crack Density: An Analytical Model

Consider the extended representative volume element (ERVE) shown in Fig. F.1 in which the composite is divided into NL/δ discrete cells where L is a characteristic length of composite;[‡] δ is the effective length over which the fiber crack influences the local fiber stress and N is the number of fibers in the ERVE. The elastic modulus

---

[†]The statistical model for fiber fracture is discussed in greater detail in chapter three.
[‡]Typically, L is the gage length of the laminate.
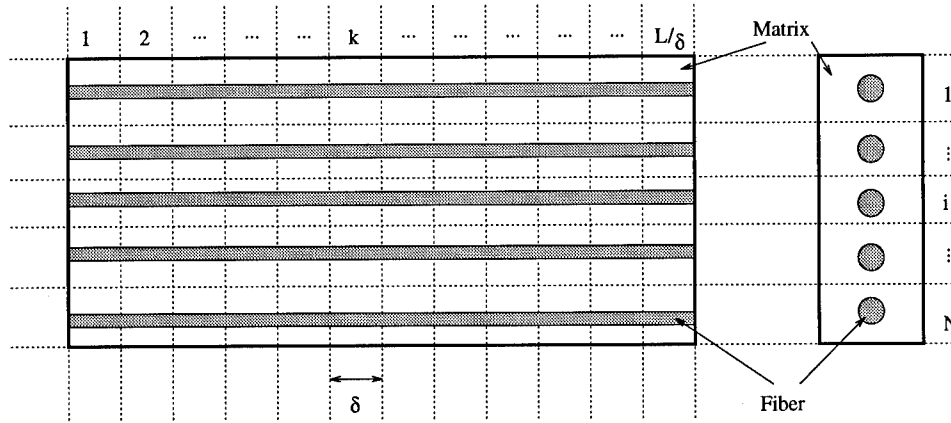
Figure F.1   Extended representative volume element (ERVE).

of each cell is assumed to be

$$E_c = \begin{cases} v_f E_f + v_m E_m & \text{uncracked fiber} \\ v_m E_m & \text{cracked fiber.} \end{cases} \qquad (F.2)$$

Additionally,

$$L\epsilon = \sum_{k=1}^{L/\delta} \delta\, {}^i\epsilon_c^k \qquad \text{for any } i \qquad (F.3)$$

and

$$N\sigma = \sum_{i=1}^{N} {}^i\sigma_c^k \qquad \text{for any } k \qquad (F.4)$$

where ${}^i\epsilon_c^k$ is the strain corresponding to the cell in row i and column k and ${}^i\sigma_c^k$ is the associated stress. It may be shown that

$$\sigma = \frac{\delta}{NL} \sum_{k=1}^{L/\delta} \left\{ \sum_{i=1}^{c_k} v_m E_m\, {}^i\epsilon_c^k + \sum_{i=c_k+1}^{N} \left(v_f E_f + v_m E_m \right) {}^i\epsilon_c^k \right\} \qquad (F.5)$$

where c_k is the total number of cells with cracked fibers in column k. Letting the total number of cells be c and assuming a uniform distribution of fiber cracks

$(c_k = c\delta/L \quad \forall k)$, then

$$\sigma = \left\{ v_f \left(1 - \frac{c\delta}{NL}\right) E_f + v_m E_m \right\} \epsilon \tag{F.6}$$

where $c\delta/NL$ is recognized as the normalized fiber crack density.

Now since fiber failure is assumed to initiate at a critical fiber strain energy U_{cr_f} and since

$$U_f = \sum_{k=1}^{L/\delta} \sum_{i=1}^{N} \frac{1}{2E_f} \left(E_f \,^i\epsilon_c^k\right)^2, \tag{F.7}$$

it is determined that

$$U_{cr_f} = \left(1 - \frac{c\delta}{NL}\right) U_f. \tag{F.8}$$

By definition $D = c\delta/NL$ and therefore from the above relation

$$D = 1 - \frac{U_{cr_f}}{U_f}. \tag{F.9}$$

As mentioned, Eq. (F.9) overestimates the extent of fiber fracture during quasi-static loading of brittle composites. As a result, it was determined that some empirical constants would be required. However, the number of empirical constants, as well as their availability were concerns of the present analysis. As shown in the next section, D was assumed to follow a Weibull failure distribution in which only a single empirical constant needed to be determined. Further, this constant is easily obtained.

F.2 Fiber Crack Density: A Statistical Model

For the present study, the probability of fiber failure or equivalently, the cumulative distribution of fiber crack density, is represented by the parameter D. Furthermore, fiber failure is accounted for in the current shear-lag formulation by modifying the (fiber) stress boundary condition along the plane of the matrix cracks according

F-3

to Eq. (F.10).

$$\sigma_f \left(x = \frac{\pm L}{2} \right) = \frac{\sigma}{v_f(1 - D)} \tag{F.10}$$

This is the same approach as employed by Rouby and Reynauld [163].

Statistical approaches are commonly used to model the failure of fibers in reinforced composites [35, 64, 141, 162, 163, 201, 214] The classical paper in this area is by Rosen in which the composite was treated as a *chain-of-bundles* where the concept of a "weakest link" was applied to determine the cumulative crack density of fiber fractures [161]. The chain-of-bundles approach assumes that each fiber may be divided into a number of evenly spaced segments (or links) of length δ_f such that the total length of the fiber is given by $L_f = \delta_f N_f$ where N_f is the total number of fiber links. Each fiber link is assumed to be characterized by a strength distribution of the Weibull type. The characteristic distance δ_f represents the length over which the local constituent stresses are influenced by the fractured fiber, and depends largely on τ_i [161]. In his analysis, Rosen assumed that each link was characterized by a two-parameter strength distribution function, $\mathcal{G}(\sigma)$ [161].

$$\mathcal{G}(\sigma) = \delta_f r_1 r_2 \sigma^{(r_2 - 1)} \exp(-r_1 \delta_f \sigma^{r_2}) \tag{F.11}$$

The scaling and shape constants r_1 and r_2 are evaluated from empirical data.

More recently, Curtin [36] presented an analysis which assumed that the fiber crack density was given by

$$D = 1 - \frac{1}{\exp(\Phi(L, \sigma)^m)} \tag{3.121}$$

where

$$\Phi(L, \sigma) = \frac{L}{L_o} \left(\frac{\sigma}{\sigma_o} \right) \tag{F.12}$$

and σ_o is the stress required to cause one failure, on average, in a fiber of length L_o [36]. These data (σ_o and L_o) are again determined experimentally. The Weibull modulus, m, characterizes the variability of the data about the average [36].

For the present study, the fiber strength distribution is again assumed to be of a Weibull form; however, instead of using the fiber stress to characterize the distribution as in the previous cases [36,161], the fiber strain energy, U_f, is used to model fiber fracture. For this study, the percentage of fracture fibers is given by

$$D = 1 - \frac{1}{\exp\left(\left[1 - \frac{U_{cr_f}}{U_f}\right]^{\hat{m}}\right)} \qquad (F.13)$$

where U_{cr_f} is the *critical fiber strain energy* defined as the average strain energy in the fiber when fiber fracture initiates, and $\hat{m}$ is now the Weibull modulus. The argument $1 - U_{cr_f}/U_f$ is chosen based upon the analysis presented in the previous section. Further, it is recognized that Eqs. (F.11), (3.121) and (F.13) all represent cumulative fracture distributions with Φ of the form

$$\Phi = r_1 \left(\frac{\sigma}{\sigma_o}\right)^{r_2} \qquad (F.14)$$

where r_1 and r_2 are constants. However, the distribution in the present study assumes that there exists a threshold stress below which no fiber failure occurs, i.e.

$$\Phi = r_1 \left(\frac{\sigma - \sigma_{ff}}{\sigma_o}\right)^{r_2}. \qquad (F.15)$$

The stress at which fiber failure initiates, σ_{ff}, is defined as the stress at which a maximum or saturated crack density is obtained for $D = 0$, and is determined analytically from Eq. (3.117).

Failure distributions similar to Eq. (3.121) have also been used to predict matrix cracking in brittle composites [37,117,179]. However, fiber failure in ceramic

composites is distinguishable from matrix cracking by one important factor. During matrix failure, the fibers are, in general, able to carry the additional stress. However during fiber failure, there is a critical fraction of broken fibers beyond which additional load will fail the composite. The critical fraction of fractured fibers is denoted D^* where if $D \geq D^*$, composite failure occurs. Hence, $D \in [0, D^*]$ where $D^* < 1$.

The parameter D^* may be related to the traditional Weibull modulus, m, by Eq. (F.16) as reported in reference 163.

$$D^* = \frac{2}{m + 2} \tag{F.16}$$

From Eq. (F.13), the current Weibull modulus, $\hat{m}$, is also dependent on D^* as given by Eq. (F.17).

$$\hat{m} = \frac{\ln\left\{\ln\left(\frac{1}{1 - D^*}\right)\right\}}{\ln\left(1 - \frac{U_{cr_f}}{U_f^*}\right)} \tag{F.17}$$

where U_f^* is the average fiber strain energy at composite failure. Since the damage configuration at composite failure is not known *a priori*, $\hat{m}$ must be determined. The constant $\hat{m}$ is obtained by fitting empirical *stress-strain* for the unidirectional laminate. Further, obtaining and fitting the experimental stress-strain data is easily accomplished. Also, based on Eqs. (F.16) and (F.17), a range for $\hat{m}$ may be estimated based upon reported values for m. A common range of m for a SiC/CAS composite is between 2 and 10 which corresponds to a range of 1.25 to 5.5 for $\hat{m}$ [36,37,163]. For a unidirectional SiC/CAS laminate, $\hat{m} = 2.0$ is found to match well with empirical data [175]. Finally, D^* is assumed to be a constant of laminate lay-up for the same material, and is found to be 0.42 for SiC/CAS [175].

When accounting for the fracture of fibers in this manner, the fiber stress, $\sigma_f(x)$, in Eq. (3.45) becomes

$$\sigma_f(x) = \begin{cases} \sigma_{f_o} + \dfrac{\cosh(\beta x)}{\cosh[\beta(L/2 - d)]}\left(\dfrac{\sigma}{v_f(1-D)} - \sigma_{f_o} - 2\dfrac{d}{r_f}\tau_i\right) & \text{bonded region} \\[1em] \dfrac{\sigma}{v_f(1-D)} - \dfrac{2}{r_f\tau_i}(L/2 - |x|) & \text{debonded region.} \end{cases} \tag{B.16}$$

From this, the remaining stresses, $\sigma_m(x)$ and $\tau_i(x)$, may be determined from Eqs. (3.8) and (3.10). For the cross-ply laminate, the fractured fibers are accounted for in the analysis by replacing the quantity v_f appearing in the definitions for the constants c_1-c_4 (chapter three) with $v_f(1-D)$. For completeness, a brief discussion of Weibull statistics is provided.

F.3   Weibull Statistics

Ceramic materials have randomly distributed imperfections (e.g. voids and inclusions) within their microstructure. These defects are statistical in both size and location. It has been well established that the failure distribution for brittle cylindrical fibers can be described by a statistical distribution known as the *Weibull distribution*. For such a distribution, the probability density function[†], $f(x)$, is given by the following two parameter (α and β) distribution

$$f(\sigma) = L\alpha\beta\sigma^{(\beta-1)}\exp\left\{-L\alpha\sigma^\beta\right\} \tag{F.18}$$

where L is the fiber length, σ is the fiber strength. Furthermore, the cumulative failure distribution, $F(x)$ and the expected value, μ_x, are

$$F(\sigma) = 1 - \exp\left\{-L\left(\frac{\sigma}{\alpha}\right)^\beta\right\}, \tag{F.1}$$

[†]The area under the probability density curve defines the probability.

$$\mu_x = (L\alpha)^{(-1/\beta)} \cdot \Gamma(1 + 1/\beta) \qquad (\text{F.19})$$

where $\Gamma()$ is the well-known gamma function. Note that μ_x is also the mean (nominal) fiber stress [25]. It may also be shown that

$$\ln\left[\ln\left(\frac{1}{1 - F(\sigma)}\right)\right] = \beta \ln \sigma + \ln \alpha. \qquad (\text{F.20})$$

The constants, α and β, may be determined by fitting empirical fiber crack density data according to Eq. (F.20).

The Weibull distribution assumes that the fibers is composed of a number of segments of the same length, and in which each segment has an equal probability of failure according to Eq. (F.1). In engineering mechanics, the cumulative survival probability [Eq. (F.1)] for continuous fibers is typically written as

$$D = 1 - \exp\left\{\left(\frac{\sigma}{\sigma_o}\right)^m\right\}^{-1} \qquad (\text{F.21})$$

where σ_o is some characteristic fiber strength and m is the tradition Weibull modulus. From Eq. (F.21), σ_o corresponds to a survival probability of 0.37 percent. Figure F.2 shows schematically the strength distributions for various values of m. The shape and scaling parameters, σ_o and m, may be determined by fitting empirical data; however, their solution is somewhat involved since the variation in D versus σ, as shown in Fig. F.2, cannot be solved for directly.

F.4 Fiber Crack Density: An Alternate Approach

In chapter three, it was shown that the instantaneous average crack spacing could be estimated by ensuring that the matrix strain energy never exceeded some critical value, U_{cr_m}, according to Eq. (3.117).

$$U_{m_o} + U_m(L) = U_{cr_m} \qquad (3.117)$$
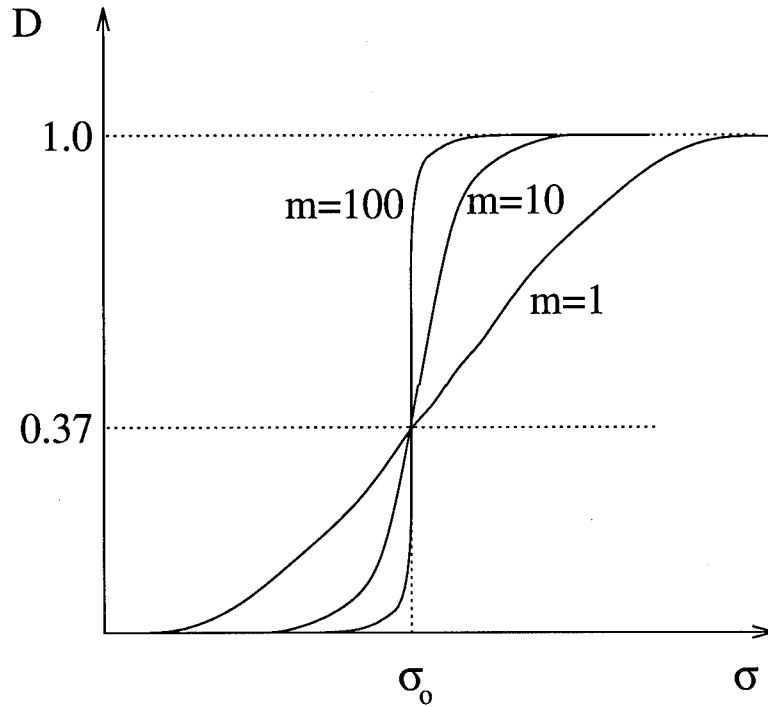
Figure F.2   Cumulative probability distributions based upon a Weibull formulation.

The parameter U_{m_o} is the matrix strain energy which would exist if the composite was undamaged. The fact that matrix cracks do exist and some energy is transferred from the matrix to the fiber is accounted for by the term $U_m(L)$. The constant U_{cr_m} is assumed to be a known lamina property and was termed the *critical matrix strain energy.*

It may be shown that Eq. (F.9) can be reformulated in terms of the *critical fiber strain energy* according to the following equation in which the fraction of broken fibers in now the perturbed parameter.

$$U_{f_o} + U_f(D) = U_{cr_f} \qquad \text{(F.22)}$$

Note, that the variable D in Eq. (F.22) loses it physical significance since D must increase in order for the left hand side of Eq. (F.22) to decrease. Hence, the actual number of fractured fibers must still be determined empirically. However, the two

problems can be posed in a similar manner. In both cases, there exists some damage parameter, P, which fails according to Eq. (F.23)

$$P = (1 - \chi) \, P_o + \chi P_{sat} \tag{F.23}$$

where P_o is the initial parameter value; P_{sat} is the final magnitude, and χ is the damage index $\in [0, 1]$. For the current analysis, $P \in \{L, d, v_f\}$. Further, based on the assumed critical strain energy relations (e.g. $U_{P_o} + U_P(\chi) = U_{P_{cr}}$),

$$\chi = \frac{P_o - \mathcal{F}(U_P)}{P_o - P_{sat}} \tag{F.24}$$

where $\mathcal{F}(U_P)$ is an inverse function of the strain energies. For matrix cracking, $\mathcal{F}(U_P)$ is known directly; however, when considering fiber failure, $\mathcal{F}(U_P)$ cannot be determined and therefore is assumed.

F.5   Aside: Fiber/Matrix Debonding

Recall that interface debonding is assumed to occur whenever the interface shear stress, $\tau_i(x)$, exceeds the ultimate strength of the interface, τ_{ult}. Hence, under this maximum stress approach, the debond length may be determined by ensuring that $\tau_i(x = L/2 - d) = \tau_{ult}$. With the addition of fiber fracture, the extent of debonding for the unidirectional laminate is given by Eq. (F.25).

$$d = \frac{1}{2} r_f \left\{ \frac{v_m}{v_f} \frac{\sigma_{m_o}^*}{\tau_i} + \frac{E_f}{E_1} \frac{D}{1 - D} \frac{\sigma}{\tau_i} \right\} - \frac{1}{\beta G} \frac{\tau_{ult}}{\tau_i} \tag{F.25}$$

where

$$\sigma_{m_o}^* = \frac{E_m}{E_1} \frac{\sigma}{1 - D} + E_1 (\alpha_1 - \alpha_m) \Delta T \tag{F.26}$$

Equation (F.25) must also be solve iteratively, however, a simple Newton iteration scheme is suitable, e.g.

$$d_{n+1} = d_n - \frac{d_n + \dfrac{\tau_{ult}}{\beta G \tau_i} - \dfrac{r_f}{2}\left\{ \dfrac{v_m}{v_f}\dfrac{\sigma_{m_o}^*}{\tau_i} + \dfrac{E_f}{E_1}\dfrac{D}{1-D}\dfrac{\sigma}{\tau_i}\right\}}{1 + \dfrac{\tau_{ult}}{\tau_i}\left\{\dfrac{G^2-1}{G}\right\}}. \qquad (F.27)$$

For cross-ply laminates, the maximum stress criterion is again adopted for debonding. However, the debonding is assumed to occur only within the 0° plies of the cross-ply laminate. Accordingly, the debond lengths are determined numerically from the following two coupled equations.

$$-\frac{r_f}{2}\left\{ c_3\beta \cosh(\phi_l) + c_4\beta \sinh(\phi_l) + \mathcal{H}\lambda \frac{\sinh\left(\lambda x_{t_{|x=\phi_l}}\right)}{\cosh\left(\lambda L_t/2\right)}\right\} = \tau_{ult} \qquad (F.28)$$

$$\frac{r_f}{2}\left\{ c_3\beta \cosh(\phi_r) + c_4\beta \sinh(\phi_r) + \mathcal{H}\lambda \frac{\sinh\left(\lambda x_{t_{|x=\phi_r}}\right)}{\cosh\left(\lambda L_t/2\right)}\right\} = \tau_{ult} \qquad (F.29)$$

where τ_{ult} is the ultimate interface shear stress of the bonded fiber and matrix, and $\phi_l = \beta\left(-L/2 + d_l\right)$ and $\phi_r = \beta\left(L/2 - d_r\right)$.

Appendix G. Strain Ratchetting in Unidirectional Laminates: An Analytical Model

In an attempt to capture the influence of strain ratchetting which is observed in fatigue tests of ceramic composites, the modeled fiber stress is augmented by a constant stress, $\Delta\sigma(N)$. This quantity, $\Delta\sigma(N)$, is an approximation for the additional stress experienced by an undamaged fiber when adjacent fibers fracture and pull-out from the surrounding matrix according to a uniform distribution. Furthermore, the introduction of this stress is necessary since the shear-lag model, in the traditional manner, fails to capture the continuous progression in permanent strain (e.g. strain ratchetting) which results from fiber pull-out.

Once a fiber fractures and debonds, the extent of pull-out is dependent on the interface resistance, τ_i, as well as any obstructions which may collect along the interface (e.g. surface asperities, debris from broken fibers and/or matrix). Furthermore, upon unloading, the fiber crack opening does not necessarily vanish due to the surface obstructions, fiber warping, and Poisson's effects. Since these phenomena restrict constituent slip, they may be modeled within the unidirectional unit-cell as a region which never debonds nor slips upon unloading. The introduction of this *permanently bonded region* (PBR) represents areas within the laminate where slip is obscured, and more importantly, the application of this frictional region leads to an *analytical solution* for the development of permanent strain. The development is present in this appendix.

Since the modified fiber stress distribution, as shown in Fig. 3.17, is assumed linear, $\Delta\sigma(N)$ may be determined provided the stress at any point is known. This point may be taken anywhere, i.e. $x_o = \gamma L/2$ where $\gamma^\dagger$ defines the region within the shear-lag model where debonding is prevented (i.e. $\tau_{ult} = \infty$). Note that this

---

$^\dagger 0 \leq \gamma \leq 1$

constraint has only been introduced to find $\sigma_f(x_o)$ and the constituent stresses will be defined in the limit [Eq. (G.1)] as the permanently bonded region vanishes.

$$\Delta\sigma(N) = \lim_{\gamma \to 0} \Delta\sigma(N,\gamma) \qquad (G.1)$$

When evaluating the limit of Eq. (G.1), stress equilibrium must be maintained. Further two constraints need to be taken into account. The first is to ensure that the fiber carries all of the stress along the plane of the matrix crack [i.e. $\sigma_m(x = \pm L/2) = 0$]. The second constraint is derived from the fact that upon complete unloading, the strain in the matrix is known *a priori* [Eq. (3.125); Fig. 3.17].

During loading, the constituent stresses within the permanently bonded region remain unchanged from those previously determined [Eq. (3.45)]; however, since slip is prevented during unloading within this region, the resulting shear-lag equations produce a $\Delta\sigma(N,\gamma)$ which may be determined since the matrix strain is defined upon unloading. The additional fiber displacement due to $\Delta\sigma(N)$ is now defined by $\delta(N)$ according to Eq. (G.2).

$$\delta(N) = \frac{\Delta\sigma(N)L}{E_f} \qquad (G.2)$$

The desired stress $\Delta\sigma(N)$ may now be determined by evaluating $\delta(N,\gamma)$ as $\gamma \to 0$ under the aforementioned considerations. As expected, $\Delta\sigma(N)$ depends on the extent of composite damage, the maximum applied stress, and the degradation of the interface shear.

G.1 Formulation of $\Delta\sigma(N)$

The formulation of $\Delta\sigma(N)$ consists primarily of three steps. For the analysis, consider a unit-cell which has length L (i.e. $x \in [-L/2, L/2]$) and which is assumed to contain a PBR ($x \in [-\gamma L/2, \gamma L/2]$) which neither debonds during loading, nor slips during unloading (Fig. G.1). The first step of the analysis is to determine the
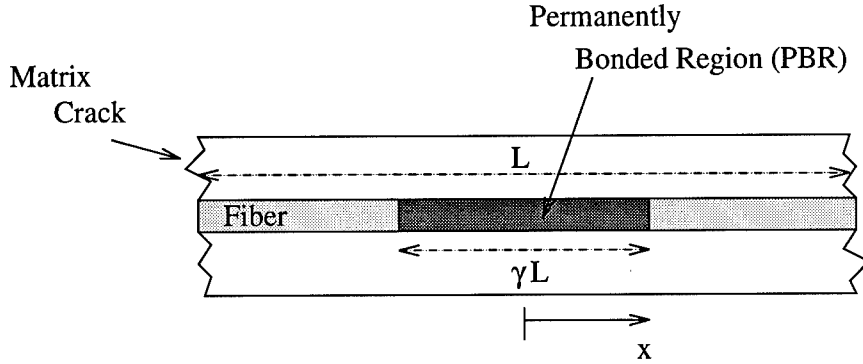
Figure G.1 A modified unidirectional unit-cell incorporating a permanently bonded region (PBR) for analysis purposes.

constituent stresses $\sigma_f(x)$ and $\sigma_m(x)$ during a complete loading and unloading cycle. After unloading, the residual matrix *strain* is not consistent with the expected value due to the presence of the PBR, and therefore, the constituent stresses must be adjusted to ensure the desired result is obtained. The adjustment of the constituent stresses constitutes the second step of the analysis. The final step in finding $\Delta\sigma(N)$ lies in determining the fiber stress as the permanently bonded region vanishes (i.e. $\gamma \to 0$). Each of these three steps are now considered.

G.1.1 Residual Constituent Stresses in the Modified Unit-Cell.   Because of the assumed geometry, only one-half of the unit-cell needs to be modeled. Hence, consider only the axial coordinates: $x \in [0, L/2]$. It may be shown that during loading the stress in the fiber is

$$\sigma_f(x) = \frac{\sigma}{v_f(1-D)} - \frac{2\tau_i}{r_f}\left(\frac{L}{2} - x\right) \qquad \text{for} \quad x \in [\gamma L/2, L/2], \qquad \text{(G.3)}$$

$$\sigma_f(x) = \sigma_{f_o} + \frac{\cosh(\beta x)}{\cosh(\beta\gamma L/2)}\left\{\frac{\sigma}{v_f(1-D)} - \sigma_{f_o} - (1-\gamma)\frac{\tau_i L}{r_f}\right\} \quad \text{for} \quad x \in [0, \gamma L/2].$$
$$\text{(G.4)}$$

Further, since the interface is not permitted to debond within the PBR, the shear stress which develops along the fiber/matrix interface may exceed the ultimate

strength of the interface τ_{ult}. Recall that previously under the maximum stress debonding criterion, τ_{ult} was assumed to be the maximum obtainable value for $\tau_i(x)$. This is no longer the case, i.e. $\tau_i(x = \gamma L/2) \geq \tau_{ult}$. Now, if we define ($\doteq$), $\hat{\tau}_{ult}$ to be the maximum shear stress which develops under the new geometry (i.e. $\hat{\tau}_{ult} \doteq \tau_i(x = \gamma L/2)$ at $\sigma = \sigma_{max}$), then it may be shown that

$$\hat{\tau}_{ult} = \frac{\beta r_f}{2} \tanh\left(\beta\gamma L/2\right) \left\{ \frac{\sigma}{v_f(1-D)} - \sigma_{f_o} - (1-\gamma)\frac{\tau_i L}{r_f} \right\}_{|\sigma = \sigma_{max}} . \tag{G.5}$$

Moreover,

$$\tau_i\left(x = \gamma L/2\right) = \hat{\tau}_{ult} \tag{G.6}$$

since slip is not permitted within the PBR during unloading. By enforcing the equality in Eq. (G.6), the fiber stress along the PBR during unloading becomes

$$\sigma_f(x) = \sigma_{f_o} + \frac{\cosh(\beta x)}{\cosh(\beta\gamma L/2)} \left\{ \frac{\sigma}{v_f(1-D)} - \sigma_{f_o} + (1-\gamma)\frac{\hat{\tau}_i L}{r_f} \right\} \tag{G.7}$$

where

$$\hat{\tau}_i = \frac{r_f}{(1-\gamma)L} \left\{ \frac{1}{\beta r_f} \frac{2\hat{\tau}_{ult}}{\tanh\left(\beta\gamma L/2\right)} - \frac{\sigma}{v_f(1-D)} + \sigma_{f_o} \right\} . \tag{G.8}$$

Furthermore, the fiber stress *outside* the PBR is

$$\sigma_f(x) = \frac{\sigma}{v_f(1-D)} + (1-\gamma)\frac{\hat{\tau}_i L}{r_f} - \frac{2\tau_i}{r_f}\left(x - \frac{\gamma L}{2}\right) . \tag{G.9}$$

The latter is determined by ensuring the fiber stress remains continuous.

The stress in the matrix may be determined from Eqs. (G.7) and (G.9) since equilibrium requires that

$$\sigma_m(x) = \frac{\sigma}{v_m(1-D)} - \frac{v_f}{v_m}\sigma_f(x) + (1-\gamma)\frac{v_f L}{v_m r_f}\left(\tau_i - \hat{\tau}_i\right) . \tag{G.10}$$

Then, upon complete unloading, the fiber/matrix constituent stresses may be determined by evaluating Eqs. (G.7) through (G.10) at $\sigma = \sigma_{min}$. In performing the

analysis, one finds that the matrix strain resulting from Eq. (G.10) is in disagreement with the known magnitude for a completely debonded interface. Hence, the next step in the analysis is to adjust the constituent stresses within the unit-cell to ensure that the desired matrix strain is predicted.

G.1.2 Re-Evaluating the Residual Strain. For a completely debonded interface, the matrix strain resulting from load cycling of a unidirectional laminate is readily available. Let $\bar{\epsilon}_m$ define this strain; then under the present shear-lag formulation,

$$\bar{\epsilon}_m = \frac{2}{E_m L} \int_0^{L/2} \frac{v_f}{v_m} \frac{2\tau_i}{r_f} \left(x - L/2\right) dx. \tag{G.11}$$

However, due to the introduction of the permanently bonded region into the unit-cell, the predicted strain does not equal $\bar{\epsilon}_m$, and therefore, it is necessary to adjust the former distribution to ensure the resulting matrix strain is equal to $\bar{\epsilon}_m$. This is accomplished by superimposing a constant stress $\Delta\sigma_m$ on the previous solution to obtain the desired value. In other words, define $\Delta\sigma_m$ such that

$$\frac{2}{E_m L} \int_0^{L/2} \left\{ \sigma_m(x) - \Delta\sigma_m \right\} \, dx = \bar{\epsilon}_m \tag{G.12}$$

where $\sigma_m(x)$ is defined by Eq. (G.10) and $\Delta\sigma_m$ is the required stress adjustment. The latter may be determined directly from Eq. (G.12), and is a function of γ.

Pictorially, this process is illustrated in Fig. G.2. The unmodified matrix stress distribution, as predicted by Eq. (G.10), is represented schematically by the dotted line in this figure. The adjusted (dashed line) and desired (solid line) stresses are also shown. As is evident from Fig. G.2, the predicted stress is increased uniformly until the adjusted and "actual" stress distributions represent equivalent strains.

G.1.3 Removal of the PBR Constraint. The final step in the analysis is to consider the resulting fiber stress as the permanently bonded region vanishes. For this part of the analysis, let's again introduce the parameter $\delta(N)$ which represents
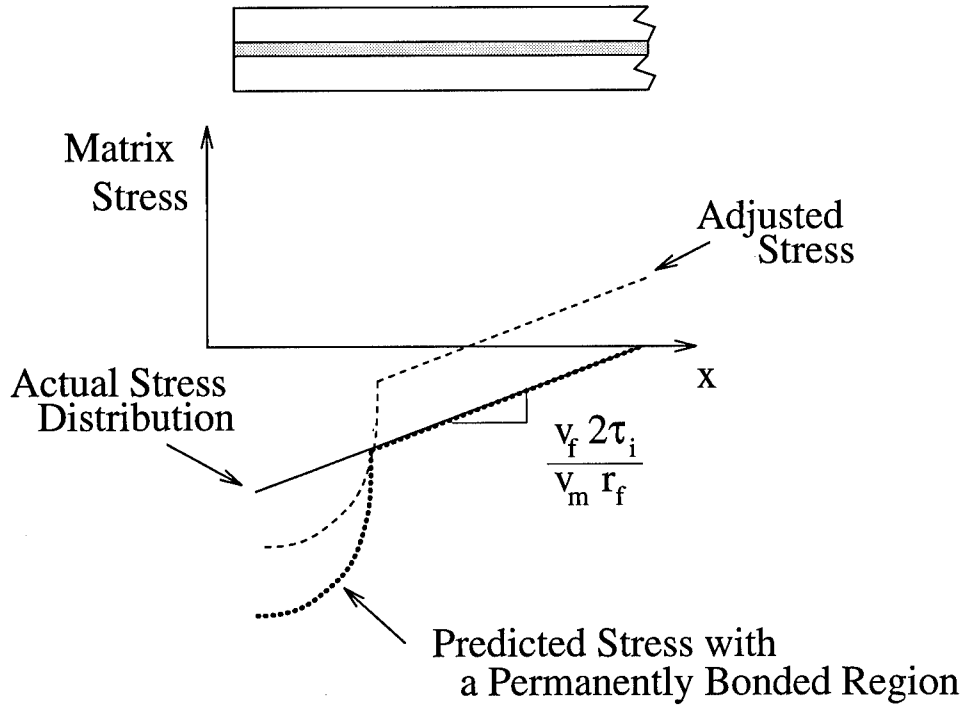
Figure G.2   Stress distributions after unloading for a completely debonded interface and an interface with a permanently bonded region.

the fiber pull-out distance associated with the stress $\Delta\sigma(N)$ [Eq. (G.2)]. Further, given the adjusted matrix stress, as determined in the previous section, the following relations [Eqs. (G.13) and (G.14)] may be shown to be true.

$$
\begin{aligned}
\delta(N) = \frac{1}{E_f} \Bigg\{ & \int_0^{\gamma L/2} \sigma_{f_o} + \frac{v_m}{v_f}\Delta\sigma_m + \frac{\cosh(\beta x)}{\cosh(\beta\gamma L/2)} \left\{ \frac{\sigma}{v_f(1-D)} + (1-\gamma)\frac{\hat{\tau}_i L}{r_f} \right\} dx \\
& + \int_{\gamma L/2}^{L/2} \frac{\sigma}{vf(1-D)} + \frac{v_m}{v_f}\Delta\sigma_m + (1-\gamma)\frac{L}{r_f}(\hat{\tau}_i - \tau_i) - \frac{2\tau_i}{r_f}(x - L/2)\, dx \\
& - \int_0^{L/2} \frac{2\tau_i}{r_f}(x - L/2)\, dx \Bigg\}\Bigg|_{\sigma = \sigma_{min}}
\end{aligned}
\tag{G.13}
$$

and

$$
\Delta\sigma(N) = \frac{1}{\beta L}\left\{ \left[\frac{\sigma_{max} - \sigma_{min}}{v_f(1-D)} - \left(\sigma_{f_{o_{max}}} - \sigma_{f_{o_{min}}}\right) \right] [\gamma\beta L - 2\tanh(\gamma\beta L/2)] \right\} \\
+ \frac{\tau_i}{2\beta r_f}\left\{ (3\gamma - 2)\gamma\beta L + 4(1-\gamma)\tanh(\gamma\beta L/2) \right\}
\tag{G.14}
$$

Finally, equating Eq. (G.13) into Eq. (G.2) and considering the limit as $\gamma \to 0$, the desired stress, $\Delta\sigma(N)$, is found to be

$$\Delta\sigma(N) = \frac{v_m E_m + Dv_f E_f}{v_f(1-D)E_1}\sigma_{max} - \frac{2\tau_i(N)}{r_f}L \qquad (4.3)$$

where the interface shear is assumed to degrade with load cycling, i.e. $\tau_i = \tau_i(N)$. As expected, the extent of fiber pull-out is dependent on the maximum applied stress (σ_{max}), the interface resistance $[\tau_i(N)]$, and the composite's state of damage (D, L and d). The final constituent stresses upon unloading are illustrated in Fig. G.3. Note
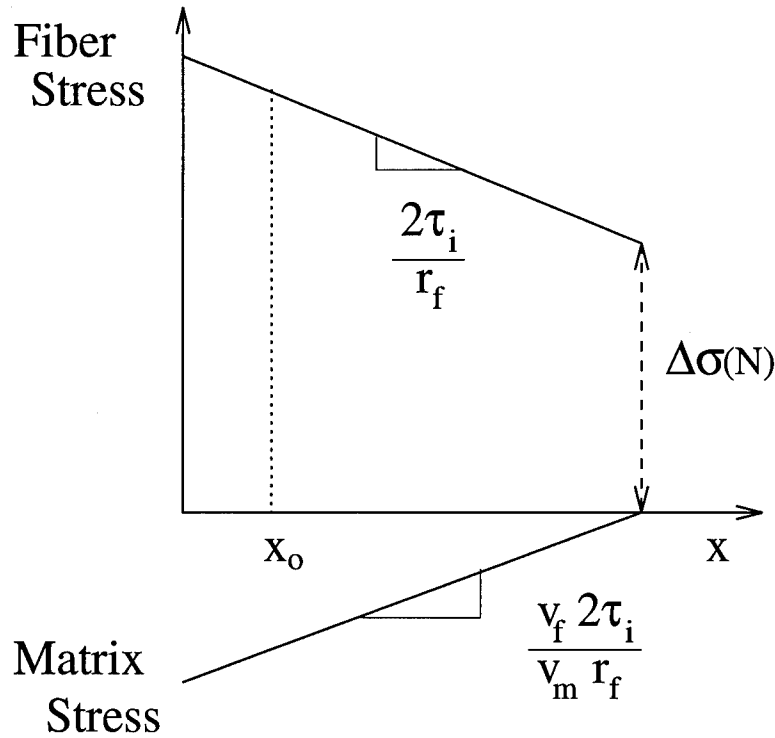
Figure G.3 Final constituent stress distributions.

that the matrix stress is as desired, and the fiber stress is adjusted appropriately. In fact, the application of the permanently bonded region is simply a mathematical means for determining the fiber stress at a single point, x_o. In this case, $x_o = \gamma L/2$. Furthermore, once the stress at this point is determined, the fiber stress is known everywhere since the distribution varies linearly with slope $2\tau_i/r_f$.

Appendix H. Strain Ratchetting in Cross-Ply Laminates: An Analytic Model

Under the current shear-lag formulation, once the fiber/matrix interface completely debonds, the residual strain upon unloading becomes constant, and therefore, the analysis is unable to capture the strain ratchetting behavior observed during experimental fatigue tests of cross-ply ceramic matrix composites. However, as observed with the unidirectional model, the ratchetting behavior can be modeled simply by augmenting the assumed fiber stress by a constant amount $\Delta\sigma(N)$. In this manner, the stress-strain hysteresis loops continue to "march out" as observed experimentally. In addition, a closed-form solution for $\Delta\sigma(N)$ can be found if a permanently bonded region (PBR) is introduced into the analysis. The formulation of $\Delta\sigma(N)$ is provided in this appendix, and it is presented in three steps.

H.1 Formulation of $\Delta\sigma(N)$

The first part of the analysis lies in determining the residual fiber/matrix constituent stresses, $\sigma_f(x)$ and $\sigma_m(x)$, within the 0° ply. These stresses will differ from those presented in chapter three due to the assumed PBR. The second step of the analysis involves augmenting the aforementioned stress fields such that the predicted matrix strain equals the matrix strain which is known to exist for a debonded interface. Finally, the stress $\Delta\sigma(N)$ is determined through examination of the fiber stress as the PBR vanishes. These three steps are now considered.

H.1.1 Residual Constituent Stresses in the Modified Unit-Cell.

During loading, since γ is fixed, the interfacial shear $\tau_i(x)$ at $x = \pm\gamma L/2$ may exceed the ultimate bond strength of the interface, τ_{ult}, i.e. $\tau_i\left(\pm\gamma L/2\right) \geq \tau_{ult}$. Let $\hat{\tau}_{ult_l} \doteq \tau_i\left(-\gamma L/2\right)$ and $\hat{\tau}_{ult_r} \doteq \tau_i\left(\gamma L/2\right)$ define these maximum shear stresses. Then from

Eq. (F.29), it may be shown that

$$\hat{\tau}_{ult_l} = -\frac{r_f}{2}\left\{c_3\beta\cosh\left(\beta\gamma L/2\right) - c_4\beta\sinh\left(\beta\gamma L/2\right) + \frac{\mathcal{T}\lambda}{\cosh\left(\lambda L_t/2\right)}\sinh\left(\lambda x_{t|_{x=-\gamma L/2}}\right)\right\}$$

(H.1)

and

$$\hat{\tau}_{ult_r} = \frac{r_f}{2}\left\{c_3\beta\cosh\left(\beta\gamma L/2\right) + c_4\beta\sinh\left(\beta\gamma L/2\right) + \frac{\mathcal{T}\lambda}{\cosh\left(\lambda L_t/2\right)}\sinh\left(\lambda x_{t|_{x=\gamma L/2}}\right)\right\}$$

(H.2)

where

$$c_3 = \frac{\chi_l + \chi_r}{2\cosh\left(\beta\gamma L/2\right)},$$

(H.3)

$$c_4 = \frac{\chi_l - \chi_r}{2\sinh\left(\beta\gamma L/2\right)},$$

(H.4)

$$\chi_l = \sigma_f^l - \mathcal{T}\frac{\cosh\left(\lambda x_{t|_{x=\phi_l}}\right)}{\cosh\left(\lambda L_t/2\right)} - \sigma_f^o,$$

(H.5)

$$\chi_r = \sigma_f^r - \mathcal{T}\frac{\cosh\left(\lambda x_{t|_{x=\phi_r}}\right)}{\cosh\left(\lambda L_t/2\right)} - \sigma_f^o,$$

(H.6)

$$\sigma_f^l = \frac{1}{v_f}\left\{\frac{b+d}{b}\sigma - \frac{d}{b}\sigma_T\left(x_{t|_{x=-L/2}}\right)\right\} - \frac{2}{r_f}\tau_i(1-\gamma)L/2,$$

(H.7)

$$\sigma_f^r = \frac{1}{v_f}\left\{\frac{b+d}{b}\sigma - \frac{d}{b}\sigma_T\left(x_{t|_{x=L/2}}\right)\right\} - \frac{2}{r_f}\tau_i(1-\gamma)L/2.$$

(H.8)

Furthermore, since slip is not permitted within the bonded region, $\tau_i(-\gamma L/2) = \hat{\tau}_{ult_l}$ and $\tau_i(\gamma L/2) = \hat{\tau}_{ult_r}$ during unloading. Now if

$$\overline{\{(-L/2)\}} \doteq \frac{1}{v_f(1-D)}\left\{\frac{b+d}{b}\sigma - \frac{d}{b}\sigma_T\left(x_{t|_{x=-L/2}}\right)\right\}$$

(C.31)

and

$$\overline{\{(L/2)\}} \doteq \frac{1}{v_f(1-D)}\left\{\frac{b+d}{b}\sigma - \frac{d}{b}\sigma_T\left(x_{t|_{x=L/2}}\right)\right\}$$

(C.32)

then the fiber stress within the unit-cell is given by Eqs. (H.9) through (H.11).

$$\sigma_f(x) = \overline{\{(-L/2)\}} + \frac{2\tau_i}{r_f}(L/2 + x) + \mathcal{C}_l \quad \text{for} \quad x \in [-L/2, -\gamma L/2] \qquad (H.9)$$

$$\sigma_f(x) = \hat{c}_3 \sinh(\beta x) + \hat{c}_4 \cosh(\beta x) + \frac{\mathcal{T} \cosh\left(\lambda x_{t_{|x=x}}\right)}{\cosh\left(\lambda L_t/2\right)} + \sigma_f^o \quad \text{for} \quad x \in [-\gamma L/2, \gamma L/2]$$

$$(H.10)$$

$$\sigma_f(x) = \overline{\{(L/2)\}} + \frac{2\tau_i}{r_f}(L/2 - x) + \mathcal{C}_r \quad \text{for} \quad x \in [\gamma L/2, L/2] \qquad (H.11)$$

where

$$\mathcal{C}_l = -\hat{c}_3 \sinh\left(\beta\gamma L/2\right) + \hat{c}_4 \cosh\left(\beta\gamma L/2\right) + \frac{\mathcal{T} \cosh\left(\lambda x_{t_{|x=-\gamma L/2}}\right)}{\cosh\left(\lambda L_t/2\right)} + \sigma_f^o$$

$$- \frac{2\tau_i}{r_f}L/2(1-\gamma) - \overline{\{(-L/2)\}} \qquad (H.12)$$

$$\mathcal{C}_r = \hat{c}_3 \sinh\left(\beta\gamma L/2\right) + \hat{c}_4 \cosh\left(\beta\gamma L/2\right) + \frac{\mathcal{T} \cosh\left(\lambda x_{t_{|x=\gamma L/2}}\right)}{\cosh\left(\lambda L_t/2\right)} + \sigma_f^o$$

$$- \frac{2\tau_i}{r_f}L/2(1-\gamma) - \overline{\{(L/2)\}} \qquad (H.13)$$

$$\hat{c}_3 = \frac{\hat{\chi}_l + \hat{\chi}_r}{2\cosh\left(\beta\gamma L/2\right)} \qquad (H.14)$$

$$\hat{c}_4 = \frac{\hat{\chi}_l - \hat{\chi}_r}{2\sinh\left(\beta\gamma L/2\right)} \qquad (H.15)$$

$$\hat{\chi}_l = \frac{1}{\beta}\left\{-\frac{2\hat{\tau}_{ult_l}}{r_f} - \frac{\mathcal{T} \sinh\left(\lambda x_{t_{|x=-\gamma L/2}}\right)}{\cosh\left(\lambda L_t/2\right)}\right\} \qquad (H.16)$$

$$\hat{\chi}_r = \frac{1}{\beta}\left\{\frac{2\hat{\tau}_{ult_r}}{r_f} - \frac{\mathcal{T} \sinh\left(\lambda x_{t_{|x=\gamma L/2}}\right)}{\cosh\left(\lambda L_t/2\right)}\right\} \qquad (H.17)$$

Because the constituent stresses upon unloading are desired, Eqs. (H.9) through (H.17) are evaluated at $\sigma = \sigma_{min}$. Finally, the matrix stress within the unit-cell may be determined using Eqs. (H.9) through (H.11) and the standard equilibrium relations. The matrix stress is provided below. Note that these are the stresses which result upon unloading and where a PBR is considered.

$$\sigma_m(x) = -\left\{ \frac{v_f}{v_m} \frac{2\tau_i}{r_f} (L/2 + x) + \frac{1}{v_m(1-D)} \frac{d}{b} \left[\sigma_T \left(x_{t_{|x=x}} \right) - \sigma_T \left(x_{t_{|x=-L/2}} \right) \right] \right\}$$
$$\text{for} \quad x \in [-L/2, -\gamma L/2] \tag{H.18}$$

$$\sigma_m(x) = \frac{1}{v_m(1-D)} \left\{ \frac{b+d}{b} \sigma - \frac{d}{b} \sigma_T \left(x_{t_{|x=x}} \right) \right\} + \frac{v_f}{v_m} \left\{ C_l - \sigma_f(x) \right\} \tag{H.19}$$
$$\text{for} \quad x \in [-\gamma L/2, 0]$$

$$\sigma_m(x) = \frac{1}{v_m(1-D)} \left\{ \frac{b+d}{b} \sigma - \frac{d}{b} \sigma_T \left(x_{t_{|x=x}} \right) \right\} + \frac{v_f}{v_m} \left\{ C_r - \sigma_f(x) \right\} \tag{H.20}$$
$$\text{for} \quad x \in [0, \gamma L/2]$$

$$\sigma_m(x) = -\left\{ \frac{v_f}{v_m} \frac{2\tau_i}{r_f} (L/2 - x) + \frac{1}{v_m(1-D)} \frac{d}{b} \left[\sigma_T \left(x_{t_{|x=x}} \right) - \sigma_T \left(x_{t_{|x=L/2}} \right) \right] \right\}$$
$$\text{for} \quad x \in [\gamma L/2, L/2] \tag{H.21}$$

where $\sigma_f(x)$ is the fiber stress defined by Eq. (H.10). As observed in the unidirectional analysis, the matrix strain resulting from Eqs. (H.18) through (H.21) is in disagreement with the known magnitude for a completely debonded, fully slipped, interface after unloading. Hence, the next step in the analysis is to adjust the constituent stresses within the unit-cell to ensure that the desired matrix strain is predicted.

H.1.2 Re-Evaluating the residual strain. For a completely debonded interface, the expected matrix stress upon unloading is as shown in Eqs. (H.22) and (H.23) for the current shear-lag formulation. In addition, Eqs. (H.22) and (H.23) represent

the desired, or "correct", matrix stresses (i.e. $\gamma = 0$), and are evaluated at $\sigma = \sigma_{min}$.

$$\sigma_m(x) = -\frac{1}{v_m(1-D)}\frac{d}{b}\left\{\sigma_T\left(x_{t_{|x=x}}\right) - \sigma_T\left(x_{t_{|x=-L/2}}\right)\right\} - \frac{v_f}{v_m}\frac{2\tau_i}{r_f}\left(L/2 + x\right)$$

$$\text{for} \quad x \in [-L/2, 0]$$

(H.22)

$$\sigma_m(x) = -\frac{1}{v_m(1-D)}\frac{d}{b}\left\{\sigma_T\left(x_{t_{|x=x}}\right) - \sigma_T\left(x_{t_{|x=L/2}}\right)\right\} - \frac{v_f}{v_m}\frac{2\tau_i}{r_f}\left(L/2 - x\right)$$

(H.23)

$$\text{for} \quad x \in [0, L/2]$$

As in the previous unidirectional case, the matrix stress can be appropriately adjusted by a constant amount $\Delta\sigma_m$ so that the matrix strain is correct, i.e.

$$\Delta\sigma_m = -\frac{1}{L}\int_{-L/2}^{L/2}\left\{\sigma_{m_1}(x) - \sigma_{m_2}(x)\right\}\ dx\big|_{\sigma = \sigma_{min}}$$

(H.24)

where $\sigma_{m_1}(x)$ is the matrix stress in Eqs. (H.22) and (H.23) and $\sigma_{m_2}(x)$ is the matrix stress in Eqs. (H.18) through (H.21). The final step of the analysis is to consider the axial fiber stress as the permanently bonded region vanishes.

H.1.3 Removal of the PBR Constraint.   Given Eq. (H.24), an equivalent crack opening displacement $\delta(N)$, as discussed in appendix G, may be formulated from Eq. (H.25).

$$\delta(N) = \frac{2}{E_f}\int_0^{L/2}\sigma_f(x) - \frac{2\tau_i}{r_f}\left(L/2 - x\right)\ dx$$

(H.25)

Moreover,

$$\delta(N) = \frac{L}{E_f}\Delta\sigma(N),$$

(G.2)

$$\Delta\sigma(N) \doteq \frac{v_m}{v_f}\Delta\sigma_m.$$

(H.26)

The stress $\Delta\sigma(N)$ may finally be determined by equating Eqs. (H.25) and (G.2) and allowing $\gamma \to 0$. After much algebraic manipulation,

$$
\begin{aligned}
\Delta\sigma(N)= {} & \frac{b+d}{b}\frac{1}{v_f(1-D)}\left\{\sigma_{max}-\sigma_{min}\right\}-\left\{\sigma^o_{f_{max}}-\sigma^o_{f_{min}}\right\}-\frac{2\tau_i(N)}{r_f}L \\
& +\frac{d}{b}\frac{1}{\cosh\left(\lambda L_t/2\right)}\cdot\left\{\frac{1}{v_f(1-D)}\left[-\cosh\left(\lambda L_t/2\right)+\frac{1}{2}\cosh\left(\lambda x_{t_{|x=-\gamma L/2}}\right)\right.\right. \\
& \left.\left. +\frac{1}{2}\cosh\left(\lambda x_{t_{|x=\gamma L/2}}\right)\right]-\frac{E_f}{E_1}\cosh\left(\lambda x_{t_{|x=0}}\right)\right\}\left\{\sigma^o_{T_{max}}-\sigma^o_{T_{min}}\right\}. \qquad (5.1)
\end{aligned}
$$

The reader may verify that upon removal of the $90°$ plies, Eq. (5.1) reduces to the unidirectional case [Eq. (4.3)].

Appendix I. Closed-Form Estimates for Several Laminate Constants.

The shape of the uniaxial stress-strain response for a unidirectional ceramic-matrix laminate is a good indicator of the extent of damage within the composite microstructure, and as such, the ability to predict the stress-strain behavior numerically is important for characterizing the residual (remaining) strength and modulus of a CMC component. For the methodology formulated as part of the current doctoral research, the unidirectional stress-strain response may be determined and is dependent on the basic constituent properties, Γ_c; the frictional shear along the interface, τ_i; the operating and processing temperature differential, ΔT; the fiber volume fraction, v_f, and the extent of composite damage (L, d and D) according to Eq. (I.1).

$$\epsilon = \mathcal{F}(\Gamma_c, \ \tau_i, \ \Delta T, \ v_f, \ L, \ d, \ D) \ \sigma \qquad (I.1)$$

where $\Gamma_c = \{E_f, \ \alpha_f, G_f, \ E_m, \ \alpha_m, \ G_m\}$ and $\mathcal{F}()$ is some constitutive relation relating these various parameters, e.g. Eq. (3.6). Moreover, based upon the assumed failure criteria used in the current analysis for the different damage modes, Eq. (I.1) can be written as a function of the interface strength, τ_{ult}; the critical energies, U_{cr_m} and U_{cr_f}, and the Weibull modulus $\hat{m}$, i.e.

$$\epsilon = \mathcal{F}(\Gamma_c, \ \Delta T, \ v_f, \ \tau_i, \ \tau_{ult}, \ U_{cr_m}, \ U_{cr_f}, \ \hat{m}) \ \sigma. \qquad (I.2)$$

Clearly, the parameters τ_i, τ_{ult}, Γ_c, ΔT, and v_f are material and processing constants which can be chosen to optimize the composite's behavior for a given application. This is not as apparent with the remaining parameters U_{cr_m}, U_{cr_f}, and $\hat{m}$. However, based upon the definitions of U_{cr_m}, U_{cr_f}, and $\hat{m}$, Eq. (I.2) can be written as shown in Eq. (I.3) in which all the required parameters can be determined analytically.

$$\epsilon = \mathcal{F}(\sigma_{cr}, \ \hat{m}, \ \sigma_{ff}, \ \hat{\Gamma}_c) \ \sigma \qquad (I.3)$$

where $\hat{\Gamma}_c$ is the set of known material and processing constants: Γ_c, τ_i, τ_{ult}, ΔT, and v_f. The stress at which fiber fracture is assumed to initiate is σ_{ff}. *The purpose of this appendix is to provide closed-form estimates for these parameters based upon the known properties (e.g. $\hat{\Gamma}_c$); in turn, making the current analysis completely analytic.* Both unidirectional and cross-ply laminates are investigated. Note that the stress-strain plots presented in earlier chapters are generated using Eq. (I.3) in which σ_{cr} and $\hat{m}$ were empirically derived.

I.1   Unidirectional Laminates

For analysis purposes, it is convenient to divide the stress-strain curve of a unidirectional laminate into regions which can be characterized by dominant damage modes (e.g. matrix cracking and fiber failure). Figure I.1 represents such a procedure and is provided to help define some of the terms typically used when segmenting the stress-strain curve. Schematic drawings of laminates with corresponding degrees of damage are also illustrated in this figure. Matrix cracking, interface debonds, and fiber fractures are all shown. The high-lighted stresses in this figure are defined as follows.

$\sigma_{mc} \rightarrow$ crack initiation stress

$\sigma_{cr} \rightarrow$ critical composite stress

$\sigma_{sat} \rightarrow$ stress at which matrix cracking ceases (saturation stress)

$\sigma_{ff} \rightarrow$ stress corresponding to the initiation of fiber fracture

$\sigma_{ult} \rightarrow$ ultimate laminate stress

$\epsilon_{ult} \rightarrow$ ultimate laminate strain

Note that the stresses σ_{cr} and σ_{ff} appear explicitly in Eq. (I.3). Furthermore, since $\hat{m}$ is dependent on some of the remaining terms shown in Fig. I.1, a clear understanding of the above definitions will prove helpful in the remaining discussion.
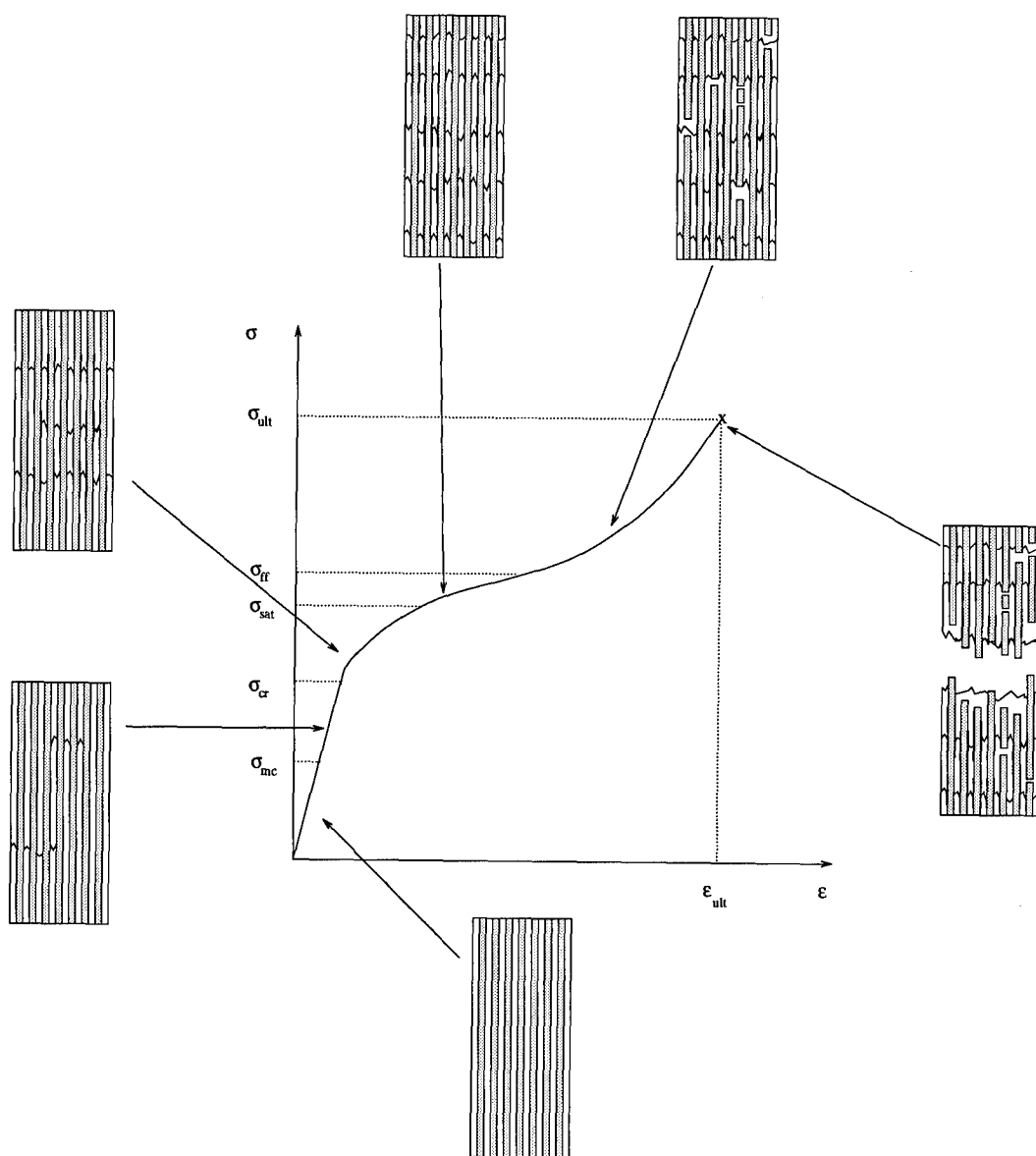
Figure I.1   Unidirectional stress-strain response and corresponding damages.

Procedures for estimating these parameters (σ_{cr}, σ_{ff}, and $\hat{m}$) are now provided. As presented in the next section, there is an abundance of formulae for estimating the critical composite stress, σ_{cr}. Unfortunately, as is often the case when multiple solutions are presented, none of the solutions represent a universal answer.

I.1.1   Critical Composite Stress.   The critical composite stress, σ_{cr}, may be estimated using either the energy balance solutions similar to ACK or the stress intensity approaches such as MCE (reference chapter two). For the energy balance solutions, the condition for matrix cracking is determined by ensuring that the formation of the matrix cracks is energetically consistent. This requires that the energies before and after crack formation satisfy Eq. (I.4)

$$\Delta U - \Delta W = g_m^c \tag{I.4}$$

where ΔU is the change in internal energy and ΔW is the work done during crack formation. The classical solution, as originally derived by ACK, is

$$\sigma_{cr} = \left\{ \frac{12\gamma_m v_f^2 \tau_i E_f E_1^2}{v_m r_f E_m^2} \right\}^{1/3} . \tag{A.21}$$

Equation (A.21) is derived in chapter two, and represents an estimate for σ_{cr} based upon a unit-cell with a fully debonded interface and no thermal stresses.

More recently, Kuo considered a similar analysis using the shear-lag model in which both residual thermal stresses and a partially bonded interface were considered [103]. The energies considered in the analysis were the fracture surface energy (U_c), the fiber/matrix debonding energy (U_{db}), the energy dissipated due to frictional interface fiber sliding (U_s), the fiber strain energy increment (ΔU_f), the decrease in matrix strain energy (ΔU_m), and the work done by external load (ΔW). For two-constituent composites which fail only after multiple fractures, the relationship

I-4

among these terms is

$$U_c + U_{db} + U_s + \Delta U_f \leq \Delta U_m + \Delta W \qquad (I.5)$$

where

$$U_c = 2\pi\gamma_m(R^2 - r_f^2) = A_m g_m^c, \qquad (I.6)$$

$$U_{bd} = 8\pi\gamma_{db}r_f d = 2\pi r_f \cdot 2d \cdot g_{db}^c, \qquad (I.7)$$

$$U_s = 4\pi r_f \tau_i \int_{L/2-d}^{L/2} [\Delta\bar{u}_f(x) - \Delta\bar{u}_m(x)] \, dx, \qquad (I.8)$$

$$\Delta U_f = \frac{\pi r_f^2}{2E_f} \int_{-L/2}^{L/2} [\sigma_f^2(x) - \sigma_m^2(x)] \, dx, \qquad (I.9)$$

$$\Delta U_m = \frac{\pi(R^2 - r_f^2)}{2E_m} \int_{-L/2}^{L/2} [\sigma_{m_o}^2 - \sigma_m^2(x)] \, dx, \qquad (I.10)$$

$$\Delta W = \frac{\pi R^2 \sigma}{E_f} \int_{-L/2}^{L/2} [\sigma_f(x) - \sigma_{f_o}] dx. \qquad (I.11)$$

Substituting these equations into Eq. (I.5), the following general relation for the critical composite stress may be found. The solution for σ_{cr} is determined by searching for the lowest stress satisfying Eq. (I.12).

$$2\gamma_m \frac{v_m}{v_f} + 4\gamma_{db}\frac{d}{r_f} + 4\frac{\tau_i}{r_f}\frac{E_1}{E_m E_f v_f}\left[\left(\sigma_{m_o} - \frac{v_f}{v_m}\frac{2}{r_f}\tau_i L\right)\frac{d}{2} + \frac{v_f}{v_m}\frac{\tau_i}{r_f}\left(\frac{1}{2}L - \frac{2}{3}d\right)d^2\right]$$

$$+\frac{1}{E_f}\left[\left(\left(\frac{v_m}{v_f}\sigma_{m_o} - \frac{2}{r_f}d\tau_i\right)\frac{2}{\beta}\tanh\left(\beta\left[L/2 - d\right]\right) - \sigma_{f_o}d\right)\sigma_{f_o}\right.$$

$$+\left(\frac{v_m}{v_f}\sigma_{m_o} - \frac{2}{r_f}d\tau_i\right)^2\left\{\frac{L/2 - d}{2\cosh^2\left(\beta[L/2 - d]\right)} + \frac{1}{2\beta}\tanh\left(\beta\left[L/2 - d\right]\right)\right\}$$

$$\left.+\frac{\sigma}{v_f}d\left(\frac{\sigma}{v_f} - \frac{2}{r_f}\tau_i d\right) + \frac{4}{3}\left(\frac{\tau_i}{r_f}\right)^2 d^3\right]$$

$$=$$

$$\frac{v_m}{v_f}\frac{1}{E_m}\left[\sigma_{m_o}^2 d + \frac{1}{\beta}\left(\frac{3}{2}\sigma_{m_o} + \frac{v_f}{v_m}\frac{\tau_i}{r_f}d\right)\left(\sigma_{m_o} - 2\frac{v_f}{v_m}\frac{\tau_i}{r_f}d\right)\right.$$

$$\left.\tanh\left(\beta\left[L/2 - d\right]\right) - \left(\sigma_{m_o} - 2\frac{v_f}{v_m}\frac{\tau_i}{r_f}d\right)^2\frac{L/2 - d}{2\cosh^2\left(\beta[L/2 - d]\right)} - \frac{4}{3}\left(\frac{v_f}{v_m}\frac{\tau_i}{r_f}\right)^2 d^3\right]$$

$$+\frac{2}{E_f v_f}\sigma\left[\left(\frac{v_m}{v_f}\sigma_{m_o}\right)d + \frac{1}{\beta}\left(\frac{v_m}{v_f}\sigma_{m_o} - \frac{2}{r_f}d\tau_i\right)\tanh\left(\beta\left[L/2 - d\right]\right) - \frac{\tau_i}{r_f}d^2\right] \quad (I.12)$$

Although the general solution of the critical stress can only be determined numerically, closed-form solutions exist for two limiting cases. The first case assumes a perfectly bonded fiber ($d = 0$) and an infinite crack spacing ($L = \infty$). The second limiting case is for a completely debonded interface ($d = L/2$). The solutions for these two cases are as shown below.

For a completely bonded interface,

$$\sigma_{cr} = \left(\frac{4}{3}\frac{\beta\gamma_m E_1 E_f v_f}{E_m}\right)^{1/2} - E_1(\alpha_1 - \alpha_m)\Delta T \quad (I.13)$$

and for a fully debonded interface

$$\sigma_{cr} = \left(\frac{12\tau_i\gamma_m E_1^2 E_f v_f^2}{r_f v_m E_m^2}\right)^{1/3} - E_1(\alpha_1 - \alpha_m)\Delta T. \quad (I.14)$$

Note that the latter is the ACK solution with an additional term accounting for the thermal stresses.

Budiansky *et al* also considered some related cases. In particular, fully bonded and partially bonded solutions were obtained for the conditions of steady-state crack growth [20]. Their solutions are shown below.

For a fully bonded interface,

$$\sigma_{cr} + \frac{E_1(\alpha_f - \alpha_m)\Delta T}{1 + \dfrac{v_m E_m}{v_f E_f}} = \mathcal{B} \left\{ \frac{6 v_f^2 E_f}{v_m^2 E_1(1 + \nu_m)} \right\}^{1/4} \sqrt{\frac{2\gamma_m}{r_f E_m}} \tag{I.15}$$

where

$$\mathcal{B} = \left\{ \frac{2 E_1 v_m^3}{-6 \ln v_f - 3 v_m(3 - v_f)} \right\}^{1/4}. \tag{I.16}$$

For a partially bonded interface,

$$\sigma_{cr} + \frac{E_1(\alpha_f - \alpha_m)\Delta T}{1 + \dfrac{v_m E_m}{v_f E_f}} = \sigma_o \sqrt{\frac{1 + 4 \dfrac{v_f}{v_m} \dfrac{d}{r_f} \dfrac{\gamma_{db}}{\gamma_m}}{\sqrt{\left\{ 1 + \dfrac{\mathcal{B}^2}{v_m} \sqrt{\dfrac{6 E_1}{E_f(1 + \nu_m)}} \right\} \dfrac{d}{r_f}}}} \tag{I.17}$$

where σ_o is the right hand side of Eq. (I.15).

Several solutions for σ_{cr} have been presented using the stress intensity approaches [127, 129, 196]. References 127 and 129 represent closed-form solutions whereas Reference 196 is a numerical approximation. For brevity, only the MCE solution is provided below.

$$\frac{\sigma_{cr}}{\sigma_m} = \frac{1}{3} \left(\frac{a}{c_m} \right)^{-1/2} + \frac{2}{3} \left(\frac{a}{c_m} \right)^{1/4} \tag{I.18}$$

where

$$c_m = \left(\frac{\pi K_1^c}{\alpha J} \right)^{2/3} \tag{I.19}$$

$$\sigma_m = \frac{3}{\sqrt{\pi}} \left(\frac{(K_1^c)^2 \alpha J^2}{\pi} \right)^{2/3} \qquad (I.20)$$

$$K_1^c = \frac{E_1}{E_m} K_m \qquad (I.21)$$

$$\alpha = \frac{8\tau_i v_f^2 E_f (1 - \nu)}{v_m E_m r_f \sqrt{\pi}} \qquad (I.22)$$

$$K_m = \sqrt{2\gamma_m E_m} \qquad (I.23)$$

$$J = 1.2 \qquad (I.24)$$

Several estimates for the critical composite stress are shown in Table I.1. In particular, estimates are shown for the original ACK solution; Kuo's solutions for a completely debonded (db) and fully bonded (bd) interface; the partially bonded (part. bd) and fully bonded solutions of BHE, and the MCE solution. The results were generated with Eqs. (A.21) through (I.18), and the material property data list in Table I.2. These data are for a SiC/CAS composite. Kuo's debonded solution [Eq. (I.14)] does the best job of matching the empirical value of 200 MPa for σ_{cr}. In general, however, the estimates grossly over predict σ_{cr}. This can, in part, be attributed to the uncertainties in several of the assumed material constants. Figure I.2 illustrates how the critical stresses varies with the constants γ_m and τ_i as predicted by Eqs. (A.21) and (I.14). The values $\gamma_m = 20$ N/m and $\tau_i = 20$ MPa correspond to the monolithic matrix surface energy and the push-out estimate, respectively and as observed previously, these seem to overestimate the laminate values.

Table I.1   Critical composite stress estimates.

ACK	Kuo (db)	Kuo (bd)	BHE (part. bd)	BHE (bd)	MCE
404.8	293.0	-111.5	1912.0	1028.0	2.1E15

I.1.2   Weibull Modulus.   As presented in appendix F, the Weibull modulus, $\hat{m}$ which governs the progression of fiber fractures, can be determined by fitting

Table I.2   Input Parameters.

E_f	210 GPa	E_m	95.5 GPa
v_f	0.38	r_f	7.5 μm
α_f	3.1E-6 /°C	α_m	4.5E-6 /°C
ΔT	-1000 °C		
τ_i	20 MPa	τ_{ult}	220 MPa
G_f	65 GPa	G_m	38 GPa
ν_f	0.2	ν_m	0.2
d	60E-6 mm	a	2 r_f
γ_m	20 N/m	γ_{db}	$\gamma_m/3$

empirical stress-strain data. However, $\hat{m}$ may also be calculated from Eq. (F.17) if the critical fraction of broken fibers, D^*; the critical fiber strain energy, U_{cr_f}, and the average fiber strain energy at laminate failure, U_f^*, are known.

$$\hat{m} = \frac{\ln\left\{\ln\left(\frac{1}{1-D^*}\right)\right\}}{\ln\left\{1 - \frac{U_{cr_f}}{U_f^*}\right\}} \qquad (F.17)$$

Based on this relation, formulae relating D^*, U_{cr_f} and U_f^* are desired. These are now investigated.

The critical fraction of broken fibers, D^*, is related to the traditional Weibull shaping parameter, m, and the composite's ultimate stress, σ_{ult} via the following two equations [14,163].

$$D^* = \frac{2}{m+2} \qquad (F.16)$$

$$\sigma_{ult} = v_f S_c \frac{m+1}{m+2} \left\{\frac{2}{m+2}\right\}^{1/(m+1)} \qquad (I.25)$$

where S_c is a characteristic fiber strength. Further, two of the three parameters σ_{ult}, m, and/or S_c are assumed to be known laminate properties and are now included in the definition of $\hat{\Gamma}_c$. The remaining terms, U_{cr_f} and U_f^*, are both based on the
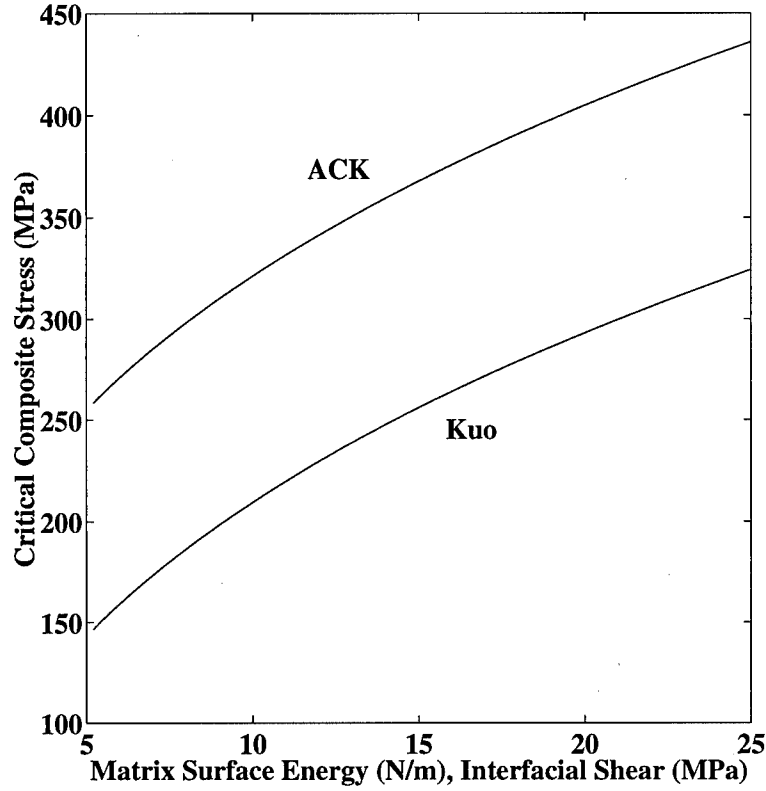
Figure I.2   Critical composites stress (σ_{cr}) as a function of the matrix surface energy (γ_m) and/or the interface shear stress (τ_i).

average fiber strain energy, which from Eq. (3.45), is defined as follows.

$$U_f = \frac{A_f}{v_f^2 r_f^2 \beta E_f} \left[(\tau_i v_f d)^2 (H + 4\beta d/3) - v_f r_f \tau_i d (2\sigma\beta d + \sigma_{m_o} v_m H + 4 v_f \sigma_{f_o} G) \right.$$

$$\left. + 2 v_f v_m r_f^2 \sigma_{f_o} \sigma_{m_o} G + \frac{1}{2}\beta(v_f r_f \sigma_{f_o})^2 (L - 2d) + \beta d (r_f \sigma)^2 \right.$$

$$\left. + 1/4(v_m r_f \sigma_{m_o})^2 H \right] \qquad (I.26)$$

where $G = \tanh\left[\beta(L/2 - d)\right]$ and

$$H = \frac{\beta(L - 2d) + \sinh[\beta(L - 2d)]}{\cosh\left[\beta(L/2 - d)\right]^2} \qquad (E.10)$$

As with the matrix strain energy, Eq. (I.26) can be expressed as the sum of the fiber strain energy for an undamaged laminate, U_{f_o}, and an additional term, $U_f(L, d)$,

I-10

which accounts for the energy transferred between the constituents because of the damage, i.e.

$$U_f = U_{f_o} + U_f(L, d). \tag{I.27}$$

In this manner, U_{cr_f} and U_f^* can be defined by the following.

$$U_{cr_f} = \left\{ U_{f_o} + U_f \left(L_{ff}, d_{ff} \right) \right\} \big|_{\sigma \, = \, \sigma_{ff}} \tag{I.28}$$

$$U_f^* = \left\{ U_{f_o} + U_f \left(L^*, d^* \right) \right\} \big|_{\sigma \, = \, \sigma_{ult}} \tag{I.29}$$

where L_{ff} and d_{ff} are the crack spacing and debond length at $\sigma = \sigma_{ff}$ and L^* and d^* are the corresponding lengths evaluated at $\sigma = \sigma_{ult}$. Based upon Eqs. (I.28) and (I.29), the estimate for $\hat{m}$ requires first calculating L_{ff}, d_{ff}, σ_{ff}, L^*, and d^*. The first three parameters can be determined from Eqs. (3.117) and (3.2.2) since under the current analysis, σ_{ff} is defined as the stress at which a maximum or saturated crack density is obtained for $D = 0$, and is therefore known directly. Furthermore, by definition, $L^* = L_{sat}$, and, as such, can be approximated by Eq. (I.30) [8, 37, 179].

$$L^* \simeq 1.337 \frac{r_f}{2\tau_i} \left\{ \frac{v_m}{v_f} \frac{E_m}{E_1} \sigma_{cr} - E_f(\alpha_1 - \alpha_f)\Delta T \right\} \tag{I.30}$$

Finally, it is reasonable to suspect that at composite failure, the interface is completely debonded and, therefore,

$$d^* = \frac{1}{2} L^*. \tag{I.31}$$

Based on Eqs. (F.17) through (I.31), the previous constitutive relation, Eq. (I.3), can be written as

$$\epsilon = \mathcal{F}(\hat{\Gamma}_c)\sigma \tag{I.32}$$

where $\hat{\Gamma}_c = \{E_f, \ E_m, \ \alpha_f, \ \alpha_m, \ G_f, \ G_m, \ \Delta T, \ v_f, \ \tau_i, \ \tau_{ult}, \ \sigma_{ult}, \ m, \ \gamma_m\}$.

Equation (I.32) is the desired solution in which the composites strain in a function solely of the applied stress and known laminate properties.

I.2 Cross-Ply Laminates

As with the unidirectional laminate, it is convenient to segment the stress-strain curve for the cross-ply laminate into regions characterized by the various modes of failure. To help define some of the relevant terms, Fig. I.3 is provided. This figure also illustrates several laminates with appropriate damages. The stresses labeled in Fig. I.3 are defined as follows:

$\sigma_{cr}^{90} \rightarrow$ critical composite stress for the 90° plies

$\sigma_{sat}^{90} \rightarrow$ saturation stress for the 90° plies

$\sigma_{mc} \rightarrow$ crack initiation in the 0° plies

$\sigma_{cr}^{0} \rightarrow$ critical composite stress for the 90° plies

$\sigma_{sat}^{0} \rightarrow$ saturation stress for the 90° plies

$\sigma_{ff} \rightarrow$ stress corresponding to the initiation of fiber fracture

$\sigma_{ult} \rightarrow$ ultimate laminate stress
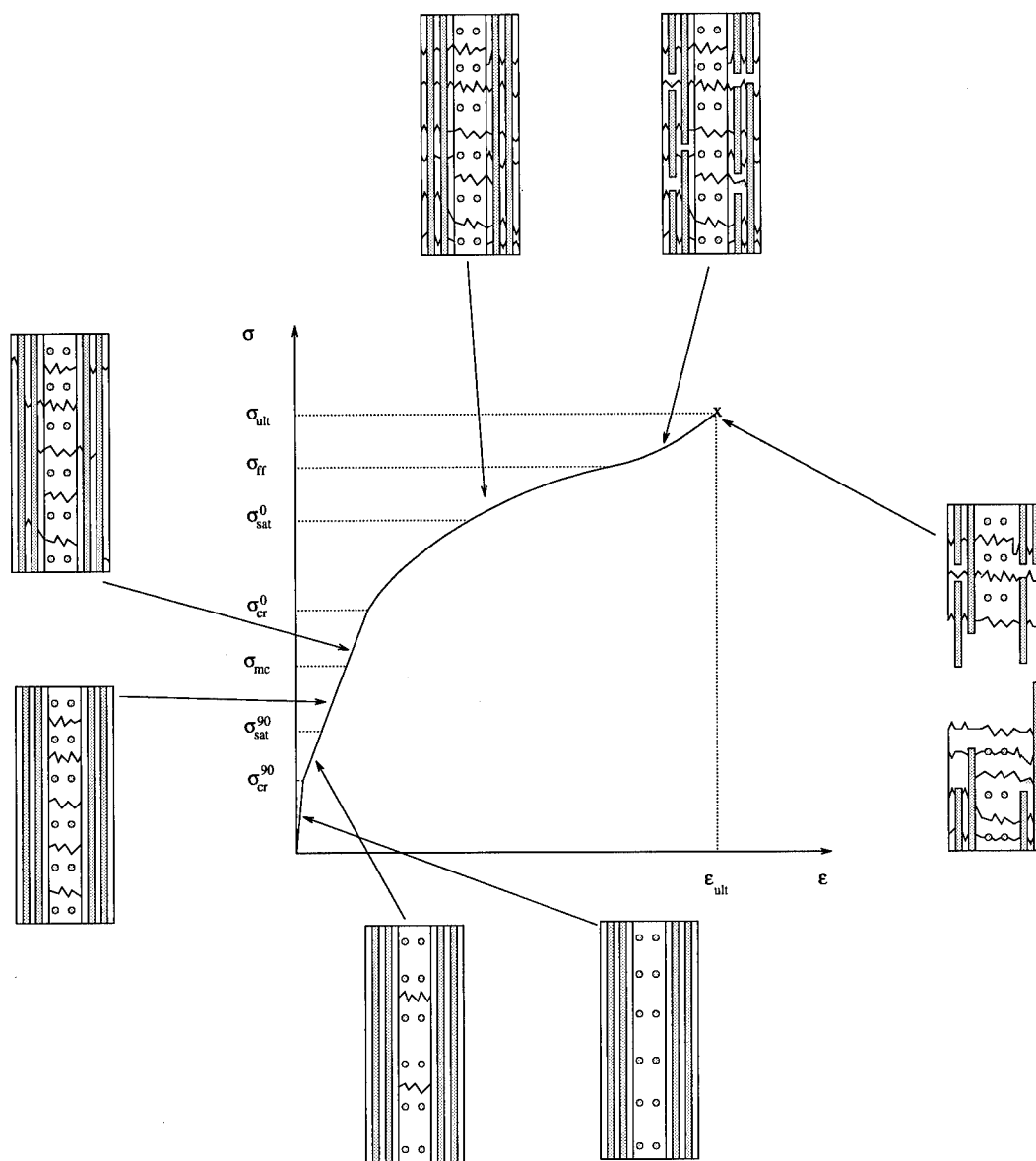
Figure I.3 Stress-strain response of a cross-ply laminate.

As with the unidirectional laminate, estimates for the critical stresses; final damage configuration, and ultimate laminate stresses are required for the complete analytical analysis. These are now investigated.

I.2.1 Critical Composite Stress. Due to their orientation, the fibers of the 90° plies do not contribute much to the strength of the laminate. As a result, the transverse plies may be modeled as a monolithic ceramic. Furthermore, it is reasonable to suspect that failure can be predicted using a maximum stress criterion. Hence, σ_{cr}^{90}, may be estimated from Eq. (I.33).

$$\sigma_{cr}^{90} = \frac{E_c}{E_2}\sigma_{m_{ult}} - E_2(\alpha_c - \alpha_2)\Delta T \tag{I.33}$$

The latter matches well with empirical data [123].

The critical stress in the 0° plies, σ_{cr}^0, may again be determined from Eq. (I.5). However, for a general damage state, the energy and work terms in this equation must be determined numerically. Kuo, however, presents the results for a few discrete cases in which the damage state within the composite is assumed symmetric and predictable [103]. For example, if at $\sigma = \sigma_{cr}$, only a single crack which extends throughout the entire *laminate* cross-section is assumed to exist then

$$\sigma_{cr}^0 = \frac{b}{b+d}\left(\frac{\beta\gamma_m E_1 E_f v_f}{E_m}\right)^{1/2} - \frac{b}{b+d}E_1(\alpha_1 - \alpha_m)\Delta T. \tag{I.34}$$

If the fiber/matrix interface is assumed to be debonded then

$$\sigma_{cr}^0 = \frac{b}{b+d}\left(\frac{12\tau_i\gamma_m E_1^2 E_f v_f^2}{E_m}\right)^{1/3} - \frac{b}{b+d}E_1(\alpha_1 - \alpha_m)\Delta T. \tag{I.35}$$

Finally, if only damage within the $0°$ ply is assumed then

$$\sigma_{cr}^0 = \left(\frac{12\tau_i\gamma_m E_c^2\left(bv_f E_f + dE_2\right)^2}{r_f v_m E_f E_m^2 b(b+d)}\right)^{1/3}\left(\frac{1+\Gamma_1+\Gamma_1\Gamma_2}{1+2\Gamma_1+2\Gamma_1\Gamma_2}\right)^{1/3}-\frac{b}{b+d}E_1(\alpha_1-\alpha_m)\Delta T$$

(I.36)

where $\Gamma_1 = (dE_2)/(bE_1)$ and $\Gamma_2 = (v_m E_m)/(v_f E_f)$.

An alternate solution is presented by Evans et al [53]. The solution, as appears in Eq. (I.37), represents a lower bound for the critical stress.

$$\sigma_{cr}^0 = \sqrt{\frac{E_c\gamma_m}{gt}} - \sigma^{th}\frac{E_L + E_T}{2E_T}$$

(I.37)

The parameters, E_L and E_T, are the ply modulus in the longitudinal and transverse directions, respectively. Further, t is the ply thickness and g is a function ranging between 1/3 and 2/3 [53].

$I.2.2$ *Weibull Modulus.* Estimation of the Weibull Modulus requires that the ultimate composite stress, σ_{ult}, and the final damage configuration, L_T, L, d, and D be known. Estimates are provided by Evans et al [53,54].

Bibliography

1. Aboudi J.A. "Closed Form Constitutive Equations for Metal-Matrix Composites," *International J. of Engineering Science*, 8:1229–1240 (1987).

2. Aboudi J.A. "Micromechanical Analysis of Composites by the Method of Cells," *Applied Mechanics Review*, *42*(7):193–221 (July 1989).

3. Agarwal B.D. and Broutman L.J. *Analysis and Performance of Fiber Composites* (Second Edition). New York: John Wiley & Sons, 1990.

4. Agins D.M. *Static Fracture Behavior of a Ceramic Matrix Composite at Elevated Temperatures*. MS thesis, AFIT/GAE/ENY/93D-1, School of Engineering, Air Force Institute of Technology (AETC), Wright-Patterson AFB, Ohio, December 1993.

5. Allen R.F. and Bowen P. "Fatigue and Fracture of a SiC/CAS Continuous Fibre Reinforced Glass Ceramic Matrix Composite at Ambient and Elevated Temperatures," *Ceramic Engineering and Science Proceedings*, *14*(7-8):265–272 (1993).

6. Allen R.F., Beevers C.J. and Bowen P. "Fracture and Fatigue of a Nicalon/CAS Continuous Fibre-Reinforced Glass-Ceramic Matrix Composite," *Composites*, *24*(2):150–156 (1993).

7. Aveston J. and Kelly A. "Theory of Multiple Fracture of Fibrous Composites," *J. Mater. Sci.*, *8*:352–362 (1973).

8. Aveston J., Cooper G.A. and Kelly A. "Single and Multiple Fracture, The Properties of Fiber Composites." *Conference Proceedings*. 15–26. National Physical Laboratory, Guildford, UK. IPC Science and Technology Press Ltd., 1971.

9. Bader M.G., Bailey J.E., Curtis P.T. and Parvizi A. "The Mechanisms of Initiation and Development of Damage in Multi-Axial Fibre-Reinforced Plastic Laminates." *Mechanical Behaviors of Materials 3*. 227–239. Proceedings of the Third International Conference held in Cambridge, England, 1979.

10. Bailey J.E., Curtis P.T. and Parvizi A. "On the Transverse Cracking and Longitudinal Splitting Behavior of Glass and Carbon Fibre Reinforced Epoxy Cross-Ply Laminates and the Effect of Poisson and Thermally Generated Strain," *Proc. R. Soc. Lond., A.*, *366*:599–623 (1979).

11. Ballarini R. and Muju S. "Stability Analysis of Bridged Cracks in Brittle Matrix Composites," *Journal of Engineering for Gas Turbines and Power*, *115*(1):127–138 (January 1993).

12. Barsoum M.W., Kangutkar P. and Wang A.S.D. "Matrix Crack Initiation in Ceramic Matrix Composites Part I: Experiments and Test Results," *Composites Science and Technology*, *44*:257–269 (1992).

13. Baste S. "Fatigue Damage Evaluation in Ceramic Matrix Composites," *Review of Progress in Quantitative Nondestructive Evaluation*, *14B*:2027 (1995).

14. Beyerle D.S., Spearing S.M. and Evans A.G. "Damage Mechanisms and the Mechanical Properties of a Laminated 0/90 Ceramic/Matrix Composite," *J. Amer. Cer. Soc.*, *75*(12):3321–3330 (1992).

15. Bleay S.M., Scott V.D. and Harris B. "Wear Studies of Fibre-Reinforced Ceramic Matrix Composites," *J. Matr. Sci. Letters*, *13*:663–667 (1994).

16. Bobit J.-L. and Lamon J. "Thermal Residual Stresses in Ceramic Matrix Composite - I. Axisymmetrical Model and Finite Element Analysis," *Acta Metall. Mater.*, *43*(6):2241–2253 (1995).

17. Botsis J. and Beldica C. "Strength Characteristics and Fatigue Crack Growth in a Composite with Long Aligned Fibers," *International Journal of Fracture*, *69*:27–50 (1994/1995).

18. Bowen H.K. "Advanced Ceramics," *J. Amer. Cer. Soc.*, *73*(2):169–176 (1990).

19. Brondsted P., Heredia F.E. and Evans A.G. "In-Plane Shear Properties of 2-D Ceramic Matrix Composites," *J. Amer. Cer. Soc.*, *77*(10):2569–2574 (1994).

20. Budiansky B., Hutchinson J.W. and Evans A.G. "Matrix Fracture in Fiber-Reinforced Ceramics," *J. Mech. Phys. Solids*, *34*:167–189 (1986).

21. Butkus L.W. and Holmes J.W. "Thermomechanical Fatigue of Nicalon-Reinforced Calcium Aluminosilicate Glass-Ceramic," *Ceramic Engineering and Science Proceedings*, *11*(9-10):442–448 (1992).

22. Cao H. and Thouless M. "Tensile Tests of Ceramic-Matrix Composites: Theory and Experiment," *J. Amer. Cer. Soc.*, *73*:2091–2094 (1990).

23. Cawley J D., Eckel A.J. and Glime W.H. "Interphase Carbon Films in Ceramic Matrix Composites: Oxidation Behaviour," *British Ceramic Proceedings, Number 54*:15 (1995).

24. Charalambides P.G. "Fiber Debonding in Residually Stressed Brittle Matrix Composites," *Journal of the American Ceramic Society*, *73*(6):1674–1680 (June 1990).

25. Chawla K.K. *Composite Materials: Science and Engineering*. New York: Springer-Verlag, 1987.

26. Chiang Y.C., Wang A.S.D. and Chou T.W. "On Matrix Cracking in Fiber Reinforced Ceramics," *J. Mech. Phys. Solids*, *41*(7):1137–1154 (1993).

27. Cho C., Holmes J.W. and Barber J.R. "Estimation of Interfacial Shear in Ceramic Composites from Frictional Heating Measurements," *J. Amer. Cer. Soc.*, *74*(11):2802–2808 (1991).

28. Cho C., Holmes J.W. and Barber J.R. "Distribution of Matrix Cracks in a Uniaxial Ceramic Composite," *J. Amer. Cer. Soc.*, *75*(2):316–324 (1992).

29. Choi S.R., Salem J.A. and Palko J.L. "Comparison of Tension and Flexure to Determine Fatigue Life Prediction Parameters at Elevated Temperatures," *Ceramic Engineering and Science Proceedings*, *14*(7-8):308 (1993).

30. Choi S.R., Salem J.A. and Palko J.L. "Oxidation of Carbon in Fiber-Reinforced Ceramic Matrix Composites," *Ceramic Engineering and Science Proceedings*, *15*(5):967–976 (1994).

31. Copper R.F. and Chyung K. "Structure and Chemistry of Fiber-Matrix Interfaces in Silicon Carbide-Fiber-Reinforced Glass-Ceramic Composites: An Electron Microscopy Study," *J. Mater. Sci.*, *22*:3148–3160 (1983).

32. Cox H.L. "The Elasticity and Strength of Paper and Other Fibrous Materials," *British J. Appl. Phys.*, *3*:72–79 (1952).

33. Coyle T.W., Fuller E.R. and Swanson P. "Fracture Mechanics Characterization of Crack/Fiber Interactions in Ceramic Matrix Composites," *Ceramic Engineering and Science Proceedings*, *8*(7-8):630–635 (1987).

34. Coyle T.W., Palamides T.R., Freiman S.W., Fuller E.R. and Deshmukh U.V. "Crack-Fiber Interactions in Ceramic Matrix Composites." *High Temperature Structural Composites: Synthesis, Characterization, and Properties.* Proceeding of the 1987 Northeast Regional Meeting of TMS, May 1987.

35. Curtin W.A. "Exact Theory of Fibre Fragmentation in a Single-Filament Composite," *J. Mater. Sci.*, *26*:5239–5253 (1991).

36. Curtin W.A. "Theory of Mechanical Properties of Ceramic-Matrix Composites," *J. Amer. Cer. Soc.*, *74*(11):2837–2845 (1991).

37. Curtin W.A. "Multiple Matrix Cracking in Brittle Matrix Composites," *Acta Metall. Mater.*, *41*(5):1369–1377 (1993).

38. Curtin W.A. "*In Situ* Fiber Strengths in Ceramic-Matrix Composites from Fracture Mirrors," *J. Amer. Cer. Soc.*, *77*(4):1075–1078 (1994).

39. Daniel I. M. and Anastassopoulos G. "Failure Mechanisms and Damage Evolution in Crossply Ceramic- Matrix Composites," *International Journal of Solids and Structures*, *32*(3/4):341–355 (1995).

40. Daniel I.M., Anastassopoulos G. and Lee J.W. "Failure Mechanisms and Interfacial Shear Strength in Brittle-Matrix Composites." *Advances in Experimental Mechanics and Biomimetics 29*, edited by W.F. Jones. 57–69. New York, NY: American Society of Mechanical Engineers, 1992.

41. Dannemann K.A. and Mandell J.F. "Tensile Damage Development in Fiber-Reinforced Ceramic Matrix Composites," *Materials Science and Engineering*, *A177*(1-2):95–114 (1994).

42. Dauskardt R.H. "Cyclic Fatigue-Crack Growth in Grain Bridging Ceramics," *J. Engr. Mater. and Tech.*, *115*(3):244–250 (1993).

43. David B. *Elementary Engineering Fracture Mechanics*. Dordrecht: Kluwer Academic Publishers, 1986.

44. Delale F., Zhang H.Q., Liaw B.M. and Zhang S.J. "Tensile Damage Behavior of Ceramic Matrix Composites Under High Temperature," *Fracture and Damage*, *27*:103–108 (1992).

45. Dharani L.R. and Fangsheng, Ji. "3-D Shear Lag Model for the Analysis of Interface Damage in Ceramic Matrix Composites." *Recent Advances in Composite Materials 56*, edited by White S.R., Hahn H.T. and Jones W.F. 47–56. Joint Applied Mechanics and Materials Summer Conference, Los Angeles, California, 1995.

46. Dharani L.R., Chai L. and Pagano N.J. "Steady-State Cracking in Ceramic Matrix Composites," *Composites Science and Technology*, *39*:29–43 (1990).

47. Domergue J.-M., Vagaggini E. and Evans A.G. "Relationships Between Hysteresis Measurements and The Constituent Propertie of Ceramic Matrix Composites: II, Experimental Studies On Unidirectional," *Journal of the American Ceramic Society*, *78*(10):2721 (1995).

48. Dusza J. "Fracture Characterization of Ceramic Matrix Composites: A Fractographic Approach," *Key Engineering Materials*, *108-110*:323 (1995).

49. Dvorak G.J. and Laws N. "Analysis of Progressive Matrix Cracking in Composite Laminates II. First Ply Failure," *J. of Comp. Maters.*, *21*:309–329 (April 1987).

50. El Mahi A., Berthelot J.-M. and Brillaud J. "Stiffness Reduction and Energy Release Rate of Cross-Ply Laminates During Fatigue Tests," *Composite Structures*, *30*:123–130 (1995).

51. Elahi M., Liao K., Lesko J., Reifsnider K. and Stinchcomb W. "Elevated Temperature Cycle Fatigue of Silicon Carbide Fiber Reinforced Silicon Carbide Matrix Composites," *Ceramic Engineering and Science Proceedings*, *15*(4):3–12 (1994).

52. Evans A.G. "Perspective on the Development of High-Toughness Ceramics," *J. Amer. Cer. Soc.*, *75*(2):187–206 (1990).

53. Evans A.G., Domerque J.-M. and Vagaggini E. "Methodology for Relating the Tensile Constitutive Behavior of Ceramic-Matrix Composites to Constituent Properties," *J. Amer. Cer. Soc.*, *77*(6):1425–1435 (1994).

54. Evans A.G., Zok F.W. and McMeeking R.M. "Fatigue of Ceramic Matrix Composites," *Acta Metall. Mater.*, *43*(3):859–875 (1995).

55. Fang N.J. and Chou T.W. "Characterization of Interlaminar Shear Strength of Ceramic Matrix Composites," *J. Amer. Cer. Soc.*, *76*(10):2539–2548 (1993).

56. Flaggs D.L. "Prediction of Tensile Matrix Failure in Composite Laminates," *J. of Comp. Matr.*, *19*:29–50 (January 1985).

57. Fukunaga H., Chou T.W., Peters P.W.M. and Schulte K. "Probabilistic Failure Strength Analyses of Graphite/Epoxy Cross-Ply Laminates," *J. of Comp. Matr.*, *18*:339–356 (July 1984).

58. Garrett K.W. and Bailey J.E. "Multiple Transverse Fracture in 90° Cross-Ply Laminates of a Glass Fibre-Reinforced Polyester," *J. Mater. Sci.*, *12*:157–168 (1977).

59. Glime W.H. and Cawley J.D. "Oxidation of Carbon Fibers and Films in Ceramic Matrix Composites: A Weak Link Process," *Carbon*, *33*(8):1053–1060 (1995).

60. Goodman L.E. and Klumpp J.H. "Analysis of Slip Damping with Reference to Turbine-Blade Vibration," *J. of Applied Mechanics*, *23*:421–429 (1956).

61. Griffith A.A. "The Phenomena of Rupture and Flow in Solids," *Philosophical Transactions*, *221*:163–198 (1920).

62. Gudaitis J.J. *Fatigue Behavior of a Cross-Ply Ceramic Matrix Composite Under Strain Controlled Tension-Tension and Tension-Compression Loading.* MS thesis, AFIT/GAE/ENY/93D-17, School of Engineering, Air Force Institute of Technology (AETC), Wright-Patterson AFB, Ohio, December 1993.

63. Guild F.J., Ogin S.L. and Smith P.A. "Modelling of 90° Ply Cracking in Crossply Laminates, Including Three-Dimensional Effects," *J. Comp. Mat.*, *27*(7):646–667 (1993).

64. Gulino R. and Phoenix S.L. "Weibull Strength Statistics for Graphite Fibres Measured from the Break Progression in a Model Graphite/Glass/Epoxy Microcomposite," *J. Mater. Sci.*, *26*:3107–3118 (1991).

65. Habib F.A., Cooke R.G. and Harris B. "Cracking in Brittle Matrix Composites," *British Ceramic, Transactions and Journal*, *89*(4):115 (July 1990).

66. Han Y.M. and Hahn H.T. "Ply Cracking and Property Degradations of Symmetric Balanced Laminates Under General In-Plane Loading," *Composites Science and Technology*, *35*:377–397 (1989).

67. Han Y.M., Hahn, H.T. and Croman R.B. "A Simplified Analysis of Transverse Ply Cracking in Cross-Ply Laminates," *Composites Science and Technology*, *31*(3):165–177 (1988).

68. Harris B., Habib F.A. and Cooke R.G. "Matrix Cracking and the Mechanical Behavior of SiC-CAS Composites," *Proc. R. Soc. Lond.*, *437*:109–131 (1992).

69. Hashin Z. "Analysis of Stiffness Reduction of Cracked Cross-Ply Laminates," *Engineering Fracture Mechanics*, *25*(5/6):771–778 (1986).

70. He M.Y. and Hutchinson J.W. "Crack Deflection at an Interface Between Dissimilar Elastic Materials," *Int. J. Solids Structures*, *25*(9):1053–1067 (1989).

71. Hedgepeth J.M., "Stress Concentration in Filamentary Structures." NASA TN D-882, May 1961.

72. Highsmith A.L. and Reifsnider K.L. "Stiffness-Reduction Mechanisms in Composite Laminates," *ASTM STP 775*, 103 (1982).

73. Ho C.Y. and El-Rahaiby S.K. "Assessment of the Status of Ceramic Matrix Composites Technology in the United States and Abroad," *Ceramic Engineering and Science Proceedings*, *13*(7-8):3–20 (1992).

74. Holmes J.W. "Influence of Stress Ratio On the Elevated-Temperature Fatigue of a Silicon Carbide Fiber-Reinforced Silicon Nitride Composite," *J. Amer. Cer. Soc.*, *74*(7):1639–1645 (July 1991).

75. Holmes J.W. and Cho C. "Frictional Heating in a Unidirectional Fibre-Reinforced Ceramic Composite," *J. Matr. Sci. Lett.*, *11*:41–44 (1991).

76. Holmes J.W. and Cho C. "Experimental Observations of Frictional Heating in Fiber-Reinforced Ceramics," *J. Amer. Cer. Soc.*, *75*(4):929–938 (1992).

77. Hsueh C.-H. "Matrix Cracking Stresses of Unidirectional Ceramic Matrix Composites," *Key Engineering Materials*, *108-110*:457 (1995).

78. Hsueh C.H. "Analytical Evaluation of Interfacial Shear Strength for Fiber-Reinforced Ceramic Composites," *J. Amer. Cer. Soc.*, *71*:490–493 (1988).

79. Hsueh C.H. "Matrix Cracking with Frictional Bridging Fibres in Continuous Fibre Ceramic Composites," *J. Mater. Sci.*, *30*(7):1781–1789 (1995).

80. Huang C.M., Xu Y., Xiong F. and Zangvil A. "Laser Ablated Coatings On Ceramic Fibers for Ceramic Matrix Composites," *Materials Science & Engineering. A. Structural Materials : Properties, Microstructure and Processing*, *191*(1/2):249 (1995).

81. Hutchison J.W. and Jensen H.M. "Models of Fiber Debonding and Pullout in Brittle Composites with Friction," *Mech. Mater.*, *9*:139–163 (1990).

82. Jayaraman K., Reifsnider K.L. and Swain R.E. "Elastic and Thermal Effects in the Interphase: Part I. Comments on Characterization Methods.," *J. Comp. Tech. and Research*, *15*(1):3–13 (1993).

83. Jayaraman K., Reifsnider K.L. and Swain R.E. "Elastic and Thermal Effects in the Interphase: Part II. Comments on Modeling Studies.," *J. Comp. Tech. and Research*, *15*(1):14–22 (1993).

84. Ji F.S., Dharani L.R. and Mall S. "Fracture Analysis of Transverse Cracking in 90° Plies of Cross-Ply Composite Laminates," *In press* (1995).

85. Karandikar P. and Chou T.W. "Characterization and Modeling of Microcracking and Elastic Moduli Changes in Nicalon/CAS Composites," *Composites Science and Technology*, *46*:1–11 (1993).

86. Karandikar P.G. *Evolution of Damage and Mechanical Response in Ceramic Matrix Composites under Monotonic and Fatigue Loadings: Experimental Characterization and Modeling*. PhD dissertation, Department of Mechanical Engineering, University of Delaware, 1992.

87. Karandikar P.G., Chou T.W. and Parvizi-Majidi A. "Effect of Interface Design on the Mechanical Behavior of a Nicalon-Glass Composite," *Ceramic Engineering and Science Proceedings*, *14*(7-8):880–889 (1993).

88. Karpur P., Matikas T.E. and Krishnamurthy S. "Ultrasonic Characterization of the Fiber-matrix Interphase/interface for Mechanics of Continuous Fiber Reinforced Metal Matrix and Ceramic Matrix Composites," *Composites Engineering*, *5*(6):697 (1995).

89. Kaw A.K. and Besterfield G.H. "Mechanics of Multiple Periodic Brittle Matrix Cracks In Unidirectional Fiber-reinforced Composites," *International Journal of Solids and Structures*, *29*(10):1193–1208 (1992).

90. Keat W.D., Larson M.C. and Cleary M.P. "Computational and Experimental Simulation of 3-D Fracture in Ceramic Fiber-Ceramic Matrix Composites," *Ceramic Engineering and Science Proceedings*, *12*(7-8):1389–1407 (1991).

91. Kent R.M. and Hecht N.L. "Analysis of Local In Situ Strain in Ceramics and Ceramic Matrix Composites," *Ceramic Engineering and Science Proceedings*, *14*(7-8):492–499 (1993).

92. Kerans R.J. "The Role of Coating Compliance and Fiber/Matrix Interfacial," *Scripta metallurgica et materialia*, *32*(4):505–509 (1995).

93. Kerans R.J. and Parthasarathy T.A. "Theoretical Analysis of the Fiber Pullout and Pushout Tests," *J. Amer. Cer. Soc.*, *74*(7):1585–1596 (1991).

94. Kerans R.J., Hay R.S., Pagano N.J. and Parthasarathy T.A. "The Role of the Fiber-Matrix Interface in Ceramic Composites," *Ceramic Bulletin*, *68*(2):429–442 (1989).

95. Khobaib M. and Zawada L. "Tensile and Creep Behavior of a Silicon Carbide Fiber-Reinforced Aluminosilicate Composite," *Ceramic Engineering and Science Proceedings*, *12*(7-8):1537–1555 (1991).

96. Kim R.Y. "Experimental Observation of Progressive Damage in SiC/Glass-Ceramic Composites," *Ceramic Engineering and Science Proceedings*, *13*(7-8):281–289 (1992).

97. Kim Y.W. and Hong C.S. "Progressive Failure Model for the Analysis of Laminated Composites Based on Finite Element Approach," *J. of Reinforced Plastics and Composites*, *II*:1078–1090 (October 1992).

98. Kobayashi T., Shockey D.A. and Johnson S.M. "A Detailed Look At Microfailure Processes in a Brittle Matrix Fiber Composite," *Ceramic Engineering and Science Proceedings*, *12*(7-8):1408–1417 (July 1991).

99. Kooner S., Lawrence C.W. and Derby B. "High Temperature Interfacial Shear Strength Testing of Ceramic Matrix Composites," *Ceramic Engineering and Science Proceedings*, *14*(7-8):229–236 (1993).

100. Kotil T., Holmes J.W. and Comninou M. "Origin of Hysteresis Observed During Fatigue of Ceramic-Matrix Composites," *J. Amer. Cer. Soc.*, *73*:1879–1883 (1990).

101. Kumaria S. and Singh R.N. "Influence of Residual Stresses and Interfacial Shear Strength On Matrix Properties in Fibre-reinforced Ceramic Matrix Composites," *Journal of Materials Science*, *30*(22):5716 (1995).

102. Kumaria S., Singh R.N. and Bhatt R.T. "Effect of Flaw Size On First Matrix Cracking Stress in Fiber- Reinforced Ceramic Composites," *Ceramic Transactions*, *46*:731 (1995).

103. Kuo W.S. *Damage of Multi-Directionally Reinforced Ceramic Matrix Composites*. PhD dissertation, Department of Mechanical Engineering, University of Delaware, August 1992.

104. Kuo W.S. and Chou T.W. "Nonlinear and Damage Behavior of Ceramic-Matrix Cross-Ply Composites." *Winter Annual Meeting of the American Society of Mechanical Engineering*. 97–107. Damage Mechanics and Localization, American Society of Mechanical Engineers, Applied Mechanics Division, AMD v 142. Publ. by ASME, New York, NY., 1992.

105. Kuo W.S. and Chou T.W. "Elastic Response and Effect of Transverse Cracking in Woven Fabric Brittle Matrix Composites," *J. Amer. Cer. Soc.*, *78*(3):783–792 (1995).

106. Kuo W.S. and Chou T.W. "Multiple Cracking of Unidirectional and Cross-Ply Ceramic Matrix Composites," *J. Amer. Cer. Soc.*, *78*(3):745–755 (1995).

107. Lamon J., Rebillat F. and Evans A.G. "Microcomposite Test Procedure for Evaluating the Interface Properties of Ceramic Matrix Composites," *Journal of the American Ceramic Society*, *78*(2):401 (1995).

108. Lamouroux F., Valles J.L. and Steen M. "Influence of Damage On the Creep Behaviour of Ceramic Matrix Composites," *Composites Engineering*, *5*(10/11):1379 (1995).

109. Larson M.C. *Theoretical and Experimental Analysis of Toughening in Brittle Matrix - Brittle Fiber Ceramic Composites with Frictional Interfaces.* PhD dissertation, Department of Mechanical Engineering, Massachusetts Institute of Technology, June 1992.

110. Larson M.C. "Fracture Propagation Near a Frictionally-Constrained Fiber Interface," *Composites Engineering*, 5(1):25 (1995).

111. Laws N. and Dvorak G.J. "Progressive Transverse Cracking in Composite Laminates," *J. of Comp. Matr.*, 22:900–916 (1988).

112. Lee J.W. and Daniel I.M. "Progressive Transverse Cracking of Crossply Composite Laminates," *J. of Comp. Matr.*, 24:1225–1243 (1990).

113. Lee J.W. and Daniel I.M. "Deformation and Failure of Longitudinally Loaded Brittle-Matrix Composites." *Proceedings of the Tenth Symposium on Composite Materials: Testing and Design*, edited by G.C. Grimes. 204–221. ASTM, 1992.

114. Lee K.N. and Jacobson N.S. "Chemical Stability of the Fiber Coating/Matrix Interface In Silicon-Based Ceramic Matrix Composites," *Journal of the American Ceramic Society*, 78(3):711 (1995).

115. Lee S.S. and Stinchcomb W.W. "Damage Mechanisms of Cross-Ply Nicalon/CAS-II Laminates Under Cyclic Tension," *Ceramic Engineering and Science Proceedings*, 15(4):40–48 (1994).

116. Li M. and Guiu F. "High Temperature Stability of the Matrix-Fibre Interface in a SiC/SiC Composite," *Scripta Metallurgica* et *Materialia*, 31(8):1067–1072 (1994).

117. Liangbo D. and Fuqun F. "Statistical Analysis of Failure of Unidirectionally Fibre-Reinforced Composites with Local Load-Sharing," *International Journal of Fracture*, 59:69–81 (1993).

118. Lim S.G. and Hong C.S. "Prediction of Transverse Cracking and Stiffness Reduction in Cross-Ply Laminated Composites," *J. of Comp. Matr.*, 23:695–713 (1989).

119. Liu S. and Nairn J.A. "The Formation and Propagation of Matrix Microcracks in Cross-Ply Laminates During Static Loading," *J. Reinf. Plast. Comp.*, 11(2):158–178 (1992).

120. LLorca J. and Singh R.N. "Influence of Fiber and Interfacial Properties on Fracture Behavior of Fiber-Reinforced Ceramic Composites," *J. Amer. Cer. Soc.*, 74(11):2882–2890 (1991).

121. Lu M.C. "Evaluation of Interfacial Properties in Ceramic Coating/Fiber Composites," *Ceramic Engineering and Science Proceedings*, 11(9-10):1761–1777 (1990).

122. Lu M.C. and Hsueh C.H. "Effects of Friction in Ceramic Coating/Fiber Composites," *J. Comp. Matr.*, *24*(6):572–593 (1990).

123. Mall S. and Bachmann S.E. "Transverse Cracking in a Fiber Reinforced Ceramic Matrix Composite." *Proc. of the 6th Japan-U.S. Conference on Composites*. 262–270. 1993.

124. Mall S. and Kim R.Y. "Failure Mechanisms in Laminates of Silicon Carbide/Calcium-Aluminosilicate Ceramic Composite," *Composite*, *23*(4):215–222 (July 1992).

125. Mall S., Fink W.E. and Kim R.Y. "Mechanical Behavior of a Fiber Reinforced Ceramic Composite under Off-Axis Loading," *Advanced Composite Materials*, *2*(1):69–83 (1992).

126. Marshall D.B. and Evans A.G. "Failure Mechanisms in Ceramic-Fiber/Ceramic-Matrix Composites," *J. Amer. Cer. Soc.*, *68*(5):225–231 (1985).

127. Marshall D.B., Cox B.N. and Evans A.G. "The Mechanics of Matrix Cracking in Brittle-Matrix Fiber Composites," *Acta Metall. Mater.*, *33*:2013–2021 (1985).

128. Maxwell P.C. "Congressional Perspective on Advanced Ceramics," *Ceramic Bulletin*, *67*(8):1357–1359 (1988).

129. McCartney L.N. "Mechanics of Matrix Cracking in Brittle-Matrix Fiber-Reinforced Composites," *Proc. Roy. Soc. London*, *A-409*:329–350 (1987).

130. McCartney L.N. "The prediction of cracking in biaxially loaded cross-ply laminates having brittle matrices," *Composites*, *24*(2):84–92 (1993).

131. McCullum D.E., Hecht N.L., Chuck L. and Goodrich S.M. "Summary of Results of the Effects of Environment on Mechanical Behavior of High-Performance Ceramics," *Ceramic Engineering and Science Proceedings*, *12*:1886–1913 (1991).

132. Metherell A.F. and Diller S.V. "Instantaneous Energy Dissipation Rate in a Lap Joint - Uniform Clamping Pressure," *J. of Applied Mechanics*, *35*(1):123–128 (1968).

133. Mukunda V.G. and Dharani L.R. "A Comparison of Classical and Consistent Shear Lag Models For Failure Analysis of Unidirectional Composites," *Engineering Fracture Mechanics*, *45*(6):865–874 (August 1993).

134. Mumm D.R. and Faber K.T. "Fiber Debonding and Pullout Processes in Ceramic Composites," *Ceramic Engineering and Science Proceedings*, *13*(7-8):70–75 (1992).

135. Mumm D.R. and Faber K.T. "Interfacial Debonding and Sliding in Brittle-matrix Composites Measured Using An Improved Fiber Pullout Technique," *Acta Metallurgica Et Materialia*, *43*(3):1259–1270 (1995).

136. Murthy P.L.N. and Chamis C.C. "Towards the Development of Micromechanics Equations for Ceramic Matrix Composites via Fiber Substructuring." *36th International SAMPE Symposium and Exhibition*. 2249–2263. How Concept Becomes Reality, International SAMPE Symposium and Exhibition, v 36 pt. 2., Publ. by SAMPE, Covina, CA., 1991.

137. Nairn J.A. "Fracture Mechanics of Unidirectional Composites," *J. Reinforced Plastics and Composites*, *9*:91–101 (January 1990).

138. Nairn J.A. and Hu S. "The Formation and Effect of Outer-Ply Microcracks in Cross-Ply Laminates: A Variational Approach," *Engineering Fracture Mechanics*, *41*(2):203–221 (1992).

139. Nairn J.A., Hu S. and Bark J.S. "A Critical Evaluation of Theories for Predicting Microcracking in Composite Laminates," *J. Mater. Sci.*, *28*:5099–5111 (1993).

140. Naslain R.R. "Ceramic Matrix Composites," *Philosophical Transactions of the Royal Society of London Series A, Physical Sciences and Engineering*, *1697*:485 (1995).

141. Neumeister J.M. "A Constitutive Law for Continuous Fiber Reinforced Brittle Matrix Composites with Fiber Fragmentation and Stress Recovery," *Journal of the Mechanics and Physics of Solids*, *41*(8):1383–1404 (August 1993).

142. Ogin S.L., Smith P.A. and Beaumont P.W.R. "Matrix Cracking and Stiffness Reduction during the Fatigue of a (0/90)$_s$ GFRP Laminate," *Composites Science and Technology*, *22*:23–31 (1985).

143. Opalski F.A. *Fatigue Behavior of a Cross-Ply Ceramic Matrix Composite Under Tension-Tension and Tension-Compression Loading*. MS thesis, AFIT/GAE/ENY/92D-02, School of Engineering, Air Force Institute of Technology (AETC), Wright-Patterson AFB, Ohio, December 1992.

144. Opalski F.A. and Mall S. "Tension-Compression Fatigue Behavior of a Silicon Carbide Calcium-Aluminosilicate Ceramic Matrix Composite," *J. of Reinforced Plastics and Composites*, *13*:420–438 (1994).

145. Pagano N.J. and Brown H.W. "The Full-Cell Cracking Mode in Unidirectional Brittle-Matrix Composites," *Composites*, *24*(2):69–83 (1993).

146. Parthasarathy T.A., Marshall D.B. and Kerans R.J. "Analysis of the Effect of Interfacial Roughness On Fiber Debonding and Sliding in Brittle Matrix Composites," *Acta Metallurgica Et Materialia*, *42*(11):3773–3784 (1994).

147. Parvizi A., Garrett K.W. and Bailey J.E. "Constrained Cracking in Glass Fibre-Reinforced Epoxy Cross-Ply Laminates," *J. Mater. Sci.*, *13*(1):195–201 (1978).

148. Persh J. "Department of Defense Directions for Engineering Ceramics," *Ceramic Bulletin*, *68*(6):1174–1176 (1989).

149. Peters P.W.M., Martin E. and Quenisset J.M. "Slip and Frictional Shear Stresses in Ceramic Matrix Composites," *Journal of Composite Materials*, *29*(5):550 (1995).

150. Prewo K.M. "Tension and Flexural Strength of Silicon Carbide Fibre-reinforced Glass Ceramics," *J. Mater. Sci.*, *21*:3590–3600 (1986).

151. Prewo K.M. "Fatigue and Stress Rupture of Silicon Carbide Fibre-Reinforced Glass-Ceramics," *J. Mater. Sci.*, *22*:2695–2701 (1987).

152. Pryce A.W. and Smith P.A. "Behavior of Unidirectional and Crossply Ceramic Matrix Composites Under Quasi-Static Tensile Loading," *J. Mater. Sci.*, *27*:2695–2704 (1992).

153. Pryce A.W. and Smith P.A. "Matrix Cracking in Unidirectional Ceramic Matrix Composites Under Quasi-Static and Cyclic Loading," *Acta Metall. Mater.*, *41*(4):1269–1281 (1993).

154. Pryce A.W. and Smith P.A. "Matrix Cracking in Crossply Ceramic Matrix Composites Under Quasi-Static and Cyclic Loading," *Acta Metall. Mater.*, *42*(3):861–870 (1994).

155. Raghuraman S. and Stubbins J.F. "Fatigue Crack Growth in Advanced Ceramic Materials," *Ceramic Engineering and Science Proceedings*, *14*(7-8):237–248 (1993).

156. Ramakrishnan V. and Jayaraman N. "Mechanistically Based Fatigue-damage Evolution Model For Brittle Matrix Fibre-reinforced Composites," *Journal of Materials Science*, *28*(20):5592 (October 1993).

157. Reifsnider K.L. "Some Fundamental Aspects of Fatigue and Fracture Response of Composite Materials." *14th Annual Meeting of Society of Engineering Science.* Lehigh University, Bethleham PA, November 1977.

158. Reifsnider K.L., Henneke E.G. and Stichcomb W.W. "Defect-Property Relationships in Composite Materials," AFML-TR-76-81, Part IV. Air Force Materials Laboratory (June 1979).

159. Robertson D.D. and Mall S. "Micromechanical Relations for Fiber-Reinforced Composites Using Free Transverse Shear Approach," *ASTM Journal of Composites Technology and Research*, 181–192 (Fall 1993).

160. Robertson D.D. and Mall S. "Micromechanical Analysis for Thermoviscoplastic Behavior of Unidirectional Fibrous Composites," *Composites Science and Technology*, *50*:483–496 (1994).

161. Rosen B.W. "Tensile Failure of Fibrous Composites," *AIAA Journal*, *2*(11):1985–1991 (1964).

162. Rosen B.W. "Thermomechanical Properties of Fibrous Composites," *Proc. Roy. Soc. Lond.*, *319*:79–94 (1970).

163. Rouby D. and Reynaud P. "Fatigue Behavior Related to Interface Modification During Load Cycling in Ceramic-Matrix Fibre Composites," *Composites Science and Technology*, *48*:109–118 (1993).

164. Saada A.S. *Elasticity: Theory and Applications* (Second Edition). Malabar, Florida: Krieger Publishing Company, 1989.

165. Shuler S.F., Holmes J.W. and Wu X. "Influence of Loading Frequency of the Room-Temperature Fatigue of a Carbon-Fiber/SiC-Matrix Composite," *J. Amer. Cer. Soc.*, *76*(9):2327–2336 (1993).

166. Singh D. and Singh J.P. "Effect of High-Temperature Loading on Mechanical Properties of Nicalon Fibers and Nicalon Fiber/SiC Matrix Composites," *Ceramic Engineering and Science Proceedings*, *14*(7-8):1153–1164 (1993).

167. Singh R.N. "Influence of Interfacial Shear Stress on First Matrix Cracking Stress in Ceramic Matrix Composites," *J. Amer. Cer. Soc.*, *72*:2930–2937 (1990).

168. Smith P.A. and Wood J.R. "Poisson's Ratio as a Damage Parameter in Static Tensile Loading of Simple Crossply Laminates," *Composites Science and Technology*, *38*:85–93 (1990).

169. Soerensen B.F. and Talreja R. "Toughness of Damage Tolerant Continuous Fibre Reinforced Ceramic Matrix Composites," *Journal of the European Ceramic Society*, *15*(11):1047 (1995).

170. Solti J.P., Mall S. and Robertson D.D. "A Simplified Approach for Modeling Cross-Ply Ceramic Matrix Composites Under Quasi-Static Loading." *ICCE/2: Second International Conference on Composites Engineering*, edited by D. Hui. 691–692. International Community for Composites Engineering and College of Engineering, University of New Orleans, 1995.

171. Solti J.P., Mall S. and Robertson D.D. "Criteria for Matrix Failure in Ceramic Matrix Composites," *In press* (1995).

172. Solti J.P., Mall S. and Robertson D.D. "Micromechanics Analysis of Fatigue in Cross-Ply Ceramic Matrix Composites," *In press* (1995).

173. Solti J.P., Mall S. and Robertson D.D. "Modeling Behavior of Cross-Ply Ceramic Matrix Composites Under Quasi-Static Loading," *Advanced Composite Materials, In press* (1995).

174. Solti J.P., Mall S. and Robertson D.D. "Modeling Damage in Unidirectional Ceramic Matrix Composites," *Composites Science and Technology, 54*:55–66 (1995).

175. Solti J.P., Mall S. and Robertson D.D. "Modeling of Progressive Damage in Unidirectional Ceramic Matrix Composites." *Recent Advances in Composite Materials 56*, edited by White S.R., Hahn H.T. and Jones W.F. 1–11. Joint Applied Mechanics and Materials Summer Conference, Los Angeles, California, 1995.

176. Solti J.P., Mall S. and Robertson D.D. "A Simplified Approach for Modeling Fatigue in Unidirectional Ceramic Matrix Composites," *Journal of Composites Technology and Research, In press* (1996).

177. Sorensen B.F. and Talreja R. "Effects of Nonuniformity of Fiber Distribution On Thermally- Induced Residual Stresses and Cracking in Ceramic Matrix Composites," *Mechanics of Materials : An International Journal, 16*(4):351–364 (November 1993).

178. Sorensen B.F., Talreja R. and Sorensen O.T. "Micromechanical Analysis of Damage Mechanisms in Ceramic Matrix Composites During Mechanical and Thermal Cycling," *Composites, 24*(2):129–140 (1993).

179. Spearing S.M. and Zok F.W. "Stochastic Aspects of Matrix Cracking in Brittle Matrix Composites," *J. Engr. Mater. and Tech., 115*(3):314–418 (1993).

180. Sudheendra H.N., Saini V., Hsu D.K. and Jeong H. "Measurement of Elastic Moduli in Ceramic Compacts and Ceramic Matrix Composites As a Function of Porosity Content," *Review of Progress in Quantitative Nondestructive Evaluation, 14B*:1217 (1995).

181. Sudreau F., Olangnon C., Fantozzi G. and Leclercq O. "A Refined Statistical Approach to Thermal Fatigue Life Prediction," *J. Mater. Sci., 27*(20):5539–5546 (1992).

182. Swanson S.R. "On the Mechanics of Microcracking in Fiber Composite Laminates Under Combined Stress," *J. Engr. Mater. and Tech., 111*:145–149 (1989).

183. Talreja R. "Transverse Cracking and Stiffness Reduction in Composite Laminates," *J. of Comp. Mater., 19*:355–375 (July 1985).

184. Talreja R. "Fatigue of Fibre-Reinforced Ceramics." *Proceedings of the 11th. Risø International Symposium on Metallurgy and Materials Science: Structural Ceramics - Processing, Microstructure, and Properties.* 145–159. Risø National Laboratory, Roskilde, Denmark, 1990.

185. Talreja R. "Continuum Modelling of Damage in Ceramic Matrix Composites," *Mechanics of Materials*, *12*(2):165–180 (October 1991).

186. Tandon G.P. and Pagano N.J. "Modeling of Interfacial Debonding in Brittle Matrix Composites." *Proceedings of the 7th Technical Conference of the American Society for Composites*. 307–316. Proceedings of the American Society for Composites 1992. Publ. by Technomic Publ. Co. Inc., Lancaster, Pa., 1992.

187. "The New Materials Society Challenges and Opportunities." Vol. 1: New Materials Markets and Issues, Vol. 2: New Materials Science and Technology, U.S. Department of the Interior, Bureau of Mines, 1990.

188. Timoshenko S. and Goodier J.N. *Theory of Elasticity* (Second Edition). New York: McGraw-Hill Book Company, Inc., 1951.

189. Vagaggini E., Domergue J.-M. and Evans A.G. "Relationships Between Hysteresis Measurements and The Constituent Properties of Ceramic Matrix Composites: I, Theory," *Journal of the American Ceramic Society*, *78*(10):2709 (1995).

190. Vaidya R.U. and Chawla K.K. "Effect of Strain Rate on the Fracture of Ceramic Fiber Reinforced Glass Matrix Composites," *J. Matr. Sci. Lett.*, *29*(13):3535–3541 (1991).

191. Vogel W.D. and Spelz U. "Cost-Effective Production Techniques for Continuous Fiber Reinforced Ceramic Matrix Composites," *Ceramic Transactions*, *51*:255 (1995).

192. Vogel W.D., Hertel D., Rebstock K. and Haug T. "Integrated Oxidation Protection of Ceramic Matrix Composites," *Silicates Industriels*, *60*(7/8):189 (1995).

193. Walter M.E. and Ravichandran G. "An Experimental Investigation of Damage Evolution in a Ceramic Matrix Composite," *J. Engr. Matrs. and Tech.*, *117*:101–107 (Jan 1995).

194. Wang A.S.D. and Crossman F.W. "Initiation and Growth of Transverse Cracks and Edge Delamination in Composite Laminates, Part 1. An Energy Method," *J. Comp. Mat.*, *14*:71–87 (1980).

195. Wang A.S.D., Chou P.C. and Lei S.C. "A Stochastic Model for the Growth of Matrix Cracks in Composite Laminates," *J. of Comp. Mater.*, *18*:239–254 (May 1984).

196. Wang A.S.D., Huang X.G. and Barsoum M.W. "Matrix Crack Initiation in Ceramic Matrix Composites Part II: Models and Simulation Results," *Composites Science and Technology*, *44*:271–282 (1992).

197. Wang S.W. and Parvizi-Majidi A. "Mechanical Behavior of Nicalon™ Fiber-Reinforced Calcium Aluminosilicate Matrix Composites," *Ceramic Engineering and Science Proceedings*, *11*(9-10):1607–1616 (1990).

198. Wang Y., Hui C.Y. and Jagota A. "Transverse Fracture in Laminated Fiber-reinforced Brittle Matrix Composites," *Mechanics of Materials : An International Journal*, *15*(3):183–200 (May 1993).

199. Weidenaar W.A. *Behavior of a Centrally Notched Cross-Ply and Unidirectional Ceramic Matrix Composite in Tension-Compression Fatigue*. MS thesis, AFIT/GAE/ENY/92D-26, School of Engineering, Air Force Institute of Technology (AETC), Wright-Patterson AFB, Ohio, December 1992.

200. Weitsman Y. and Beltzer A.I. "An Eccentric Shear-lag Model and Implications on the Strength of Fibrous Composites," *Int. J. Solids Structures*, *29*(11):1417–1431 (1992).

201. Weitsman Y. and Zhu H. "Multi-Fracture of Ceramic Composites," *J. Mech. Phys. Solids*, *41*(2):351–388 (1993).

202. Wijeyewickrema A.C. and Keer L.M. "Matrix Fracture in Brittle Matrix Fiber-reinforced Composites," *International Journal of Solids and Structures*, *28*(1):43 (1991).

203. Worthem D.W. and Ellis J.R. "Thermomechanical Fatigue of Nicalon™/CAS Under In-Phase and Out-of-Phase Cyclic Loadings," *Ceramic Engineering and Science Proceedings*, *14*(7-8):292–302 (1993).

204. Wu X.and Holmes J.W. ""'Tensile Creep and Creep-Strain Recovery Behavior of Silicon Carbide Fiber/Calcium Aluminosilicate Matrix Ceramic Composites," *J. Amer. Cer. Soc.*, *76*(10):2695–2700 (1993).

205. Xia Z.C. and Hutchinson J.W. "Matrix Cracking of Cross-Ply Ceramic Composites," *Acta Metall. Mater.*, *42*(6):1933–1945 (1994).

206. Xia Z.C., Carr R.R. and Hutchinson J.W. "Transverse Cracking in Fiber-Reinforced Brittle Matrix, Cross-Ply Laminates," *Acta Metall. Mater.*, *41*(8):2365–2376 (1993).

207. Yang X.F. and Knowles K.M. "On the First-Matrix-Cracking Stress in Unidirectional Fiber-Reinforced Brittle Materials," *J. Mater. Res.*, *8*(2):371–376 (1993).

208. Yue C.Y., Loh N.L. and Lee L.J. "The Interfacial Properties of Metal-Matrix and Ceramic Matrix Composites," *Mechanical and Corrosion Properties. A, Key Engineering Materials*, *108/110*:165 (1995).

209. Zawada L.P., Butkus L.M. and Hartman G.A. "Room Temperature Tensile and Fatigue Properties of Silicon Carbide Fiber Reinforced Aluminosilicate Glass," *Ceramic Engineering and Science Proceedings*, *1*(9-10):1592–1606 (1990).

210. Zawada L.P., Butkus L.M. and Hartman G.A. "Tensile and Fatigue Behavior of Silicon Carbide Fiber-Reinforced Aluminosilicate Glass," *J. Amer. Cer. Soc.*, *74*(11):2851–2853 (1991).

211. Zhang J., Fan J. and Soutis C. "Analysis of Multiple Matrix Cracking in $[\pm\Theta_m/90_n^\circ]$ Composite Laminates. Part 2: Development of Transverse Ply Cracks," *Composites*, *23*:299 (1992).

212. Zhu H. and Weitsman Y. "Failure Progression in Unidirectionally Reinforced Ceramic Composites." *Damage Mechanics in Composites 32*, edited by D.H. Allen. 155–179. ASME, 1992.

213. Zok F.W. and Spearing S.M. "Matrix Crack Spacing in Brittle Matrix Composites," *Acta Metall. Mater.*, *40*(8):2033–2043 (1992).

214. Zweben C. and Rosen B.W. "A Statistical Theory of Material Strength With Application To Composite Materials," *J. Mech. Phys. Solids*, *18*:189–206 (1970).

Vita

Captain James P. Solti ██ b. He
graduated from Harbor High School in 1984 and attended the United States Air
Force Academy from 1984-1988. Upon graduating on 1 June 1988, Captain Solti
earned a Bachelor of Science Degree in Engineering Sciences; was commissioned as a
second lieutenant in the United States Air Force, and was assigned to the Weapons
Integrations Technology Section of the Aeromechanics Division, Air Force Armament
Laboratory, Eglin Air Force Base, Florida. While in Florida, Captain Solti earned a
Masters of Science in Management from Troy State University, May 1991. In June of
1991, Captain Solti entered the Air Force Institute of Technology, Graduate School of
Engineering, Wright-Patterson Air Force Base, Ohio, and graduated with a Master
of Science degree in Aeronautical Engineering in December, 1992. He subsequently
entered the Doctoral program in January of the following year. Captain Solti is
married to the former Christine Miller of Sheridan, Wyoming. They were married
████████████ in Colorado Springs.

Permanent address: 2716 Douglas Road
                    Ashtabula, OH 44004

VITA-1

REPORT DOCUMENTATION PAGE

Public reporting burden for this collection of information is estimated to average 1 hour per response, including the time for reviewing instructions, searching existing data sources, gathering and maintaining the data needed, and completing and reviewing the collection of information. Send comments regarding this burden estimate or any other aspect of this collection of information, including suggestions for reducing this burden, to Washington Headquarters Services, Directorate for Information Operations and Reports, 1215 Jefferson Davis Highway, Suite 1204, Arlington, VA 22202-4302, and to the Office of Management and Budget, Paperwork Reduction Project (0704-0188), Washington, DC 20503.

1. AGENCY USE ONLY (Leave blank)	2. REPORT DATE March 1996	3. REPORT TYPE AND DATES COVERED Doctoral Dissertation

4. TITLE AND SUBTITLE
MODELING OF PROGRESSIVE DAMAGE IN FIBER-REINFORCED CERAMIC MATRIX COMPOSITES

5. FUNDING NUMBERS

6. AUTHOR(S)
James P. Solti, Capt, USAF

7. PERFORMING ORGANIZATION NAME(S) AND ADDRESS(ES)
Air Force Institute of Technology, WPAFB OH 45433-6583

8. PERFORMING ORGANIZATION REPORT NUMBER
AFIT/DS/ENY/96-2

9. SPONSORING/MONITORING AGENCY NAME(S) AND ADDRESS(ES)
Aero-Propulsion and Power Directorate
Mr. Ted Fecke
WL/POTC, WPAFB OH 45433

10. SPONSORING/MONITORING AGENCY REPORT NUMBER

11. SUPPLEMENTARY NOTES

12a. DISTRIBUTION/AVAILABILITY STATEMENT
Approved For Public Release;
Distribution Unlimited

12b. DISTRIBUTION CODE

13. ABSTRACT (Maximum 200 words)

An analytic methodology is developed to model the response of fiber-reinforced ceramic matrix composites (CMCs) when subjected to monotonic and fatigue loadings. The analysis requires the formulation of (1) a micromechanics model which defines the laminate's geometry and constitutive relationship; (2) failure criteria which estimate the extent of microstructural damage, and, finally, (3) a means of analyzing frictional slip, fiber pull-out, interfacial wear and laminate failure. For the present study, the behavior of unidirectional and cross-ply CMCs is investigated using modified shear-lag theory in conjunction with a set of failure criteria with a minimum reliance on empirical data. The damage mechanisms considered are matrix cracking, fiber/matrix interfacial debonding and fiber fracture. The stress-strain response under monotonic tensile loading, and the fatigue life (S-N relationship) and stress-strain hysteresis under cyclic loading obtained from the present solution are compared with their experimental counterparts. They are in good agreement with one another. As expected, the assumed degradation in the frictional resistance along the constituent interface plays a dominant role in determining the material response.

14. SUBJECT TERMS
Ceramic Matrix Composites, Shear-Lag Theory, Composite Modeling, Micromechanics Analysis, Fatigue, Damage Progression, CMCs

15. NUMBER OF PAGES
336

16. PRICE CODE

17. SECURITY CLASSIFICATION OF REPORT UNCLASSIFIED	18. SECURITY CLASSIFICATION OF THIS PAGE UNCLASSIFIED	19. SECURITY CLASSIFICATION OF ABSTRACT UNCLASSIFIED	20. LIMITATION OF ABSTRACT UL